The Pennsylvania State University

The Graduate School

Graduate Program in Neuroscience

MAGNETIC RESONANCE IMAGING AND HISTOLOGICAL ANAYLYSIS

OF BETA – AMYLOID PLAQUES IN HUMAN ALZHEIMER'S DISEASE AND

APP/PS1 TRANSGENIC MICE

A Dissertation in

Neuroscience

by

Mark David Meadowcroft

Submitted in Partial Fulfillment
of the Requirements
for the Degree of

Doctor of Philosophy

May 2009

The dissertation of Mark David Meadowcroft was reviewed and approved* by the following:

Qing X. Yang
Professor of Radiology and Neurosurgery
Dissertation Advisor
Chair of Committee

James R. Connor
Distinguished University Professor
Vice-Chair of the Department of Neurosurgery

Paul J. Eslinger
Professor of Neurology

Michael B. Smith
Affiliate Professor of Radiology

Robert J. Milner
Professor of Neural and Behavioral Sciences
Director of the Neuroscience Graduate Program

* Signatures are on file in the Graduate School.

ABSTRACT

Alzheimer's Disease (AD) is a progressive neurological disorder characterized by the hallmark beta-amyloid (Aβ) plaques and neurofibrillary tangles (NFT) found in the neocortex of brain tissue samples. Other associated pathological changes in the brain consist of degeneration of brain tissue via loss of neurons and neuronal changes associated with loss of synapses and dendritic branch dearborization (1). The disease consists of a general progression of cognitive and memory impairment leading to an insidious dementia like state followed by eventual patient fatality. Above the age of 65 years old the incidence rate of Alzheimer's increases exponentially with age. It is believed that one in ten individuals older than the age of 65 and approximately half of those older than 85 years old have been diagnosed with the disease (2). Approximately 5 million Americans have AD at the present time and with the increased survival age of the world's inhabitants it is therefore poised to become a greater public health threat as our population ages.

Histopathological investigation currently is the only approach that can accurately diagnose an individual with Alzheimer's disease; however these methods can only be completed post mortem. Methods to noninvasively examine tissue *in vivo* have been of great interest in the study of AD and other neurological disorders. Magnetic resonance imaging offers the unique ability to perform detailed *in vivo* evaluation of neural tissue to aid in this endeavor. Imaging of beta-amyloid plaques in human Alzheimer's disease and transgenic models that mimic plaque production has been challenging for AD research. The

development of MR imaging technology capable of visualizing and quantifying Aβ plaques in the Alzheimer's brain is critically important for translational and clinical investigations. Understanding the transverse MR relaxation associated with the neurodegenerative processes in AD would provide insight into future technologies that will aid in clinical studies. Currently, the histo-pathological basis of image contrast and the relaxation mechanism associated with Aβ plaques is not well understood. Analysis and comparison between histology of a tissue sample and MRI in a one-to-one fashion is of importance for validating new imaging methods and contrasts, especially in molecular imaging research. To help in this endeavor, our development of a histological RF coil has been realized and implemented. Formaldehyde fixed tissue samples are cut on a cryostat, placed between two glass coverslips for positioning inside of the histological coil for MR imaging, then following the scanning protocols are carefully removed and histologically stained. The experimental data collected with the histological coil demonstrate the feasibility of imaging thin slices of tissue samples and unambiguously co-registering these MR images to various histological staining results. With the aid of the coil, T_2^*-weighted images and parametric maps were directly compared to histology stains acquired form a set of Alzheimer's disease and transgenic APP/PS1 tissue slices. For AD tissue samples, transverse T_2^* relaxation due to Aβ plaques is shown to be directly associated with the gradation of iron concentration and to a minor degree with plaque size. For the transgenic APP/PS1 model, which generates Aβ plaques and aims to mimic pathology, plaque morphology and size were associated with

image contrast and transverse relaxation. It has been assumed within the MR community that MR contrast associated with beta-amyloid plaques is due to iron concentration alone. However, the contrast due to transgenic plaques with considerably less iron load are equally conspicuous as the human AD plaques in the MR images. These data suggest a duality in the relaxation mechanism were both high focal iron concentration and highly compact fibrillar beta-amyloid masses cause rapid proton transverse magnetization decay. For human AD tissue, the former mechanism is likely the dominant source of T_2^* relaxation; for APP/PS1 animals, the latter is likely the major cause of increased transverse proton relaxation rate in beta-amyloid plaques. Histological evaluation on the APP plaques and AD plaques demonstrate important differences in iron load and plaque morphology that are hypothesized to be related to differences in transverse relaxation mechanisms. This insight is essential for understanding the histo-pathological underpinning of MRI measurements associated with Aβ plaques.

Transgenic mouse models that reproduce neuropathology are important in understanding disease etiology and testing new clinical procedures. Utilization of the transgenic APP/PS1 model brought into the light important dissimilarities between the naturally occurring Aβ plaques found in the AD brain and those engineered to amass in the transgenic model. Understanding the benefits and disadvantages of the APP/PS1 mouse model is important in considering the outcome from studies involving their usage and eventually transitioning these treatments to the *in* vivo AD brain. Using various histological stains and

microscopy methods aimed at viewing plaques morphology, iron management and inflammatory response we show that there are distinct differences between the naturally occurring human AD plaques and those found in the APP/PS1 model. Clear morphological differences in plaque composition and ultra-structure allude to differences in amyloidogenesis and component fibril formation. Transgenic animal plaques are morphologically distinct from Alzheimer's plaques as seen in both low magnification traditional microscopy and ultra-high magnification transmission electron microscopy. Microglial and astrocyte staining shows a differing pattern of inflammatory response being much more pronounced in the AD neural tissue compared to the transgenic tissue. Iron mismanagement and focal iron deposition is found ubiquitously throughout the AD tissue cortex, with plaques showing a close relationship to iron accumulation within them, and is not seen in the transgenic model. The data presented here emphasizes pronounced histological grounds for MR relaxation differences between naturally occurring Aβ plagues in the AD brain and those instituted to produce in the APP/PS1 transgenic mouse model. The data suggest that utilization of these transgenic models for various magnetic resonance, histological and pharmacological studies of Alzheimer's disease should be done with the consideration of these observations.

The evolution and translation of the MR approaches outlined in this work into the clinical domain to accurately diagnose AD and quantify *in vivo* beta-amyloid plaques would be advantageous for future medical diagnosis. The data presented here represents a foundation for understanding the transverse

relaxation mechanisms associated with beta-amyloid plaques in Alzheimer's disease. Translating these results to an *in vivo* clinical setting presents a challenge to the MR community. Currently the methods presented here are beyond the resolution limitations and time constraints of low field clinical scanners. However, with advancements in future MR technology there is potential for expanding this research into a valid system.

TABLE OF CONTENTS

LIST OF FIGURES

LIST OF TABLES

LIST OF ABBREVIATIONS

Å   angstrom

AA   amino acid

Aβ   beta-amyloid

$A\beta_{40}$ beta-amyloid – 40 amino acids in length

$A\beta_{42}$ beta-amyloid – 42 amino acids in length

AD   Alzheimer's disease

Al   aluminum

APP   amyloid precursor protein

APP/PS1   amyloid precursor protein / presenilin 1

ApoE   apolipoprotein E

ApoE4   apolipoprotein E4

B_0 external static magnetic field

B_1 RF magnetic field

C   capacitance

^{12}C   carbon

°C   Celcius

C57BL/6   laboratory strain of black 6 mice

Ca   calcium

cDNA   circular deoxyribonucleic acid

cm   centimeter

Co   copper

dB   decibel

dH_2O	distilled Water
DAB	3,3' – diaminobenzine
DNA	deoxyribonucleic acid
EC	extracellular
FAD	familial Alzheimer's disease
Fe	iron
Fe^{+2}	ferrous iron
Fe^{+3}	ferric iron
$FeCl_3$	ferric chloride
FITC	fluorescein isothiocyanate
g	gram
GFAP	glial fibrillary acidic protein
H	hydrogen
^1H	hydrogen proton
H_2O_2	hydrogen peroxide
H-ferritin	heavy chain subunit of ferritin
HCl	hydrochloric acid
IBA1	ionized calcium-binding adaptor molecule 1
IC	intracellular
IgG	immunoglobulin G
kb	kilobase pair
kDa	kilodalton
kg	kilogram

L	inductance
L-ferritin	light chain subunit of ferritin
MHz	megahertz
mg	milligram
MGE	multi gradient echo
ml	milliliter
mm	millimeter
mM	millimolar
MR	magnetic resonance
MRI	magnetic resonance imaging
MRM	magnetic resonance microscopy
ms	millisecond
n	number
N	nitrogen
NaCl	sodium chloride
NEX	number of excitations (averages)
nm	nanometer
NFT	neurofibrillary tangle
P	phosphorus
PBS	phosphate buffered saline
PBST	phosphate buffered saline with tween
$OH^{\cdot}$	hydroxyl radical
PS1	presenilin 1

PS2	presenilin 2
RER	rough endoplasmic reticulum
R_2	$1/T_2$ – transverse relaxation
R_2^*	$1/T_2^*$ – rapid loss in transverse magnetization
RF	radio frequency
ROI	region of interest
ROS	reactive oxygen species
s	second
SNR	signal-to-noise ratio
SOD	superoxide dismutase
T	tesla
T_1	longitudinal relaxation
T_2	transverse relaxation
T_2^*	rapid loss in transverse magnetization
TEM	transmission electron microscopy
TM	transmembrane
TMHF	3,5,5 – trimethylhexanoyl-ferrocene
TE	echo-time
TR	time to repeat
μl	microliter
μm	micrometer
V	volt
Zn	zinc

ACKNOWLEDGEMENTS

This thesis encompasses a large scope of work that only would have been possible with continued support from those around me . . . family, friends, and co-workers. To my mom, dad, bro Jim and Alison; thank you for always being there and supporting me, even when the road gets bumpy. To all of my instructors along the way; those like Mr. Kerns who established a fascination within me for science, Jeff Hollerman who taught me that the brain is awe-inspiring (aka, really cool) and Ron Mumme who said that all things in biology are somehow interconnected.

I would like to sincerely thank my colleagues, mentors and friends who have helped direct me along the way. To my graduate thesis advisor Dr. Qing Yang for providing me a place to grow, treating me like another son and for being patient because science doesn't always follow a straight line to discovery. To Dr. Michael Smith who taught that a deeper understanding of basic science principles is at the heart of sound scientific discovery. To the entire Center for NMR Research workforce, past and present alike, for being a second family even into the wee hours of the night. To the entire Connor laboratory, my second scientific home who provided not only insights into the science but friendship throughout my time in Hershey. To close friends who have asked the question a million times 'so what do you do?' but who always were there for me. And last but not least; to my dog Rusty . . . who is always smiling when I walk through the door and listens intently no matter what.

Chapter 1

Introduction

1.1 – Alzheimer's disease

Alzheimer's disease (AD) is a progressive neurological disorder with increasing prevalence in modern society and currently is the sixth leading cause of death in the United States. As many as five million American's are currently living with Alzheimer's disease, which is expected to sharply rise over the next century due to the ever increasing human lifespan leading to increasing amounts of elderly individuals in our society. Alzheimer's disease is the most common form of dementia and is generally described as a loss of memory, neuronal function and intellectual abilities that interfere with daily life. It was first described in 1906 by the German physician Alois Alzheimer, but is considered to have been prevalent undiagnosed in human society for thousands of years prior to its modern description (3). Classical pathological changes seen in AD include the formation and presence of beta-amyloid (Aβ) senile plaques and neural fibrillary tangles (NFT) in the human neocortex. The pathogenesis of Aβ plaques in the AD brain has been found to start in the entorhinal cortex (archicortical regions such as the hippocampal formation) of the human brain and progress rostrally towards the frontal lobes, caudal-laterally towards the temporal lobes and dorsally into the sensory motor cortex (4). Within these affected regions there is massive neuronal loss leading to neocortical atrophy in these regions. There is no known cure for AD and diagnosis is based upon clinical and familial

observation of the resulting dementia and impending inability to lead a normal life. Positive diagnosis of the disease with absolute certainty is currently only available with histological and pathological analysis of post mortem tissue samples during autopsy.

1.1.1 – Genetic mutations involved in Alzheimer's

With the mapping of the human genetic sequence and the ability to quickly and accurately complete genetic screening of affected individuals and their family members numerous genetic mutations associated with the disease have been discovered in the last two decades. Approximately 10 percent of AD cases are believed to be of the early onset familial AD (FAD) variety, which exhibit autosomal dominant inheritance, with the remaining 90 percent being sporadic AD with a later clinical onset (5). The role of each mutation is still being elucidated within the scientific community with each playing a role is what is currently being understood as the disease process. The etiology of AD is multifaceted and amazingly complex with numerous genetic factors that each playing an individual role in the whole disease process.

1.1.1.1 – Amyloid Precursor Protein – APP

Amyloid precursor protein (APP) is an integral type I membrane protein expressed in numerous tissue types and predominantly is found concentrated near the synaptic cleft of neurons. The function of is not currently known but it has been implicated in both cholesterol metabolism (6) and synaptic function and

as such with neural plasticity having been demonstrated that hippocampal neuron cells in cultures that lack APP have enhanced excitatory postsynaptic currents and increased synaptic vesicle pools (7). In addition, APP knockout mice have been produced that are viable and have the phenotypic effect of impaired long-term potentiation illustrating the importance of APP in memory function (8). APP is sequentially processed by at least three proteinases termed α, β and γ-secretases along two pathways, one amyloidogenic (producing beta-amyloid) and the other non-amyloidogenic. Cleavage by α-secretase or β-secretase occurs within the luminal/extracellular domain and results in the shedding of nearly all the ectodomain to yield two different peptides termed APPsα or APPsβ. The sequence is then cut by γ-secretases within the membrane to produce either p3 (α-secretase cleavage, non-amyloidogenic) or Aβ (β-secretase cleavage, amyloidogenic) (9) (Figure 1.1.1.1.1). The genetic sequence for APP is found on chromosome 21 and contains an estimated 18 exons in 240 kilobases of DNA. Individuals with Down syndrome invariably form similar plaques and classical AD pathology by the age of 50 years due to the fact that they have a trisomy of chromosome 21 that leads to the overproduction of APP, pointing to the importance of APP in plaque formation (10). Dysregulation of APP processing leads to increased levels of Aβ which induces cell death processes and disturbed axonal transport, leading to defects in cognition, synaptic plasticity and development of tau pathology (9). There are several isoforms that have been found in humans ranging from 365 to 770 amino acids long due to several alternative splicing pathways, with specific isoforms being

expressed in certain cell lines presumably due to alternative functionality (11).

The amino acid sequence for APP has been functionally conserved across

species and denotes the underlying importance of the yet to be determined

conserved physiological function of APP (9). There are many known genetic

mutations in APP, with the most widely recognized being a double mutation in

position 670/671 known as the "Swedish mutation" due to its prevalence in the

Swedish population resulting in a 695 amino acid long peptide (12). Many

individuals who harbor APP mutations develop familial AD rather than the more

common sporadic AD, which is not linked to any known APP mutation. Research

has shown that virtually any mutation in the APP gene sequence leads to an

overproduction of beta-amyloid and enhanced plaque formation.

Figure 1.1.1.1.1

Schematic diagram of APP sequential processing (not drawn in scale). EC: extracellular; TM: transmembrane; IC: intracellular. Aβ domain is highlighted in red. For simplicity, only one cleavage site is shown for each enzyme. The APP peptide is cleaved extracellularly by α-secretase or β-secretase and is then cut by γ-secretases within the membrane to produce either p3 (α-secretase cleavage, non-amyloidogenic) or Aβ (β-secretase cleavage, amyloidogenic). (Figure from Zheng *et al.*, 2006 (9))
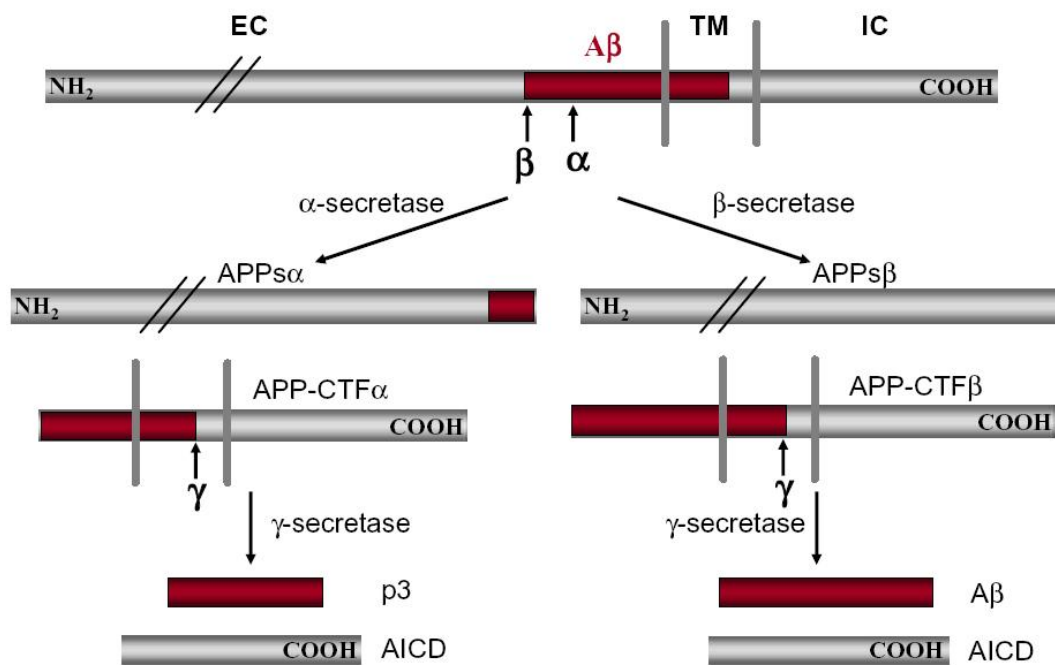
1.1.1.2 – Presenilin 1 and 2

Presenilin 1 and 2 (PS1 and PS2) are multi-pass transmembrane proteins that assemble with other proteins (nicastrin, PEN-2, and APH-1) to form into an active gamma-secretase complex (13). PS1 is a 467 amino acid long polypeptide that is believed to contain between 7 to 9 trans-membrane spanning domains and includes a large hydrophilic loop region located within the cytosol (5). Vertebrate systems possess two presenilin genes, PSEN1 on chromosome 14 in humans that encodes for PS1 and PSEN2 on chromosome 1 which encodes for PS2 (10). Homologues of the presenilins have been found in other mammals and evolutionarily lower life forms including fruit flies (*Drosophila*), frogs (*Xenopus*), nematodes (*Caenorhabditis elegans*), fungi, and plants (*Arabidopsis thaliana*) (14), and indeed PS1 and PS2 have a high degree of homology between themselves (10,15). The connection between the presenilin proteins and AD was exposed when it was established that mutations in PS1 and PS2 are causative in approximately 50% of patients with familial AD (5), and are the primary cause of AD with onset before the age of 55 years (10). Within the last 25 years more than 50 different mutations in PS1 have been described in families with FAD, relaying the importance of these proteins in the pathogenesis of AD (5). All mutations in the presenilins are missense mutations, with the majority in hot spots encoded by exon 8 from residue 260 – 290, except for the mutation resulting in the deletion of exon 9 (PS1ΔE9) (10). The different severe structural changes due to multiple mutation sites results in a paradoxical phenomena where some cause a partial loss of γ-secretase function and others

cause an increase in function (10,16). It appears that the difference occurs based on where the mutation resides. Within the cell the presenilins are located in the membrane of the endoplasmic reticulum and the *cis*-Golgi apparatus (10). The generation of beta-amyloid from APP is known to be a normal processing event in cells, with roughly 90 percent of that normally formed being $A\beta_{40}$ and 10 percent terminating at amino acid 42 ($A\beta_{42}$). Pathogenic mutations in presenilins modify APP processing leading to the selective amplification of $A\beta_{42}$ production (10,17). Currently the mechanism by which mutant presenilins exert their effect on APP processing is not known. Indeed, the normal mechanism by which the presenilins function in the γ-secretase complex is not known either. One model proposes that presenilins are involved in the intracellular trafficking of APP guiding it to specific catalytic binding domains in the γ-secretase complex (10). It is a matter of debate as to the theory of how APP is processed by γ-secretase and the presenilins, but it is known that the last step in processing the APP peptide to produce either $A\beta_{40}$ or $A\beta_{42}$ is carried out by this complex. This leads to the strong suggestion that mutations in presenilins resulting in the alteration of γ-secretase function is one of the main culprits in AD pathogenesis (18). The role of the presenilins is not limited to the cleavage of the APP peptide sequence, as it has been linked the cleavage of numerous other proteins (Notch-1, caspases, β-catenin, to name a few) involved in neuronal development, skeletal formation, and apoptosis. The importance of presenilins is highlighted by the fact that homozygous knockout mice for PS1 do not survive, whereas heterozygous knockout mice are viable without any sign of a phenotypic abnormality (10).

Figure 1.1.1.2.1

Schematic diagram of PS1 membrane topology based on the eight-

transmembrane-domain model. Amino acid residues that are mutated in the

various FAD PS1 mutations are depicted as closed circles. (Figure from

Thinakaran, 1999 (5))

Lumen

Membrane

Cytosol
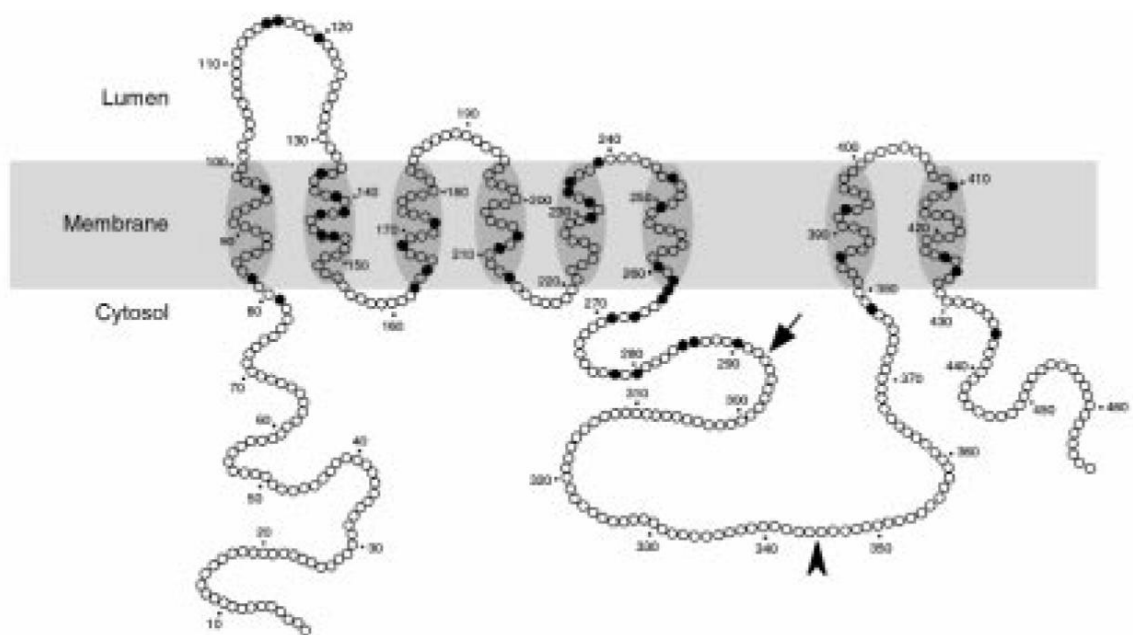
1.1.1.3 – Apolipoprotein E4

Apolipoprotein E4 (ApoE4) is one of the three major ApoE 299 amino acid isoforms whose polymorphic genetic sequence has been mapped to chromosome 19 in humans. The other forms consist of ApoE2 and ApoE3 and are found throughout the human population in differing densities. ApoE3 is considered the neutral genotype, is found in approximately 60 percent of the population, and is not associated with any genetic disorders, unlike ApoE2 and ApoE4. Individuals whom are homozygous for ApoE4 have an estimated 20 times risk of developing AD at some point in their lives (19). Approximately 40 – 65 percent of individuals with AD have at least one copy of the ApoE4 isoform (19). The normal function of the apolipoproteins is to bind lipids and other triglyceride-rich lipoprotein constituents in the liver to form lipoprotein complexes for transport throughout the bloodstream for storage. It has been found that the apolipoproteins are specifically expressed by astrocytes and microglia in neural tissue and are involved in the enhanced direct protein-to-protein proteolytic break-down of the Aβ peptide and disposal through the blood brain barrier (Figure 1.1.1.3.1), supporting a protective role in AD (20-23). The exact mechanism by which the apolipoproteins interact with beta-amyloid is unknown but it has been proposed that they act as an intracellular and extracellular chaperone molecule that influence Aβ deposition, fibril formation and clearance (22,24). The three isoforms have different abilities to perform this role with the ApoE4 variant being the less effective of the three in breaking down the beta-amyloid peptides (20). Apolipoproteins have been found co-localized with beta-

amyloid plaques in human AD tissue samples, both in newly forming and

established plaques (25). This first lead scientists to believe that apolipoproteins

were involved in the generation of beta-amyloid plaques, but while it has been

also been surmised that they are involved in plaque clearance due to clearance

studies using plaque generating mouse models (24). Interestingly, ApoE positive

plaques are seen more frequently in homozygous ApoE4/4 AD brains that in non

ApoE4 carrying and heterozygous ApoE4 AD brains (25). This supplicates the

question as to whether the ApoE4 protein specifically helps induce the formation

of beta-amyloid plaques by potentially concentrating $A\beta$ in brain regions

inundated with too much beta-amyloid. If this is the case then the

apolipoproteins have a duality in mechanism based on the variant(s) the

individual has in their genome (23). ApoE2 and more so for ApoE3 are viewed

as proteins that aid in the clearance of extracellular beta-amyloid while the

ApoE4 genotype, via a yet to be determined mechanism, aids in the chaperoning

of beta-amyloid to facilitate plaque formation. It is a matter of speculation into the

mechanism by which ApoE4 aids plaque formation, but the affinity of the different

ApoE variants for beta-amyloid seems to be at the core of the issue. ApoE

association with $A\beta$ compromises the fundamental lipoprotein binding function of

apoE such that it selectively binds beta-amyloid instead of lipids (26). It could be

that ApoE4 has such a high affinity for $A\beta$ that it is not able to release the peptide

for disposal through the blood brain barrier.   This would concentrate the ApoE4-

$A\beta$ complex throughout affected brain regions such that it ultimately would find its

way to newly formed plaques where the extremely high affinity for self assembly

of the Aβ peptides would strip the peptide from the apolipoprotein (21).

Figure 1.1.1.3.1

ApoE and Aβ plaque formation. ApoE has been implicated in the clearance and deposition of Aβ with pleiotropic effects such that genes encoding ApoE2,3 and 4 influence multiple phenotypic traits. Complexed with Aβ, ApoE facilitates the cellular uptake of Aβ, and ultimately disposal of the peptide through the blood brain barrier. ApoE is also required for the extracellular deposition of Aβ as amyloid via an unknown mechanism. (Figure from Hirsch-Reinshagen *et al.*, 2008 (23)).

Glia

apoE

ABCA1

apoE

Neurons
and Glia

ABCG1

apoE

Blood
Brain
Barrier

Aβ

apoE

Aβ

Cellular uptake
via apoE
receptors

Aβ deposits

15
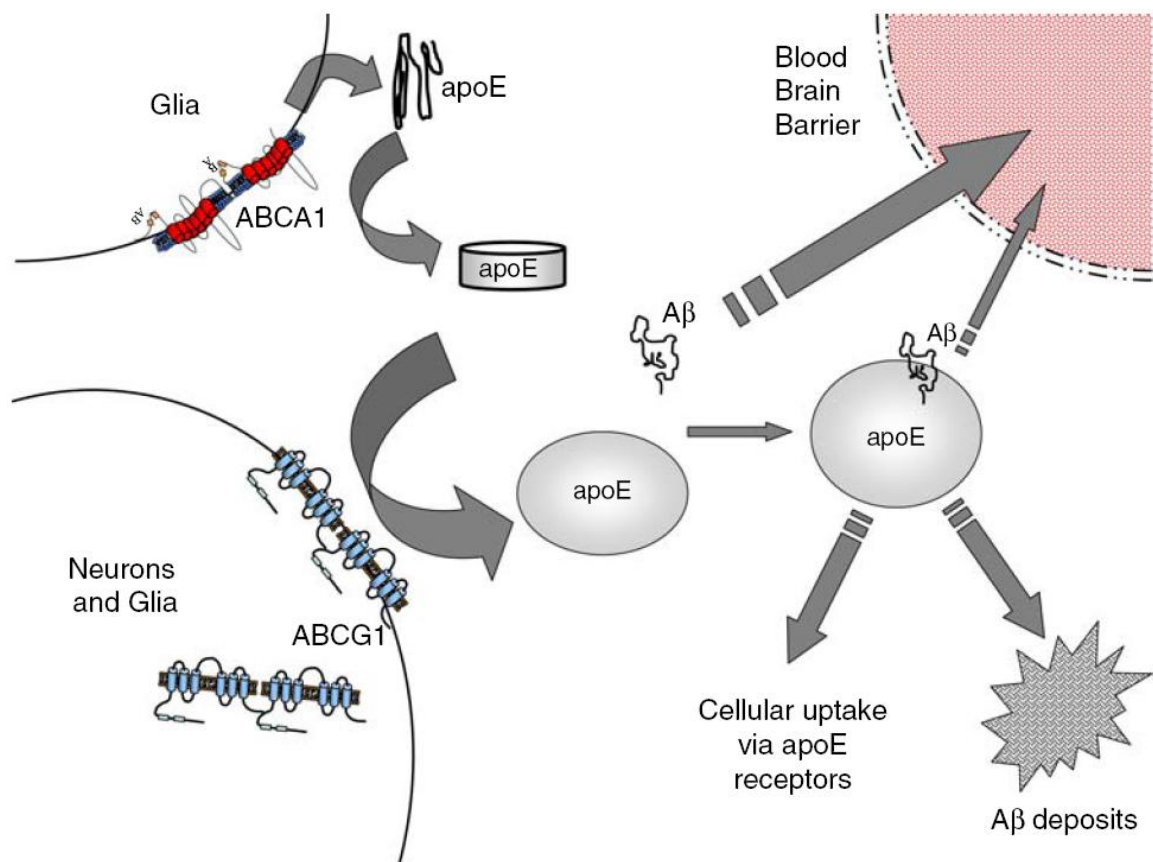
1.1.2 – Beta-Amyloid Plaque Formation

Several human proteins have been identified that form amyloid fibrils *in vivo* (27). More than twenty degenerative conditions affecting the central nervous system feature the deposition of proteins in the form of amyloid fibrils and plaques (28) (Table 1.1.2.1 for a list of amyloid associated diseases). Through the study of these diseases, it has become apparent that the formation of amyloid like structures in not an unusual feature of these proteins but rather a general misfolding property of many polypeptide chains (29). The formation of beta-amyloid plaques is a traditional hallmark associated with the AD brain. However, despite extensive study the exact mechanism by which plaques form is currently unknown. The constituent peptide players, environmental subtleties, and genetic mutations have been associated with plaque formation but their interaction between each other *in vivo* has not been clearly elucidated.

The formation of beta-amyloid from the amyloid precursor protein has been relatively well worked out, but still remains elusive as far as the selective production of $A\beta_{40}$ verses $A\beta_{42}$. As discussed earlier in the APP and presenilin sections, beta-amyloid is the product of the cleavage of APP to form either the amyloidogenic beta-amyloid or p3 (Figure 1.1.1.1.1). APP is first synthesized in the lumen of the endoplasmic reticulum and then undergoes extensive post-translational modification (30). The peptide is then selectively spliced in the extracellular domain as it is excreted by proteases in the secretase family, α-secretase and β-secretase. When sliced by the alpha variant at amino acid 612 the end result is known as the p3 peptide and is the non-amyloidogenic pathway.

Splicing by beta at the 596 amino acid site results in the amyloidogenic formation

of beta-amyloid, generally either 40 or 42 amino acids long but can also be

truncated either on the N-terminal or C-terminal end to form a variety of potential

peptides (31). Following alpha and beta cleavage the peptide is then cleaved

further down the C-terminus direction by γ-secretase in either the 637 or 639

amino acid locations (Figure 1.1.2.1 for splicing locations along the APP peptide).

The cleaved resulting peptide is then released into the cytosol where it is either

maintained intracellularly or excreted by a yet unknown mechanism into the

extracellular domain (30). Figure 1.1.2.2 illustrates the cleavage sequence.

Figure 1.1.2.3 illustrates a potential secretory pathway for Aβ to the extracellular

domain.

Once in the extracellular domain beta-amyloid undergoes specific protein

misfolding and self polymerization to form amyloid fibrils. The 42 amino acid

variant of the peptide has been shown to be much more willing to misfold and

self aggregate to form fibril bundles. This is hypothesized to be due to the

additional two hydrophobic amino acids are found in the $A\beta_{42}$ peptide. When

hydrophilic amino acid substitutions are made for hydrophobic ones during bench

synthesis they reduce the ability of the peptides to aggregate upon themselves

(32). It has been shown that 10-14 AA residues are sufficient for amyloidal fibril

formation (33). Substitution of these hydrophobic residues with other random

hydrophobic residues still results in fibril formation with differing levels of affinity

for one another. These views point toward the notion that the hydrophobic

regions are responsible for the fibril formation (34) because generic

hydrophobicity rather than specific side chains promote aggregation of $A\beta_{42}$. As would be expected with protein tertiary structure, the same is also true when substitutions are made for charged amino acids with non-charges ones, the charge-charge interactions function in concert with the non-ionic hydrophobic interactions (35). When the peptides aggregate together they form both parallel and anti-parallel β-sheet structures with strong hydrogen bonding between the peptides (Figure 1.1.2.4). In reality the beta-amyloid peptides form a twisted β-sheet due to the side chains on the amino acids and because the twisted β-sheet represents a lower energy state than a flat β-sheet (36). The separation between stacked β-sheets is approximately 4.7 Å which is seen to dominate during X-ray diffraction studies giving rise to β-strands when multiple peptides form β-sheets next to one another (37). The β-sheets are then arranged stacked upon one another in such a way that the β-sheets are arranged perpendicular to the axis of the fibrils to form protofilaments (Figure 1.1.2.5) (38). The diameter of the protofilaments is approximately 30 Å, which then arrange upon themselves parallel to each other to form a beta-amyloid fibril of approximately 100 Å in diameter (Figure 1.1.2.6). The beta-amyloid fibril core structure is helical with multiple protofilaments twisting around one another giving a helical repeat (one full twist) of 115.5 Å composed of 24 β-strands (36) (Figure 1.1.2.7). These mature fibrils then aggregate upon themselves via hydrophobic and charged attraction to form beta-amyloid plaque seeds which then overtime accumulate more Aβ fibrils to form beta-amyloid plaques.

Table 1.1.2.1

A list of various human diseases featuring amyloid formation. From

http://en.wikipedia.org/wiki/Amyloid.

Disease	Protein Featured
Alzheimer's disease	Beta amyloid
Type 2 diabetes mellitus	IAPP
Parkinson's disease	Alpha-synuclein
Transmissible spongiform encephalopathy aka "Mad Cow Disease"	Prion
Huntington's Disease	Huntingtin
Medullary carcinoma of the thyroid	Calcitonin
Cardiac arrhythmias	Atrial natriuretic factor
Atherosclerosis	Apolipoprotein AI
Rheumatoid arthritis	Serum amyloid A
Aortic medial amyloid	Medin
Prolactinomas	Prolactin
Familial amyloid polyneuropathy	Transthyretin
Hereditary non-neuropathic systemic amyloidosis	Lysozyme
Dialysis related amyloidosis	b2-Microglobulin
Finnish amyloidosis	Gelsolin
Lattice corneal dystrophy	Kerato-epithelin
Cerebral amyloid angiopathy (Icelandic type)	Cystatin
systemic AL amyloidosis	Immunoglobulin light chain AL
Yeast Prions [Sup35], Rnq1 (parastitic type infection in yeast)	
Sporadic Inclusion Body Myositis	S-IBM
pheochromocytoma	
Osteomyelitis	
Multiple myeloma	

Figure 1.1.2.1

Cleavage locations of α-,β-,and γ-secretase. Beta cleaves APP after Met596 (β)

and Tyr606 (β'), whereas alpha processes APP within the amyloid β-peptide

sequence (α), thereby generating the p3 peptide. γ-Secretase cleavage in the

transmembrane region generates amyloid β peptides of mainly 40 and 42 amino

acid residues long (γ40 and γ42). The asterisks indicate the locations of

mutations causing familial AD. (Figure from De Strooper and Annaert, 2000

(30)).
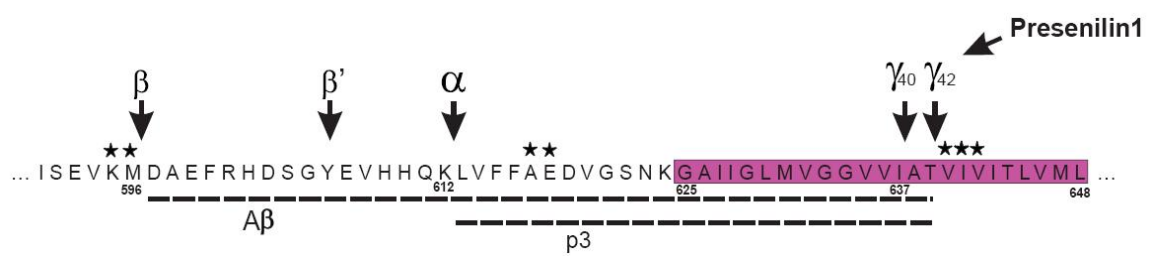
Figure 1.1.2.2

Illustration of beta-amyloid splicing and excretion. Beta secretase cleaves the

APP peptide in the extracellular domain followed by gamma secretase in the

transmembrane region to form the beta-amyloid peptide. (Figure from the

National Institute on Aging, National Institutes of Health)
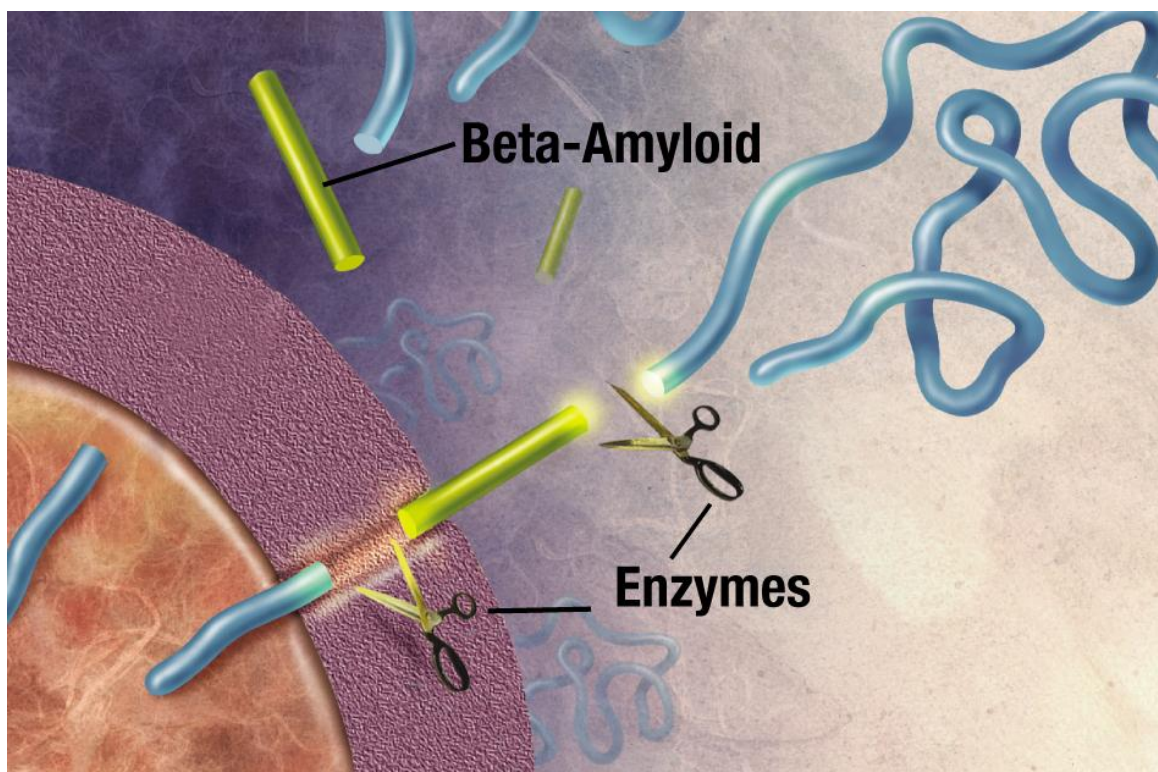
Figure 1.1.2.3

Proposed mechanism for APP and Aβ transportation throughout the cell and into the extracellular space. Putative localization of APP processing in neurons. Following translation in the RER, APP is transported through the Golgi and into the plasma membrane. Full-length APP and C-terminal fragments are re-internalized via the endosomal system and either directed back to the trans-Golgi or incorporated into secondary lysosomes for degradation (solid arrows). C-terminal fragments are cleaved to release the intracellular domain of APP which may modulate gene transcription in the nucleus (dashed arrows). β-Secretase activity is found at the cell surface as well as in secretory vesicles and the trans-Golgi. α-Secretase activity is found in secretory vesicles and endosomes/lysosomes; its activity at the cell surface is uncertain. (Figure from Turner *et al.*, 2003 (31))

Membrane

Secr. Ves.

β

α

Endo.

β

γ

1° Lys.

Trans-G.

β

α

γ

2° Lys.

β

γ

Cis-G.

RER

Nuc.

Full-length APP

sAPPα

sAPPβ

Aβ

p3

C-83

C-99

AICD

26
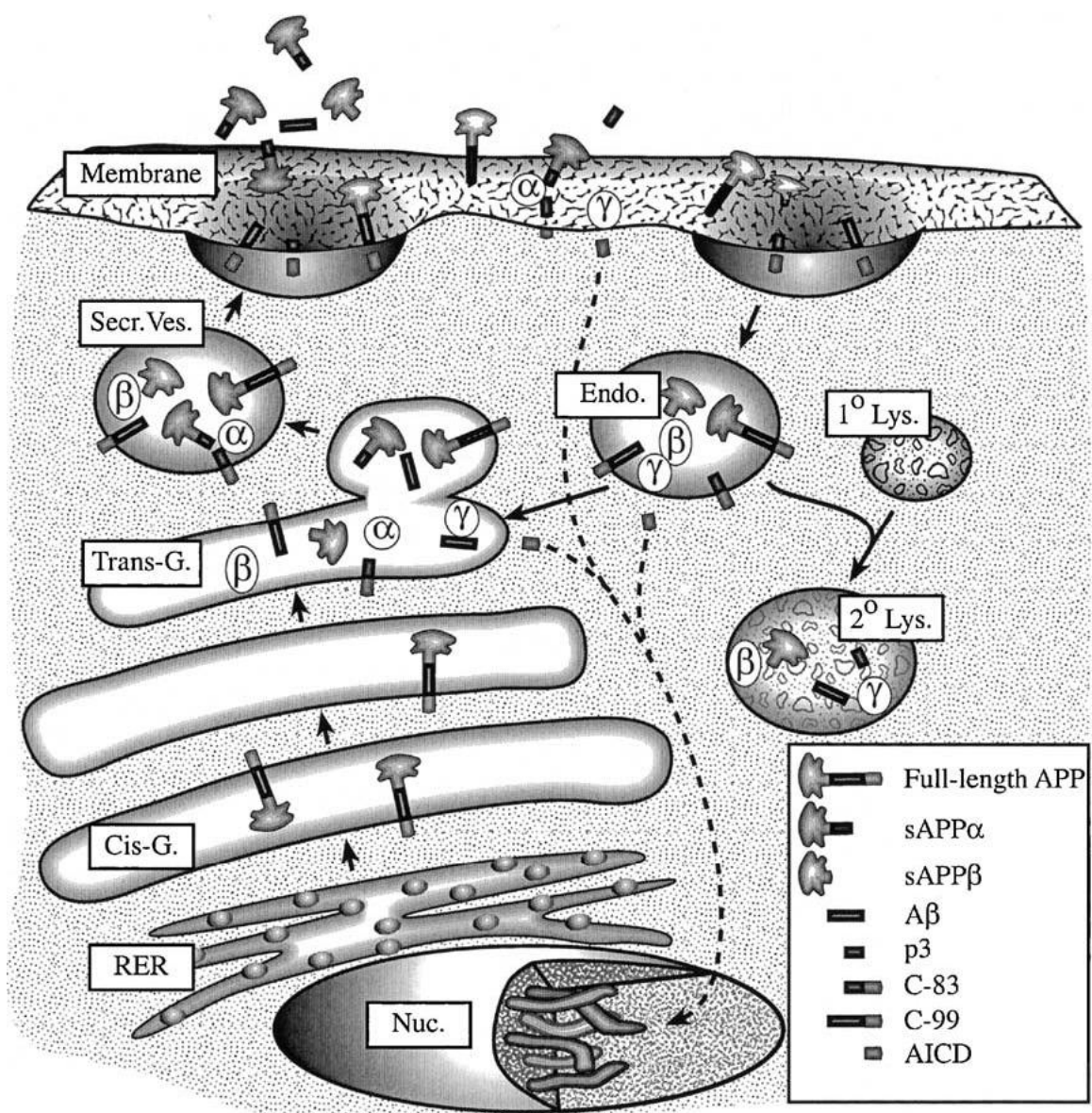
Figure 1.1.2.4

Schematic of β-sheet structure. Representation of hydrogen-bonding patterns in β-sheet structure, showing antiparallel (a) and parallel (b) arrangements of hydrogen bonding. (Figure from Serpell *et al.*, 1997 (36))

a

b
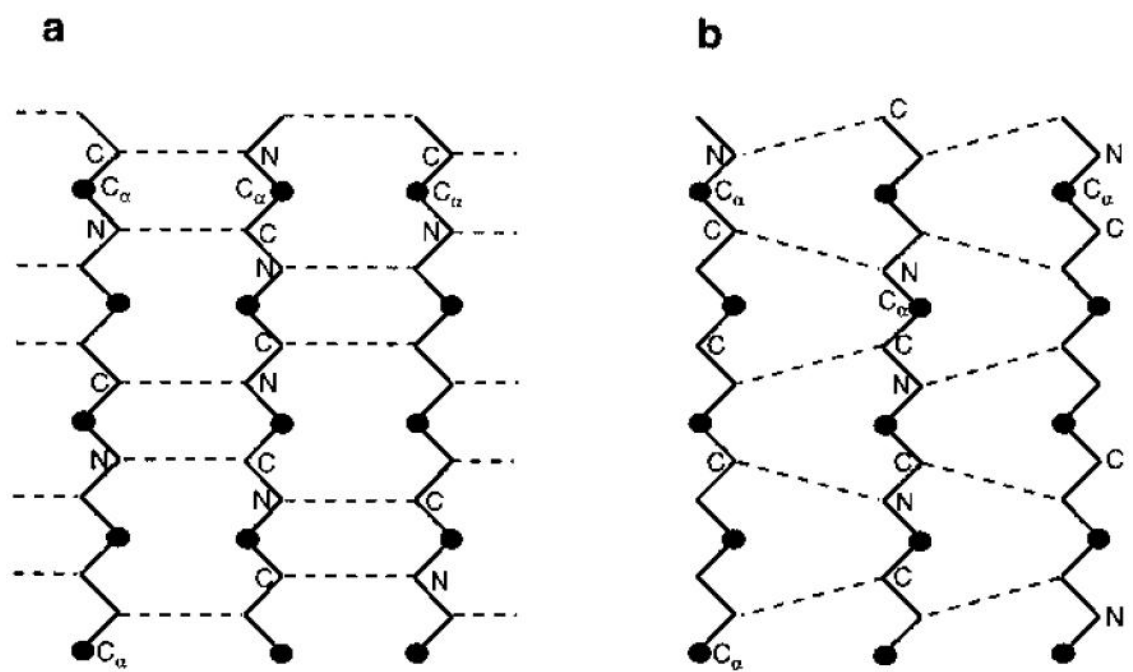
Figure 1.1.2.5

Close up view of a proposed amyloid fibril composed of two proto-filaments. The β-sheets are arranged stacked upon one another in such a way that the β-sheets are arranged perpendicular to the axis of the fibrils and are coming out of the paper. (Figure from Nelson *et al.*, 2005 (38))

Figure 1.1.2.6

Illustration of amyloid fibril size and structure. Schematic diagram showing the probable hierarchical assembly of structures making up a mature amyloid fibril from the continuous hydrogen-bonded β-sheet structure within a protofilament to the organization of the protofilaments. (Figure from Stromer and Serpell, 2005 (37))

100 Å

~30 Å

Fibril

Several protofilaments

Protofilament

β-sheet structure

4.7 Å

subunit (Aβ)

~10 Å
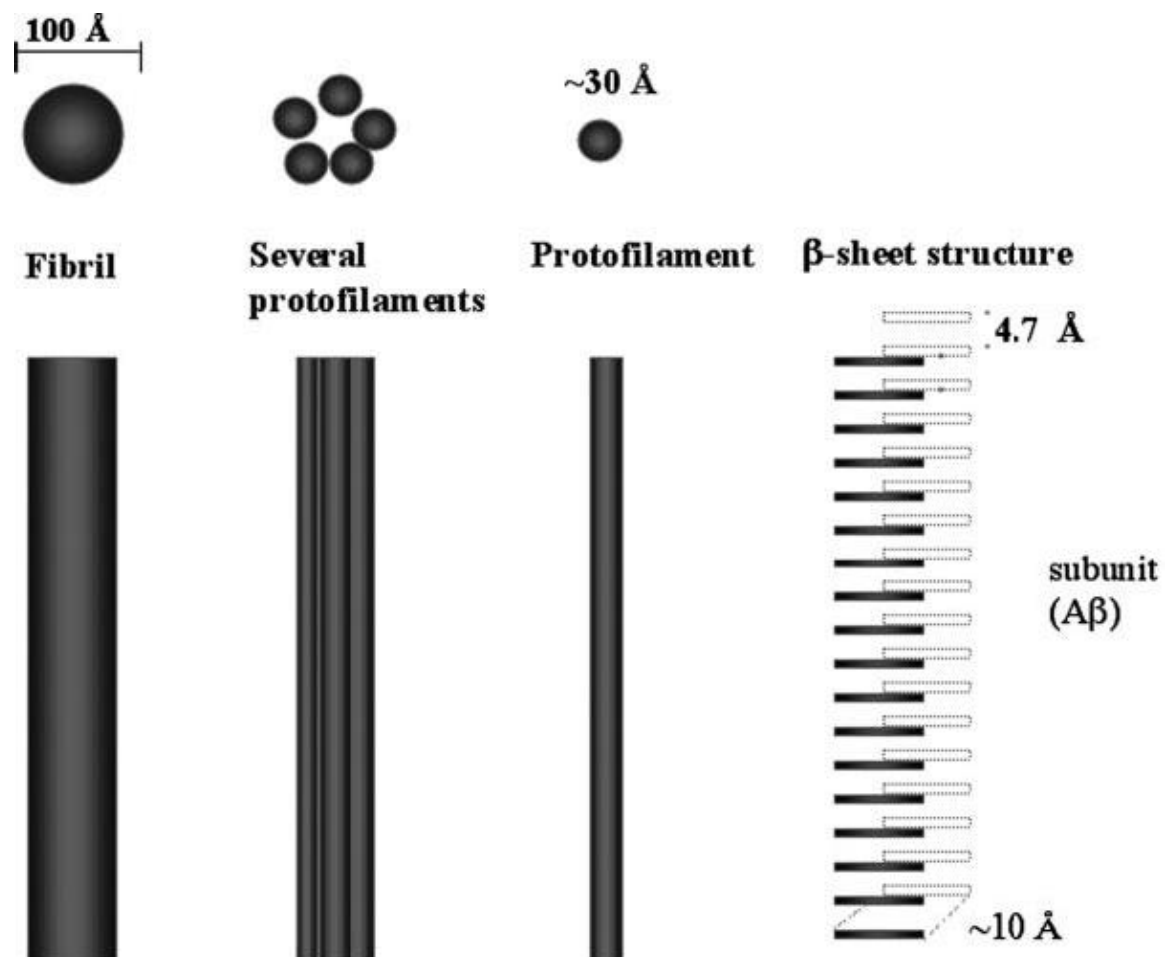
Figure 1.1.2.7

Molecular model of the common core protofilament structure of amyloid fibrils. Numerous β-sheets (four illustrated here) make up the protofilament structure. These sheets run parallel to the axis of the protofilament, with their component β -strands perpendicular to the fibril axis. With normal twisting of the β -strands, the β -sheets twist around a common helical axis which coincides with the axis of the protofilament, giving a helical repeat of 115.5 A° containing 24 β -strands. (Figure from Serpell *et al.*, 1997 (36))

115 Å

24 β–strands
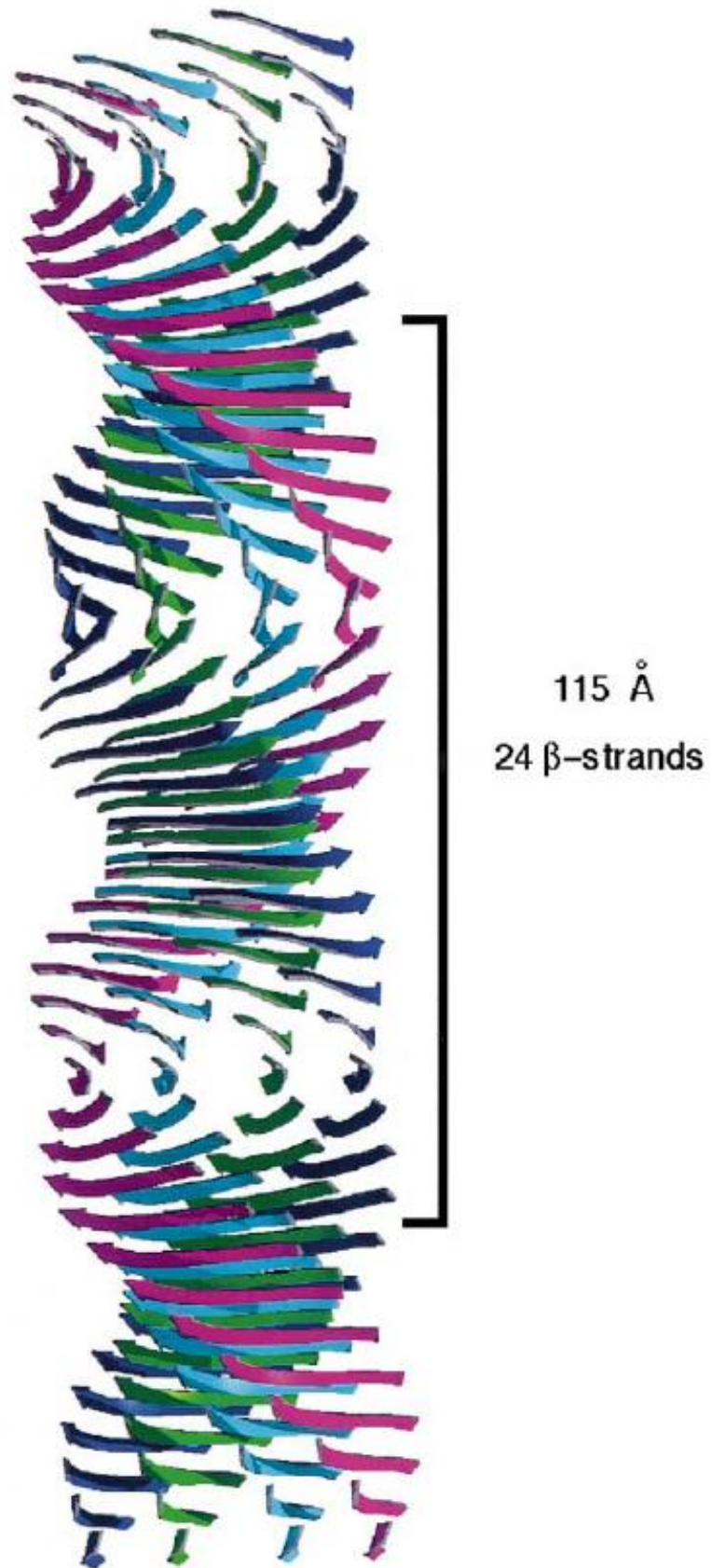
1.1.2.1 – Classification and Morphology of Human Alzheimer's Plaques

When mature Aβ fibrils aggregate upon one another to eventually form beta-amyloid plaques it does not produce consistent plaque morphology and uniformity throughout the AD brain and thus different plaque types arise. The reason for this has been hypothesized to be due to a number of potential factors. Two main hypotheses have been developed to account for the observation that there are plaques with varying morphology in the AD brain. The first states that one type of plaque gradually is converted into another, that plaque stages represent the morphological history of a single plaque. The second hypothesis is that each plaque type evolves independently of the others and that unique *in vivo* environmental factors are responsible (39). There have been numerous classifications of plaque type based on morphology improvised by different investigators (40,41) but there is a general agreement that there are three main plaque classifications throughout human AD neural tissue. Plaques can be classified and assigned into three distinct types, either dense-cored, fibrillar or diffuse (39) (Figure 1.1.2.1.1). Dense-cored plaques have also been described as 'burned out' or 'compact' plaques by other investigators and generally have a solid core composed of a dense arrangement of highly fibrillar Aβ. The core of the plaques is surrounded by a fibrillar halo or coronal region with a relative void of space between the coronal region and the core of the plaque. Both the core and the halo region stain positive for thioflavin-S indicating that they are specifically composed of fibrillar beta-amyloid due to the knowledge that thioflavin-S only is able to bind via intercalation of its aromatic side chains into

the stacked β-sheets of mature fibrils that are long enough (42). Fibrillar plaques

stain positive for thioflavin-S and exhibit dense Aβ accumulation within the

plaque structure without forming a dense spherical core. Dense core and fibrillar

plaques generally are from 30 – 75 µm in diameter, and are found to be as large

as 100 µm. Diffuse plaques are composed mainly of less-fibrillar Aβ fibrils that

are not as long as those found in the other two classifications and stain only

minimally with thioflavin-S and must be viewed microscopically with Aβ antibody

staining. This results in a patchy morphology that many have described as a

'cotton-wool' plaque and are generally much larger than the fibrillar plaques at

upwards of 200 µm in diameter (40,41).

There is support for both hypotheses on the formation of plaques in the

literature. All plaque types are found in both preclinical and end-stage

Alzheimer's disease (39). The proportion in which they are found differs though

to the stage (43,44) of the AD neural tissue. In the preclinical cases there are a

greater proportion of diffuse plaques while in the end-stages of AD there are

more fibrillar plaques (dense-core and fibrillar) and fewer diffuse plaque deposits.

It is possible that both hypotheses are correct in that plaques form independently

of one another but are also able to 'age' into other classes over time. The

genesis of new plaques is assumed to occur even in the late stages of AD such

that early diffuse plaque formation is possible and is seen in tissue samples.

Additionally, in preclinical stages dense-cored plaques are found, along with

diffuse plaques, but in small quantities (some would say insufficient amounts to

cause clinical symptoms, but it remains controversial as to whether plaques are

the cause of or result of the disease). If one were to adhere to the 'aging plaque' dogma, then the progression of plaques would first start out as diffuse, then gain fibrillar $A\beta_{42}$ over time to form fibrillar plaques and eventually recruit more $A\beta_{42}$ and the less fibrillar $A\beta_{40}$ to form dense cored plaques (40). While this variant self aggregates less readily upon itself, the recruitment of the less fibrillar $A\beta_{40}$ occurs because it attaches to the framework of the $A\beta_{42}$ seeds. It must be maintained that there are numerous factors in the genesis of plaques, mostly environment factors involved with the specific brain milieu that they are forming in. In brain regions such as the basal ganglia more diffuse plaques are formed with fibrillar plaques being rarely found in late state AD (41). While it is unknown as to why this occurs, there are two possibilities. The first follows that age hypothesis and would be that this brain region forms plaques at a later time than the cortex, and as such only has time to develop diffuse plaques. The second would follow the environmental hypothesis and state that the diffuse plaques are only forming due to environmental limitations. As a whole it seems that the variability in plaques found within the spectrum of AD staging is potentially due to both factors, aging and environment.

Figure 1.1.2.1.1

Classification of beta-amyloid plaques in human Alzheimer's disease. (A, i-iii) Series of three optical sections taken through a dense-cored plaque stained with thioflavin-S in a preclinical AD case (83 years). Images show a distinct central core (arrow) of β-amyloid surrounded by a void or clearing and then an outer spherical rim of β-amyloid (arrowhead). (B, i-iii) A similar set of images sectioned through a fibrillar plaque stained with thioflavin-S in a preclinical AD case (81 years). The fibrillar plaques showed dense β-amyloid accumulations throughout the plaque structure. In the central regions these accumulations often appeared as spoke-like accumulations (arrow), emanating from a denser central accumulation. Distinct pores within the plaque were obvious in deeper sections. (C, i-iii) A set of sequential confocal images sectioned through a diffuse plaque labeled with an antibody to β-amyloid in an end-stage AD case (74 years). (Figure from Dickson, 2001 (39))
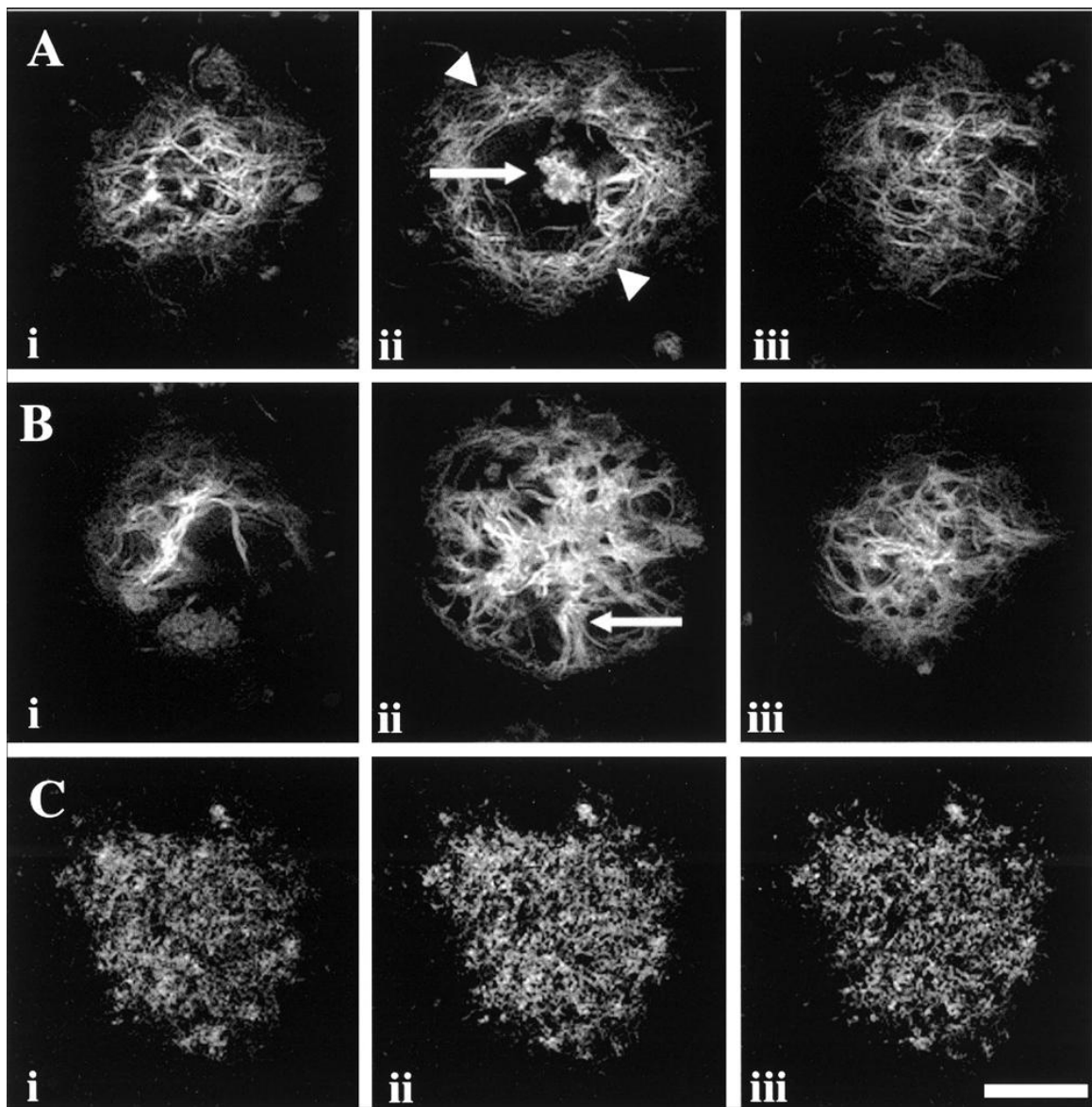
1.1.2.2 – Beta-amyloid Plaques and AD

It was once commonly believed that the mature amyloid fibrils in the form of mature plaques were the sole responsible party involved in the neurodegenerative processes associated with the disease. This hypothesis was brought into a gray area when studies viewed the burden of amyloid plaques in the tissue and compared the number of mature plaques with cognitive decline and neuronal loss in the tissue. The data from several separate studies illuminated that there are inconsistencies between the correlation of amyloid burden in tissue and cognitive decline or neuronal loss (39). There are alternative views that the more soluble form of Aβ may be of greater pathological importance than the insoluble beta-amyloid that plaques are comprised of (45,46). The distinction between intracellular and extracellular beta-amyloid upon AD pathogenesis has also been drawn into the light in recent years with studies and their individual neurotoxic effects.

In cell cultures where soluble extracellular $A\beta_{40}$ and $A\beta_{42}$ is introduced into the culture medium at concentrations believed to be found within the *in vivo* AD brain the extracellular Aβ did not induce any neurotoxicity (46). This indicates that soluble extracellular peptides are not directly responsible for neurodegeneration, in an *in vitro* cell culture system at least. In order for extracellular beta-amyloid to cause neurodegeneration the peptides must aggregate to form insoluble fibrils which invokes oxidative injuries followed by neuronal death (47) (more on this in the oxidative stress section). When intracellular concentrations of $A\beta_{42}$ are increased neuronal apoptosis results

40

albeit with a yet unknown mechanism of action, but it has been speculated to be due to overloading of the endoplasmic reticulum (48) or alterations in axonal structure and transport (49) leading to apoptotic signaling. Apoptotic features have been observed in AD neural tissue but the involvement of apoptosis in AD neurodegeneration has been difficult to observe when looking at lesions produced several years in the past (50).

The relationship between intracellular and extracellular beta-amyloid is slowly being provided, but there are many questions as to the dynamics between their relationship. In mouse models, the appearance of extracellular plaques is proceeded by the accumulation of intracellular beta-amyloid (51). This provides some evidence that the two pools of Aβ are somehow related and the accumulation of extracellular beta-amyloid may be in part dependent upon the intracellular accumulation of Aβ (49,51). The method by which soluble extracellular beta-amyloid accumulates outside the cell and eventually forms insoluble fibrillar plaques is purely speculative. There is some evidence to support that beta-amyloid is directly released during final gamma-secretase cleavage into the extracellular space (51). There is also evidence that it is transported and released into the extracellular space at the synaptic terminals where it is known to accumulate and potentially disrupt neuron to neuron transmission (52). There also remains the possibility that intracellular accumulation of beta-amyloid is caused via receptor or membrane mediated endocytosis of extracellular Aβ where it is brought into the cell in an attempt to degrade extracellular beta-amyloid but overloads the system and results in

intracellular accumulation (53). There is yet another possibility in that when excess intracellular beta-amyloid accumulates and eventually leads to cellular death (autolysis) this causes the release of intracellular beta-amyloid into the extracellular matrix contributing to extracellular stores (54). Clearly the relationship between intracellular and extracellular Aβ is complex and as such is under intense research to elucidate their exact dynamics.

1.2 – Iron and the Body

Iron is fundamental and absolutely required for the normal functioning of most life on Earth. It is an essential element necessary for numerous biological functions within the body due to its biochemical reduction and oxidation properties. Its ability to change valence and donate and accept electrons with surrounding ions gives it a vital role in energetic processes that rely on electron transport. While this property is necessary for numerous biological functions, free iron the body can have extremely toxic repercussions when not properly maintained.

1.2.1 – Normal Metabolism of Iron in the Body

Iron is the most abundant metal in the human body, existing biologically in both ferrous (Fe^{+2}) and ferric (Fe^{+3}) forms (55). Iron plays a vital role in oxygen transportation within hemoglobin, is involved in DNA synthesis with ribonucleotide reductase, electron transport in cytochromes, the citric acid cycle, myelination, and the synthesis of neurotransmitters (56-58). Most individuals

who are maintaining proper iron balance and have adequate nourishment have approximately 4 grams of iron within their bodies. The majority of this is found in hemoglobin within red blood cells to carry oxygen and carbon dioxide during respiration and accounts for 3.5 grams of iron. Within the soft tissue of the body there is approximately 500mg and the skeletal system accounts for 150 mg. Iron circulating through the body is found in blood plasma bound to transferrin and accounts for 4 mg of the total. Iron intake and excretion are approximately 1 mg per day each, although these can vary according to gender due to female menstruation which can increases excretion to 2mg per day (59,60) (Figure 1.2.1.1). There is no pathway in the body for the excretion of large amounts of iron per se, other than the process of bleeding. Iron normally is expelled from the body among shed skin cells, hair fibers and cells along the lower intestinal tract lost during defecation (61). This places emphasis on the body to properly maintain iron intake and storage because excess iron cannot leave the body in rapid manner.

Iron intake is obtained through dietary means by absorption through the intestinal lumen. Duodenal cells along the absorptive villus of the intestinal lumen act as sensors of dietary iron intake and overall total body iron (via unknown mechanisms) and regulate intake or iron accordingly (61). Dietary iron may be taken up as either free iron (ferrous or ferric) or as iron found bound to heme. Free iron is principally present in the diet as ferric iron which is insoluble and must be converted to the soluble ferrous form by a reductase in the luminal surface of the duodenal enterocyte (59). After reduction (if necessary), iron is

transported across the apical membrane by the divalent metal transporter where it is stored in the cell for a short period bound within ferritin or is directly transferred into circulation by the iron transporter ferroportin-1 where it is then bound by transferrin, brought primarily to the liver and where it is stored within ferritin (59) (Figure 1.2.1.2). Transferrin is a blood plasma glycoprotein which binds iron reversibly for iron ion delivery via receptor mediated endocytosis (61). Ferritin is a ~450 kDa globular protein comprised of 24 subunits to create a spherical shell of approximately 8 nm inside diameter that stores up to 4500 iron atoms within its core in the form of crystalline ferrihydrite (62,63). There are two forms of ferritin found within the body depending on the subunits they consist of, heavy (H) or light (L). L-ferritin is primarily found within the liver and is involved in long term iron storage for regulatory purposes. H-ferritin is found throughout the body and is involved in the rapid uptake and release of iron to sustain metabolic processes within cells and to promptly help protect against excessive iron detoxification (64,65).

In the brain, iron is found bound to heme within hemoglobin and in iron containing proteins as non-heme iron. The amount of iron stored in the brain as non-heme iron in ferritin accounts for approximately one-third of the total iron in the brain (66-68). There is a progressive increase of brain iron throughout life. At birth a very low iron concentration is present, then follows an extremely rapid increase occurring during the first year of life due to rapid myelination (58). Iron concentration then slowly increases during the first two decades and eventually plateaus to a maximum level at approximately thirty years of age (67). The

distribution of iron in the brain is not homogenous and is largely dependent upon location and function within brain regions. The highest levels of brain iron is found in the extrapyramidal system within the globus pallidus, substantia nigra, red nucleus and myelinated fibers of the putamen. Moderate levels are found in the majority of the forebrain, midbrain and cerebellar structures and the lowest levels are found in the brain-stem and spinal cord (66,68). The regions in the brain with the highest concentration of iron contain more iron than any other organ in the body with the exception of the liver (67). This renders iron homeostasis and regulation within neural tissue to be extremely important. Iron entering the brain must cross the blood brain barrier via receptor mediated transportation. Although not completely understood, iron bound to transferrin binds to transferrin receptors found on the apical surface of endothelial cells lining the neural blood vessels and is then internalized and ported across the basil membrane via the divalent metal transporter protein into cerebral spinal fluid or via a glial route to awaiting neuronal cells (69).

Figure 1.2.1.1

Iron stores in the body. (Figure from J.F. de Wolff, 2004,

http://commons.wikimedia.org/wiki/File:Iron_metabolism.svg)

Red blood cells
(3500 mg)

Reticulo-endothelial system
Spleen, liver

*

Bone marrow
(150 mg)

Blood plasma
(4 mg)

Oral intake
(1 mg/day)

* Ineffective red blood
cell production

Tissues
(500 mg)

Excretion
(1 mg/day)

Figure 1.2.1.2

Iron absorption in the body. Ferric iron is reduced to ferrous iron in the intestinal lumen by a membrane reductase where it is transported across the plasma membrane by the divalent metal transporter (DMT-1). Within cells, iron is stored as ferritin or exported across the basolateral surface by the iron transporter ferroportin. Exported iron is converted to ferric iron by the membrane oxidase and bound to transferrin for distribution to tissues. (Figure from Ezquer, 2006 (59))
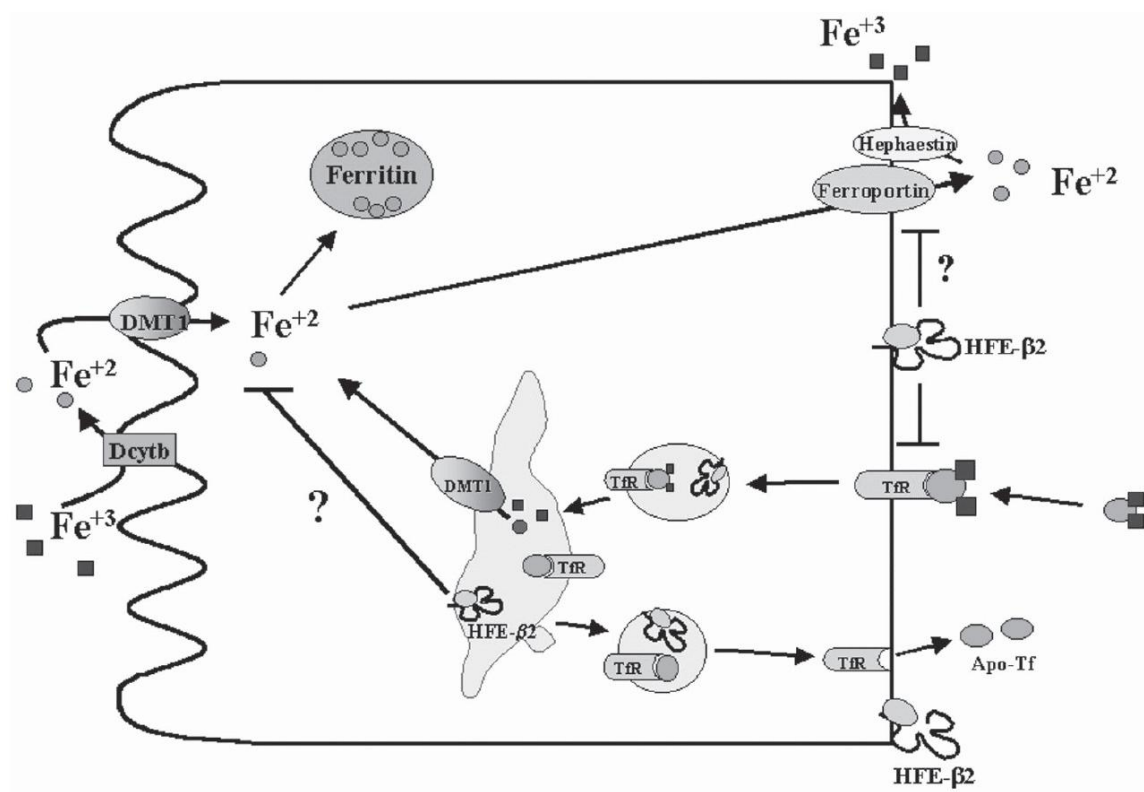
1.2.2 – Iron and Alzheimer's disease

Research in the past two decades has shown that misregulation of iron in the body is associated with a number of human neurological disorders. Post-mortem and *in vivo* magnetic resonance imaging studies have shown that there are significantly increased iron levels in the substantia nigra of patients with Parknson's disease compared to age matched control brains (70-72). Iron content has been found to be increased in gray and white matter of patients with amyotrophic lateral sclerosis (73). Reduction of iron due to an unknown cause is seen in patients with restless legs syndrome, especially within the substantia nigra. The symptoms of these individuals are somewhat alleviated with intravenous iron therapy and dopaminergic therapy highlighting the importance of iron in neurotransmitter synthesis (74). Data also strongly implicates a disruption of iron homeostasis in Alzheimer's disease as demonstrated by neuronal alterations in normal iron distribution and iron regulatory proteins (75).

1.2.2.1 – Iron Imbalance

Iron homeostasis in the Alzheimer's disease brain has been shown to be regionally disrupted based on cellular and protein observations. Quantitative studies on iron in AD brain have shown that iron is 67 percent higher in gray matter and 27 percent higher in white matter compared to age matched controls (76). In the motor cortex gray matter, iron and ferritin levels are both elevated in AD brains but have a 64 percent decrease in transferrin levels (55). These data suggests that iron mobilization is diminished in this brain region (77). Within the

gray matter of the occipital cortex iron levels do not seem to significantly increase with age while ferritin levels do show an increase in concentration. This is interesting considering that the occipital cortex is one of the least affected regions and shows a high ferritin to iron ratio, alluding to the benefit of ferritins ability to store and compartmentalize free iron. Within white matter, transferrin levels are consistently reduced in AD throughout the entire brain by approximately 40 percent (77). Ferritin in white matter is decreased by upwards of 40 percent with the same relative amount of iron present. Without the ability to regulate iron transport and storage while still containing the same amount of iron presents a danger to neural tissue. This creates an environment where unbound free iron is able to detrimentally interact and cause oxidative damage to tissues it comes in contact with. There is a general tendency in the AD brain to have reduced amounts of transferrin and ferritin with a concomitant increase of free iron (56). It is of considerable interest that brain regions which are less susceptible to AD related atrophy show the highest ferritin/iron ratio while those regions that are most susceptible have the lowest ferritin/iron ratio. It seems apparent that the ability to store and properly sequester free iron in regions with the highest ferritin/iron ratio is beneficial in reducing neurodegeneration (55).

Iron acquisition, sequestration, and management is usually under the control of the oligodendrocytes in normal neural tissue (78). Histological studies on iron, transferrin and ferritin unearth an abnormal pattern of cellular staining in AD brains. It is observed that the normal cellular distribution of transferrin in oligodendrocytes, which is responsible for transportation of iron, is altered in the

AD brain such that the majority of transferrin is found within astrocytic bodies (56,75,77). The absence of detectable transferrin in oligodendrocyte cells suggests a specific disruption of iron mobilization to this population of cells. The loss of ferritin in these cells suggests that myelination could be altered as iron is believed to be requisite during this process (58,75). The unusual detection of transferrin in astrocytes seems to have ties to the transfer of iron through the blood brain barrier. Excessive amounts of ferritin and free iron are found around blood vessels in AD tissue suggesting that iron uptake into the brain is compromised and no longer under tight regulation (77). Overall the collective data suggest that iron homeostasis is disrupted in AD neural tissue and changes in levels of iron and iron regulatory proteins could be highly related to the pathogenesis of Alzheimer's disease.

1.2.2.2 – Iron and Beta-Amyloid

It is known that metal ions can play a role in Aβ fibril formation, but the association *in vivo* to how they aid in Aβ fibril formation and plaque genesis is not completely understood. The component fibrils of the Aβ plaques are known metalloproteins and possess metal chelation regions in their amino-acid sequence (79-81). The conversion of Aβ's secondary protein structure has been shown to occur in the presence of divalent metal ion's like Fe^{+2} (82). It is well documented that iron is found tightly associated with many beta-amyloid plaques. Microglia cells associated with plaques consistently stain positive for intracellular

iron and these cells are found within the plaque boundary and have processes that extend into plaques (75,83-85). However, it is clear from iron stains of beta-amyloid plaques that there is a considerable amount of free iron not associated with any cellular structure that is bound within the amyloid fibrils of the plaques. The relationship of iron to plaque generation is not currently well understood within the literature. It is largely unknown whether the generation of the plaque causes the aggregation of iron to form a core, or if intracellular iron causes the formation of the beta-amyloid protein around it. It is known that iron can aid in the creation of fibrillar beta-amyloid seeds when iron is introduced in a solution of soluble $A\beta_{42}$ (86,87). This highly suggests that free iron found throughout the AD brain aids in the formation of beta-amyloid plaques. However, there is an alternative explanation for the relationship between iron and the ability of the beta-amyloid peptide as a metalloprotein. It has been suggested that beta-amyloid might have a neuroprotective function in the AD brain as it might act as a iron metal chelator (88,89). Therapies involving the chelation of metals in AD have been suggested to reduce the beta-amyloid load and neurocognitive effects of the disease (90). Specifically, the usage of the chelator clioquinol has been shown to reduce beta-amyloid aggregation in solutions and has been used in animal models with modest results at reduction of plaque burden (91). Clinical trials are underway with the usage of this chelator as a therapy for AD and show promise based on the hypothesis that decreasing metal ions are pivotal in the formation and degradation of beta-amyloid plaques (92-94).

1.2.2.3 – Oxidative Stress

The brain is the most aerobically active organ in our bodies consuming 20 percent of the total oxygen we take in due to its high metabolic requirements. Maintenance of the oxidative balance is imperative in the brain and is normally under tight regulation by antioxidants that are present in higher quantities in the brain than any other organ (79). This balance is altered in the AD brain due to the oxidative potential of iron if it is not properly maintained in tissue. In addition to the vital physiological roles that iron has a role in, iron is highly toxic when not regulated properly within the body. Free iron catalyses the production of oxygen free radicals via the Fenton reaction.

$$(1)\ Fe^{+2} + H_2O_2 \rightarrow Fe^{+3} + OH^{\cdot} + OH^{-}$$

$$(2)\ Fe^{+3} + H_2O_2 \rightarrow Fe^{+2} + OOH^{\cdot} + H^{+}$$
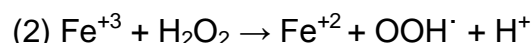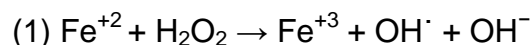
These reactive oxygen species (ROS) are devastating to neuronal cells and cause a wide variety of cellular dysfunction leading ultimately to cellular apoptosis and death. Oxidative stress can result in a number of deleterious cellular consequences including lipid peroxidation, glycoxidation, protein oxidation, protein crosslinking and DNA fragmentation (95). The half-lives of the ROS varies dependent upon the chemical structure of the radical. Hydroxyl radicals have very fast half-lives and as such their reactions are limited to sites near their generation. There are however other radicals that are generated that have much longer half-lives of a few seconds and thus can diffuse away from their sites of generation and transport their oxidant function to other target sites (96).

There is a clear relationship between beta-amyloid plaques and oxidative stress. Plaques have been shown to be sinks for oxidative ROS created by metal ions where the region surrounding the plaques exhibit oxidative markers (87,97). Ferrous iron bound to beta-amyloid has been shown to facilitate the reduction of O_2 to peroxide. The hydrophobic environment in the beta-amyloid plaques acts as a reservoir for the oxygen substrate and creates a microenvironment where bound iron facilities the electron transfer from the reduced metal ion to the dioxygen molecule (97). This creates a redox cycle where iron ions cycle between oxidation states that then repeatedly transfers electrons to successive oxygen molecules (79,87,97). The cycle in hypothesized to follow this pathway:

(1) $A\beta + Fe^{+3} \rightarrow A\beta + Fe^{+2}$ (Reduction of the metal ion)

(2) $Fe^{+2} + O_2 \rightarrow Fe^{+3} + \cdot O_2^-$

(3) $\cdot O_2^- + \cdot O_2^- + 2H \rightarrow H_2O_2 + O_2$ (production of H_2O_2)

(4) $Fe^{+2} + H_2O_2 \rightarrow Fe^{+3} + OH^\cdot + OH^-$ (Fenton Chemistry)

(5) $\cdot O_2^- + H_2O_2 \rightarrow OH^\cdot + OH^- + O_2$ (Haber -Weiss reaction)
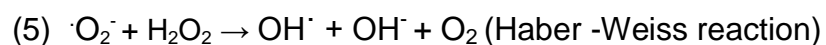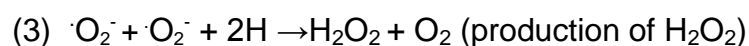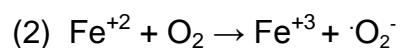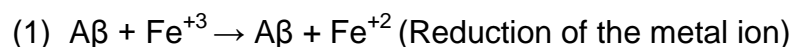
The first reaction involves the reduction of the metal ion by beta-amyloid which is then oxidized by oxygen, in turn reducing the oxygen. The reduced oxygen can then combine with hydrogen to produce hydrogen peroxide which is then reduced by ferrous iron to form hydroxyl radicals in the Fenton reaction.

Alternatively, reduced oxygen can bind with hydrogen peroxide to directly produce hydroxyl radicals in a Haber – Weiss reaction (79).

In normal brain tissue the low concentration of ferrous iron and competitive substrates for hydrogen peroxide normally ensure that the production of ROS is not favored in *vivo (87)*. In AD tissue, with imbalances in iron homeostasis and increased free labile iron, the system becomes overwhelmed and unable to maintain an oxidative balance. Measurements of protein oxidation (protein carbonyls) show elevated levels of oxidative stress in the frontal lobes, hippocampus, and superior temporal gyrus with normal results in the cerebellum in AD patients that correlates well with AD histopathology (98-104). Other makers of oxidative stress are indicated in measurements of antioxidant enzyme concentrations. The antioxidant glutathione transferase is altered in several regions of the AD brain including the hippocampus (105) while the antioxidant superoxide dismutase (SOD) displays elevated expression in AD neural tissue (106). The results from numerous investigation teams points to an increase in the production of oxidative species and an alteration in the antioxidant ability of the AD brain. The increased production of reactive oxygen species overwhelms the normal antioxidant capacity of the brain resulting in widespread oxidative stress and neuronal cell death throughout AD neural tissue.

1.3 – Animal Mouse Models of Alzheimer's Disease

Several mouse models of Alzheimer's Disease have been developed that attempt to mimic individual components of the disease etiology. The various

models aim at replicating one or a combination of the following aspects of

Alzheimer's; lesions associated with the disease (beta-amyloid plaques and

neurofibrillary tangles), symptomatology, or biological mechanisms responsible

for the disease. The three levels of the animal models (symptoms, lesions and

cause) are independent of one another and different models exhibit distinctive

characteristics. Individual types of animal models of Alzheimer's are shortly

reviewed herein for APP, PS1 and APP/PS1 models, specifically, in view of the

fact that a APP/PS1 line was utilized in this work.

1.3.1 – Injection of Beta-Amyloid

The reproduction of the lesions associated with AD has been attempted

with via the direct injection of β-amyloid $_{(1-42)}$ into the neuronal parenchyma.

These injections show some sign of pathological processes in the form of

enlarged ventricles and neuronal damage to hippocampal structures. Spatial

memory deficits are seen on water maze tests hypothetically accountable to the

neuronal damage associated with neuronal loss in the hippocampal structures

(107). The injections do not directly reproduce amyloidal plaque or neurofibrillary

tangles lesions of the disease.

1.3.2 – Transgenic Expression Models

Through the power of transgenic technology, it is possible to reproduce

specific lesions found in AD within animal models. Elevating the levels of

transgene product has helped model autosomal dominant human

neurodegenerative diseases mostly in transgenic mouse models. The

mammalian prion protein has been utilized as a vehicle to express foreign

proteins in the central nervous system. Specifically, the hamster prion protein

allows the insertion of a sequencing region up to 45 kb in an open reading frame

within a single exon (108). Standard pronuclear injection is used where a

linearized DNA cosmid construct is injected into one of the pronuclei during the

single cell stage of a fertilized egg. This egg is then transferred into the oviducts

of pseudopregnant foster mice and upon which the cosmid replicated along with

nuclear division throughout all subsequent dividing cells. The cosmid's reading

frame is transcribed to a functional transgene product utilizing the cells intrinsic

nuclear encoding allowing a "gain-of-function". Upon birth, approximately 20% of

the pups have integrated the injected DNA into their genomes. Various DNA

sequences, up to 45 kb pairs in length, can be inserted into each cosmid allowing

for a variety of end products.

1.3.2.1 – APP Transgenic Models

Seventeen amino acids differ in the mouse and human APP gene

sequence, three of which are located in the Aβ sequence (109). However,

increasing the level of mouse APP does not produce Aβ deposition, presumably

due to the differences in the amino acids between human and mouse APP and

Aβ. The first attempts to transfect the beta-amyloid peptide sequence itself

resulted in intracellular deposition of beta-amyloid only, resulting in cellular death

because the beta-amyloid was neurotoxic (110). It was deemed necessary to

transfect the entire human APP genetic sequence in hopes that it would properly be synthesized and that the mouse molecular machinery would cleave the APP to produce beta-amyloid peptide. Three isoforms of human amyloid precursor protein (hAPP) have been used as transgenes, the 695, 751 and 770 amino acid variants. Transfecting the APP gene induces overproduction of the protein, from which the truncated beta-amyloid$_{(1-40/42)}$ peptide is taken. Data from the different mouse lines that have been derived indicate that the onset and severity of amyloid deposits in directly linked to levels of $A\beta_{42}$ peptide. APP transgenic mice generate extremely high amounts of $A\beta_{42}$ and generate beta-amyloid plaques. However, none of the APP models reflect a complete picture of AD neuropathology because of the lack of neurofibrillary tangles and prominent neurodegeneration (111).

1.3.2.2 – PS1 Transgenic Models

Mouse models revolving around PS1 genetics were first created by knocking out the gene for endogenous mouse PS1. This resulted in a non-viable mouse line because a null for PS1 results in death late in gestation due to alternative responsibilities of the γ-secretase complex to cleave other important proteins necessary for during gestation (111). In an effort to recreate a mouse model that utilized the point mutations on the PS1 gene a mouse model was created were transgenes expressing familial AD associated mutations in the PS1 gene sequence, variant A246E, were introduced. Brain measurements of these mice had highly significant increases in the level of $A\beta_{42}$. However, since the

altered transgene product was still splicing the endogenous mouse APP peptide

the results were varied as far as plaque deposition. The amino acid difference

between hydrophobic residues on the human and mouse APP amino acide

sequence, especially those on the Aβ sequence, were deemed responsible.

1.3.2.3 – APP/PS1 Transgenic Models

The next logical step in the production of a mouse model that recreated

beta-amyloid plaques and perhaps other AD like neuropathologies was to

combine the FAD mutations in both the APP and PS1 gene into one mouse

model. Animals that co-express both mutations develop numerous amyloid

deposits much earlier than mice that express human APP or human PS1 alone,

at approximately six through nine months of age (112-114). The mice have

elevated $A\beta_{42}/A\beta_{40}$ ratios in brain homogenates that is not seen in single

transfected APP or PS1 mice (111). AD like pathology was substantially

enhanced as far as plaque production and composition while the mice revealed

deteriorations in brain function as tested with water mazes. The mice still do not

develop numerous other AD like pathologies, namely neurofibrillary tangles and

widespread cerebral atrophy.

1.4 – MRI Quantification of Iron

The basic principles of magnetic resonance imaging was first described

and measured by Isidor Rabi in 1938 when he discovered the magnetic

resonance phenomenon (115), and then was refined independently by Felix

Bloch (116) and Edward Purcell (117) in 1946. Rabi was awarded the Nobel Prize in Physics in 1944 for this work and Bloch and Purcell were co-awarded the prize in 1952. It was noticed that magnetic nuclei, like ^{1}H and ^{31}P, absorbed RF energy at a specific energy when placed in a magnetic field. The phenomenon when absorption occurs was described as having the nuclei in resonance with the magnetic field. It was discovered that different atoms resonate at different frequencies at a given field strength, and that the resonance of atoms in a molecule would describe molecular structure information. When atoms such as hydrogen, carbon^{13}, fluorine, sodium and phosphorus are in a magnetic field they align themselves along the dominant magnetic field as then act like small bar magnets with dipoles (118). The breakthrough for the motivation behind medical applications of MR technology came when Raymond Damadian in 1971 showed that the nuclear magnetic relaxation times of tissues and tumors differed.

1.4.1 – MRI 101 – Basics of Magnetic Resonance Imaging

In the majority of clinical MR imaging and the MR experiments in this work, the vast majority of nuclei being imaged are hydrogen in water (protons). Hydrogen is also found in other macromolecules (proteins, lipids, etc.) but the signal acquired from them decays much more rapidly and in general is not detected. A fundamental property of atomic nuclei is that they posses spin. Different atoms posses' different spin states, with hydrogen having a spin of ½. This spin may be positive or negative. A nucleus with a spin produces a magnetic field around it, termed the magnetic moment. The strength of the

magnetic moment depends upon the mass and rate of spin of the nucleus. Just as a the magnetic needle of a compass aligns with the earth's magnetic field, the magnetic moment of the nucleus will also align with an external magnetic field. Depending on the spin state (+ or -), a proton can align either parallel or anti-parallel to external field (B_0). When a proton with a spin state of + ½ aligns to the external magnetic field the net result is the generation of a small magnetic moment aligned parallel or in the direction of the B_0 external magnetic field. When a proton with a spin state of - ½ aligns to the external magnetic field this results in the creation of a magnetic moment that is opposite or anti-parallel to the external magnetic field (Figure 1.4.1.2). The magnetic moment does not align precisely along the external magnetic field, but is tilted at an angle. The interaction of an external magnetic field on the protons and this angle causes the nuclei to precess about the B_0 field axis. The speed of precession of the proton about the axis of the static B_0 magnetic field direction is determined by the Larmor equation, which factors in the strength of the external field and the gyromagnetic ratio of the precessing nuclei. At a field strength of 1 Tesla, the set frequency of procession that is equal to 42.58 MHz/T (termed the Larmor frequency) (Figure 1.4.1.1). The parallel spin state results in a lower energy state because the created magnetic field is in alignment with the external field. The opposite is true for the anti-parallel spin state, as it is in a higher energy state with its created magnetic field in opposition to the external field (Figure 1.4.1.3). Due to the lower energy state, the parallel spin state is found slightly more in protons throughout a sample in an external magnetic field. The

population of spin states at the lower energy level is slightly larger than at the

higher level, creating a very small excess of spins in one direction verses another

(approximately 1 out of 100,000 at 1.5 Tesla). However, the very small

difference in population between the two energy states results in very small

signal. Considering the amount of protons in a sample following Avogadro's

number, the net spin excess is great enough to be measureable from an outside

source (119).

Figure 1.4.1.1

Proton precession around an external magnetic field. Spinning protons precess about the axis of the external B_0 field. The frequency of the precession (Larmor frequency) is directly proportional to the strength of the magnetic field. (Figure from Stark, 1999 (120))

Magnetic Moment

Nucleus
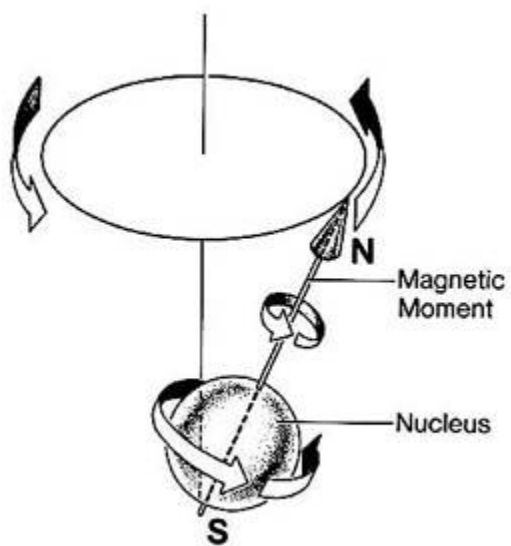
Figure 1.4.1.2

Parallel and anti-parallel quantum spin state. On the left, a proton in a parallel

spin state resulting in a net magnetization aligned with the external magnetic

field. The proton on the right is in an anti-parallel spin state with the net magnetic

moment in the opposite direction of the external magnetic field. (Figure from

Stark, 1999 (120))
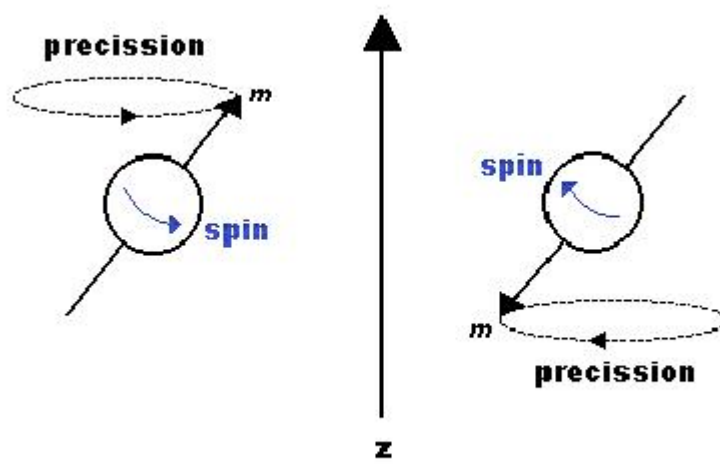
Figure 1.4.1.3

Spin states of protons. The parallel spin state is of lower energy than the anti-parallel spin state because the parallel state results in a magnetic moment that is parallel or in the same direction as the external magnetic field. (Figure from Hoffman, 2008; http://chem.ch.huji.ac.il/nmr/whatisnmr/whatisnmr.html)

The case of the spin-½ nucleus

A nucleus with spin at higher energy generates a magnetic field in the opposite direction to the external magnetic field.

The Nuclei are electrically charged and many have spin that causes them to behave like a magnet

No field

Energy gap corresponds to radio frequency

B_0

External magnetic field

A nucleus with spin at higher energy generates a magnetic field in the direction of the external magnetic field

Tissue magnetization represents a source of potential signal for the generation of an MR image. To accomplish this, the magnetization of the protons must be rotated away from their alignment along the B_0 magnetic field. Energy in the form of an RF pulse can be applied from an RF transmit coil that alters the sample's magnetization. The applied RF pulse must be adjusted to the same Larmor frequency at which the proton being imaged processes in the B_0 field. This converts some of the magnetization along the B_0 axis into magnetization along the perpendicular axes. Magnetization along the B_0 field is termed longitudinal magnetization and that along the perpendicular axis transverse magnetization (118). The RF pulse also exchanges energy with the protons and some of them are lifted to a higher energy spin state. After an RF pulse is applied by an RF transmit coil, the perpendicular magnetization is lost quickly while the longitudinal magnetization recovers back to its original precessional state. Induced transverse magnetization recovers at a different rate back to its pre-RF pulse value of 0. The change of transverse magnetization induces an electrical current causing a net magnetic flux and oscillating current through an RF receive coil. This current is perceived as the MR signal. Recoveries of longitudinal and transverse relaxation are termed relaxation. Longitudinal relaxation is referred to as spin-lattice relaxation and follows an exponential decay with a time constant termed T_1. Longitudinal relaxation reflects the process that the energy transferred to the protons by the RF pulse is transferred back to the protons surroundings or lattice (118). T_1 for a given sample is defined as the amount of time it takes to recover 63 percent (1-1/e) of

70

its original longitudinal magnetization after the RF pulse. Transverse relaxation, also termed spin-spin relaxation, is referred to as T_2 and is defined as the amount of time it takes for 63 percent of the transverse magnetization to dissipate (118-120).

The data collected by the receive coil contains information only on the net amount of change in transverse or longitudinal relaxation but does not relay any information on the spatial location of this change within the sample. To relay this information, the application of other external magnetic fields in required. It was realized that applying a spatially changing magnetic field, or field gradient, across the sample produced a proton magnetization signal with varying frequency components depending on spatial location in the magnetic gradient. The magnitude of the differing gradient of magnetization across the sample must be known and back calculated from the resulting spin frequency to find the spatial location of the spinning proton. This magnetic field gradient is applied by a linear gradient coil that changes the magnetic field linearly in a set direction. The gradient directions are set in three dimensions allowing three dimensional imaging when slices are selected dependent upon pulses chosen at a specific frequency and bandwidth. In multi-dimensional MR imaging, the protons in the imaging slice are selectively excited by a combination of a frequency selective RF pulse and a field gradient perpendicular to the imaging plane. The bandwidth of the RF pulse and the amplitude of the slice-selection gradient determine slice thickness and location. The phase of rotation of the protons along one axis (read axis) are aligned with one another, while the phase of protons precession along

the other axis (phase encoding) is changed such that it adds another dimension

to the data collection. This results in protons with different frequencies and

phases throughout the selected slice of the sample dependent upon spatial

location. The computer of the MR scanner takes this mixture of different signals

and sorts through the different frequencies and phases for protons with the same

frequency by means of the Fourier transform. This results in an output of how

much signal (amplitude) of a specific frequency and phase is present at a specific

location and then assigns spatial information based on proton frequency and

phase in grayscale contrast seen in MR images (118-120).

Tissue relaxation rate is dependent upon properties of the tissue that

cause it to relax along the longitudinal or transverse axis at different rates. This

is caused by a number of factors, including the amount of protons present in that

tissue and factors that cause protons to relax along either axis at increased rates

thus shortening their time of relaxation. These perturbations that cause relaxation

to occur more rapidly can be inherent tissue properties, i.e. more protons in gray

matter verses white matter and faster relaxation of protons in fat verses water or

they can be due to properties of the tissue that is due to an alteration in the

normal tissue properties, i.e. more protons in cancerous tissue verses healthy

tissue or proximity to paramagnetic particles. Transverse T_2 relaxation can occur

due to a variety of reasons; magnetic dipole-dipole coupling, electric quadrupole

coupling, chemical shift anisotropy, scalar coupling and spin-rotation interaction

(120,121). Of all these interactions, the most important upon proton relaxation in

MRI is magnetic dipole-dipole coupling. This is because protons do not possess

a quadrupole moment as they do not have more than 2 different spin states. Coupling of the proton nucleus to magnetization variations due to atomic level electron currents (chemical shift, scalar and spin-rotation coupling) are small compared to dipole-dipole interactions due to the small field variations caused by electrons (unless there is an unpaired electron as with a paramagnetic material) (120-122).

1.4.2 – Quantitative Iron Measurement with MRI

In an ideal system within a homogenous magnetic field, all nuclei would transversally relax with the same time constant. In real systems, there are differences in the chemical/molecular environment which can lead to a distribution relaxation time constants. This distribution can lead to a diffusion of the magnetic spin vectors causing a loss of signal. Magnetic field inhomogeneities caused my particles altering the magnetic flux of the static field cause a loss of nuclei frequency and phase coherence. The degree of which is dependent on the location of the nuclei in relation to the magnetic field perturbation. The corresponding transverse relaxation time constant is termed T_2^*, and is much shorter than T_2. There is a relationship between T_2 and T_2^* written as:

$$\frac{1}{T_2 *} = \frac{1}{T_2} + \frac{1}{T_2'}$$

Or

$$R_2 * = R_2 + R_2'$$

Where T_2' is the time constant for relaxation due to magnetic inhomogeneities or $\gamma \Delta B_0$, where γ represents the gyromagnetic ratio, and ΔB_0 the difference in strength of the locally varying field.

This important factor causes modifications to tissue relaxation rates. Particles induce magnetic field inhomogeneities in the static B_0 that, when in close proximity to protons, cause the protons to loss the energy gained from the RF pulses at an increased rate. There are a variety of particles that cause protons to alter their relaxation properties, some of which are used clinically to differentiate tissue with similar relaxation times i.e. contrast enhancers to visualize tumors that are relatively homogenous with their surroundings. Iron particles cause perturbations in the magnetic field homogeneity throughout the tissue and cause the rapid loss of signal due to the large magnetic moment associated with the iron atom (approximately 1000 times greater than hydrogen protons) (123). A single particle can affect the signal in a dephasing region far away from the particle affecting a volume of proton signals that is much larger than the original particle volume. Iron is ferromagnetic and has permanent domains of electron spin magnetic moments that produce very strong macroscopic magnetic fields. Iron has a high permeability and high susceptibility that causes strong spin-spin coupling with nearby protons producing static dephasing of protons within the vicinity of iron particles. Particles of iron act to concentrate the magnetic field lines (flux), creating field changes in regions. This produces field in-homogenous in the static magnetic field compared to the surrounding tissue (119).

As such, ferric iron (Fe^{+3}) causes the rapid reduction in T_2 and T_2* rates in protons in the direct vicinity of the iron particle. The effect of ferrous (Fe^{+2}) iron on T_2* and T_2 relaxation is much less prominent than that caused by the ferric form (124). This is believed to be due to the short electronic relaxation time of Fe^{+2}, while Fe^{+3} effectively increases T_2 relaxivity through the paramagnetic dipole-dipole mechanism (125). It has been well documented that iron will increase proton transverse relaxation rates and that the relaxation rate difference is proportional to the concentration of iron ions (123,126-128). It has generally been considered that ferritin and hemosiderin (degraded ferritin) are the distinct forms of non-heme iron in the normal non-diseased brain present in sufficient quantities to affect MR contrast (123,129).

Ferritin exhibits extremely interesting magnetic characteristics and proton interactions that are not easily described by classical theory. Current theoretical models describe the relaxation of water protons in the presence of magnetized nano-particles. The outer sphere model predicts that relaxation of protons is caused by the diffusion of water protons through an inhomogeneous magnetic field created by the magnetic particles. The model predicts that there is a quadratic dependence of relaxation ($1/T_2$) upon the magnetic moment of a spherical particle and magnetic field strength (63,130-135). It has been found that the contributions of the outer sphere theory for solutions of iron oxide nano-particles underestimates the measured relaxation rates and does not fully describe the proton relaxation. In studies using ferritin solutions at differing magnetic field strengths it was found that relaxation $1/T_2$ to field strength exhibits

a linear dependence (63,125,133,136). This also correlates well to MR data

describing a linear relationship between $1/T_2$ relaxation and the iron found in the

globus pallidus as the majority of iron (at least 80 percent) found in this structure

is in the form of loaded ferritin (63,137). The inner sphere model predicts the

occurrence of proton exchange with hydrated spherical magnetic particles (130).

The theory aims to describe the relaxation of bound protons to hydrated iron

oxides. Hydrated iron oxides are known to interact with hydroxyl groups

(protons) on their surface in an amphoteric way (able to act as an acid or a

base). Amphoterism can occur with metalloids that have amphoteric oxides and

also with amino acids and proteins, which have amine and carboxylic acid

groups. There is a problem with this model describing the relaxation mechanism

of ferritin in that the theory predicts a quadratic dependence of relaxation rate

with magnetic field strength (130). A model that does describe a linear

relationship between field strength and relaxation is the static dephasing regime

(130,132,138). This model describes the transverse relaxation of

homogeneously distributed static protons in the presence of a magnetic field

generated by randomly distributed and oriented dipoles (123,130,138). Studies

have shown the this model does not satisfy the experimental results seen in

ferritin solutions (130,132). Iron load within the ferritin core has an effect upon

relaxation as well. It was assumed that iron load would be proportional and

directly affect the relaxation dependent upon the amount of iron present in the

core with a quadratic dependence explained by simple paramagnetism.

Interestingly, this is true for low iron loading factors within the core but when the

core reaches a threshold amount of iron within it and begins nucleation to form

the ferrihydrite crystalline structure it produces a linear relationship between field

strength and $1/T_2$ relaxation (125) (Figure 1.4.2.1) (Figure 1.4.2.2). This is

because the ferrihydrite core of ferritin is antiferromagnetic; however, because of

the size of small ferromagnetic clusters of the loaded ferrihydrite core, ferritin is

also superparamagnetic (123,139). Clearly, classical theories do not accurately

describe the proton relaxation properties of ferritin. Gossiun *et al.* has proposed

a new theory to explain the relaxation mechanism of ferritin named the proton

Figure 1.4.2.1

Ferritin and ferrihydrite core. Representation of the ferritin spherical protein shell

and the ferrihydrite iron oxyhydroxide mineral core. (Figure from Krispin, 2008;

http://www.physik.uni-augsburg.de/exp2/nano/nano.en.shtml)

Protein - Dimers

8 nm

12.5 nm
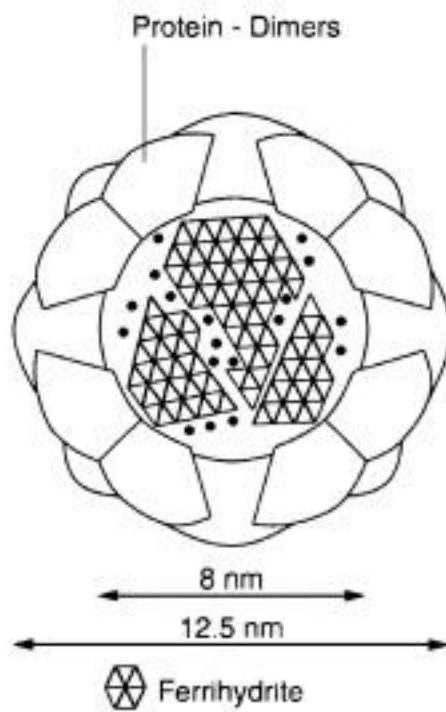
Ferrihydrite

Figure 1.4.2.2

Molecular structure of ferrihydrite iron oxyhydroxide mineral ($Fe_5HO_8 \cdot 4H_2O$)

found within the ferritin core. Figure from Michel, 2007;

http://www.aps.anl.gov/Science/Highlights/2007/20070801.htm)
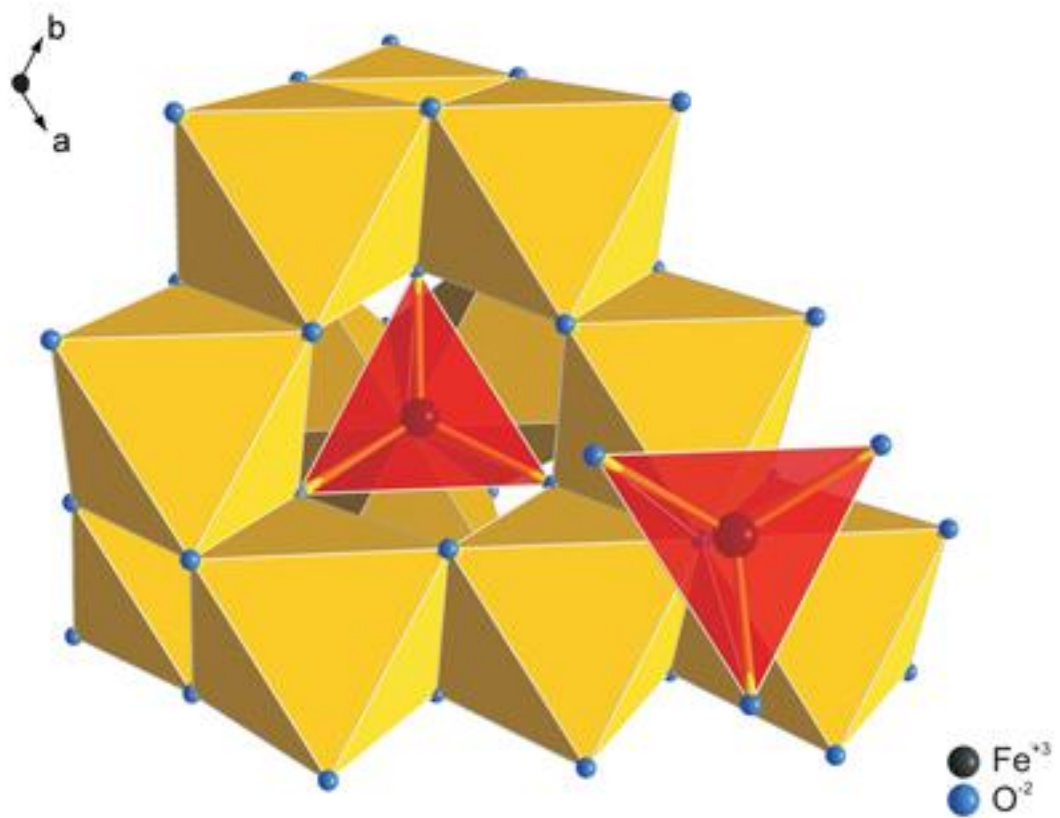
exchange dephasing model (PEDM) (130). The model accounts for the fast-exchange mechanism between both absorbed protons and diffusing protons each with their own relaxation rates that together describe the relaxation rate of the whole system.

Measuring iron in the body with magnetic resonance imaging has proved to be a difficult endeavor. There is a pressing need for quantitative means of measuring iron in the body that are non-invasive, safe, and accurate for clinical diagnosis and management of patients with iron overload. Diseases that could benefit from quantitative measurement of iron include thalassemia major, sickle cell disease, aplastic anemia, myelodysplasia, restless leg syndrome, Parkinson's disease, Alzheimer's disease, and other disorders (140). The majority of MR studies investigating the quantification of iron in the body study hepatic (liver) (127,128,141-143), cardiac (144) and brain (70,72,136,145-148) iron concentrations. Currently the best method of measuring iron status of the body is through liver biopsy but the discomfort and risk of the procedure limit its usage (140). MR procedures to quantify iron load have described a number of methodologies from dual to multi-echo T_2 and T_2^* imaging (127,140,141,149), phase imaging (123), susceptibility imaging (127,150-152) to using multiple magnetic field strengths in serial (153). Each method has its own advocates and promising results within the iron quantification field.

1.5 – Basics of RF Coils

The primary function of the RF system is to generate and collect MR signals. When tissue or a sample is placed in the magnetic field, the magnetic dipoles of the protons are forced to align with main field (B_0). The sample acquires a slight net magnetization (longitudinal) due to the forced alignment of protons to precess about the B_0 field. An RF coil is used to induce a current which creates an external magnetic field (B_1) generated at a right angle to the static field at a frequency that is tuned and matched to the Larmor frequency of the proton. This results in the exertion of torque on the precessing protons due to the perpendicular B_1 field to the static B_0 field. This tilts the protons away from alignment with the B_0 field towards the B_1 field in the transverse plan. The RF pulse is then stopped and the proton then gradually precesses in a complex spiral back towards the B_0 field. While the proton is coming back to alignment with the static B_0 field there is a small amount of magnetization produced which induces of a small current in the RF receiver coil. This current is the resulting MR signal that contains the frequency and phase data from the sample. The voltage of the signal received is on the order of one tenth of a microvolt while the transmitted signal to induce the B_1 field is on the order of hundreds of volts resulting in a few milliTesla (or micro) of magnetization (120).

1.5.1 – Radio-Frequency Coil Design

An RF coil can have three possible functions, transmission of the RF signal to align protons along B_1, reception of the transverse signal, or both transmit and receive. To transmit or receive signal, an RF coil must be tuned and matched to the resonate frequency of the proton (or other atom) at the Larmor frequency. The coil must be able to maintain this resonance and efficiently store energy at this frequency. All imaging coils are composed of an inductor and a set of capacitive elements to achieve this goal. The inductance (L) and capacitance (C) of the inductor capacitor circuit determines the resonant frequency of an RF coil such that;

$$\omega = \frac{1}{\sqrt{LC}}$$

A basic diagram of an RF coil can be seen in figure 1.5.1.1. The inductance coil is represented by (L) can be made of various metals, usually copper, which have a natural resistance (r). Capacitance is generated by variable capacitors, C_1 and C_2, which function to tune and match, respectively, the frequency of the coil. With sample loading the frequency of the coil goes down due to coupling with the sample, thus the variable capacitors allow the tuning and matching to the set frequency when a sample is inserted (120).

Figure 1.5.1.1

Simple RF coil circuit design. L is the inductance coil with a natural resistance (r) due to the inherent properties of the metal they are made of. C_1 and C_2 are variable capacitors to tune and match the coil when a sample is inserted.
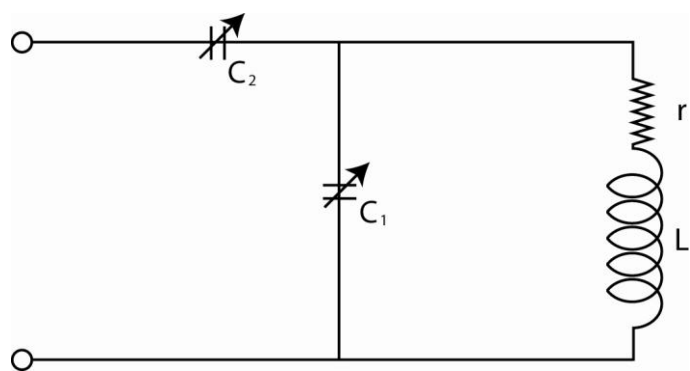
A basic principle of RF coil design is that the B_1 transmitting coil must generate a rotating magnetic field that is perpendicular to the B_0 field to create proton torque that causes the proton to align with along the transverse plane (B_1). If the generated B_1 field lies parallel to the B_0 field then there will not be an induced change in the precession of the proton along the transverse plane. The physical properties of a coil such as coil size around the sample are very important considerations. The magnetic coupling between an RF coil and a sample is maximized by making the coil as physically small as possible to accommodate the sample (154). The inherent noise of a coil is increased as the diameter of the coil increases due to the thermal motion of electrons in the conductor, termed Johnson–Nyquist noise. This affects the overall performance of the coil and reducing resistance increases coil sensitivity which increases the coils signal to noise ratio. There is always inherent noise due to the thermal motion in the conductor, but there is also inherent noise in the sample as due to the high electrolyte content of cells and body fluids. These ions result in a relatively high conductivity for the tissue and eddy currents are created with the application of an RF pulse that dissipate power, which enlarges with an increase in magnetic field frequency (also hence the reason for the variable capacitors). For coils that are a large diameter the majority of the noise is due to the large sample they can accommodate. For coils that are less than 3mm, the major source of noise arises from the coil itself (120,154).

There are a vast amount of coils sizes and geometries that have been produced for various applications. In general, coils are developed for very

specific applications, such as head, body trunk or limb imaging. The premise

behind much of this work in this thesis was instigated by the desire to image a

specific sample, very thin slices of neural tissue. This presented and challenge

with numerous hurdles which had to be overcome to produce a coil that

accommodated the sample with enough signal to noise to yield high quality MR

images.

Chapter 2

Histological Coil Design and Implementation

2.1 – Direct Magnetic Resonance Imaging of Histological Tissue Samples at 3.0 T

2.1.1 – Abstract

Direct imaging of a histological slice is challenging. The vast difference in dimension between planar size and the thickness of histology slices would require an RF coil to produce a uniform radiofrequency magnetic (B1) field in a two-dimensional plane with minimal thickness. A novel RF coil designed specifically for imaging a histology slice was developed and tested. The experimental data demonstrated that the coil was highly sensitive and capable of producing a uniform B1 field distribution in a planar region of histological slides, allowing for acquisition of high resolution T2 images and T2 maps from a 60 μm thick histology sample. The image intensity and T2 distributions were directly compared with histological staining of relative iron concentration of the same slice. This work demonstrates the feasibility of using a micro-imaging histology coil to image thin slices of pathologically diseased tissue to obtain a precise one-to-one comparison between stained tissue and MR images.

2.1.2 – Introduction

Magnetic resonance imaging (MRI) has been applied to a variety of *in vivo* applications because of its capability in providing high and versatile soft tissue contrasts. However, interpretations of the changes in observed image contrast

associated with the experimental interventions or pathological conditions need to be validated histologically. When comparing MR images to histological methods, a tissue sample of a given organ in whole or in part is traditionally imaged first and then cut, stained and compared to MR images of selected slices (155). This presents a challenge when correlating histological results with MR images because precise co-registration of tissue samples with MR images is notoriously difficult. This method requires that the histology samples be cut in the same planar orientation as MR images. Alternatively, previous investigations utilized three-dimensional MR scans to create rotatable three-dimensional MR models of tissue blocks, which allowed for the rotation of the image slice into a specific orientation with a visual inspection in order to compare to traditional two-dimensional or confocal three-dimensional histological images (156,157). This kind of co-registering process is time consuming and prone to human errors and subjective variability. In addition, the slice thickness of an MR image is generally much larger than the histological tissue slice resulting in a mismatch between the MRI and histology results. In this case, a number of histological slices need to be cut sequentially and assessed as if stacked upon each other to match the thickness of one MR slice selection. With this approach, it is difficult to perform quantitative comparison and analysis of MR images with histology.

Ideally, precise correlation between tissue histology and MRI studies could be obtained using the same tissue sample for both analyses. The implementation of such an approach would require the design and construction

of a specific RF coil able to directly image a thin slice of histological sample. In

optimization of an RF coil for this purpose, it is particularly important to obtain an

adequate signal-to-noise ratio (SNR) because of small voxel size and the minute

volume of tissue being imaged (on the order of 4.5×10^{-3} cm^3) (154,158). To

increase the SNR of an image, it is necessary to maximize the filling factor of the

coil, which, in turn, requires an RF coil design conforming to the geometry of the

histology slice. The vast aspect ratio between planar size and the thickness of

the histology slice require that the coil design criteria include the production of a

uniform B1 field in a two-dimensional plane with minimal thickness to maximize

the filling factor of the coil (159). In this report, we present a novel RF coil design

that is capable of imaging thin histological tissue sections, allowing direct

comparison of histology and MR images of the same tissue sample.

2.1.3 – Materials and Methods

The histological coil was designed and optimized with the aid of computer

modeling using XFDTD 6.3 (Remcom, State College, PA). The initial coil design

was first based on a flat slotted tube resonator by Bobroff *et al.* (160), consisting

of two rectangular parallel plates connected by one 664 *p*F capacitor at each of

the four corners. The optimized RF coil design consisted of a 24 mm wide U-

shape conductor strip wrapped around a dielectric material with relative

permittivity of ε_r = 5, simulating two stacked #1 thickness glass coverslips (24 x

30 x 0.150 mm) used for holding histology slices. The open end of the U-shaped

coil was connected to a voltage driving port. A square slab (24 x 24 x 0.3 mm) of

dielectric material simulating teflon with a relative permittivity of $\varepsilon_r = 2$ was placed between the perfect conductor strips next to the glass cover slips and driving port, providing distributed capacitance for the coil. This design results in a single loop of 24 mm wide copper strip tightly fitted around the histological slides. The B1 field distribution and electromagnetic properties of the flat parallel plate resonator and the histological coil were calculated and evaluated after tuning the coil models numerically to 125.44 MHz with a sinusoidal wave from a 50 ohm voltage source placed along the driving port. The total mesh size of both models consisted of 2,162,560 Yee cells with 0.3 mm in each dimension. The schematics of the initial flat slotted tube resonator, the optimized histological coil design and their corresponding calculated B1 field distributions are shown in Figs. 2.1.5.1 and 2.1.5.2, respectively.

An RF coil was constructed following the optimized histological coil design. The coil was tuned and matched to 125.44 MHz and evaluated on a 3.0 T MRI system (Bruker BioSpin GmbH, Ettlingen, Germany). The Q factor of the coil was measured with a Hewlett-Packard network analyzer and was approximately 290 when unloaded and remained unchanged when loaded with a uniform phantom. The homogeneity of the coil was evaluated with two phantoms produced by placing either 12.5 µl or 43.2 µl of 0.9 % Type A agar (Sigma, St. Louis, MO) between two cover slips. The agar results in a nearly uniform distribution of water throughout the sample and is an ideal test for image homogeneity. The 12.5 µl phantom was nearly circular and approximates the

dimensions of histological brain samples within the imaging region. The 43.2 µl

phantom was used to image the entire 24mm x 24mm coil region as this amount

of agar was calculated to fill the space of two 24mm x 30mm coverslips at a 60

µm thickness. To evaluate the B1 field homogeneity of the coil with an

experimental B1 field map, two gradient-echo images were acquired from the

phantom with 90° and 45° flip angles with 100 ms TR, 5.2 ms TE, 192 NEX with

a field of view of 40 mm x 40 mm and a matrix size of 128 x 128 for an imaging

time of 41 minutes each. From these two images the B1 field map within the

phantom sample was calculated following the method by Stollberger and Wach

(161). Subsequently, histological brain tissue sections taken from a donated

Alzheimer's disease brain specimen were used for evaluating the coil. Tissue

samples were fixed with 4% paraformaldehyde, sectioned at 60 µm using a Leica

cryostat, rinsed in phosphate buffered saline (PBS) to leach out the

paraformaldehyde, and then placed between two #1 thickness glass coverslips.

To maintain tissue hydration, 25 µl of PBS was placed onto the tissue. A

hydrophobic barrier pen was used at the edge of the coverslips to keep the

interior region between the coverslips from desiccating during imaging. The field

of view of all images was 23 mm x 23 mm with a matrix size of 128 x 128,

resulting in an in-plane voxel resolution of 179 µm^2. The 60 µm through plane

resolution, defined by the thickness of the sliced tissue, resulted in an overall

voxel size of 179 µm x 179 µm x 60 µm. A fast spin-echo T_2 imaging was

obtained using the same geometric parameters with 2500 ms TR, 12 ms TE, 128

NEX and 16 segmented acquisitions for a total image time of 92 minutes. Multi

spin-echo images were acquired with 1200 ms TR, 10 ms TE, 40 kHz bandwidth, and 64 NEX with 12 echoes for a total imaging time of approximately three hours. T_2-weighted images were generated by summation of the amplitude images from all the echoes to improve image SNR. T_2 maps were calculated from the multi spin-echo data with a linear regression method (Chips2005 software, Children's Hospital Image Processing System, Cincinnati, OH) in IDL6.1 (Research Systems, Inc., Boulder, CO). The first echo image was removed for the T_2 calculation to reduce the T_1 effect. After imaging studies, the brain tissue samples were stained for iron load with a modified Perl's prussian blue stain with 1,3-Diaminobenzene back-staining (Sigma, St. Louis, MO).

2.1.4 – Results

Figure 2.1.5.1 illustrates the design of flat slotted tube resonator and the corresponding calculated B1 field map. With such a small coil size, the B1 field of this design becomes very inhomogeneous because of the connections to the capacitor at each of the corners. Due to the small dimensions of the coil, current distribution near the feeding points and capacitive elements becomes a determining factor for B1 field homogeneity over the entire image plane. This problem was overcome by our optimized coil design depicted in Fig. 2.1.5.2 along with the corresponding calculated B1 field map. The two plates are formed with a continuous copper strip folded above and below the sample. This reduced the field inhomogeneity by eliminating four capacitive element connections. In addition, the plates were extended over a region filled with dielectric material to

94

form a distributed capacitor. The thickness of the 24 x 24 mm Teflon piece was

0.370 mm creating a total capacitance of 26.5 pf. As demonstrated in Fig.

2.1.5.2b, with such a design, the coil produced a nearly perfect homogeneous B1

distribution over the imaging region outlined by the dashed white box.

Comparison of the B1 field profiles along the crosshair in Fig. 2.1.5.1b and

2.1.5.2b indicates that the histological coil's B1 field has a greater magnitude and

is more uniform within the imaging region than the parallel plate resonator in both

dimensions. Construction was completed with Delrin around the copper strip as

seen in both the computer model and the photograph of the coil in Fig. 2.1.5.3.

Additional simulations performed with the Delrin enclosure showed that Delrin

does not have a noticeable effect upon the B1 field between the copper plates

within the imaging region.

To experimentally demonstrate the sensitivity and B1 field homogeneity of

the optimized histological coil, a T_2-weighted image and B1 field map were

obtained from the two uniform agar phantoms shown in Fig. 2.1.5.4a and

2.1.5.4b, respectively. As indicated by the images and the signal intensity

profiles along the two center orthogonal lines, the image intensity and the B1 field

of our coil are uniform over the entire imaging plane. The average signal to noise

ratio (SNR) of the phantom image in Fig. 2.1.5.4a is approximately 51. Figure

2.1.5.5 shows a T_2-weighted image obtained with the coil along with a histology

image of the same brain slice. The MR image in Fig 2.1.5.5a yields an average

SNR of 65. In the histology image with a modified Perl's stain in Fig. 2.1.5.5b,

the higher iron concentration regions such as those in the white matter appears as darker red-brown. For finer detail, the magnified regions of interest at the bottom of Fig. 2.1.5.5 were digitally post-processed to 50x magnification for the MRI images (5a) and photographed at 50x optical magnification for the bright field histological image (5b). The figure demonstrates that regions with higher focal iron concentration correspond to those having darker intensity in the MR image. High iron concentration is known to cause faster T_2 relaxation leading to hypo-intensities in T_2-weighted images. With our approach, the iron concentration shown in the histological analysis correlates T_2 contrast within MR images in a straightforward fashion.

With the high B1 field homogeneity produced by the histological coil, an accurate measurement of T_2 relaxation distribution in a histological tissue sample is possible. Figure 2.1.5.6 shows a representative T_2 parameter map (a) and average relaxation curves (b) from the two ROIs selected within white and gray matter from six tissue samples. The T_2 map exhibits a uniform distribution within the same tissue type over the slice, indicating an absence of "bias field" interference due to RF field inhomogeneity. Conversely, the T_2 values for different tissue types can be clearly delineated and reliably reproduced over multiple scans. These observations are equivalently evident in the T_2 relaxation curves, which demonstrate clear differences in T_2 decay between ROIs within the two tissue types. Each echo point along the curve has small standard deviations in signal intensity between the scans indicating that data over the six scans are

uniform and reproducible. The T_2 measurements were repeated with the histology coil from six different tissue samples of the same brain and yielded an average T_2 of 85.5 ± 2.4 ms for gray matter and 66.1 ±1.5 ms for white matter.

With the implementation of a high-field 7.0 T magnet at the Center for NMR Research it seemed a logical path to manufacture another histological to utilizing the increased magnetic field. The same design was used for the 7.0 T histology coil with modifications to both the imaging region and capacitance resulting from the Teflon between the continuous copper plate and the tune and matching circuits such that the coil would tune to the 300.44 MHz Larmor frequency. The coil utilizes a 22mm x 30mm x 0.4mm imaging space that allows two 22mm x 30mm glass coverslips with a histology sample between them to be positioned inside. The coil length was decreased from 48mm to 33 mm which decreased the size of the Teflon between the copper plates to 10mm to decrease the distributed capacitance across plates for tuning and matching. To decrease coupling between the coil and other components and aid in grounding the coil, a balanced and unbalanced circuit (Balun) was implemented into the tuning and matching circuit (162) (Figure 2.1.5.7). The additional coil and tuned capacitor in the balun acts to dissipate any residual voltage source that is present in the ground of the coaxial cable.

The resulting numerical field calculations showed that the 7.0 T coil had similar field uniformity compared to the 3.0 T coil but with an increased signal-to-noise ratio of ~204 for the 7.0 T coil verses ~65 for the 3.0 T coil. The resulting images are able to be taken at higher matrix dimensions allowing for higher

97

imaging resolution across the sample during similar time of scan durations.

Images taken with the 3.0 T coil with a matrix size of 128 x 128 over a 23mm x

23mm imaging space yielded 179µm in-plane voxel dimensions, while images

taken with the 7.0 T during a similar six hour time period with a matrix of 512 x

512 over the same 23mm x 23mm imaging region yields an in-plane resolution of

45µm. This represents a sixteen times (four in both X and Y dimensions)

increase in imaging resolution over a similar time period as the previous coil

design (Figure 2.1.5.8).

2.1.5 – Figures

Figure 2.1.5.1

(a) Schematic of the flat slotted tube resonator. Two separate copper strips are connected by a capacitor at each of the four corners. (b) Calculated transverse B_1 field component perpendicular to B_o in the center plane of the coil. The imaging region where the glass coverslips are placed is outlined by the white dashed box. The profiles of the B1 field along the cross hairs through the imaging region are shown above and to the right of the B1 map. The direction of the Bo field is noted to aid in the orientation of the coil within the magnet.

a

b
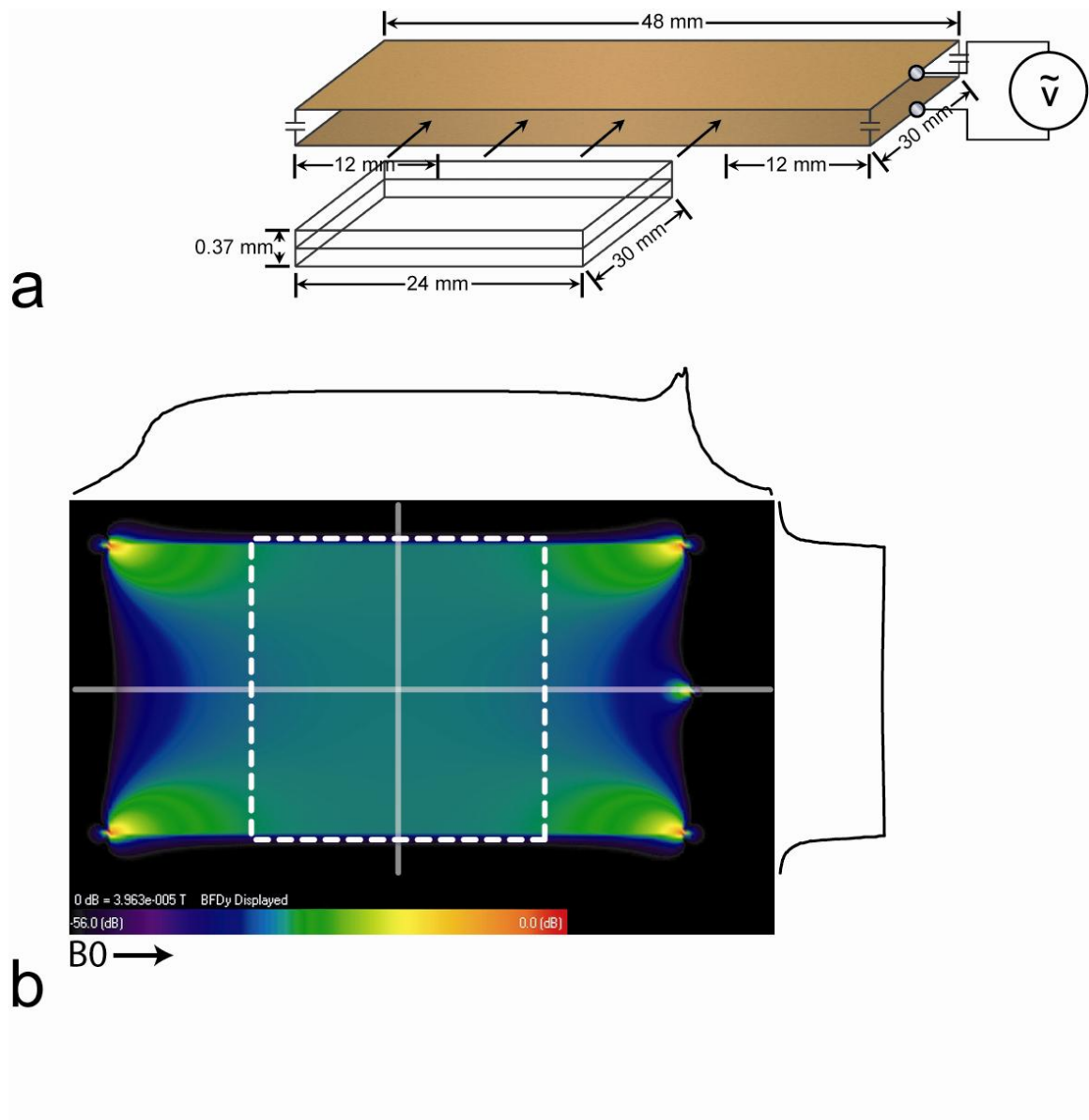
Figure 2.1.5.2

(a) Schematic of the optimized histological coil. A continuous strip of copper is wrapped around the glass coverslips and a piece of Teflon (green). Two glass coverslips with the histological sample encased between them are inserted into the opening of the coil for tissue loading. (b) Calculated transverse B1 field perpendicular to Bo in the center plane of the histological coil. The imaging region where the glass coverslips are placed is enclosed in the white dashed line. The profiles along the crosshairs demonstrate the homogeneity of the coil. The red outlined box represents the region where the Teflon is placed. The color scale in both Fig. 2.1.5.1b and 2.1.5.2b are set the same to facilitate comparison between the two designs. The profiles in Fig. 2.1.5.1b and 2.1.5.2b indicate that the homogeneity of the B1 field is improved with the optimized histological coil design. The direction of the Bo field is noted to aid in the orientation of the coil within the magnetic field.

a

0 dB = 3.963e-005 T   BFDy Displayed

-56.0 (dB)   0.0 (dB)

B0 ⟶

b
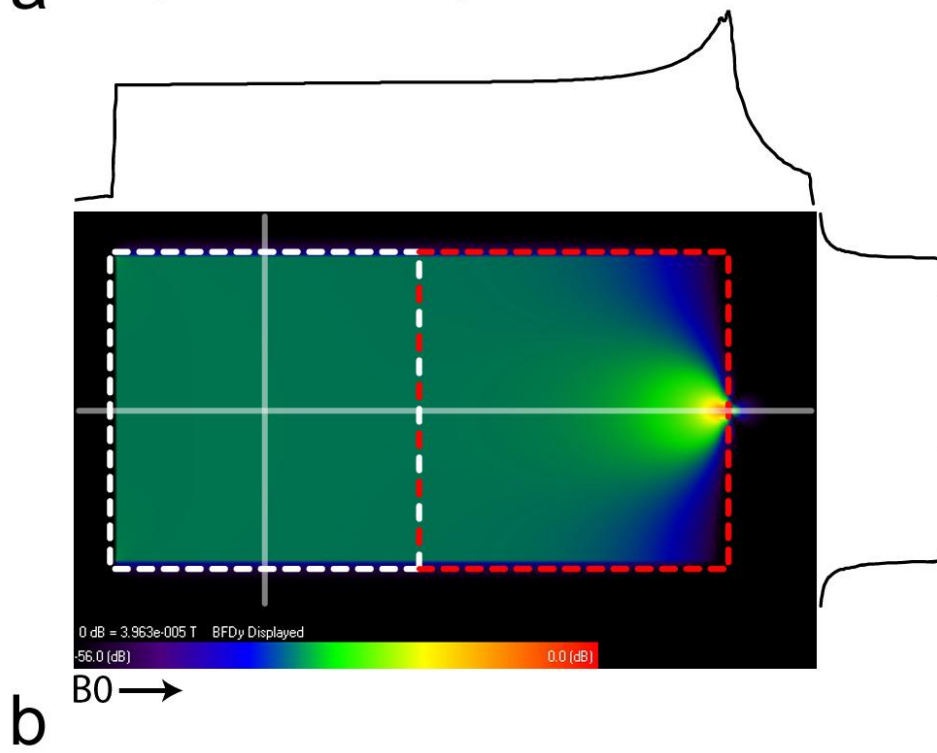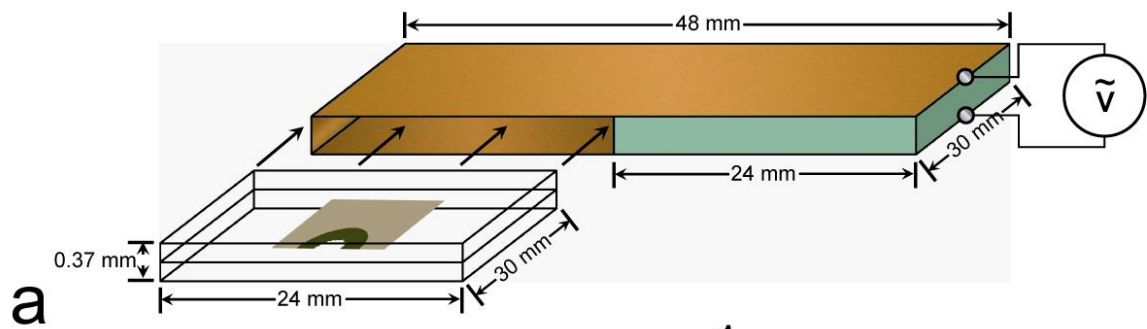
Figure 2.1.5.3

(a) Computer model of the histological coil. The Delrin acetal resin where the coil is positioned is represented by the semitransparent object. (b) Photograph of the completed coil with the 370 μm opening on the side where the tissue sample and coverslips are inserted along with tuning and matching variable capacitors and BNC connector at the end.
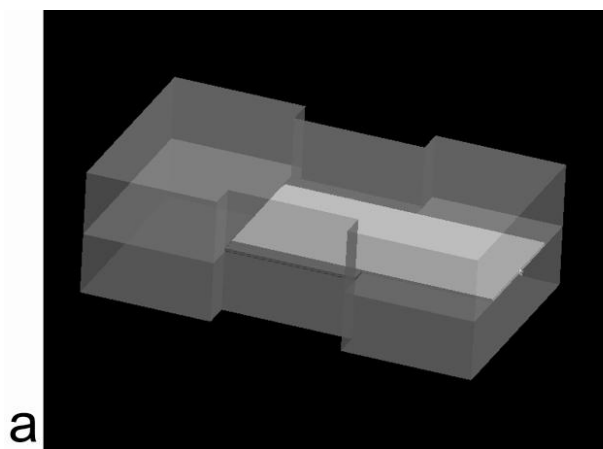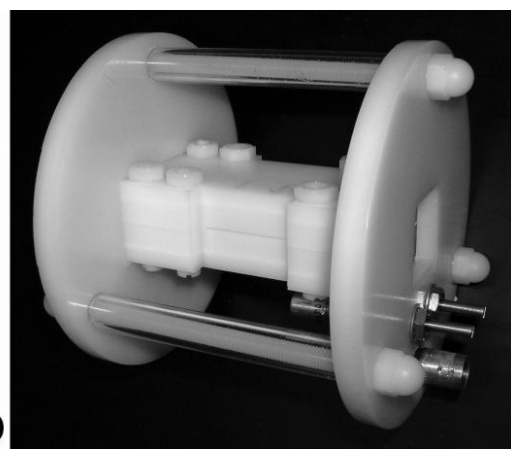
Figure 2.1.5.4

(a) T_2 weighted image obtained with the histological coil of the 12.5 µl phantom approximating the size of a tissue sample. Profiles through the horizontal and vertical center of the phantom are presented on the top and to the side of the image. (b) B1 field map of the 43.2 µl phantom with profiles demonstrating the B1 field uniformity of the coil within the imaging region. There are signal dropouts at the bottom two corners due to the drying of the agar sample and two small artifacts due to air bubbles within the sample.

a

23mm

B0 →

b

24mm

B0 →
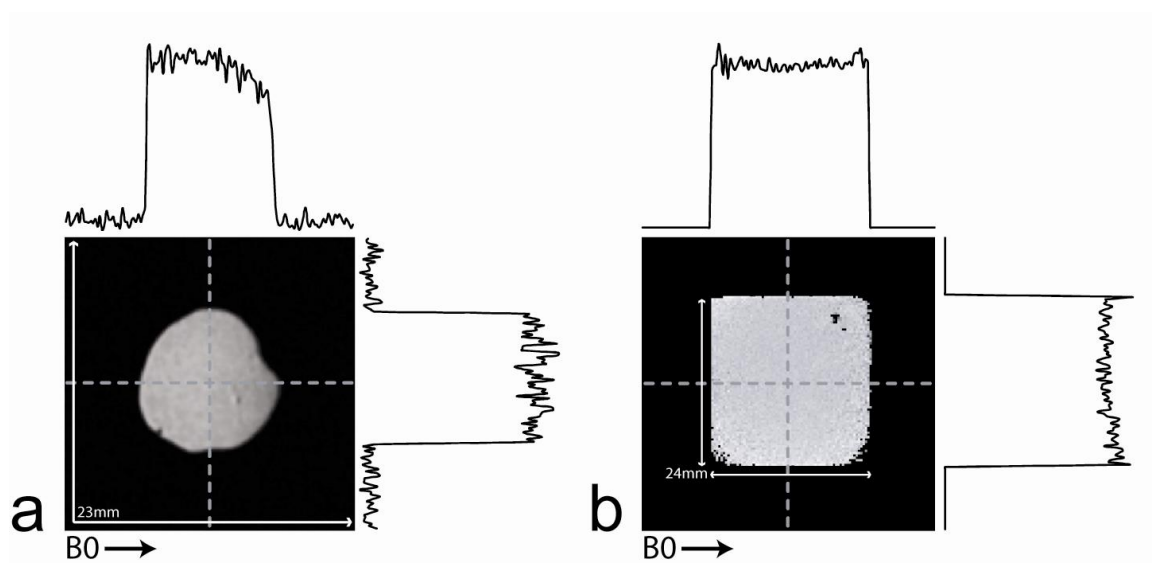
Figure 2.1.5.5

(a) T_2 weighted image of a 60 µm thick slice of human brain tissue. (b) Image of the same tissue section stained after MRI by modified Perl's Prussian blue for iron content. Dark regions are indicative of higher iron concentration within the tissue. The correlation of iron content with T_2 contrast is seen in the images where the white matter shows up as darker on the T_2 image and high in iron with the histology stain. Conversely, gray matter regions show up as brighter on the T_2 image and lower in stained iron concentration. The 50x digital enlargement of the MR image and 50x optical bright field magnification at the bottom demonstrate the close relationship between iron deposition and T_2 content. The regions of highly focal cellular iron concentration in the magnified histology image are clearly seen as darker spots in the MR image. The relative size of the iron deposition affects the magnitude of the hypo-intensities in the MR image. A typical arrowhead-type imaging artifact is visible around the large hypo-intensity in the digitally enlarged MR image. Staining artifacts at the edges of the tissue sample due to increased edge surface area are not indicative of higher iron content. Scale bars of 2000 µm for the whole tissue images and 250 µm for the 50x magnified images are included for reference. The direction of the Bo field is noted to aid in the orientation of the slice within the histological coil.
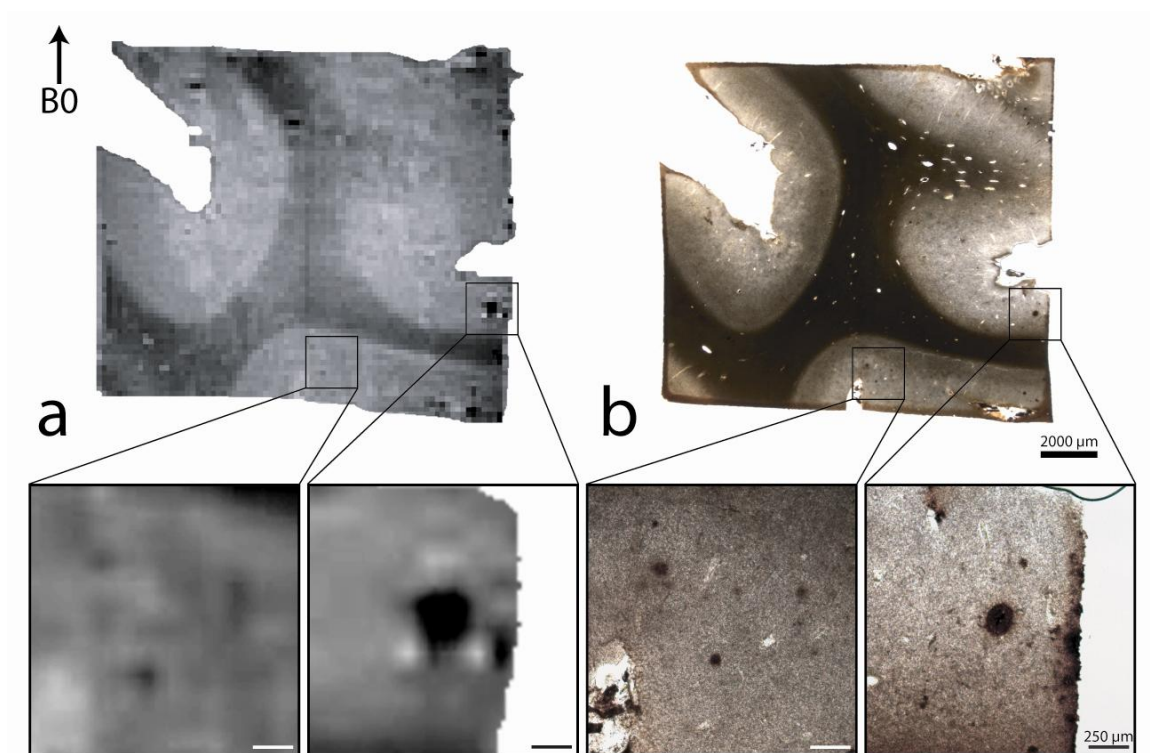
Figure 2.1.5.6

(a) T_2 parameter map generated from the same histology slice data as in Fig.

2.1.5.5. Regions of interest were selected in gray and white matter from six

individual maps and are represented by the solid and dashed boxes,

respectively. (b) Average T_2 relaxation curves (N=6) with standard deviation

bars of each echo image from the ROIs. The average T_2 in the ROI is 85.5 ± 2.4

ms for gray matter and 66.1 ±1.5 ms for white matter. The direction of the Bo

field is noted to aid in the orientation of the slice within the histological coil.
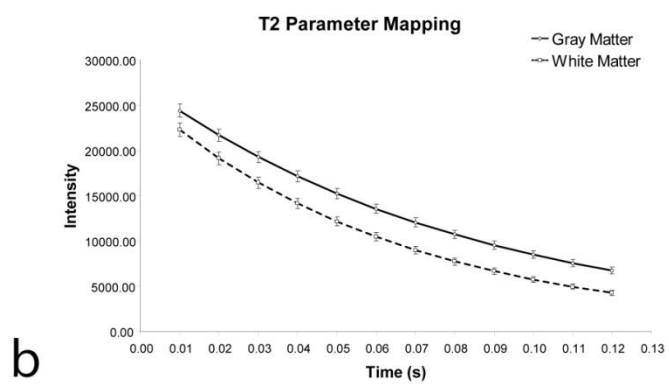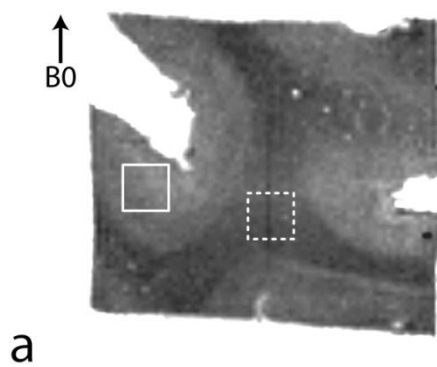
Figure 2.1.5.7

Side photograph of the 7.0 T histology coil. The fundamental 7.0 T design is similar to the 3.0 T design except for the shortening of the copper plates to reduce the distributed capacitance and the addition of a balun to reduce coupling with outside interference.

Balun

33mm

23mm
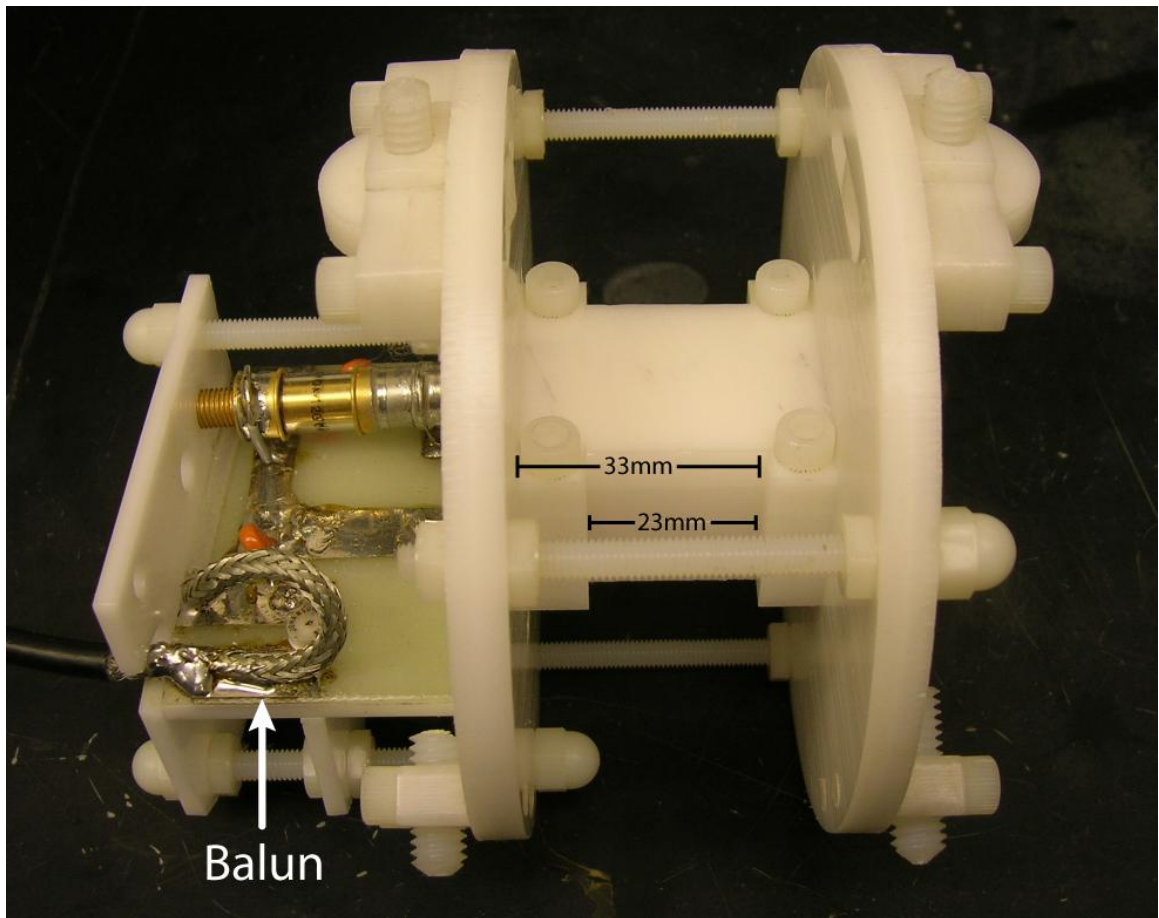
Figure 2.1.5.8

Comparison between images obtained with the 3.0 T and 7.0 T histocoils.

(a) 3.0 T histology coil MSME image made up of the addition of 8 echoes with a matrix size of 128 x 128 for an acquisition time of 5h59m. (b) 7.0 T histology coil MSME image made up of the addition of 8 echoes with a matrix size of 512 x 512 for an acquisition time of 6h15m. Both scans are of tissue from an Alzheimer's disease brain. White matter and gray matter and gray matter can clearly be made out in both images, however the increased resolution in the 7.0 T data allows the clear visualization of focal iron deposition that is not easily discernable in the 3.0 T data.
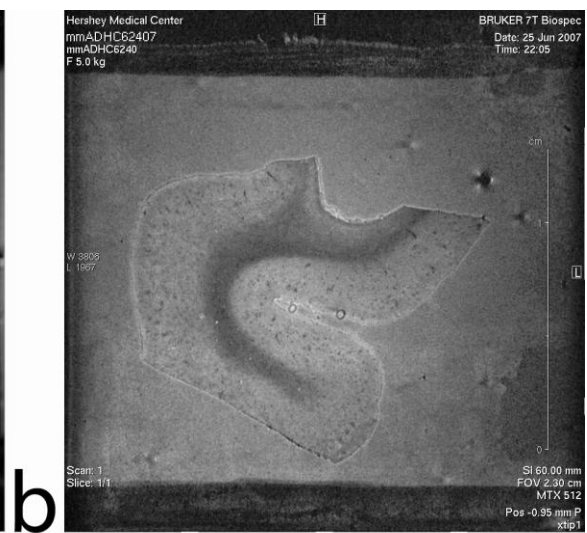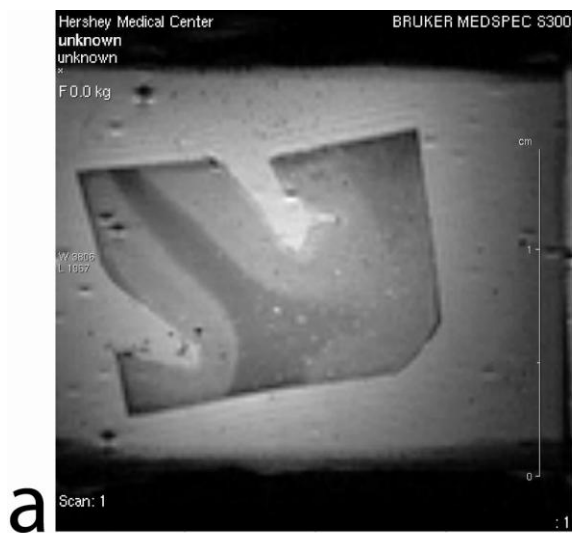
2.1.6 – Discussion

Numerous NMR micro-imaging studies have been carried out on various samples with attainable resolution on the order of several micrometers. Many of these studies continue to use small traditional birdcage volume coils (163,164), while others have investigated using Helmholtz pair coil designs (150,165). Small multi-turn solenoid volume and surface coils (166,167) remain to be the most prevalent design for high resolution images at ultra-high field strengths. Our coil, however, was designed specifically to directly image a histological sample between two standard histological #1 glass cover slips. For such an application, the coil design must meet two stringent criteria: 1) given the minute amount of tissue in a histology slide, the coil sensitivity must be maximized. This requires a compact coil design to optimize the filling factor (4) such that coil volume is minimized and the tissue is as close as possible to the conductive coil elements over the entire sample. 2) As a result of the vast difference in aspect ratio between imaging planar size and the thickness of the slice, the coil must produce a homogenous field distribution within a planar area of 24 mm x 24 mm in the histological slice. Since the two criteria appear to be mutually exclusive, the difficulty in designing such a coil arises in meeting the two criteria simultaneously. To meet criterion 1, the coil must fit the sample tightly. However, as seen in Fig. 2.1.5.1, the B1 distribution under such a condition can be dominated by the current around the terminals of the conductive elements because of the size of the coil and the close vicinity of the conductor and sample. These effects are generally insignificant for the overall field homogeneity in the

imaging region for human studies because of the relatively large size of the coil and sample. This problem can be alleviated by increasing the planar dimension as seen in the flat slotted tube resonator in Fig. 2.1.5.1. With this approach, however, the filling factor of the coil is significantly reduced since the effective coil size is considerably enlarged. In this case, the coil sensitivity is reduced as a trade off for B1 field homogeneity. In our coil design, the number of termination points is minimized to a single input pair by using a continuous copper foil and a distributed capacitor. The latter condition is created by efficiently utilizing the space that is necessary for RF field homogeneity between the input port and imaging region. The calculated B1 field and experimental image profiles in Fig. 2.1.5.2 and 2.1.5.4b are in close agreement with one another and highlight the nearly perfect homogenous field within the histological coil.

It is evident in Fig. 2.1.5.2 that our design utilizes the far end of the coil region where the electric field is weakest for imaging and the region next to the input port where the electric field is strongest for creating distributed capacitance. A decrease of the electric field in the sample results in a reduction of resistive losses within the sample (6) and an increased Q factor (168-171), which is desirable for SNR enhancement in micro-imaging. Coil design placing the tissue sample as close as possible to the coil's conductor surfaces (within 150μm, coverslip thickness) optimizes the filling factor and further enhances SNR (4).

One other major concern in designing the histological coil for optimizing RF field homogeneity is the so-called "fringe effect" in a conductor with high frequency alternating current. The current distribution, in this case, concentrates to the edge as the frequency of the alternating field increases. This fringe effect is particularly strong if the conductor is a long flat strip (172). Eddy currents in the conductor that tend to compensate the magnetic flux changes in space following Faraday's law are responsible for the creation of the fringe effect. As seen in the calculated B1 magnitude map in Fig. 2.1.5.2 and demonstrated experimentally in the phantom image in Fig. 2.1.5.4b, concentration of current along the edges is minimal in our coil design because the copper plates below and above the sample are extremely close and the currents in them are nearly equal in magnitude and opposite in direction. With such a coil configuration, the magnetic flux in the regions outside the coil above and below the plate is nearly zero and thereby minimizing the fringe effect in the conductors. This results in a nearly uniform current distribution within the copper plate and a highly concentrated and uniform magnetic flux density inside the coil. The reduction of eddy currents with our coil design equivalently increases the surface area of the conductor and therefore lowers the resistance to the total current, which increases the coil's Q factor (168,173).

This work enables the micro imaging and histological staining of the same pathologically diseased tissue sections. Post-mortem high resolution MRI studies of regions of interest and comparisons to histology of disease states are

important for biomedical research. The accurate comparison between MR

images and histology of the same tissue slices has not previously been possible.

With our coil design, we acquired MR images from a histology slide of

Alzheimer's disease brain tissue sections with high resolution and SNR. The

results in Fig. 2.1.5.5 demonstrate that the MR image contrast can associate to a

specific histology staining technique. Iron staining patterns of the tissue samples

are in a excellent agreement with the T_2 contrast distribution. Closer histological

analysis of the enlarged regions in Figure 2.1.5.5 suggests that the focal iron

deposits possibly are abnormal accumulations of iron oxide hemosiderin resulting

from microbleeds (174,175). Despite these improvements with our coil, however,

discrepancies between the images acquired with these two different imaging

modalities could occur due to sample preparation and various image artifacts,

particularly in the MR images. For example, there are two visible dark spots in

the left corner of the T_2 images that are not shown in the histological images.

These two dark spots appear to be sandwiched by the two bright pixels above

and below and are most likely the magnetic susceptibility artifacts caused by the

air bubbles trapped between the two coverslips. Thus, great care must be made

during sample preparation to remove the air pockets between the sample and

one of the two glass coverslips. Furthermore, such magnetic susceptibility

artifacts could also arise around the focal region of high iron concentration. As

seen the amplified MR image in Fig. 2.1.5.5a, there are three bright spots

forming a triangular shape around the dark circular region. While the dark region

is clearly seen in the corresponding histology images indicating a focal high iron

concentration, these bright spots are absent in the histology image. The bright spots are typical arrowhead-type imaging artifacts caused by the Bo field gradient in the proximity of the focal iron deposit (151,167,176). Hence, when comparing MR and histological images, caution must be exercised to identify the artifacts in MR images and potential morphological alterations of the sample during histology staining.

The ability to create T_2 parametric maps (Fig. 2.1.5.6a) is of importance for comparison of histology with tissue relaxation times. This allows for quantitative studies between regions of interest within the same histology slide and comparison between normal and diseased tissues. These results were acquired from a field strength used in clinical MR imaging systems which simplified our analysis for establishment of a more direct relationship between tissue relaxation times and various pathologies. In our experiment, the histological coil assessment of T_2 in formalin fixed *ex vivo* human entorhinal cortex (N=6) results in 85.5 ± 2.4 ms for gray matter and 66.1 ±1.5 ms for white matter. *In vivo* T_2 measurements using the same field strength of 3.0 T yields 109 ms and 79 for gray and white matter, respectively (177). The observed reduction in T_2 relaxation from *in vivo* conditions to formalin fixed *ex vivo* measurements follows previously reported results (178,179). Since the physical and physiological conditions such as temperature, diffusion, perfusion, and oxygenation between *in vivo* tissue and a fixed histology slide are vastly different, the T_2 values obtained with the histological coil are generally not expected to be the identical to the *in*

vivo measurements (147,178-182). The exact understanding of T_2 relaxation drop due to the fixation process is not completely understood on a molecular level. In the literature, a number of groups have studied how fixation with formaldehyde affects the T_2 relaxation of tissue samples. It has been observed that the T_2 value of freshly excised brain tissue decays exponentially during the first week of formalin fixation and plateaus following this time period (179). It is known that fixation causes a number of tissue microstructure changes that affects water motility (147). The main reaction of fixation is believed to be due to the creation of methylene bridges between amino acids in proteins (180). This cross-linking of proteins in turn affects the motility of water in the tissue sample. Following fixation, the alterations in the microstructure of the tissue cause additional barriers to water molecules that make it more difficult for them to cross resulting in decreases in water motility and overall water diffusion (181,182). Imaging of unfixed fresh tissue samples was attempted with the histological coil. However, it was found that thin slices of fresh tissue could not withstand the additional forces exerted upon it by the water surface tension between the coverslips. With all of this in mind caution should be exhibited when comparing quantitative histological coil measurements with *in vivo* results.

Implementation of the coil design at 7 Tesla (Fig. 2.1.5.7) greatly improved both the signal-to-noise ratio and more importantly the resolution of the MR images. The previous 3 T design had adequate SNR and resolution of 179 μm^2 but was greatly improved to over sixteen times this at 45 μm^2. This is extremely

beneficial when imaging tissue samples in an attempt to compare the MR images to histological images. Images taken under a microscope are at ultrahigh resolution compared to MR datasets (on the order of well under 1 μm^2 per pixel). Thus it is favorable to have as high resolution MR data to compare to these microscopic images. Of importance in the scope of this research, the size of beta-amyloid plaques in human neural tissue are approximately 30 – 100 μm in diameter. With the original histology coil design and resolution, the resolution of the voxels in the MR images meant that it was extremely difficult to view these plaques. The increased resolution of the 7 Tesla coil meant that individual plaques could be resolved in the MR images, allowing for greater measurement of individual plaque MR characteristics (Fig. 2.1.5.8).

In summary, novel RF coils at 3.0 and 7.0 Tesla specifically were designed, developed and tested for direct imaging of histology slices. The numerical simulation and experimental data demonstrated that the developed coils were highly sensitive and capable of producing a uniform B1 field distribution in a planar region of a typical histological slice, allowing for acquisition of high resolution T_2 images and T_2 maps from a histology slice. The image intensity and T_2 relaxation map were directly compared with histological staining of relative iron concentration of the same slice. The experimental results demonstrated the feasibility of using our histological coil to image thin slices of tissue and to improve co-registration with histological results. Analysis and comparison between histology of a tissue sample and MRI in a one-to-one

fashion is of importance for validating new imaging methods and contrasts, especially in molecular imaging research. Understanding the relationship between a specific pathology and the resulting MRI contrast or quantitative parameters will aid in interpretation of contrast differentials seen in clinical studies.

Chapter 3

Magnetic Resonance Imaging and Histological Analysis of Beta-Amyloid Plaques in Both Human Alzheimer's Disease and APP/PS1 Transgenic Mice

3.1 – Abstract

Imaging of beta amyloid ($A\beta$) plaques in human Alzheimer 's disease (AD) and the APP/PS1 mouse model has been of great interest for AD research. However, the histo-pathological basis of the image contrast and relaxation mechanism associated with $A\beta-$plaques has not been well-understood. With the aid of the previously developed histological coil, T_2*-weighted images and R_2* parametric maps were directly compared to histology stains acquired from the same set of Alzheimer's and APP/PS1 tissue slices. The electronic microscopy and histology images revealed substantial differences in plaque morphology and associated iron concentration between AD and transgenic APP/PS1 mice tissue samples. For AD tissues, T_2* contrast of $A\beta$-plaques was directly associated with the gradation of iron concentration. Plaques with considerably less iron load in the APP/PS1 animal tissues are equally conspicuous as the human plaques in the MR images. These data suggest a duality in the relaxation mechanism where both high focal iron concentration and highly compact fibrillar beta-amyloid masses cause rapid proton transverse magnetization decay. For human tissues, the former mechanism is likely the dominant source of R_2* relaxation; for APP/PS1 animals, the latter is likely the major cause of increased transverse proton relaxation rate in $A\beta$-plaques. The data presented are essential for

understanding the histo-pathological underpinning of MRI measurement associated with Aβ plaques in humans and animals.

3.2 – Introduction

The formation of amyloid-beta (Aβ) plaques is a neuropathological hallmark and a cardinal feature of Alzheimer's disease (AD). APP/PS1 transgenic mouse models that mimic the formation of human Aβ plaques in the mouse brain are widely used as an animal model for AD investigations. The development of an imaging technology capable of visualizing and quantifying Aβ plaques in animal models and in the AD brain is critically important for translational, preclinical and clinical research. The ability to delineate Aβ plaques with MRI has been demonstrated *ex vivo* with human brain samples (183) and *in vivo* with the mouse model (184-186). Understanding the histological basis of MRI contrast associated with Aβ plaques is essential in this endeavor. To achieve this goal, it is necessary to correlate MRI results with histological stains, which has been technologically challenging because of the limitations in co-registration of planar histology tissue samples with MR images. A prior study involving the innovation of a histological coil has addressed this long-standing difficulty (187). The ability to directly image histological samples is possible when employing the developed histological radio-frequency (RF) coil design. Consequently, MR images and histology data from the same tissue sample can be directly overlaid and compared without uncertainties of co-registration between the two imaging modalities. The goal of the current study is to use this novel technology to a)

further optimize the method for routine imaging-histology studies, b) establish the relationship between MR image contrast associated with Aβ plaques and their histology, and c) compare such relationships in human and transgenic APP/PS1 mouse tissues. Furthermore, to ultimately apply the therapies developed with the animal models to human studies, the Aβ plaque MR image-pathology relationship must be validated in humans and compared to transgenic animal data. It is hypothesized within the literature that iron found in and around the amyloid plaques is the dominant cause of the hypo-intensities seen in the MR images. Examination of the relationship between MR contrast due to Aβ plaque and iron deposition both in human AD and the APP/PS1 model is described. These data suggest that iron load alone does not account for the hypo-intensities that are observed in the T_2*-weighted images of the animal pathology. The relationship of plaque morphology and overall globular size with their manifestation in the MR image are described. The method developed in this report can be particularly useful for further validation of the histological basis of MR contrast and the development of animal models for other neurological diseases.

3.3 – Materials and Methods

Human Alzheimer's and Control Brain Samples:

Entorhinal cortex brain tissue samples from clinically and histologically determined AD subjects (n=5) and age-matched controls (n=4) were donated with consent following institutional guidelines and obtained from both internal and external sources (Harvard Brain Tissue Resource Center, McLean Hospital,

Belmont, MA). Analysis of the tissue obtained from the brain bank indicates that there was not a significant difference between the age of the subjects upon bereavement. The post mortem index between the tissue harvesting at time of death and utilization in this study was significantly different between the tissue samples, with a slightly longer time period for controls. Tissue from the entorhinal cortex was fully fixed in 4% paraformaldehyde in pH 7.3 phosphate buffered saline (PBS) after which blocks of tissue were cryogenically protected in graded sucrose solutions then sectioned at 60 μm on a cryostat. The sections were prepared for magnetic resonance imaging according to previous methods explained below (187).

Transgenic APP/PS1and Control Mice:

Transgenic mice (n=5) inserted with a chimeric amyloid precursor protein (APP) (APPSwe$_{695}$) and a mutant human presenilin 1 (A246E variant), developed by Borchelt *et al.* (108,112), were obtained commercially from The Jackson Laboratory (strain type B6C3-Tg(APP695)3Dbo Tg(PSEN1)5Dbo/J). Animals were kept in the animal facility under veterinary care with normal feeding, environmental, and handling conditions. Age-matched cage mate C57BL/6 mice (n=3) were used as a control group. Upon aging naturally until 24 months, animals were euthanized via an intra-parietal injection of sodium pentobarbital (Nembutal, 200 mg/kg) and were transcardially perfused with cold Lactated Ringer's solution (pH 7.4) followed by buffered 4% paraformaldehyde in PBS. Whole brain tissue was harvested fixed in pH 7.3 buffered 4% paraformaldehyde,

placed in graded sucrose solutions for cryo-protection, then sections were cut at 60μm and prepared for MR micro-imaging using the protocol below.

Histological slice MRI Scanning Protocols:

Histological MRI was accomplished on a 7.0 T magnet (Bruker BioSpin MRI GmbH, Ettlingen, Germany) with the histological coil (187). 60 μm tissue samples were floated in PBS for 30 minutes to allow any residual formalin and sucrose in the tissue to leach out and then encased between the two coverslips. The sample was then placed into the histological RF coil and tuned/matched to 300.48 MHz for micro-MR imaging. For T_2* imaging, multi-gradient-echo (MGE) images were acquired in 6h 32m with a TR=718, TE=6.48, FA=30°, 8 echoes with 9ms echo spacing, 64 averages, FOV=23mm x 23mm, and a matrix of 512 x 512 resulting in a final in-plane resolution of 45 μm x 45 μm.

Iron and Amyloid Staining:

After histological MR imaging, the 60 μm tissue sections were free floated and rinsed in deionized water (dH_2O) for 15 minutes. Tissue sections were co-stained for both iron and beta-amyloid with a Perl's Prussian Blue stain followed by an aqueous Thioflavin-S stain. The sections were placed in equal volumes of freshly prepared 4% potassium ferrocyanide (#P236, Fisher Scientific, Waltham, MA) and 4% hydrochloric acid (final combined concentrations 2% for each) for 30 minutes under gentle rocking followed by two rinses in dH_2O. Intensification of the iron stain was performed with 5 minutes of 3,3'-diaminobenzidine

tetrahydrochloride (DAB) staining (#D5637, Sigma, St. Louis, MO) (10 mg

dissolved in 15ml of PBS with 16 µl of 30% H_2O_2) followed by two five-minute

rinses in dH_2O. Tissue samples were then free floated in 20 ml of 1% Thioflavin-

S (#T1892, Sigma, St. Louis, MO) aqueous solution for 5 minutes, followed by

differentiation in 70% ethanol for 5 minutes and two five-minute washes in dH_2O.

Sections were mounted on histological slides with FluorSave Aqueous mounting

media (#345789, Calbiochem, San Diego, CA). To test for the possibility of

confounding interactions between the two staining methods during co-staining,

each was tested on separate tissue samples to determine their individual efficacy

and compared to the co-stained sections. A modified Perl's stain further tested

the transgenic animal tissue for minute amounts of iron within the amyloid

masses. The stain was adapted and modified from LeVine (188,189) and

employs the usage of proteinase K and detergents to break down the periphery

of the plaques forming openings in the highly hydrophobic amyloid plaques. This

allows the aqueous Perl's stain to infiltrate into the amyloid mass and is sensitive

enough to detect trace amounts of iron in the Aβ plaques.

Microscopy:

     High resolution microscopy of the tissue sections was performed using a

Nikon OptiPhot microscope and Nikon Digital Sight camera using NIS-Elements

software. Bright field microscopy under the visible light spectra was used to view

iron stains. A FITC fluorescence cube at 430 nm excitation and 550 nm emission

was used to visualize Thioflavin-S positive Aβ deposits. Whole tissue image

mosaics were created with the 40x magnification bright field of fluorescent

images using the Photomerge option in Adobe Photoshop CS (Adobe Systems

Incorporated, San Jose, CA, USA). For transmission electron microscopy (TEM),

samples were prepared by cutting tissue sections at 60 µm and staining them

with Thioflavin-S to elucidate Aβ plaque location. Known regions of Aβ plaque

distribution approximately 1 mm x 1 mm were micro-dissected from the sections

and processed for electron microscopy following traditional methods.

MRI and Histology Post Processing:

Post processing was performed using in-house software developed with

the interactive data language (IDL) 6.1 framework (Research Systems Inc., ITT

Industries, Boulder, CO, USA). The program allows for the creation of T_2*

parameter maps from MGE data with a linear regression method. Plaque

regions of interest (ROI's) were selected by averaging the relaxation of three

voxels of interest within each measured plaque. Averaging of multiple voxels

helps eliminate partial volume effects where it is possible and likely that plaques

span multiple voxels on the MR data sets. This allowed for the evaluation of

relaxation and magnitude measurements from individual plaques in both human

AD and APP/PS1 tissue. ROI's for non-plaque regions were selected in regions

known to be devoid of Aβ plaques according to the Thioflavin-S staining. For co-

registration to the staining methods, T_2* weighted images were generated by the

summation of the amplitude images from all of the echoes. Histology and MRI

images were imported into Image J (National Institutes of Health, Bethesda, MD,

129

USA) to measure Aβ plaque diameter. Freehand boundaries were drawn around

the plaques and the average pixel length of the major and minor axes from the

resulting ellipsoid were used to estimate overall diameter. A micrometer slide

was viewed at different magnifications to obtain precise measurements of the

pixel to micrometer dimensions for plaque diameter calculation.

3.4 – Results

Figure 3.5.1 shows a T_2^* weighted MR image and histological images co-

stained with thioflavin-S for Aβ plaques and a traditional Perl's stain for ferric iron

(Fe^{+3}) within the same tissue section from the entorhinal cortex of an AD subject.

The image scales of the MR scan and stain mosaic images for Aβ and iron are

the same for ease of comparison. For detailed evaluation, 40x magnification

images of four selected regions outlined with red boxes are shown on both sides

of the corresponding main images. The T_2^*-weighted images of human

Alzheimer's samples show a loss of signal in focal regions that co-registers

remarkably well to the histological iron stain. Many dark hypo-intense spots can

clearly be observed in the gray matter in the MR image in Fig. 3.5.1a. As seen in

the magnification of the thioflavin-S stain images (figure 3.5.1b), those hypo-

intensities observed in the MR images correspond to either punctate green

fluorescent Thioflavin-S positive Aβ-plaques (red arrows) or dark brown patches

indicating regions of high focal iron. Focal regions of high iron that are not

associated with Aβ plaques can be attributed to locations high in iron such as

capillary vessels, hemosiderin (degraded ferritin) or regions of iron oxide

(magnetite, hematite or wüstite) deposition (blue arrows) (175,190). Co-staining

of Aβ with Thioflavin-S and iron with a Perl's stain allows the direct comparison of

ferric iron concentration in and around the beta-amyloid plaques (Fig. 3.5.1c).

The Perl's stain of the tissue section demonstrate focal high iron concentration

associated with Aβ plaques in exceptional detail. Many of the Aβ plaques seen

in the magnified images appear to have a dark core in their centers that are

loaded with a higher concentration of iron, as indicated in the Perl's stain. This

set of images reveals an unprecedented close relationship with MRI contrast

between Aβ plaques and brain tissue iron deposition. The minimal AD plaque

size diameter that can be resolved with the T_2^* weighted sequence is 38 μm,

demonstrable with the 250 μm scale bars in the figure 3.5.1 magnifications.

Smaller human AD plaques that do not visibly contain large amounts of iron are

not as discernable on the MR images. The high iron distribution within the white

matter tracks of the human tissue is consistent with iron found in oligodendrocyte

cells making up the myelin sheaths (191). With the histological coil, the

relationship between T_2^* image contrast associated with Aβ plaques and their

association with iron deposition are demonstrated unambiguously. The presence

of higher iron deposition in the Aβ plaques is a contributing factor to T_2^* image

contrast generation. Regions of gray matter that exhibit high iron content are

clearly visible on the MR image with varying degrees of signal dropout differing in

size based on the amount of iron present at that location. MR image and

histology from a normal brain tissue are shown in Fig. 3.5.2 and demonstrate a

complete absence of Aβ plaques. The Perl's stained images of the human

control tissue sections demonstrate the known patterns of normal iron staining in regions associated with high iron concentration. Iron stains of the human control tissue (figure 3.5.2c) show the expected high diffuse iron in the white matter tracks due to the high iron concentration within the oligodendrocyte cells (58). This known phenomena can be seen with all histological iron stains and in MR images as a signal dropout. Comparison of white matter iron staining between human AD and control samples shows similar iron deposition illustrating negligible iron loss due to formalin leaching. Fluorescent microscopy shows a lack of Thioflavin-S positive Aβ staining, while nonspecific background fluorescence is present. Having neither Aβ plaques nor high focal iron regions, MR images of human control tissue (Fig. 3.5.2a) exhibit a lack of hypo-intensities in gray matter except those caused by the highlighted focal iron regions (blue arrows in Fig. 3.5.2) and coil noise. Small hypo-intensities that are seen in figure 3.5.2 are related to inhomogeneities within the copper foil used in the RF coil, small micro-pockets of air causing artifacts, or small regions of focal iron.

The corresponding images from APP/PS1 and age-matched C57BL/6 control mice tissue sections are shown in figures 3.5.3 and 3.5.4, respectively. The image scales of the animal MR images and histology mosaics for iron and Aβ plaques are the same as in the human data for ease of comparison. The widespread dark spots (red arrows) seen in the human tissue are also shown conspicuously in the T_2* image of the transgenic animal tissue within the piriform cortex (Fig. 3.5.3a). Thioflavin-S staining (Fig. 3.5.3b) confirms that these dark

spots are Aβ plaques within the APP/PS1 animal brain. MR imaging of mouse

control tissue (Fig. 3.5.4a) shows no evidence of focal hypo-intense regions in

the neo-cortex. The iron stain of the control mouse tissue in figure 3.5.4c shows

that there are no visible focal iron regions in the neo-cortex or other gray matter

regions. Thioflavin-S staining does not indicate any positive amyloid staining for

plaques in mouse control sections apart from the expected non-specific

background staining. Regions that are known to be high in iron, such as the

substantia nigra and caudate/putamen, stain dark as expected (Fig. 3.5.3c)

(192). The plaque distribution is consistent with previous studies using the

APP/PS1 transgenic mouse line (186,193-195), while plaques are not present in

the C57BL/6 control animal tissue. Measurements of the plaques within the

APP/PS1 model indicate that MR microscopy observable plaques have a

minimum diameter of approximately 40 μm, which is very similar to the human

AD samples. Smaller plaques are also visible with Thioflavin-S staining

throughout the neo-cortex (barrel fields, somatosensory, motor, and granular

cortices), hippocampus, thalamic region, caudate and putamen of the animal

brain but are not visible in the MR images. The most prominent difference

between the human AD (Fig 3.5.1b and c) and APP/PS1 mouse tissues (Fig.

3.5.3b and c) involves the focal iron concentration found in the vicinity of the Aβ

plaques. Large amounts of focal iron are found within and around the Thioflavin-

S positive amyloid plaques in the human AD tissue while very little is seen in the

APP/PS1 tissue. In the magnified images, the plaques indicated by the red

arrows in figure 3.5.3b coincide with the white patches in figure 3.5.3c,

suggesting lower iron content in these areas. This observation seems to be in

opposition to what has been demonstrated in the human AD tissues. No dark

iron cored plaques were observed in the transgenic animal histological images

compared to the human AD sections. This is also at seen at higher

magnification, as illustrated at 100x in figure 3.5.5. Aβ plaques in human AD

tissue appear to be small cored plaques surrounded by large diffuse coronas

while the plaques in the APP/PS1 mouse tissue exhibit larger dense cores made

of compact fibrillar Aβ protein deposition with a smaller diffuse corona region.

The Alzheimer's tissue samples demonstrate the localization of iron (Fig. 3.5.5b)

within the amyloid plaque mass (Fig. 3.5.5a). Transgenic animal tissue shows a

high concentration of large amyloid deposits while co-staining with the traditional

Perl's ferric iron stain does not show regions of high iron within the these

plaques. Staining capillaries high in iron serves as a positive control for the

effectiveness of the traditional Perl's stain for detecting iron, indicated by arrows

in figures 3.5.5c and 3.5.5d. Minor digestion of the Aβ plaque periphery in the

APP/PS1 tissue and staining with the modified Perl's technique are shown in

figures 3.5.5e and 3.5.5f. There is visible evidence of trace amounts of iron in

the transgenic animal plaques that was not stainable with the traditional method.

The iron load within the APP/PS1 plaques is very minute compared to the human

AD tissue. Staining the human AD tissue (not shown) with the modified Perl's

technique rendered the samples completely brown, which is indicative of iron

throughout the tissue samples. There is a possibility that the protein digestion

also exposed the ferrihydrite and magnetite core of the ferritin complexes in

these samples allowing the Prussian blue reaction to occur throughout the sample (196). This result rendered the microscopic detection of focal iron around Thioflavin-S plaques impractical for human AD sections stained in this manner. The iron stain of both APP/PS1 and control animal tissue does show appropriate tissue iron distribution as evident in the known high iron brain structures such as the substantia nigra, striatum and white matter tracks (197). High magnification 6000x and 46,000x transmission electron microscopy images of amyloid plaques from both APP/PS1 and human AD can be seen in figure 3.5.6a and b, respectively. Each plaque in figure 3.5.6a and b is similar in size, approximately 10 μm in diameter. The 6000x images include the whole plaque within the viewing plane and illustrate that Aβ plaques in the APP/PS1 model have a denser overall structure then the plaques found in human AD. Higher 46,000x magnification of the outlined regions shows fibrillar Aβ strands in both AD and APP/PS1 tissue and further demonstrates the difference in density between AD and APP/PS1 plaques.

For quantitative MRI studies, Fig. 3.5.7a graphically shows average relaxation values for regions of interest that included and excluded Aβ plaques within the AD sample and regions within the gray matter of the control sample. Average R_2^* measurements for the AD tissue samples were 30.33 ± 3.86 (1/s) in regions with plaques and 16.10 ± 2.92 (1/s) in regions without plaques. Control tissue R_2^* relaxation rate was 14.54 ± 2.01 (1/s). R_2^* relaxation rates for the regions with plaques were significantly higher ($p<0.0001$) than both the controls

and regions without plaques. Relaxation measurements in regions without plaques were not significantly different from control tissue. Average relaxation values for gray matter regions in the APP/PS1 mice that included or excluded Aβ plaques and control animals are seen in figure 3.5.7b. Average R_2^* measurements for APP/PS1 were 24.84 ± 3.67 (1/s) in regions with plaques and 18.40 ± 1.47 (1/s) in regions without plaques. C57BL/6 controls had an average R_2^* relaxation of 18.75 ± 1.03 (1/s). Regions with plaques in the APP/PS1 animals had a significantly higher R_2^* relaxation compared to both control tissue and regions without plaques ($p<0.0001$). Measurements of R_2^* relaxation were not significantly different between regions of interest in the transgenic animal devoid of plaques and control mouse tissue.

3.5 – Figures

Figure 3.5.1

T_2* weighted MR image (a) and histological images of Thioflavin-S stain for beta-amyloid plaques (b) and (c) Perl's iron stain of the same tissue section from the entorhinal cortex of an Alzheimer's disease subject. For detailed comparisons, images with 40x-magnification of four selected regions outlined with red boxes are shown on both sides of the corresponding main images. A large amount of black spots can be seen clearly in the gray matter in the MR image in (a). As seen in Fig 3.5.1b in the Thioflavin-S stain images, these black spots are shown either as bright green indicating Aβ-plaques (red arrows) or dark brown indicating small blood vessels (blue arrows). The Perl's stain of the brain tissue in (c) demonstrates focal high iron concentration in both Aβ-plaques and blood vessels. For the former, a higher iron deposition in Aβ has been previous demonstrated. For the latter, the elevated iron is likely associated with residual blood, ferritin/hemosiderin or magnetite.   As seen in Fig. 3.5.1c, select hypo-intensities in the MR that are due to beta-amyloid plaques are seen with red arrows while signal dropout due to other focal iron regions are highlighted with blue arrows in the four concurrent image magnifications. The figure illustrates that hypo-intensities seen in the T_2* weighted image correlate to plaque location and focal iron concentrations. Iron deposition is present in the beta-amyloid plaques that are viewable in the MR image sets. Scale bars for the magnifications are 250µm and 1mm for the whole images.
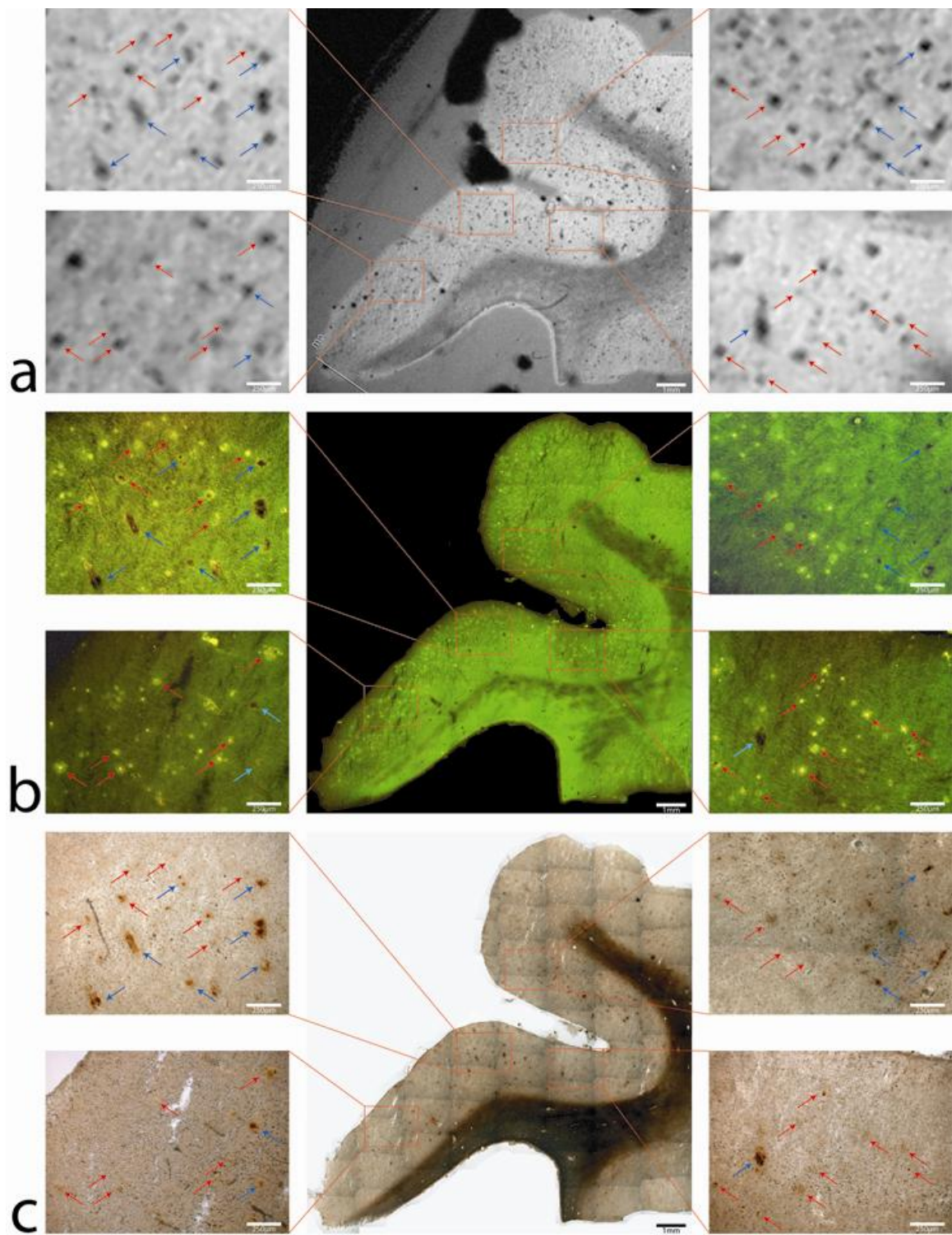
Figure 3.5.2

Magnetic resonance image, thioflavin-S and iron stains in human control subjects. (a) An MGE $T_2{}^*$ weighted image, (b) thioflavin-S and (c) Perl's iron stain of the same 60µm thick tissue section from the entorhinal cortex of an Alzheimer's disease subject. The $T_2{}^*$ image shows hypo-intensities that are due to micro pockets of air or coil inhomogeneities. The thioflavin-S stain illustrates a lack of beta-amyloid plaques in the human control subjects. Perl's staining shows high iron in white matter tracks due to oligodendrocytes and one focal iron region in gray matter that is highlighted with the blue arrow in the three images and can be seen as a signal drop in the MR image. Scale bars in all images are set at 1mm.
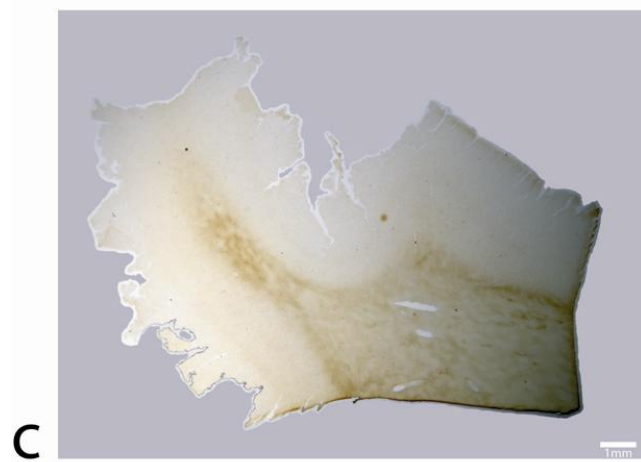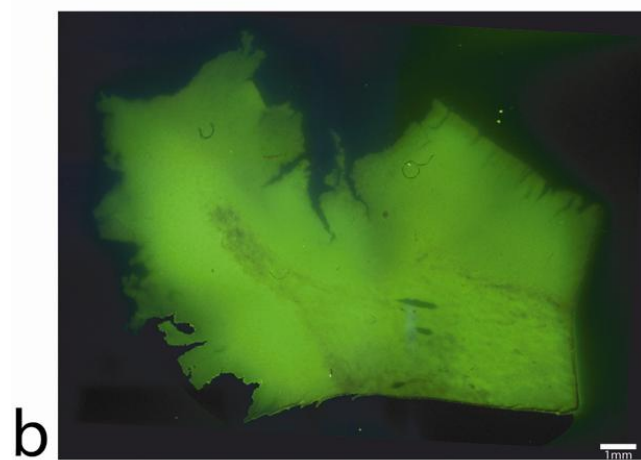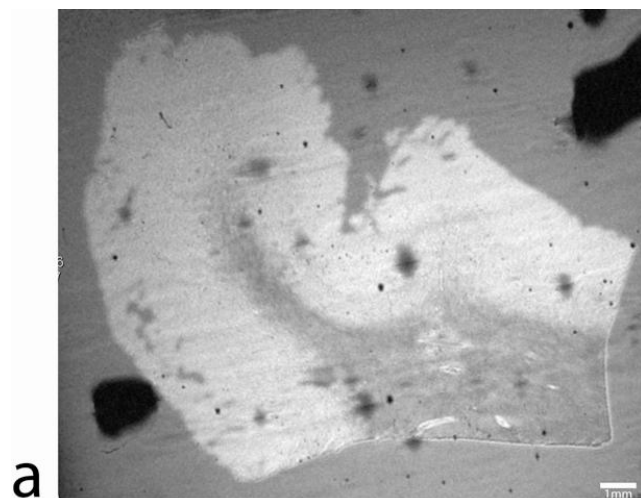
Figure 3.5.3

Co-registration of (a) magnetic resonance images, (b) beta-amyloid and (c) iron stains in the APP/PS1 mouse model. (a) An MGE T_2* weighted image of a 60µm slice from a APP/PS1 mouse brain a approximately -2.92mm Bregma. Final in-plane image resolution was 45µm x 45 µm. Image magnifications (40x) of the selected regions of interest within the left and right piriform cortex are seen below. Hypo-intensities are noted by red arrows. (b) Thioflavin-S fluorescent mosaic image of the same tissue section in 1a. Beta-amyloid staining is evident and can be seen as the bright green positions. The same regions as in 1a have been magnified with the arrows pointing toward the plaques responsible for the T_2* weighted hypo-intensities. (c) Perl's iron stain with the same magnifications and regions of interest arrows as in 3.5.1a and 3.5.2a. The figure illustrates that the hypo-intensities seen in the T_2* weighted image are in the same region as large beta-amyloid plaques approximately 50 – 60 µm in diameter. Iron deposition is not present at the plaque locations, as they seem to be regions of low iron concentration compared to the surrounding gray matter tissue. Scales bars for the magnifications are 250 µm and 1mm for the whole image.
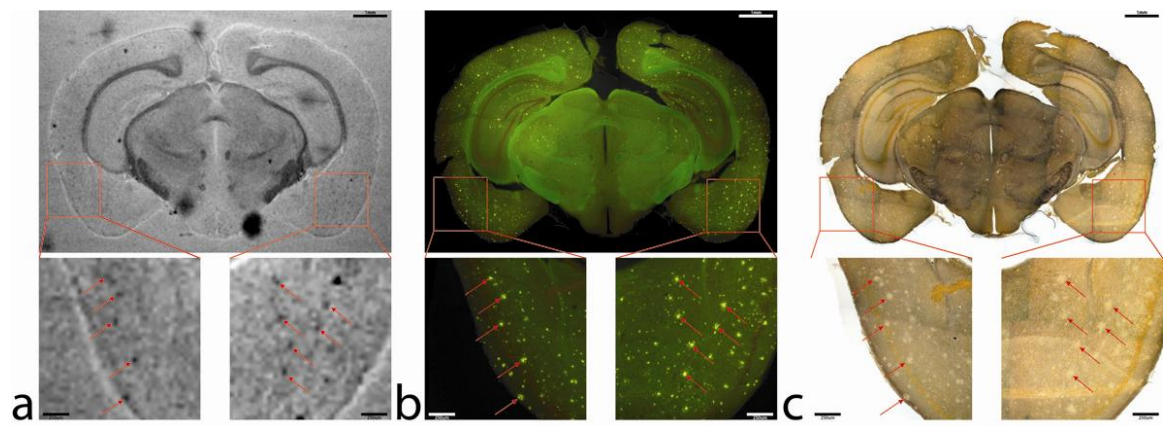
Figure 3.5.4

Magnetic resonance image, thioflavin-S and iron stains from a control C57BL/6 mouse. (a) An MGE T_2* weighted image, (b) thioflavin-S, and (c) Perl's iron stain of the same 60 μm thick section of tissue from a C57BL/6 control mouse at approximately -2.80mm Bregma. The T_2* weighted image shows hypo-intensities and iron staining at regions of known high iron concentration such as the substantia nigra, white matter tracks and the caudate/putamen. Thioflavin-S staining reveals only non-specific background staining with no beta-amyloid plaques in the control animals. There are no MR hypo-intensities that are associated with positive thioflavin-S staining. Scale bars in all images are 1mm.
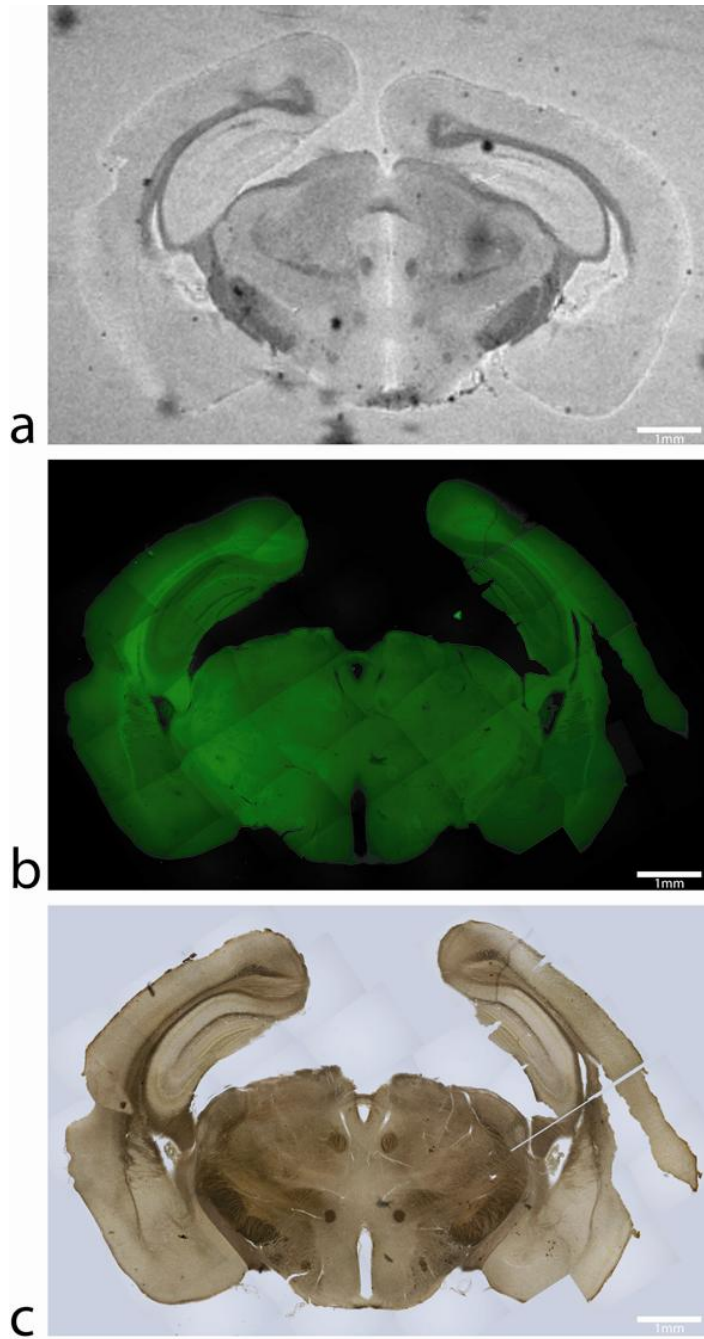
Figure 3.5.5

High magnification (100x) images of beta-amyloid plaques in both human

Alzheimer's entorhinal cortex (a,b) and APP/PS1 animals piriform cortex (c,d,e,f).

The thioflavin-S stain (a) and traditional Perl's stain (b) illustrate a close

relationship between beta-amyloid plaques and focal iron deposition in

Alzheimer's disease. This relationship between plaques (c) and iron (d) is not

clearly seen in the APP/PS1 animals with traditional Perl's staining. The arrow in

(c) and (d) illustrate iron deposition in a capillary of the APP/PS1 animal

demonstrating the positive stain for iron. Staining with a modified Perl's

technique (e,f) via degradation of the plaques' periphery proteins allows the

aqueous stain to penetrate the plaques more readily. There is an indication of

minute amounts of iron in the transgenic animal plaques that is not perceivable

with the traditional Perl's stain. Differences in plaque morphology between the

AD and APP/PS1 animals is evident in images (a) and (c,e). The human AD

plaques have a dense core of fibrillar amyloid protein with a halo of amyloid

protein around them that is less susceptible to thioflavin-S staining. APP/PS1 Aβ

plaques show a larger and denser thioflavin-S positive core with a smaller halo

region around them. The Perl's stains indicate that high concentrations of iron

found throughout the human AD plaques that associated with the amyloid protein

or within cells such as microglia inside the space the plaque has occupied.

Compared to the human AD plaques, the APP/PS1 images show a reduction in

focal iron within the plaques that is diffusely found throughout the plaque. Scale

bars for all images are 100μm.
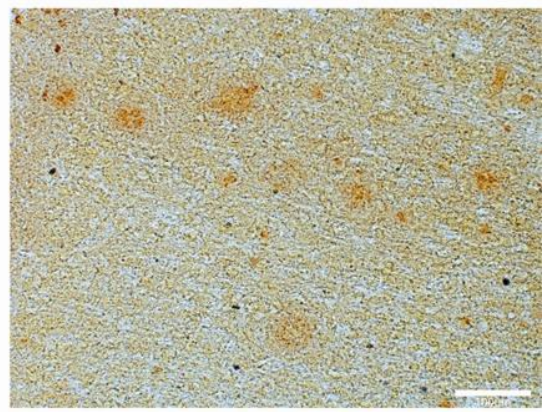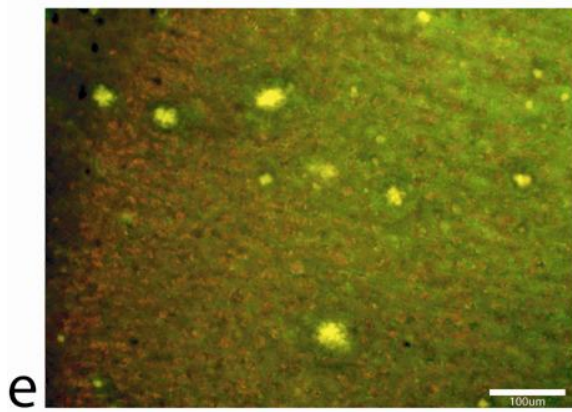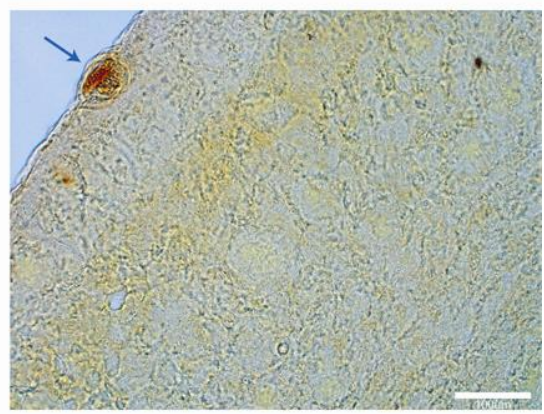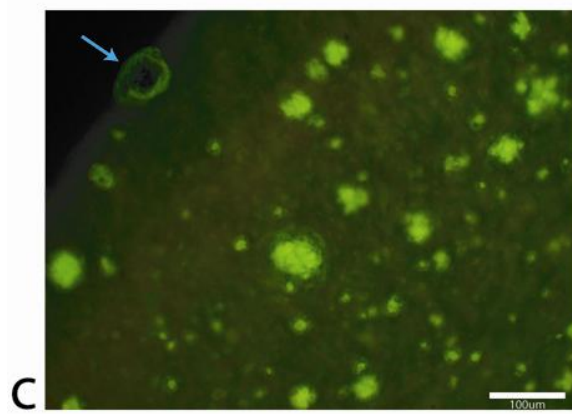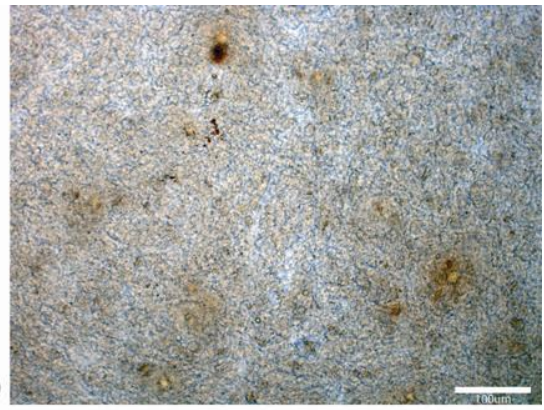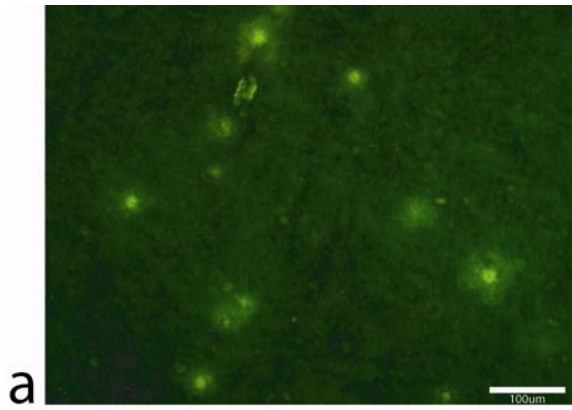
Figure 3.5.6

Transmission electron microscope images of plaques in (a) APP/PS1 and (b) human AD tissue. The 6000x magnification images of the plaques include the whole plaque within the imaging plane. The plaque diameter for both APP/PS1 and AD tissue is approximately the same, at 10 μm. The lower magnification image illustrates the denser overall structure of the beta-amyloid plaques in the APP/PS1 compared to the human AD tissue. The human AD plaques have numerous gaps present between the fibril bundles throughout them that are rarely found in the transgenic mouse plaques. 46,000x magnification of the outlined regions reveal differences in the fibrillar orientation of the beta-amyloid strands in the APP/PS1 and AD plaques. Magnification of the outlined regions also illustrates the denser nature of the APP/PS1 plaques while the human AD tissue has gaps between amyloid strand clusters.
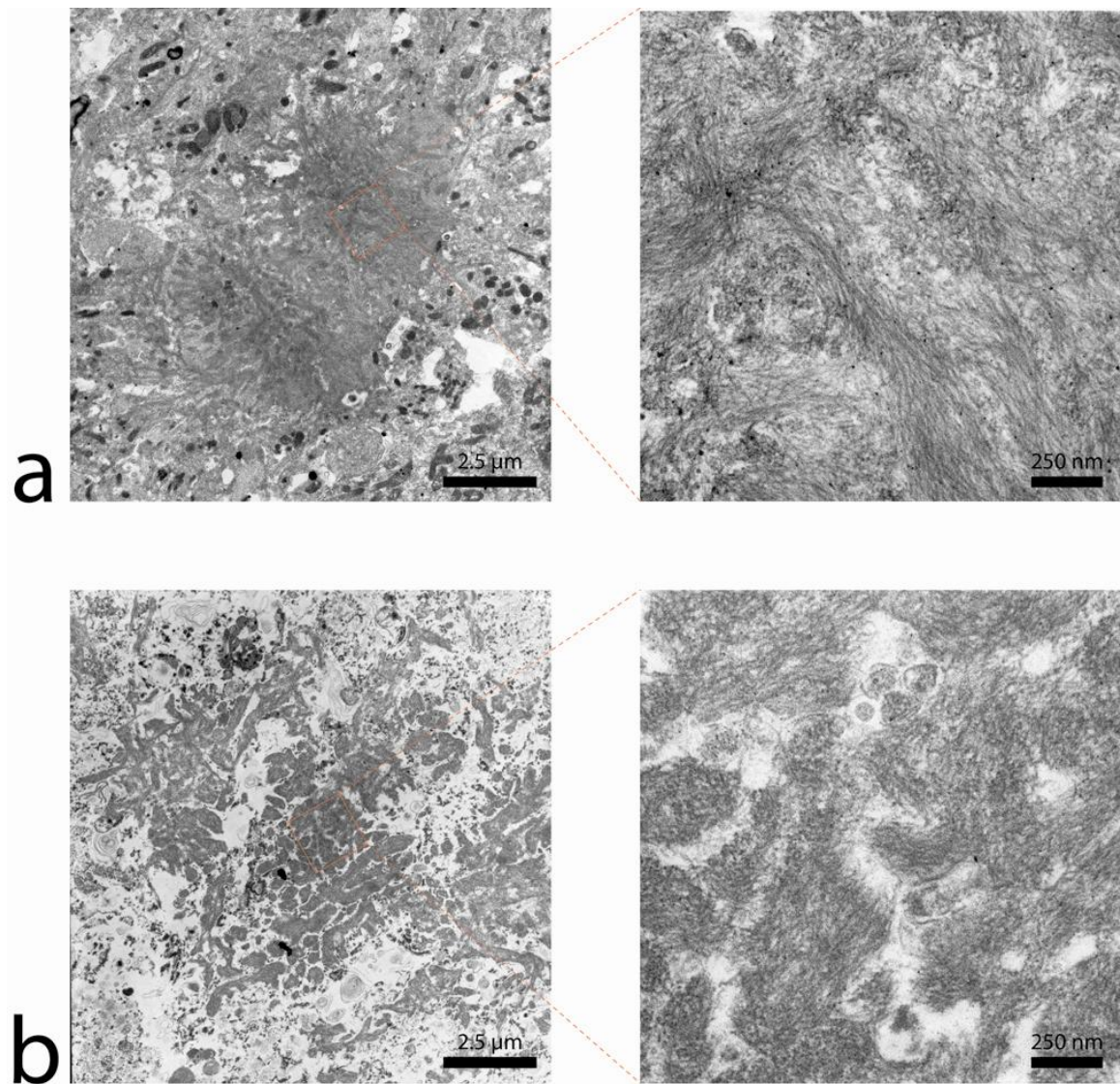
Figure 3.5.7

Bar graphs of average R_2^* rates from ROI's with plaques, without plaques and control tissue within human (a) and mouse tissue (b). The R_2^* relaxation rate of plaque ROI's in the AD tissue is significantly higher than both regions without plaques and control tissue sections. A similar trend is found in mouse data. There is also a higher R_2^* relaxation rate for the plaque ROI's in AD than in the APP/PS1 mouse, hypothesized to be due to higher iron in the AD plaques as shown with the Perl's stain in Fig. 3.5.5 (b,d and e).
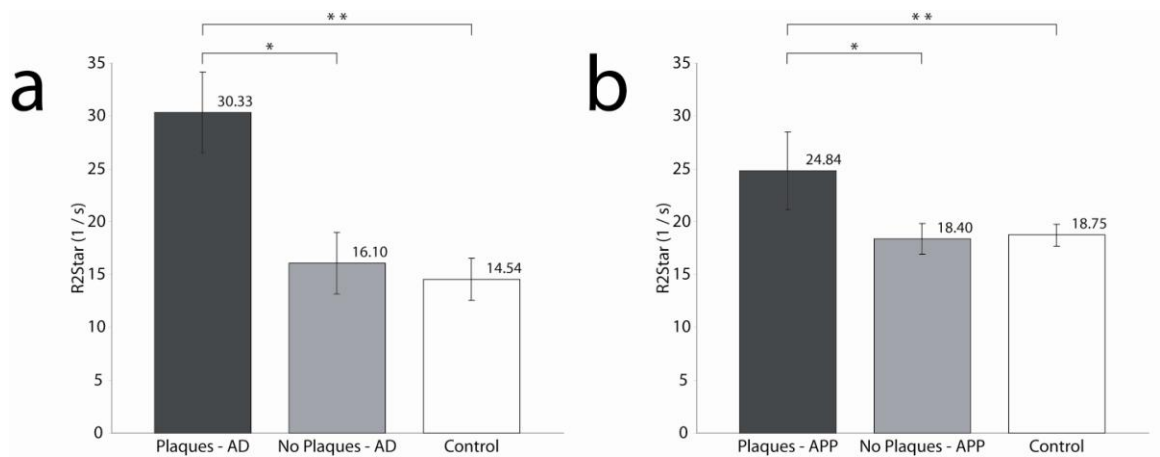
3.6 – Discussion

Understanding the relationship between beta-amyloid plaque pathology in AD and the associated MRI contrast is fundamentally important for MRI study of AD pathology. This work demonstrates the ability to image Aβ plaques in histology sections of both human AD and amyloid-generating APP/PS1 transgenic mice brains. The histological MR images taken at a field strength of 7.0 T clearly show high resolution details of Aβ plaques in human and animal samples. Previous MRI studies of Aβ plaques have been carried out with blocks of human AD brain tissue samples (183). With this approach, accurately matching histological sections of the whole tissue block with the MRI image slice is difficult. Using the histological RF coil, MRI and histological analyses were performed on the same tissue sample so that tissue pathology and associated MRI contrast changes could be precisely compared. This capability allowed us to establish a one-to-one relationship between MRI parameters and histology data acquired from human AD and APP/PS1 transgenic mouse tissue samples. Such a relationship is important for the interpretation of MRI findings in the AD brain and its animal models. Additionally, the information acquired with this technology is valuable in the development of potential therapies for AD research and investigations of other pathologies.

The MR imaging of amyloid plaques in transgenic APP/PS1 mice has been pioneered by several groups using both *in vivo* and *ex vivo* imaging methodologies (186,193,194). The hypo-intensities in the MR images of

APP/PS1 animal tissue that coincide with the plaques are similar in signal dropout and size compared to MR images of human AD plaques (Figs. 3.5.1 and 3.5.3). The cause for the hypo-intensities seen in T_2^* and T_2 weighted images of APP/PS1 mice thus has been believed to be caused by high iron accumulation in the plaques (186,193,194). However, when viewing the iron and Aβ stained images in Figs. 3.5.3 and 3.5.5, the iron concentration is considerably reduced in the APP/PS1 Aβ plaques compared to the human AD tissue in Fig. 3.5.1c, while Aβ-plaques in APP/PS1 and human AD samples are perceptibly the same when viewed with MR images. To confirm that the staining methods did not cause aberrant interactions with one another, independent iron and amyloid stains were performed yielding the same appearance as co-staining procedures. To understand this unexpected result, notice that APP/PS1 plaques in Figs. 3.5.3b and 5 show an extremely dense nature, which suggested that the current traditional Perl's staining method might not be able to stain the iron inside these plaques. The hydrophobic nature of the plaques coupled with the acidic aqueous based Perl's stain could prevent the Prussian blue reaction from occurring if the stain cannot infiltrate into the plaque. A modified Perl's stain (188) was tested that utilizes protein degradation and detergents to break down the outer surface of the plaques to allow better peripheral penetration of the aqueous stain. With the modified stain, the images in Fig. 3.5.5f indeed exposed minute focal iron distributions within the APP/PS1 transgenic animal plaques, but much less than that in the human AD plaques. As a control condition, application of the modified stain to human AD tissues resulted in dark brown staining throughout the entire

152

tissue sample (not shown). This could be due to staining of not only the free

labile iron pool but additionally iron bound inside ferritin cores that can be stained

only when the proteins are digested open with the modified staining procedure.

The above observations suggested that iron in the animal plaques is appreciably

less than that in the human plaques and the plaques in the animals are much

denser than those in human samples. Since MR images of the plaques in both

human and animals appeared essentially the same, the differing characteristics

of the animal plaques raised a fundamental question as to the cause of the MR

image contrast associated with the animal plaques.

It is well known that T_2 and T_2* relaxation and contrast can be altered in a

variety of manners. Iron bound within the ferrihydrite-like core of ferritin,

hemosiderin and an assorted number of iron oxide mineral deposits are found in

sufficient quantities in the brain to alter MRI contrast (132,133,136,198,199). As

a ferromagnetic ion, ferric iron (Fe^{+3}) is known to cause a shortening of T_2

relaxation due to the creation of microscopic magnetic field inhomogeneities that

de-phase the signal of water protons in the vicinity (123,137,197). Thus, ferric

iron in brain tissue acts as a natural contrast agent causing faster proton T_2 and

T_2* relaxation. There is some evidence to support that small amounts of ferrous

iron (Fe^{+2}) is also stained with the Perl's stain reaction (200). The effect of

ferrous iron on T_2* and T_2 relaxation is much less pronounced than that caused

by the ferric form (124) (our laboratory's unpublished data). Thus, the signal

hypo-intensities seen in the MR images associated with focal iron regions is likely

dominated by the ferric form. One other important factor associated with the MRI appearance of plaques is their size under given experimental conditions (pixel resolution, TE/TR times, etc.). The minimal plaque size viewable in our MR images of the APP/PS1 mice was similar to the AD tissue images, about 40 μm and 38 μm, respectively. Thus, due to the similarity in the plaque size for both species, plaque diameter alone does not account for the hypo-intensities seen in the APP/PS1 data. This is also supported by the fact that human AD plaques of a similar diameter with low observable iron are marginally visible on the MR images, while APP/PS1 plaques with considerably less iron association are clearly discernable on the MR images. Magnification of the thioflavin-S positive plaques (100x seen in figure 3.5.5 and 6000x & 46000x in figure 3.5.6) shows a distinct difference in plaque morphology between AD and APP/PS1 mice. Differences between human AD and the APP/PS1 Aβ plaques are most noticeable in the TEM magnifications. The human AD plaques consist of fragmented patches with random fibrillar orientation in the amyloid core while the structure of transgenic mouse plaques appears to be a highly packed aggregation of long and oriented fibrils. The decreased density of the amyloid core creates gaps that are prevalent in the human AD plaques while rarely found in the transgenic mouse plaques. The APP/PS1 mice Thioflavin-S data illustrate that, while the plaques are a similar size to those in AD tissue, the plaques have a larger center core of dense compact amyloid. In previous studies, comparison of the structure of the amyloid fibril in the transgenic APP/PS1 model and human AD is subtly different due to post-translational modifications leading to alterations

in the Aβ molecule (109,111,201). Plaques found in the APP/PS1 mouse model have a variable distribution of both human and mouse amyloid in the plaques. Diffuse plaques have an intermingled distribution of both human and mouse amyloid while dense plaques are composed of human amyloid cores surrounded by mouse amyloid (202). Thioflavin-S is known to bind to fibrillar but not to diffuse Aβ deposits (203,204). The difference in Thioflavin-S staining between human AD and APP/PS1 mice could be due to the different primary fibrillar or diffuse composition of the plaques. Many of the amino-acid residue positions within the Aβ protein are hydrophobic and are sufficient for amyloidal fibril formation (33,205). With the additional two hydrophobic amino acids found in the Aβ$_{42}$, it aggregates more readily than Aβ$_{40}$ (206). These views suggest that the hydrophobic regions are at least partially responsible for the fibril formation (34). The morphology of the mouse plaques with their large globular nature and the dense center core seem to be responsible for the T$_2$* relaxation associated with these plaques. Unlike smaller proteins, the amyloid mass found in the animal plaques is rigid and fixed in the tissue resulting in a situation where the protein mass would behave similar to a polymer-like solid. This creates a number of consequences that may affect relaxation in the plaques. First, it sets up an environment where a large amount of available surface area is present inside the plaque mass along the component Aβ fibrils. Water molecules then become bound to the hydrophilic regions of the fibril axis while repelled by the hydrophobic regions. Water in the immediate vicinity of the hydrophilic regions is bound via hydrogen bonding such that it is rotationally or irrotationally bound.

155

Layers of water are affected as they diffuse near the bound water. Cross-relaxation between the protons of bound water and the protein molecules by proton-proton magnetization exchange could lead to a more rapid relaxation of water proton. Protein wobbling due to random tumbling and thermal vibrations also must be considered which would cause altered proton-proton magnetization exchange to occur. As such, the relaxation of bound water on the Aβ fibril chains would act as a relaxation sink for water moving in the surrounding area (207,208). As a result, T_2 relaxation shortening occurs. Secondly, the magnetic susceptibility differences between the highly compact Aβ protein mass and surrounding issues could induce static dephasing in addition to that caused by deposited iron. Thirdly, tissue hydration could also be an important contributing factor for plaque contrast. The dense formation of the animal plaques as indicated in the TEM image limits free water from accessing their core. As shown by histology results, staining iron in the plaques in the APP/PS1 mouse was difficult following standard methodology without protein degradation treatment. These experimental data suggest that access of free water molecules to the animal plaque is very limited. For human samples, the gaps seen between the Aβ patches (Fig. 3.5.6b) would accommodate more free water pools. The transverse relaxation of these water molecules is shortened by the magnetic inhomogeneities caused by ferromagnetic iron in the plaques. Thus, with these observations we would suggest a dual relaxation mechanism for the generation Aβ plaques T_2* contrast associated with both the compact fibrillar protein mass and iron deposition. The focal iron concentration could play a dominant role for

rapid T_2^* relaxation in human AD plaques while the increased fibrillar density and compacted morphology would be more likely a major factor for T_2^* shortening in the APP/PS1 transgenic plaques. Although the potential relaxation mechanisms in Aβ plaques discussed above are preliminary and speculative, it is important to realize that alternative relaxation mechanisms must be considered. To thoroughly develop and validate the model of relaxation in Aβ plaques, more experimental studies are required in future investigations. In addition, caution should be used when comparing *ex vivo* R_2^* contrast obtained in the fixed tissue samples and extrapolating this to *in vivo* conditions (187).

The quantitative comparison of the R_2^* maps from different tissue types supports our hypothesis in regard to the relaxation mechanism associated with Aβ plaques. The mean R_2^* for the selected amyloid plaques in the AD tissues (Fig. 3.5.7a) is on average 90% greater than that from the ROI's without plaques and control tissue. Regions in AD gray matter with no Aβ plaques and in control tissue samples (Fig. 3.5.7a) have no statistical difference in relaxation time. However, there is a trend of faster R_2^* relaxation rates in regions without plaques throughout the Alzheimer's tissue compared to control tissue samples. This is indicative of a higher overall iron concentration in the AD neural tissue compared to the control tissue, possibly due to a systemic inability to regulate iron properly within the brain. Iron staining of the tissue samples supports this, which shows an overall increase in high focal iron in the AD tissue samples that is not seen in the control tissue. In the mouse tissue samples (Fig. 3.5.7b), the mean R_2^* for

the selected amyloid plaques is on average 56% higher than that in the ROI's without plaques and in the control tissue. The mean R_2^* of regions without plaques and of control tissue are nearly identical, indicative of similar tissue fixation across tissue sub-types and consistent preparation of tissue samples. This information alleviates the confounding possibility that separate tissue handling procedures are the source of the observed MR contrast differences. Comparison of R_2^* in ROI's with plaques in both human and APP/PS1 animals tissues reveal that the human plaques have a significantly higher R_2^* value. It is conceivable that human plaques have a duality of relaxation where both high focal iron concentration and fibrillar Aβ masses cause rapid proton transverse magnetization decay. APP/PS1 plaques exhibiting slower decay due to the reduced concentration of iron is a reasonable explanation for this result. The R_2^* for normal human tissues also appeared to be higher than that of animal tissue. This is consistent with the overall higher iron content in human neural tissue compared to the APP/PS1 animal samples. Iron staining for regions without plaques in the gray matter of APP/PS1 tissue and mouse control tissue samples exhibit similar patterns of iron staining.

These findings generate several important questions regarding the difference between Aβ plaques found naturally occurring in the human Alzheimer's brain and transgenically introduced into the APP/PS1 animal model. Previous studies have revealed that Aβ-plaques in APP/PSI animal show numerous differences from human AD plaques, including plaque morphology and

composition (109,209). The difference in morphology and the reduction of iron staining in the plaques raises the question for translating the APP/PS1 model's data to human AD as it is hypothesized that there is a link between Aβ plaques and elevated iron in the brain tissue as the cause of oxidative stress leading to cellular neurotoxicity (210,211). The relationship of iron to plaque generation is not currently well understood within the literature and is a subject of much investigation. An imbalance in the iron regulatory system and a dysfunctional difference in mineralization of iron within the ferritin core in AD subjects has been previously demonstrated (78,175). It is largely unknown whether the initial generation of the plaque causes the aggregation of iron or if aberrant regulation of extra- or intra-cellular iron stores cause the formation of the Aβ protein around it. There is general agreement that the location of Aβ plaques in human AD brain tissue coincides with focal iron deposits. Iron associated with plaques can accumulate from a number of potential sources. As a metalloprotein, free iron will bind to Aβ fibrils and collect within the plaques. Iron from ferritin, and its degradation to hemosiderin, can originate from nearby neurons and microglial cells that have migrated to the Aβ plaques and can become part of the plaque mass (77,212,213). Biogenic magnetite found proportionally higher in AD ferritin cores than normal aged human neural tissue is known to be accumulate within Aβ plaques (175,190). While it is unknown precisely how Aβ plaque aggregation occurs, it is known that metal ions do play a role in Aβ fibril formation. The conversion of Aβ's secondary protein structure to a β-sheet has been shown to occur in the presence of divalent metal ions, including ferrous iron (82). The

159

component fibrils of the Aβ plaques are known metalloproteins and possess

metal chelation regions in their amino-acid sequence (79). The MR and

histological images in Fig. 3.5.1 demonstrate that Aβ plaques are consistently

associated with elevated iron load in and around their vicinity in human AD brain

tissue. Research has shown that the co-localization of iron with the human Aβ

plaques is accompanied by endoplasmic reticulum stress induced apoptosis,

DNA oxidation and cellular damage in cells adjacent to plaques. Conversely, in

regions where Aβ plaques accumulate alone without iron there is no indication of

oxidative stress or apoptosis pathway activation (214). It has been demonstrated

that the toxicity of Aβ is amplified upon the direct interaction of iron ions with the

Aβ peptide, while unbound iron itself has no effect upon toxicity (215). This

strongly suggests that Aβ plaques by themselves are not toxic to cells adjacent to

plaques, whereas iron accumulation in and around plaques is essential for

neuronal damage. The morphology and associated iron dissimilarity between the

human AD and transgenic APP/PS1 plaques raises a question regarding differing

amyloidal genesis processes for each species. In the APP/PSI mouse model

used here, plaques are produced in the brain as early as six months after birth

and are believed to continually grow throughout the life span of the animal (216).

Current understanding of human amyloidal genesis suggests that plaque

generation occurs over years, perhaps decades, and places the plaques into

discrete classes based upon the morphology of the plaque and surrounding

tissue. It is hypothesized that plaques start out as a seed formations of Aβ

peptide and eventually become much more compact and dense over time (217).

The APP/PS1 model generates plaques at a rapid pace and iron staining indicates a reduced amount of iron associated with these plaques compared to AD tissue. It is plausible that the rapid fibrillarization from Aβ oligomers into compacted fibrillar plaques could lead to less of iron deposition within the plaques in the APP/PS1 model.

In summary, imaging of thin slices of tissue samples with the aid of the histological coil allows the one-to-one comparison of tissue pathology as seen in histological stains and different MRI methodologies. With this technique, the relaxation mechanisms for Aβ plaques in human Alzheimer's disease and the APP/PS1 mouse model were investigated with respect to their morphology and relationship with iron deposition. The histology stains of AD and APP/PS1 tissue samples were directly compared to T_2*-weighted images and R_2* parametric maps. The histological iron stains presented here support the hypothesis that iron associated with the Aβ plaques in the human AD samples plays a major role in generation of MRI T_2* contrast. Histological data from previous studies using post mortem human AD tissue (67,77,192,218) also support the notion that focal iron load in Aβ plaques is the dominant cause for faster T_2 and T_2* decay. The electron microscopy and histology data revealed that there are important differences in plaque morphology and associated iron concentration between transgenic APP/PS1 mice and human AD tissue samples. In the Alzheimer's tissue, beta-amyloid plaques with high iron concentration are clearly visible in the T_2*-weighted images while others of similar size with less focal iron are not as

discernable. In the APP/PS1 animal tissue, large plaques are equally observable as human plaques in MR imaging while iron load is considerably less than human plaques. This suggests that there is a degree of difference between the amyloid plaques in the APP/PS1 mouse model and human Alzheimer's, in respect to their morphology and relationship with *in vivo* iron stores. The increased transverse proton relaxation rate in Aβ plaques in animals is likely caused mainly by the interactions of water with the highly compacted amyloid fibril mass. The improved resolution of the *ex vivo* data set allows for the detailed comparison between tissue histology and MR contrast that is not possible with current lower resolution clinically based protocols. The extrapolation of microscopic MR images to *in vivo* applications is promising in the near future considering the rapid increase in achievable image resolution with the development of higher magnetic fields and the usage of parallel imaging technology (219). The data presented in this report are essential for understanding the histo-pathological underpinning of MRI measurement of Aβ plaques in humans and animal models for both current and future MR applications.

3.7 – Appendixes

3.7.1 – Correlating Plaque Size and Iron Load with R_2* relaxation

It was hypothesized that the hypo-intensities resulting from the beta-amyloid plaques in the Alzheimer's and APP/PS1 mice would correlate to plaque diameter (in the case of both AD and APP/PS1 tissue) and/or iron loading (in the

case of AD tissue). Detailed evaluation of plaque diameter and the optical density of the Perl's and thioflavin-S stains was undertaken to evaluate if there was any statistical correlation. Eight-echo MGE images of human AD tissue samples were imported into in-house software developed with the interactive data language (IDL) 6.1 framework (Research Systems Inc., ITT Industries,Boulder, CO) and regions of interest were selected inside the plaque to yield detailed R_2^* ($1/T_2^*$) relaxation rate and magnitude measurements of individual plaques. The same plaques were selected on bright field Perl's iron stain and thioflavin-S 40x magnification images with Image J (National Institutes of Health, Bethesda, MD) to measure Aβ plaque diameter and optical density. Calibrated optical density is measured in Image J as the average gray scale contrast on a 0 – 255 scale for selected regions of interest. An optical density for plaques was calculated by comparing the plaque optical density to the optical density of the background of the sample. This was done to standardize optical density measurements across tissue samples and stains. The relaxation rate R_2^* or magnitude was then graphed against either iron or thioflavin-s optical density or against plaque diameter to compare their correlation.

Figure 3.7.1.1

R_2* relaxation verses Aβ plaque diameter.

$y = -0.0043x + 30.68$
$R^2 = 0.0005$
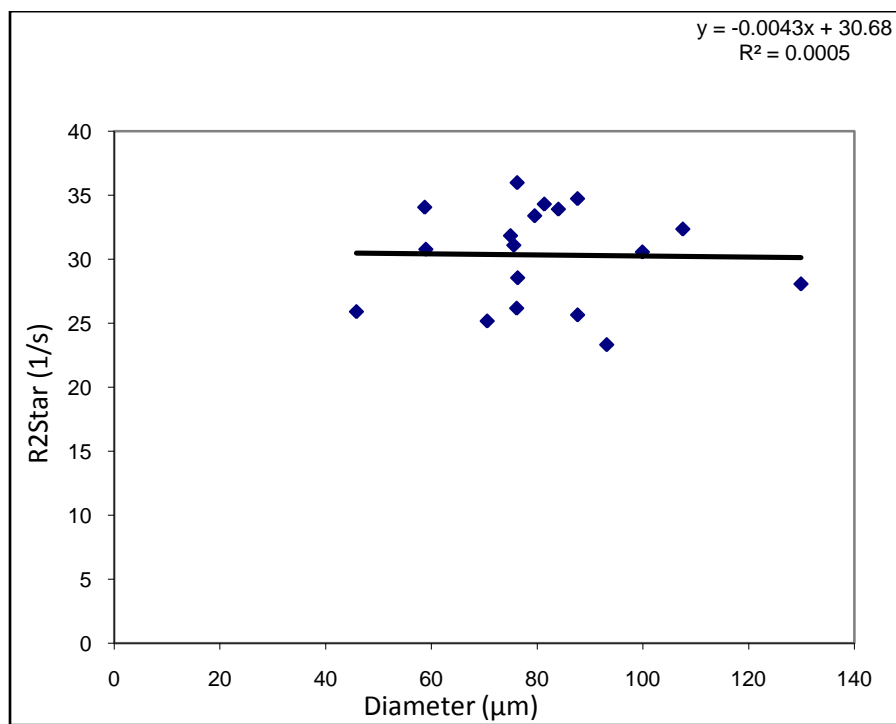
Figure 3.7.1.2

R_2* relaxation verses iron optical density ratio.

$$y = 9.4305x + 22.274$$
$$R^2 = 0.0109$$
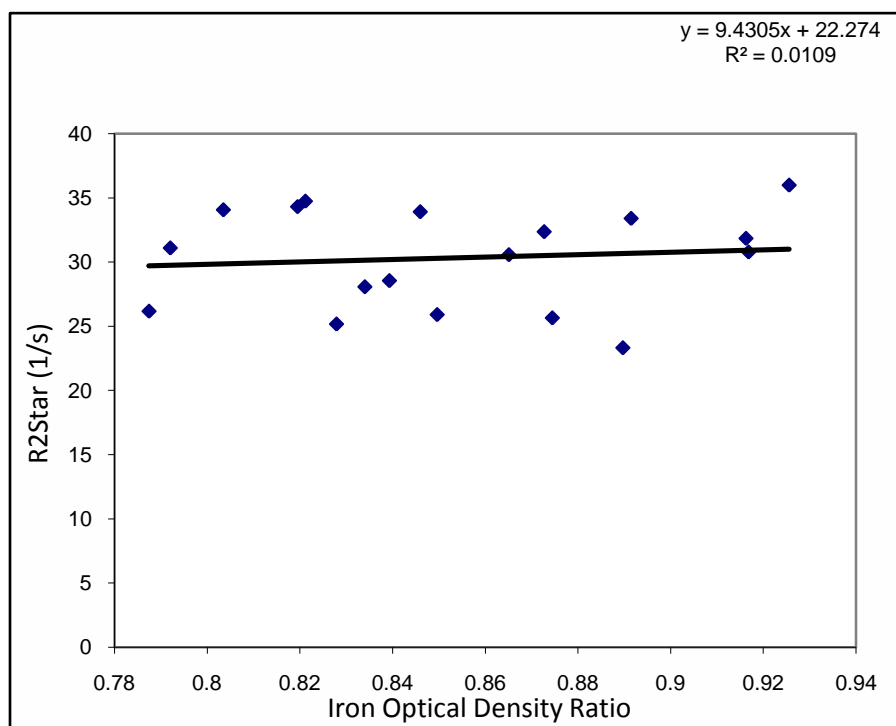
Figure 3.7.1.3

R_2* relaxation verses thioflavin-S optical density ratio.

$y = -0.0332x + 30.377$
$R^2 = 3E\text{-}06$
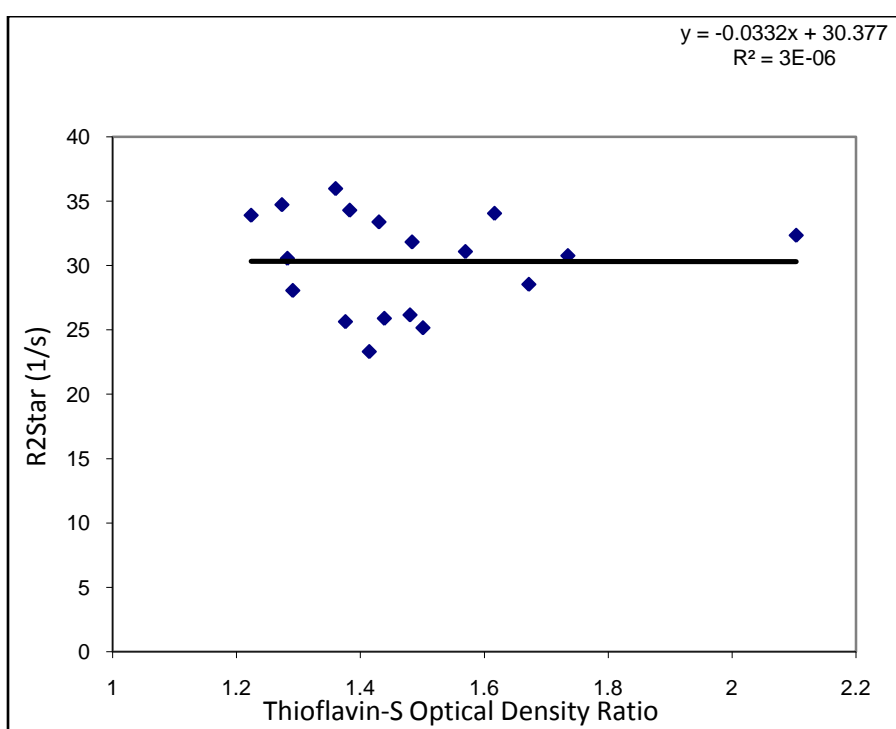
Figure 3.7.1.4

Magnitude verses Aβ plaque diameter.

y = -55.365x + 29068
R² = 0.053
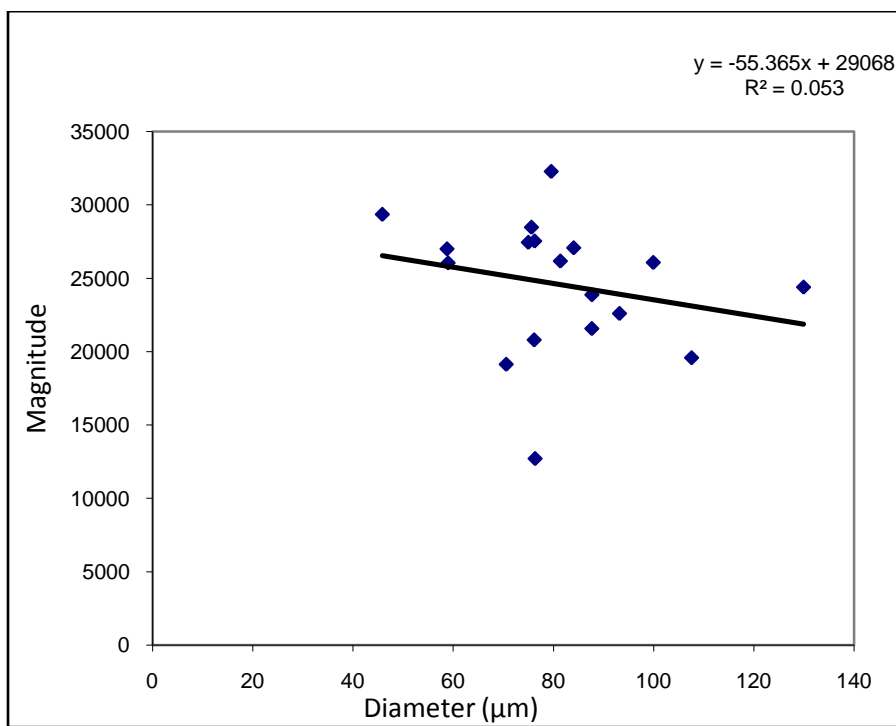
Figure 3.7.1.5

Magnitude verses iron optical density ratio.

y = 26445x + 1980.6
R² = 0.0608
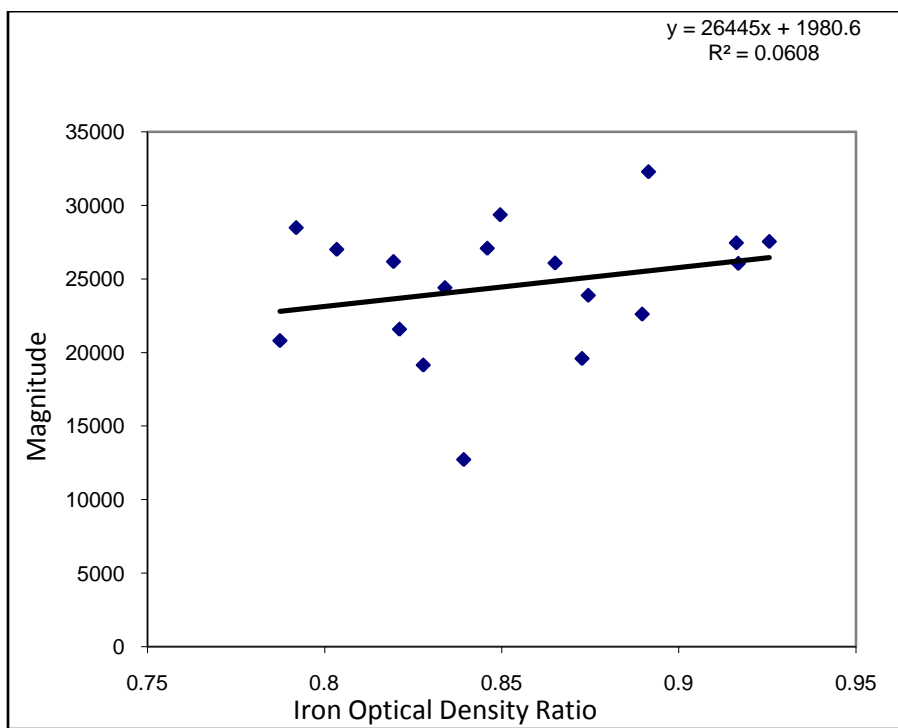
Figure 3.7.1.6

Magnitude verses thioflavin-S optical density ratio.

y = -7542x + 35723
R² = 0.1188
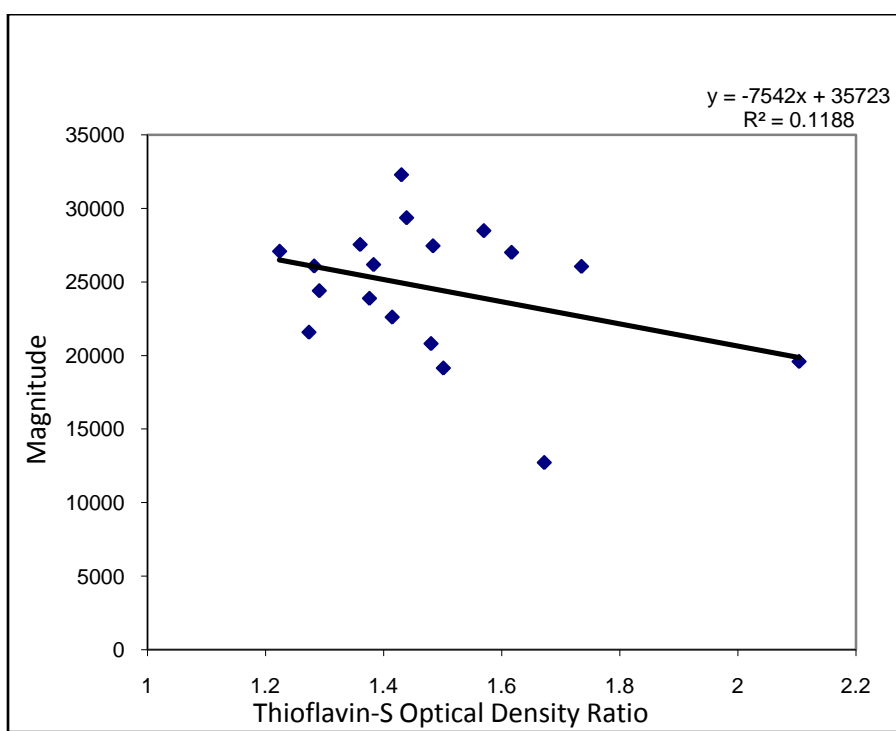
The data sets and scatter plots indicate that there is no significance for any of the correlation data between R_2^* and magnitude verses plaque diameter, iron optical density or thioflavin-S optical density (Figures 3.7.1.1 – 3.7.1.6). This is theorized to be due to a number of factors. Measurements of optical density are extremely hard to standardize across tissue stains. It was attempted to standardize the optical density by creating a ratio using the background of the stain. The inherent problem with this is that there is potential for different stains over different periods of staining to have slight differences in the optical density. All stains were standardized according to length of the procedures and concentrations of the chemicals used but there is still intrinsic variability in the stains, especially the Perl's iron stain. The Perl's stain relies upon the usage of 3,3'-Diaminobenzidine (DAB) as a chromogen which is oxidized by hydrogen peroxide in the presence of iron to give a brown precipitate. This process is highly variable even with strict time constraints implemented into the staining procedure. The thioflavin-S stain generally is very consistent even with differing timing of the staining period. There is a stage during staining that can alter the outcome of the thioflavin-S brightness when 70 percent ethanol is used to wash the wash out the residual background thioflavin-S that is not bound to beta-amyloid. However, the thioflavin-S that is bound to the beta-amyloid has an extremely high affinity for intercalation into the peptide and ethanol washing has a minimal effect upon it. There is a possibility that the thioflavin-S stain lost some florescence overtime and this affected the results. However, the microscopic images of the tissue samples were taken as soon as possible to try and minimize

176

this effect. There is the possibility that because the tissue samples were dual stained for thioflavin-S and iron that the Perl's stain is the main culprit of the lack of correlation because even under fluorescent light the dark precipitate in the Perl's stain is still slightly visible.

It is unfortunate that there were no statistically significant results to report for this evaluation. When viewing the hypo-intensities in the magnetic resonance images and comparing these to the amount of iron present at those points, it is evident that regions that stain for more focal iron have larger diameters of signal dropout in the MR images. The hypo-intensities are essentially regions devoid contrast, and relaxation in the middle of these plaques was hoped to correlate to plaque or focal iron size statistically. Perhaps measurement of the diameter of the hypo-intensities verses iron content and plaque size would be a better comparison. A limitation in the resolution of the MR data sets then becomes an ever increasing factor when attempting to measure the diameter of the microscopic hypo-intensities.

Chapter 4

Morphological and Histochemical Differences

between Human and Mouse plaques

4.1 – Histological and Cellular Differences Between Beta-Amyloid Plaques in APP/PS1 Transgenic Mice and Human Alzheimer's Disease

4.1.1 – Abstract

Transgenic mouse models that mimic neuropathology are important in understanding disease etiology and testing new treatment procedures. Mutations in human genetic sequences for the amyloid precursor protein and presenilin 1 have been introduced into mouse models that develop beta-amyloid ($A\beta$) plaques in a considerably condensed time period compared to Alzheimer's pathology. The benefit of producing plaques in less than nine months motivates the utilization of these animals for a variety of potential studies such as beta-amyloid clearance, protein processing pathways, and amyloidogenesis. As with any animal model, there exist drawbacks when comparing them to their model system. Understanding the amyloidogenic and morphological characteristics of the APP/PS1 mouse model are important in considering the outcome from studies involving their usage and eventually translating results for treatment of the Alzheimer's disease brain. Using various histological stains and microscopy aimed at examining plaque morphology, iron distribution and inflammatory response we show that there are distinct differences between the naturally

occurring human Alzheimer's plaques and the APP/PS1 mouse model. Aβ

antibody and thioflavin staining along with electron microscopy demonstrate

distinct morphological differences in plaque composition and ultra-structure

alluding to differences in plaque genesis and component fibril formation.

Microglia and astrocyte staining shows a differing inflammatory response pattern

with more pronounced response in the Alzheimer's tissue. Iron mismanagement

and focal iron deposition is found ubiquitously throughout the Alzheimer's tissue,

with plaques showing a close relationship to iron accumulation within the plaques

that is not seen in the transgenic animal model. The data presented here

emphasizes distinct differences between naturally occurring Aβ plaques in the

AD brain and those instituted to produce in the transgenic mouse model.

Utilization of these animal models for AD research should be done with this

caveat.

4.1.2 – Introduction

The extracellular accumulation of beta-amyloid (Aβ) protein, leading to the

formation of amyloid plaques are major defining neuropathological characteristic

of Alzheimer's disease (AD). Genetic screening of individuals with familial

Alzheimer's disease has identified reoccurring alterations in genes believed to be

involved in the disease process. The augmented production of Aβ peptides is

believed to be integral to the disease process according to the amyloid cascade

hypothesis (220). Central to this hypothesis is the knowledge that genetic

mutations associated with familial AD cause an increase in aberrant APP

production leading to increased Aβ production. This has lead to the development of transgenic mouse models that produce Alzheimer's like beta-amyloid plaques in the brain. In particular, animals that develop amyloid plaques age dependently are particularly important in understanding disease etiology and testing new therapies. Several transgenic mouse lines have been fashioned that over-express known human Alzheimer's mutations and develop fibrillar beta-amyloid plaques (113,221-224).

Transgenic mice that harbor chimeric mouse/human familial Alzheimer's genes for amyloid precursor protein (APPSwe$_{695}$, K595N and M596L mutations) and a mutant human presenilin 1 (PS1-A246E) under control of the mouse prion promoter develop fibrillar beta-amyloid plaques at approximately nine months of age and continually do so progressively throughout their lifespan (108,112). This model reproduces some of the neuropathological traits of AD, most notably amyloid plaques that exhibit thioflavin-S fluorescence. The exact role of amyloid deposition in Alzheimer's disease has not been elucidated but it is clear that they are involved in the disease process as they are found ubiquitously throughout the AD brain. A transgenic mouse model that reproduces and encompasses all characteristics of the Alzheimer's disease pathology has not been created. Although there are known differences in pathology between the various transgenic models and naturally occurring AD tissue, many of these mouse models have been used to study the creation and clearance of plaques with pharmacological or biochemical interventions. Care must be taken when comparing results from the transgenic model and translating these to AD neural

tissue. The assumption that the successful alleviation of plaque burden in the

transgenic brain with various methods can be transferred to the AD brain should

not be casually accepted without any doubt or reservation. Histological

investigation of the similarities and differences between Aβ plaques in the

human AD and APP/PS1 brain is the first and essential step in understanding

how best to use these models for future human studies. In this report, we have

undertaken various histological staining techniques to compare the transgenic

plaques to human AD plaques to examine morphology and histological

inflammatory response.

4.1.3 – Materials and Methods

Human Alzheimer's and Control Brain Samples:

      Entorhinal cortex brain tissue samples from clinically and histologically

determined AD subjects (n=5) and age-matched controls (n=4) were donated

with consent following institutional guidelines and obtained from both internal and

external sources (Harvard Brain Tissue Resource Center, McLean Hospital,

Belmont, MA). Analysis of the tissue obtained from the brain bank indicated that

AD tissue samples were highly positive for beta-amyloid and neural fibrillary

tangles staining consistent with a post mortem diagnosis of Braak stage VI

(43,44). There was not a significant difference between the age of the subjects

upon bereavement while the post mortem index between the tissue harvesting at

time of death and utilization in this study was slightly different between the tissue

samples (longer time period for controls). The tissue was fully fixed in 4%

paraformaldehyde in pH 7.3 phosphate buffered saline (PBS) after which blocks

of tissue approximately 1 cm x 1 cm x 0.5 cm were dissected from the entorhinal

cortex. For cryogenic protection the samples were placed in graded 10% and

20% sucrose solutions for 48 hours each, and then placed in 30% sucrose.

Tissue sections were cut at 16µm on a cryostat, mounted on poly-lysine and

gelatine coated slides and prepared for histological staining according to

individual protocols described below.

Transgenic APP/PS1and Control Mice:

Transgenic mice (n=5) inserted with a chimeric mouse/human amyloid

precursor protein (APP) and a mutant human presenilin 1, developed by Borchelt

et al. (108,112), were obtained commercially from The Jackson Laboratory

(strain type B6C3-Tg(APP695)3Dbo Tg(PSEN1)5Dbo/J). The expression

plasmid for these animals is composed of cDNA harboring human familial

Alzheimer's disease (FAD) mutations regulated by the mouse prion promoter

(MoPrP.Xho). Transgenic material introduced consists of human mutations

found in presenilin 1 (PS1-A246E) and the Swedish variant of FAD (APPSwe$_{695}$,

K595N and M596L mutations). Animals were kept in the animal facility under

veterinary care with normal feeding and handling conditions. Age-matched cage

mate C57BL/6 mice (n=3) were used as a control group. Upon aging naturally

until 24 months, animals were euthanized via an intra-parietal injection of sodium

pentobarbital (Nembutal, 200 mg/kg) and were transcardially perfused with cold

Lactated Ringer's solution (pH 7.4) followed by buffered 4% paraformaldehyde in

PBS. Whole brain tissue was harvested and placed overnight in pH 7.3 buffered

4% paraformaldehyde to allow full tissue fixation. Graded sucrose solutions of

10%, 20% and 30% were used for cryo-protection. Tissue sections were cut at

16µm on a cryostat, mounted on poly-lysine and gelatin double coated slides and

prepared for histological staining according to individual protocols described

below.

Iron and Amyloid Staining:

Tissue sections were co-stained for both iron and beta-amyloid with a

diaminobenzidine enhanced Perl's Prussian blue stain followed by an aqueous

Thioflavin-S stain. Sixteen µm tissue sections mounted on lysine and gelatin

coated slides were heated in an oven at 50°C to better adhere the samples to the

slides then rinsed in deionized water (dH_2O) for 15 minutes. The sections were

placed in equal volumes of freshly prepared 4% potassium ferrocyanide (#P236,

Fisher Scientific, Waltham, MA) and 4% hydrochloric acid (final combined

concentrations 2% for each) for 30 minutes under gentle rocking followed by two

rinses in dH_2O. Intensification of the iron stain was performed with 5 minutes of

3,3'-diaminobenzidine tetrahydrochloride (DAB) staining (#D5637, Sigma, St.

Louis, MO) (10 mg dissolved in 15ml of PBS with 16 µl of 30% H_2O_2) followed by

two five minute rinses in dH_2O. Tissue samples were then placed in 1%

thioflavin-S (T1892, Sigma, St. Louis, MO) aqueous solution for 5 minutes,

followed by differentiation in 70% ethanol for 5 minutes and two five-minute

washes in dH_2O. To preserve fluorescence, sections were covered with

183

FluorSave Aqueous mounting media and cover slipped (Catalog #345789, Calbiochem, San Diego, CA). To test for the possibility of confounding interactions between the two staining methods during co-staining, each was tested on separate tissue samples to determine their individual efficacy and compared to the co-stained sections. A modified Perl's stain further tested the transgenic animal tissue for minute amounts of iron within the amyloid masses. The stain was adapted and modified from LeVine (188,189) and employs the usage of proteinase K and detergents to break down the periphery of the plaques forming openings in the highly hydrophobic amyloid plaques. This allows the aqueous Perl's stain to infiltrate into the amyloid mass and is sensitive enough to detect trace amounts of iron in the Aβ plaques. The staining method consists of the following procedure. Tissue sections were hydrated in PBS for 15 minutes followed by immersion in sodium borohydride (10 mg/ml PBS, # 213462, Sigma, St. Louis, MO) for 30 minutes. They were then rinsed in PBS twice for five minutes and immersed in proteinase K (30 µg/ml, # P6556, Sigma, St. Louis, MO) and 0.01% Triton X-100 in PBS for 20 minutes. Next, the sections were placed in a solution of 1% hydrochloric acid, 1% potassium ferrocyanide and 1% Triton X-100 in distilled water for 30 minutes. Amplification of the iron staining was accomplished with 0.5 mg/ml 3,3'-diaminobenzidine tetrahydrochloride (DAB) and 2µl/ml of 30% hydrogen peroxide in pH 7.6 0.05 M Tris HCl for 15 minutes. The sections were rinsed twice for 5 minutes in dH$_2$O, stained with thioflavin-S aqueous solution for 5 minutes, differentiated in 70% ethanol for 5

minutes and then underwent two final five-minute dH$_2$O rinses before being mounted and cover slipped.

Immunohistochemistry Staining:

Slides with tissue samples on them were air dried at 50°C for 30 minutes then placed in 95°C Citrate Buffer (10mM sodium citrate tribasic dihydrate (#C7254, Sigma, St. Louis, MO), 0.05% Tween 20 in dH$_2$O, pH 6.0) for 15 minutes. Slides were rinsed three times with PBS for five minutes each then a water repellent circle was drawn around each section with a hydrophobic barrier pap pen to localize staining reagents. Nonspecific protein binding was blocked by 30 minute incubation with 1% Bovine serum albumin (BSA) (#A9430, Sigma, St. Louis, MO) in 1x PBS Tween (PBST)(2ml Tween 20 in 1litre PBS pH 7.3). Sections were incubated with primary antibodies at their respective dilution factors in 1% BSA in 1x PBST overnight in an airtight incubation-humidity chamber. After primary incubation, the antibody was decanted and slides rinsed in PBS three times for five minutes each. Sections were incubated with fluorescent secondary antibodies (Alexa Fluor, Invitrogen, Carlsbad, CA) in 1% BSA in 1x PBST for two hours in a humidity chamber. Following this the secondary was decanted and slides rinsed in PBS three times for five minutes each followed by mounting with FluorSave and cover-slipping.

For beta-amyloid (1-40) staining, a mouse monoclonal beta Amyloid 1-40 antibody [BAM-10] (1/100, AB7501, Abcam Inc., Cambridge, MA) was used followed by an anti-mouse red fluorescent Alexa Fluor 555 IgG (A-21422)

185

secondary antibody. Following secondary incubation and PBS rinsing tissue

sections were co-stained with 1% thioflavin S for 10 minutes, differentiated in

70% ethanol, washed twice in dH$_2$O, mounted with FluorSave and cover-slipped.

For beta-amyloid (1-42) staining, a rabbit polyclonal beta Amyloid 1-42

antibody (1/200, AB10148, Abcam Inc., Cambridge, MA) was used followed by

an anti-rabbit red fluorescent Alexa Fluor 555 IgG (A-21428) secondary antibody.

Tissue sections were then co-stained with thioflavin S according to the method

outlined above.

To stain for ferritin light polypeptides, a mouse monoclonal ferritin light

chain (D-9) antibody (1/125, SC-74513, Santa Cruz Biotechnology, Santa Cruz,

CA) was used followed by Alexa Fluor 555 IgG (A-21422) secondary. Tissue

sections were co-stained with thioflavin S to stain for fibrillar beta-amyloid

deposits. Ferritin heavy polypeptides were stained with a rabbit polyclonal ferritin

heavy chain (H-53) antibody (1/125, SC-25617, Santa Cruz Biotechnology, Santa

Cruz, CA) was used followed by Alexa Fluor 555 IgG (A-21428) secondary

antibody. Thioflavin S was used as a co-stain after antibody staining.

To stain for microglial cells, a rabbit Anti IBA-1 (Ionized calcium binding

adaptor molecule 1) antibody (1/500, 019-19741, Wako Chemicals USA, Inc.,

Richmond, VA) was used following by incubation with Alexa Fluor 555 IgG (A-

21428) secondary antibody. Thioflavin S was used as a co-stain for fibrillar beta-

amyloid after antibody staining.

To distinguish astrocytes, a polyclonal chicken anti-glial fibrillary acidic

protein (GFAP) antibody (1/250, AB5541, Millipore, Billerica, MA) was used

followed by Alexa Fluor 555 IgG (A-21437) secondary incubation. Tissue

sections were then stained with thioflavin S for fibrillar beta-amyloid visualization.

Fluoro Jade C Staining:

To identify degenerating neuronal cells and their relation to Aβ plaques, a

Fluoro-Jade C stain was utilized along with immunohistological antibody staining

for $A\beta_{40}$. Sections were first stained with $A\beta_{40}$ specific primary antibodies,

followed by Alexa Fluor 555 secondary according to the procedure above and

then rinsed twice for five minutes in PBS. Slides were then air dried for 30

minutes at 50°C to help tissue sections adhere to the slides. Slides were then

rinsed in dH_2O for two minutes followed by immersion in 0.06% Potassium

Permanganate for ten minutes followed by a rinsing for two minutes in distilled

water. Slides were immersed in the working 0.0001% Fluoro-Jade C (AG325,

Millipore, Billerica, MA) solution for ten minutes followed by rinsing them three

times for one minute each in dH_2O. Slides are then air dehydrate for 30 minutes

at 50°C followed by immersion in xylene twice for five minutes each, mounting

with cytoseal (or another xylene based mounting media), and cover-slipped.

Microscopy:

High resolution microscopy of the tissue sections was performed using a

Nikon OptiPhot microscope and Nikon Digital Sight camera using NIS-Elements

software. Bright field under the visible light spectra and phase contrast using a

phase contrast objective and condenser were used to view iron stains. A FITC

fluorescence cube at 430 nm excitation and 550 nm emission (Nikon B-22) was used to visualize thioflavin-S positive Aβ deposits and fluoro-Jade C stains. A Nikon G-2A filter cube was used to visualize the Alexo Fluor 555 secondary antibody which is excited at 550 nm and emits at 570 nm.

4.1.4 – Results

There exists a clear divergence between human AD and APP/PS1 plaque morphology, when viewed with Aβ antibodies (40 and 42 amino acid) and thioflavin-S reactivity (Fig 4.1.5.1, 100x magnification). Thioflavin-S binding of human plaques shows a dense fibrillar core surrounded by a large diffuse halo or corona region. APP/PS1 thioflavin positive plaques exhibit a larger and denser core region with a smaller diffuse thioflavin-S positive corona region. Beta-amyloid 40 antibody bound to human plaques show both the dense core and corona regions are positive for the 40 amino acid Aβ variant with a clear overlap with thioflavin-S staining. APP/PS1 plaques exhibit much more $A\beta_{40}$ reactivity that extends beyond the thioflavin positive stain. There is still an overlap between thioflavin and $A\beta_{40}$ staining but there is a non-fibrillar diffuse region outside of traditional thioflavin staining that is evident with the $A\beta_{40}$ stain. Human AD and APP/PS1 tissue both show positive intracellular $A\beta_{40}$ reactivity in numerous cells outside the plaques. Antibody staining with $A\beta_{42}$ shows that much of the dense fibrillar core of the human plaques is composed of the 42 amino-acid Aβ variant, with minimal staining in the corona region. APP/PS1 tissue shows a lack of $A\beta_{42}$ staining associated with plaques. Intracellular

188

staining of $A\beta_{42}$ is evident inside numerous human AD cells and is not seen in the transgenic tissue samples.

Astrocyte proliferation is illustrated in figure 4.1.5.2 in tissue samples from AD, human controls, APP/PS1 and mouse controls. Control tissue from both human and mouse sources exhibit a nearly random distribution of GFAP positive astrocytes throughout the microscopic field. In the AD tissue samples, there is a high likelihood of astrocytes to be found in close proximity to $A\beta$ plaques. Close examination shows that GFAP positive astrocytes are found on the periphery of nearly every human AD plaque. The astrocytes in the human AD tissue exhibit classical amebic morphology indicative of a phagocytic astrocyte state. Human control and both transgenic and control mouse sections show astrocytes in a traditional star pattern with radiating processes typical of astrocytes acting as neuronal metabolic helper cells. Conversely, mouse APP/PS1 tissue samples show a similar random staining pattern seen in control mouse sections. Beta-amyloid plaques in the APP/PS1 tissue samples are not surrounded by GFAP positive astrocytes unlike the human AD plaques.

Microglial staining and microglial inflammatory state associated with beta-amyloid plaques are seen in figure 4.1.5.3. IBA1 positive stains for microglia in human AD and age-matched controls show microglia in both ramified and active states throughout the tissue samples. AD sections show a close association with $A\beta$ plaques and activated microglia. Microglia bodies and processes are found surrounding and within the fibrillar corona region of the human plaques. Mouse control and transgenic tissue samples both exhibit positive IBA1 microglial

189

staining. Transgenic and control mouse sections show less microglial staining then both human AD and controls. Microglial activation states for mouse controls tissue resemble microglia mostly in ramified states with minimal activation. Transgenic tissue exhibits both activated and ramified microglial states, but appreciably less than that of AD tissue samples. There is an association between activated microglia and the periphery of Aβ plaques in transgenic tissue, with activated microglia surrounding plaques. Unlike the human AD plaques, there are no activated microglia found within the plaque core or coronal regions.

Light and heavy ferritin antibody staining in human and mouse tissue samples associated with thioflavin-s positive Aβ plaque staining is illustrated in figure 4.1.5.4. Cells positive for L-ferritin staining were found in both human AD and APP/PS1 tissue samples. Human L-ferritin cells were found throughout the tissue sample and also in close proximity to Aβ plaques. Cells positive for L-ferritin appear to be microglial cells in morphology and are found within the coronal region of the human plaques. There was positive L-ferritin staining within the APP/PS1 tissue samples that does not appear to be associated with the beta- amyloid plaques. Furthermore, L-ferritin staining in the animal model does not appear to be microglial in nature. Cells positive for L-ferritin in the transgenic animals appear to be specific for neurons in the granular cell layer of the cortex. H-ferritin was found in cells throughout the cortex of human AD tissue samples in a random manner with minimal association with Aβ plaques. There was no positive staining for H-ferritin in the APP/PS1 transgenic animals.

Fluoro Jade-C staining for degenerating neurons in association with $A\beta_{40}$

staining is demonstrate in figure 4.1.5.5. Human AD and control samples

exhibited positive fluoro Jade-C staining that precisely overlap with cells that also

exhibited intracellular $A\beta_{40}$. Cells stain positive for both fluoro Jade-C inside the

AD plaques and also outside their halo regions. There was no association in or

around the transgenic animal plaques and fluoro Jade-C staining. No positive

fluoro Jade-C staining in either APP/PS1 or mouse control tissue samples was

observed.

Iron staining compared to thioflavin-S positive plaques in both human AD

and transgenic APP/PS1 animals are seen in figure 4.1.5.6 and 4.1.5.7,

respectively. Figure 4.1.5.6 shows (a) thioflavin-S staining of plaques, (b) phase

contrast and (c) bright field microscopy of Perl's iron stain in the same human AD

tissue sample at 40x magnification. Thioflavin-S staining shows numerous dense

core plaques throughout the sample that stain positive for focal iron deposition

(red arrows). The majority of the human plaques exhibit a focal iron core that

can be seen in both the phase contrast and bright field images. The phase

contrast image also shows the outline of the beta amyloid plaques as opaque

due to the difference in wave length of light passing through the plaques. The

APP/PS1 (Fig. 4.1.5.7) tissue sample exhibits positive (a) thioflavin-S staining for

beta-amyloid, but does not exhibit focal iron staining in either the phase contrast

or the bright field images. Positive iron staining was found in one region (blue

arrow) that does not co-register to Aβ plaques. Similar to the human AD data,

the APP/PS1 plaques also exhibit a difference in wave length in the phase

contrast images. The phase contrast for the human data however shows a close

approximation of size of the plaques compared to the thioflavin-S staining. The

phase contrast images for the transgenic mouse data shows that the plaques are

larger in diameter then they stain in the thioflavin-S stain. This is similar to the

results in figure 4.1.5.1 where the $A\beta_{40}$ staining of diffuse amyloid is larger in

diameter then the thioflavin-S stain, which only stains fibrillar amyloid. A

modified iron stain involving protein digestion to enable access of the aqueous

Perl's iron stain of the APP/PS1 tissue is seen in figure 4.1.5.8. A minute amount

of iron is stained in association with the transgenic plaques. This stain was

attempted on human AD tissue but resulted in staining for iron throughout the

tissue sample (data not shown).

4.1.5 – Figures

Figure 4.1.5.1

Antibody stains for $A\beta_{40}$, $A\beta_{42}$ (red) and thioflavin-S (green) of Alzheimer's

disease tissue from the entorhinal cortex and APP/PS1 cortical tissue viewed at

40x magnification. $A\beta_{40}$ is found in plaques in the AD and transgenic tissue

samples as well as intracellular staining throughout both samples. Thioflavin-S

stains for fibrillar beta-amyloid and shows that the core of the AD plaques is

composed of highly fibrillar filaments with the halo or coronal region being less

compact. APP/PS1 plaques exhibit a much different morphology with a globular

fibrillar structure that radially extends from the center of plaque. Antibody

staining with $A\beta_{40}$ illustrates that the size of the APP/PS1 plaques is

underestimated with the thioflavin-S stain alone having stained for both fibrillar

and non-fibrillar beta-amyloid while the periphery of the plaques is composed of

non-fibrillar filaments. The APP/PS1 tissue exhibits much more positive beta-

amyloid 40 staining, indicative of the vast over production of beta-amyloid

overwhelming the system. Alzheimer's samples shows positive $A\beta_{42}$ staining in

the core of the plaques and intracellularly throughout the sample with minimal

staining of the coronal region. The stains indicate that the core of the Alzheimer's

plaques is composed of both 40 and 42 amino-acid variants while the coronal

region is composed primarily of $A\beta_{40}$. The APP/PS1 tissue did not stain positive

for $A\beta_{42}$ indicating that the transgenic plaques are composed primarily of the 40

amino-acid constituent due to a lack of or reduced production and incorporation

of this beta-amyloid form in the transgenic model plaques. The scale bar is

calibrated to 250 μm.
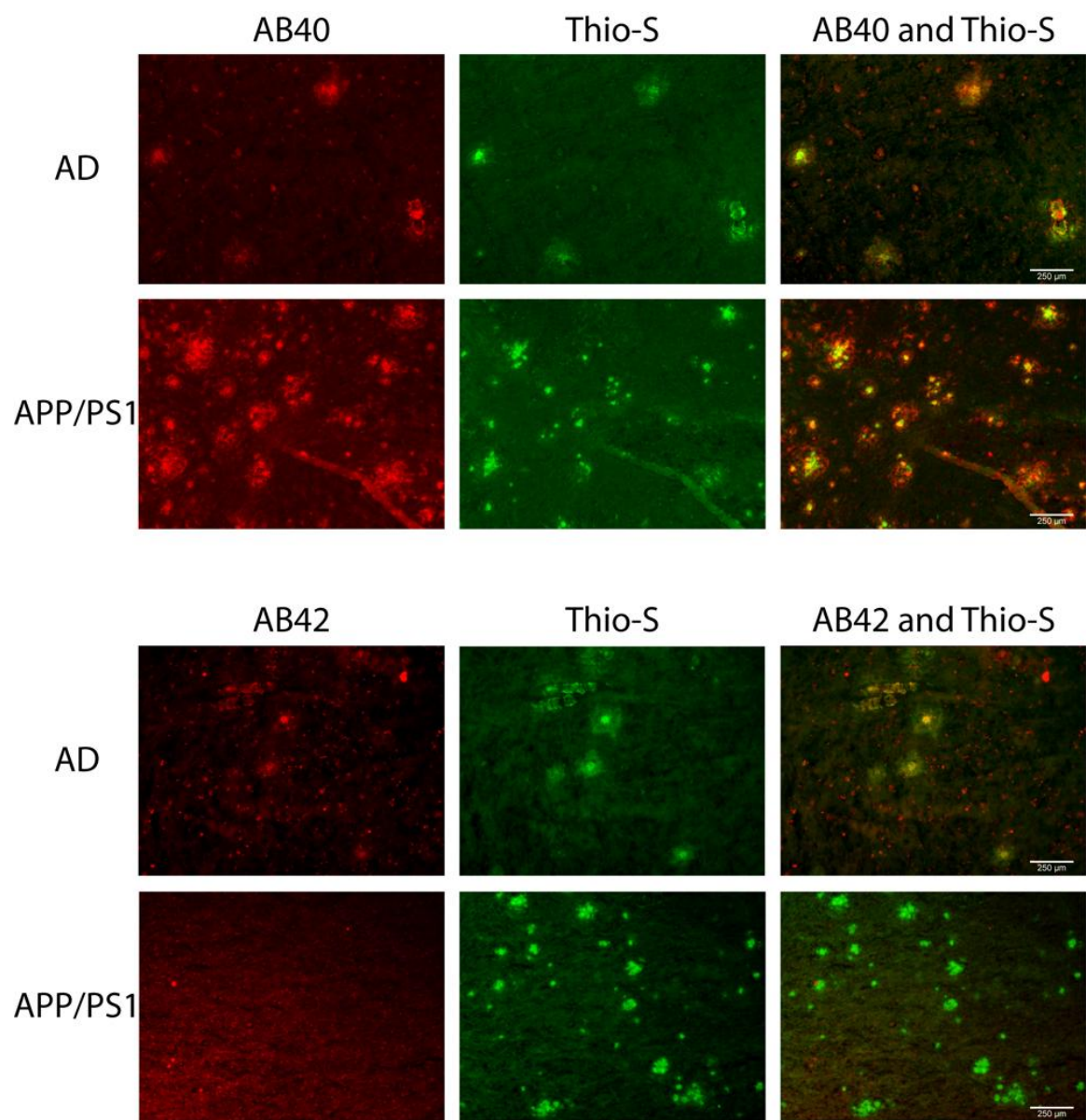
Figure 4.1.5.2

Glial fibrillary acidic protein (GFAP) (red) for astrocytes and thioflavin- S (green) staining for Aβ plaques in Alzheimer's disease, matched human controls, APP/PS1 and mouse control tissue at 100x magnification. Astrocytes in the AD tissue are seen in a motile phagocytic state surrounding the coronal region of the beta-amyloid plaques. In human control tissue, the astrocytes are observed in their normal highly branched form indicative of their supportive roll for neuronal tissue. APP/PS1 and mouse control tissue similarly stain positive for GFAP throughout the tissue samples and illustrate astrocytes in a highly branched normal supportive role. The strong association seen between astrocytes and beta-amyloid plaque in the AD tissue is not perceivable in the transgenic model. The data indicates a differential astrocytic inflammatory response to beta-amyloid plaques in the natural AD milieu compared to the transgenic model. The scale bar is standardize to 100 μm.

GFAP and Thio-S

AD
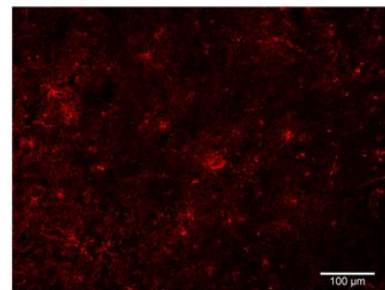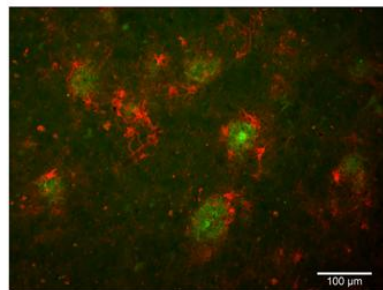
Human
Control

APP/PS1
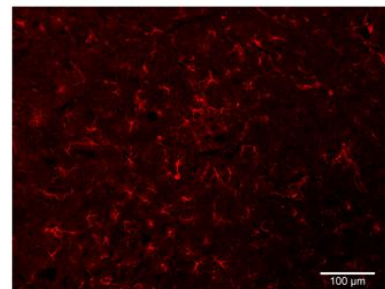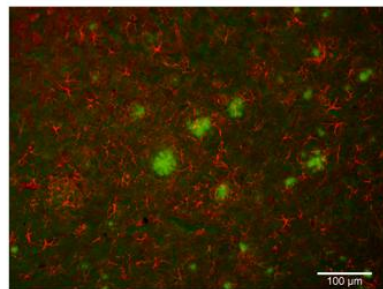
Mouse
Control

Figure 4.1.5.3

Ionized calcium-binding adaptor molecule 1 (IBA1) antibody staining for microglia (red) and thioflavin-S (green) for beta-amyloid plaques in Alzheimer's disease, human control, APP/PS1 and control mouse tissue samples at 100x magnification. Microglia the AD sample are highly associated with beta-amyloid plaque location and are seen in an activated amoeboid surrounding plaques with processes infiltrating into the coronal region. In the APP/PS1 tissue, microglial cells are also observed in an activated state associating with plaque location. The transgenic microglia are surrounding plaques but do not have exhibit processes that penetrate into the plaques. Human control tissue samples show positive microglial staining and demonstrate microglial cells in a intermediate ramified resting state with numerous processes surrounding their somas. Mouse control tissue exhibits less microglial staining overall and shows cells in a quiescent resting state. The data demonstrates a subtle difference in microglial inflammatory response for AD and APP/PS1 neural tissue samples. The scale bar is 100 μm in length.

IBA1 and Thio-S

AD

APP/PS1

Human Control

Mouse Control

Figure 4.1.5.4

Light and heavy ferritin antibody (red) and thioflavin-S (green) staining for beta-amyloid plaques in AD and APP/PS1 tissue samples at 100x magnification. L-ferritin staining in the AD tissue samples shows intracellular staining in microglial cells that are similar in morphology to those in figure 4.1.5.3. L-ferritin staining in the APP/PS1 tissue shows intracellular staining of neurons in the granular layer off cortex. There is no positive staining of microglial cells in the APP/PS1 tissue samples. H-ferritin staining of AD samples demonstrates positive intracellular neuronal staining throughout the tissue samples with minimal association to beta-amyloid plaque location. There was no positive staining for H-ferritin in the APP/PS1 tissue samples. The scale bar is set to 100 μm in length.

L-Ferritin/Thio-S   H-Ferritin/Thio-S

AD
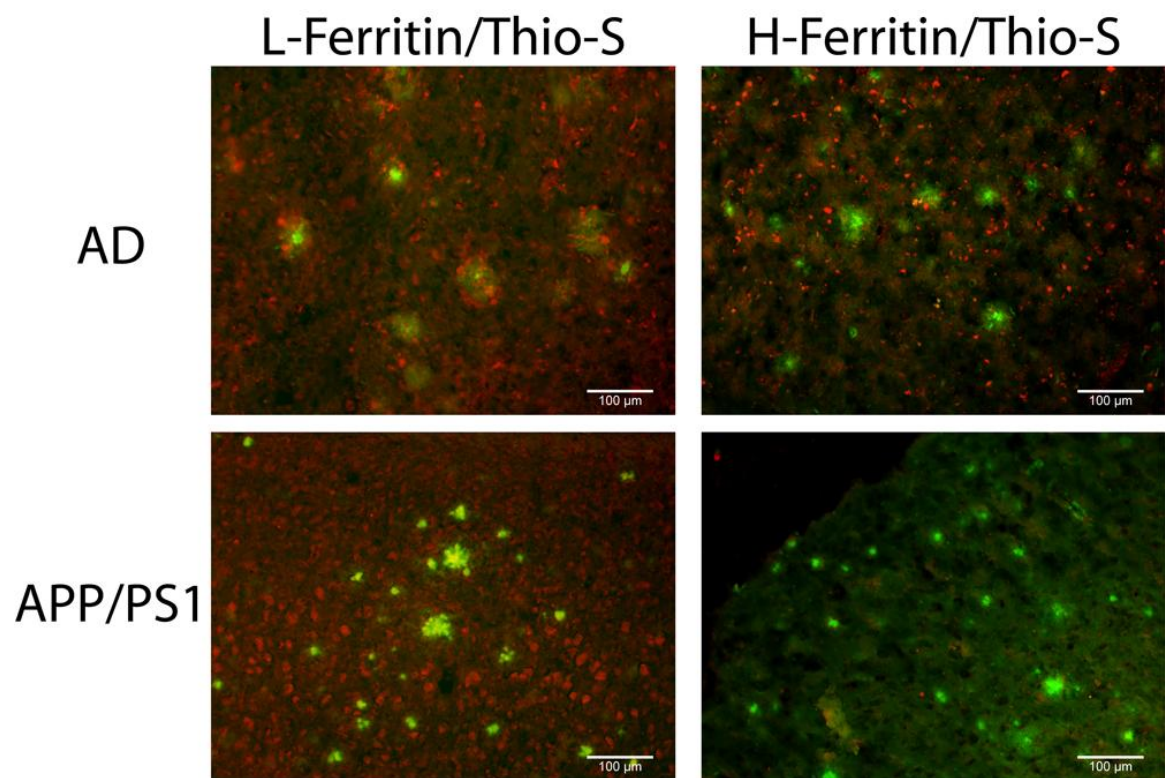
APP/PS1

Figure 4.1.5.5

Beta-amyloid 40 staining (red) and fluoro Jade-C (green) staining in Alzheimer's disease, APP/PS1, human control and mouse control tissue sections at 200x magnification. Beta-amyloid plaques staining is similar to that seen in figure 4.1.5.1 for both AD and APP/PS1 tissue samples with positive plaques and intracellular $A\beta_{40}$ staining. Fluoro Jade-C staining is positive for degenerating neurons in the AD tissue sample and overlaps precisely with intracellular $A\beta_{40}$ staining. There is no positive staining for degenerating neurons in the APP/PS1 tissue sample. Human control samples also show intracellular $A\beta_{40}$ staining that overlaps with fluoro Jade-C degenerating neurons. Mouse control tissue stains negative for both $A\beta_{40}$ and fluoro Jade-C. The scale bar is 50 μm in length.

	AB-40	Fluoro Jade C	Overlay
AD			
APP/PS1			
Human Control			
Mouse Control			
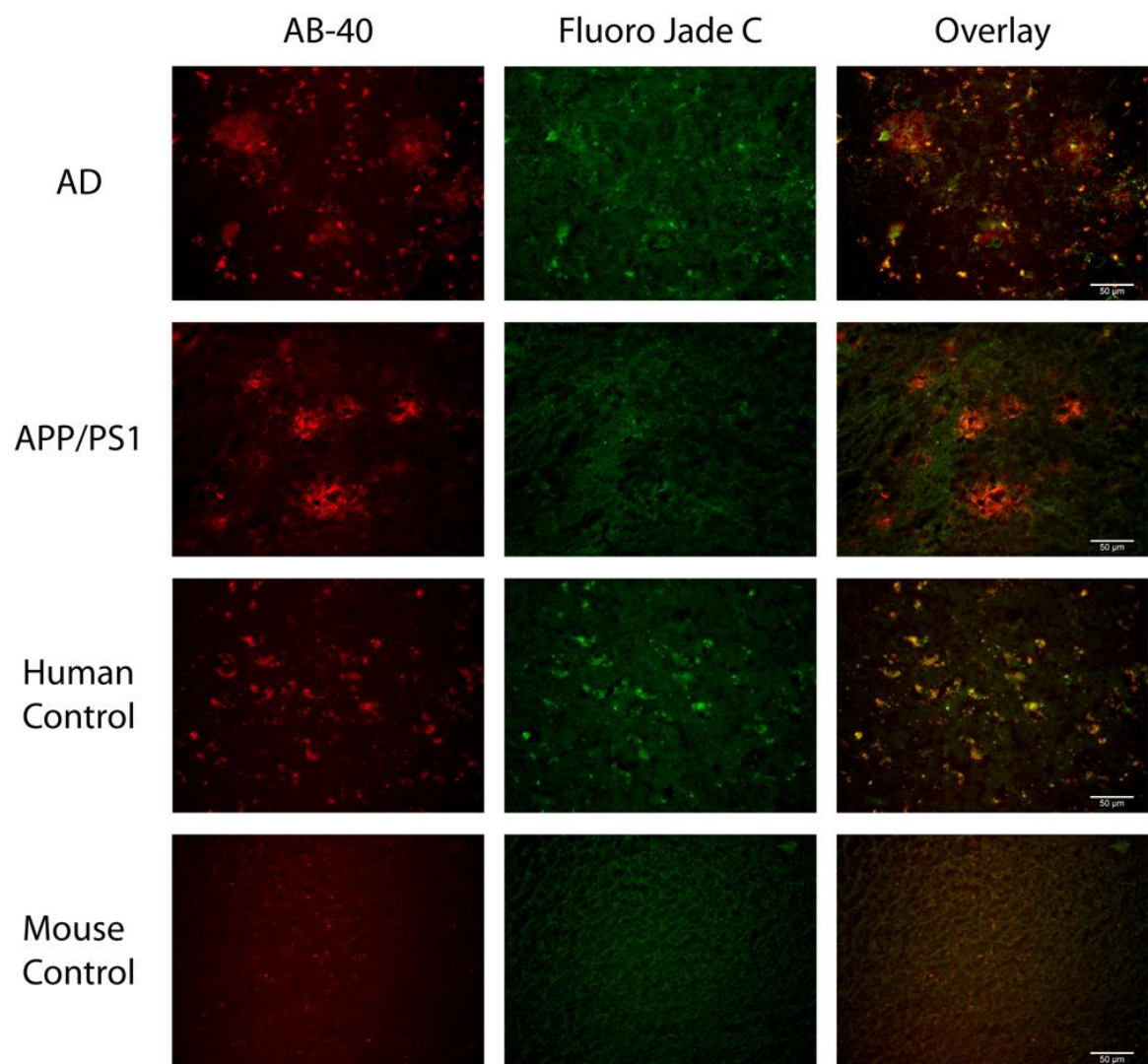
Figure 4.1.5.6

Human Alzheimer's disease stained with (a) thioflavin-S and (b,c) a traditional

Perl's stain under (a) fluorescence, (b)phase contrast and (c) brightfield at 40x

magnification. Red arrows indicate selected plaques that have iron associated

with them, while the blue arrow indicates a focal iron region not associated with a

beta-amyloid plaque and is composed of hemosiderin or magnetite. The core of

many beta-amyloid plaques in AD exhibit high iron deposition within them, as

seen in both the phase contrast and brightfield magnifications. The scale bar is

set to 250 µm.
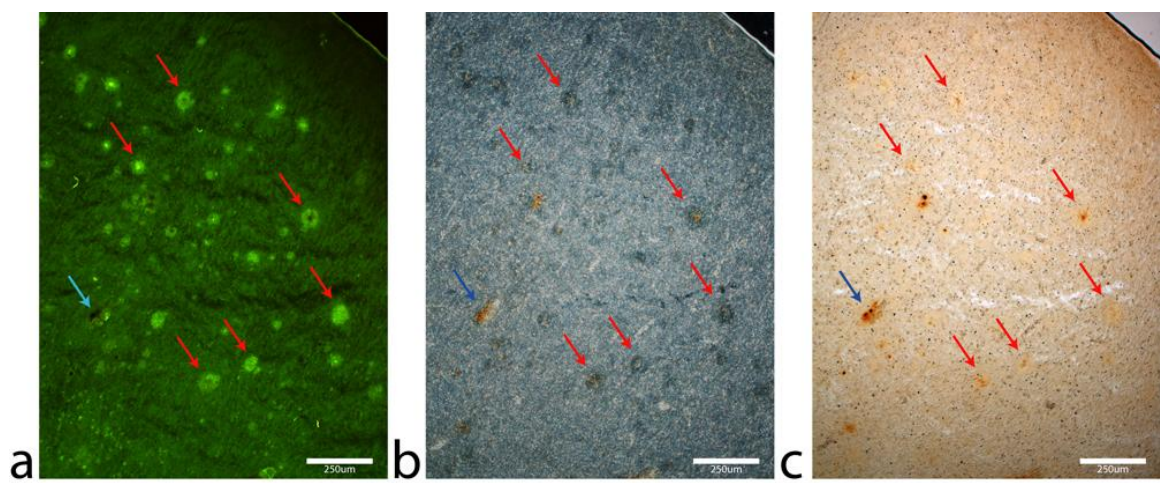
Figure 4.1.5.7

APP/PS1 tissue sample stained with (a) thioflavin-S and (b,c) a traditional Perl's stain under (a) fluorescence, (b)phase contrast and (c) brightfield at 40x magnification. The transgenic mouse tissue does not stain for positive for high focal iron associated with beta-amyloid plaques with a traditional Perl's stain. The blue arrow illustrate a focal iron deposit not associated with a plaque that indicates the Perl's stain is effective in staining iron deposits. Phase contrast microscopy show regions where beta-amyloid plaques are located where light passes through the plaque and alters the wavelength of the light. Similar to the AB_{40} stains and thioflavin-S stain in figure 4.1.5.1, the phase contrast allows the viewing of the non-fibrillar beta-amyloid surrounding the transgenic plaques that does not stain with thioflavin-S. The scale bar is set to 250 µm.
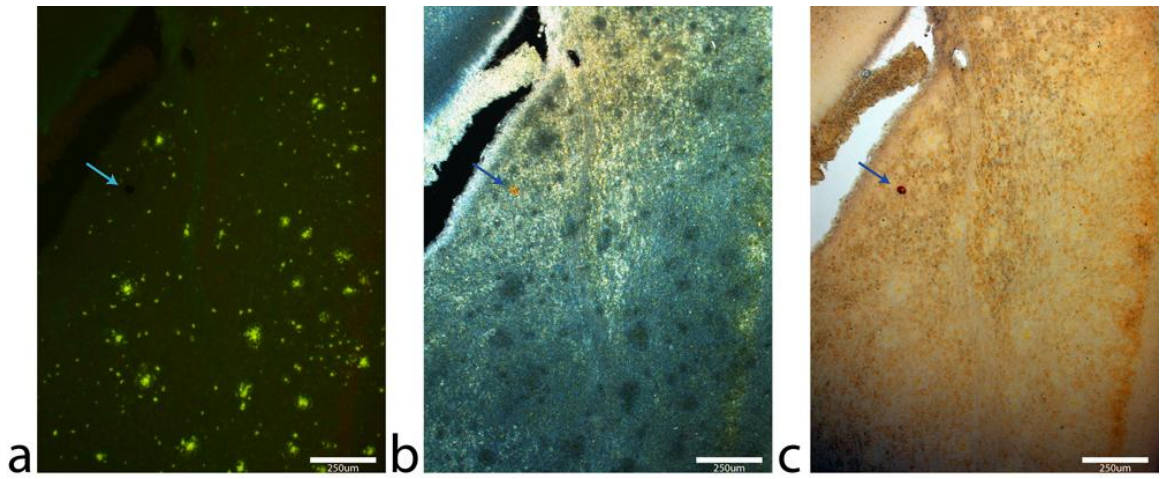
Figure 4.1.5.8

(a) Thioflavin S and (b) modified Perl's stain using protein digestion to allow
further penetration of the aqueous stain into the hydrophobic APP/PS1 plaques.
The stain indicates that there is a very minute amount of iron found in the
APP/PS1 plaques that is not stainable with traditional Perl's staining
methodology. The scale bar is set to 250 μm.
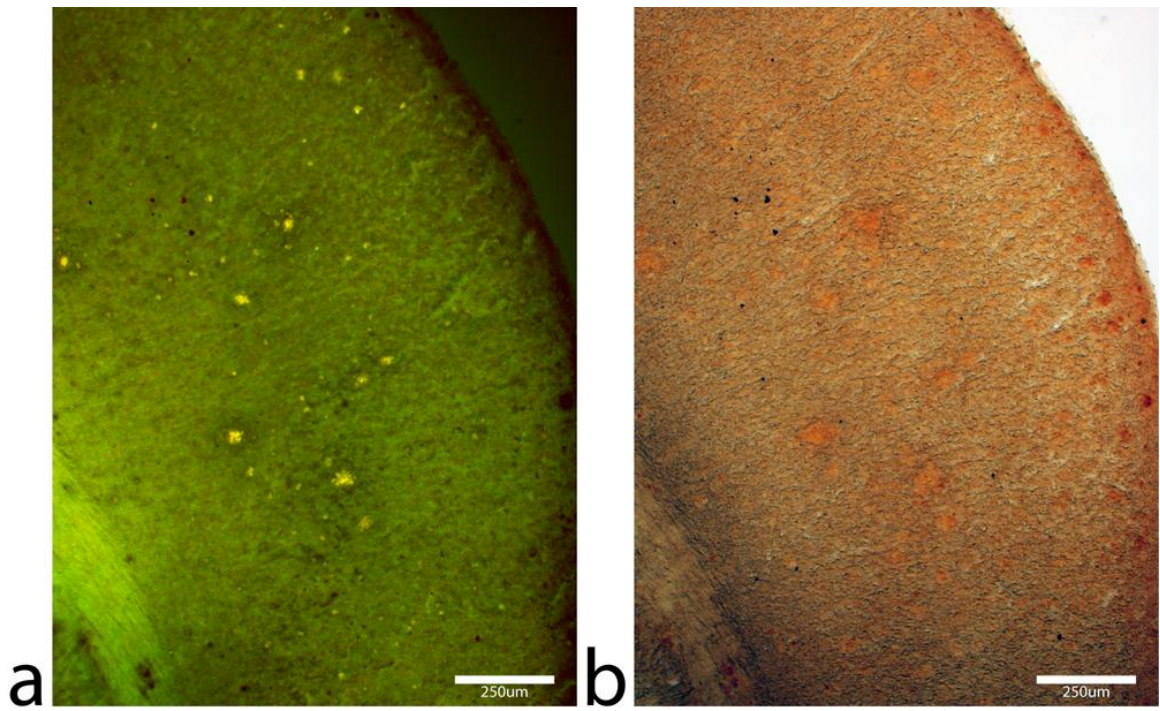
4.1.6 – Discussion

Alzheimer's disease (AD) pathology is largely characterized by the hallmark formation of beta-amyloid (Aβ) plaques within gray matter of the cerebral cortex. The creation of transgenic mouse models that generate beta amyloid plaques help mimic this pathological aspect of Alzheimer's disease. These animal models offer the ability to examine forthcoming pharmacological treatments and assess imaging technologies that potentially could be translated to human AD research and eventual treatment regiments. The time of formation of plaques in these animal models range from approximately six months to a year, and as such greatly accelerate the time of plaque development for research purposes compared to the *in vivo* disease process in AD. While these transgenic mouse models recreate *in vivo* plaque formation, plaque formation and morphology are considerably different compared to the neuronal milieu of the AD brain. The histological comparison between human and transgenic mouse Aβ plaques is critical in elucidating experimental results obtained with transgenic Aβ plaque models.

Since the first relationship between cognitive decline and Aβ plaques by Alois Alzheimer in 1907 (3) to the discovery of the 40-42 amino acid constituents of the plaques 75 years later by Allsop *et al.* (225), the exact roll of Aβ in the disease process of AD is still not currently understood. Indeed, the generation of plaques in the human AD brain from the constituent Aβ peptides has not been worked out. Research has shown that there is a relationship between elevated levels of Aβ plaque burden and cognitive decline (226,227) and as such it never-

the-less remains a central feature in the neurobiological study of the disease.

The progression of beta-amyloid plaque formation is vastly different in the

transgenic model compared to the human AD brain. The mouse brain variant of

the amyloid precursor protein differs from human APP by seventeen amino acids,

three of which are located within the region coding the Aβ peptide. Non-

transgenic normal mouse neural tissue does not produce an amyloidogenic

peptide sequence and increasing the level of mouse APP does not lead to the

production of Aβ plaques (109). Transgenic insertion of human familial APP_{695}

into the mouse leads to an increase in the production of $A\beta_{42}$ but is insufficient to

cause plaque formation. The same is true for transgenic models utilizing single

human presenilin (PS) 1 or 2 mutations of the γ-secretase protein. When mice

are co-transfected with both APP_{695} and PS1, the formation of plaques occurs at

approximately six months and increases the level of $A\beta_{42}$ which is directly linked

to the onset and concentration of amyloid deposits in these transgenic models.

In order to compare data obtained with the APP/PS1 model to human AD,

evaluation and comparison of the beta-amyloid plaques in the transgenic models

to human AD plaques must be carried out. There appear to be numerous distinct

differences between the plaques in the naturally progressing AD and the

transgenic mice. Thioflavin-S staining of the plaques shows that the animal

model has plaques which are globular in nature and are composed of filaments

that branch out radially from a central location (Fig. 4.1.5.1). Compared to the

human AD plaques they lack the typical dense core and large surrounding halo

region of the human plaques. Antibody staining of human AD and APP/PS1

plaques with both 40 and 42 amino acid variants shows apparent differences in staining patterns, which allude to fundamental differences in plaque composition, formation and morphology. It is important to note that the beta-amyloid plaques in the transgenic model also are recognized by human antibodies to Aβ, as the transcribed peptides are derived from human mutations (228). There is an underestimation of transgenic plaque size with thioflavin-S staining alone compared to $A\beta_{40}$ staining. The core of the transgenic plaques exhibit a high binding affinity for the thioflavin-S molecule, which is indicative of a highly fibrillar amyloid core within these plaques. The large coronal region that is stained only with the $A\beta_{40}$ antibody indicates that this region is composed of more diffuse beta-amyloid, which is less fibrillar in nature. $A\beta_{40}$ antibody staining also shows positive staining in regions where no or very little thioflavin-S staining is evident. These areas could be indicative of regions that are composed of non-fibrillar Aβ during the formation of new plaques. Human plaques show high amounts of fibrillar $A\beta_{42}$ mixed with lower amounts of $A\beta_{40}$ within the core of the plaques, surrounded by a halo region predominantly composed of $A\beta_{40}$. Transgenic plaques do not stain positive with $A\beta_{42}$ antibody illustrating that these plaques are not composed of the 42 amino-acid variant of beta-amyloid. These differences in morphology between human AD and transgenic plaques could be due to a number of factors. The decreased time of amyloidogenesis in the transgenic APP/PS1 model is one culpable factor. Although chronologically beneficial for performing studies using the animal models, the decrease in time for amyloid plaque formation creates an uncharacteristic environment outside that seen in

the AD neuronal milieu (111). Normal Aβ plaque progression in the AD brain

takes a number of years and perhaps decades. The APP/PS1 transgenic model

produces plaques at a greatly accelerated rate within nine months from birth.

The accelerated time in amyloid fibril formation and plaque growth are important

factors to reflect upon when considering the difference between the AD and

transgenic plaque morphology. The growth of the human AD plaques

incorporates the surrounding neuropil and cells within the fibrillar coronal region.

Transgenic plaques appear to rapidly grow radially from a central seed and force

the surrounding neural tissue away from the growing plaque mass. The factors

involved in natural AD amyloidogenesis are enormously complex and

multifaceted. *Ex vivo* synthetic beta-amyloid peptide like that found in AD

undergoes conformational changes dependent upon environmental factors such

as pH and solution conditions (36). Transgenic beta-amyloid peptide is known to

undergo different post-translational modifications compared to when it is

produced in the normal AD environment (229). This explains why work looking at

the solubility of AD and transgenic amyloid fibrils shows that transgenic fibrils are

completely soluble in buffers containing sodium dodecyl sulphate whereas

human AD fibrils are completely insoluble (229), further illustrating the chemical

and morphological dissimilarity between the two fibril types.

Intracellular staining of Aβ deposits shows a clear difference between AD

and transgenic tissue samples (Fig 4.1.5.1). Human AD samples show

intracellular staining for both $A\beta_{40}$ and $A\beta_{42}$, while there is a decrease in $A\beta_{40}$

intracellular staining and a lack of apparent staining for $A\beta_{42}$ in the transgenic

model. It is not clear from these stains if the intracellular beta-amyloid stained in the tissue samples is of the soluble type which has been associated with neuronal apoptosis (46). Staining of AD and APP/PS1 tissue with Fluoro Jade-C (Fig. 4.1.5.5) to view neuronal degeneration tissue shows a clear overlap in intracellular neuronal staining with $A\beta_{40}$ in AD and aged human controls. This is congruent with data suggesting that intracellular beta-amyloid induces neuronal apoptosis. The fact that transgenic tissue, which stains positive for amyloid plaques, and control mouse tissue do not stain with fluoro-Jade C suggests that neuronal degeneration is not occurring in regions surrounding $A\beta$ plaques and that neurons are not undergoing apoptotic signaling associated with intracellular beta-amyloid. This represents a clear and fundamental difference between the transgenic mouse model and AD. The neuronal degeneration associated with beta-amyloid is one of the underlying mechanisms responsible for the disease process. The relationship between intracellular and extracellular beta-amyloid and the mechanism by which extracellular amyloid is produced in the normal AD disease process could be due to a number of factors and seems to be different from the method by which it is produced in the transgenic APP/PS1 model. Amyloid precursor protein processing is believed to occur in the endoplasmic reticulum and trans-Golgi network (49), producing beta-amyloid through the gamma and beta-secretase cleavage pathway. This would result in intracellular amyloid accumulation when the peptide is released into the cytosol of the cell. While the exact biochemical mechanism by which extracellular amyloid is transported outside the cell in unknown, there does appear to be a dynamic

214

relationship between intracellular and extracellular beta-amyloid in the AD

disease process (49,51). It has been hypothesized that intracellular Aβ is the

initiating lesion in the development of Alzheimer's disease and extracellular Aβ

can also increase de novo production of intracellular species (230). The lack of

intracellular amyloid staining in the transgenic samples implores the question as

to the mechanism by which extracellular amyloid accumulates in the APP/PS1

model and how it differs from the natural AD process. It is plausible that the

transgenic APP is processed in the extra-cellular membrane and as such expels

amyloid directly into the extracellular environment, or by other means including

exocytotic excretion (52).

Microglial and astrocyte cells are important in Alzheimer's disease

because they respond to neuronal environmental changes. These glial cells

produce numerous regulatory proteins, inflammatory cytokines, and many

proteases and protease inhibitors molecules associated with inflammatory

function (231). Neuronal inflammatory response viewed with microglia and

astrocyte migration and proliferation is also strikingly different between the

APP/PS1 and AD samples. The involvement of microglia in the pathogenesis of

Alzheimer's disease has been well studied and collectively there is support that

inflammatory microglia involvement is an important component of the disease.

Although generally considered a positive presence during inflammatory

response, there is growing support as to the detrimental role that microglia play

during the AD disease process. The recruitment and activation of microglial cells

in and around neuritic plaques leads to the production of various cytokines and

neurotoxins, which are known to cause neuronal injury and death (83). There is a marked association between activated microglial cells with beta-amyloid plaques in the human AD samples (Figure 4.1.5.3). Microglial cells are seen surrounding and throughout the neuritic AD plaques infiltrating within the outer halo region in close proximity to the dense core. Microglial cells are known to assimilate high amounts of intracellular beta-amyloid within them due to the phagocytosis of stressed and dying neurons. There is evidence to support that the recruitment and resulting close proximity of microglial cells to initial beta-amyloid plaque formation results in the delivery of additional fibrillar peptide encouraging further plaque enlargement (85). While there is also an association with microglial cells and amyloid plaques in the APP/PS1 model, there are distinctive differences to the human AD samples. Microglial cells are fewer in number throughout the APP/PS1 samples compared to AD tissue and are visually similar in number and activation state to the control mouse tissue samples. This perhaps is indicative of less neural inflammation occurring in the APP/PS1 brains overall. Microglial cells are seen surrounding transgenic plaques but are not found within the perimeter of the plaques as in the AD samples. While there is speculation that microglial cells in the transgenic model also contribute to plaque formation (232), it is suspicious that during amyloid plaque growth the microglial cells are not engulfed and incorporated into the perimeter of the amyloid star. With the decrease in time of amyloidogenesis, there is a lack of assimilation of surrounding neural tissue as the transgenic plaques radially progress possibly as a result of the diminished time period.

While microglia are found adjacent to and surrounding APP/PS1 Aβ plaques, it seems that overwhelming of the regulatory/degradation systems due to the overabundance of extracellular beta-amyloid seems to be the source of raw Aβ peptide and the driving force toward transgenic plaque formation.

Comparison between AD and transgenic tissue samples demonstrate that there is a weak astrocytic inflammatory response in the transgenic model. The AD tissue samples exhibit a pronounced astrocytic response with a clear relationship between plaque and astrocyte location (Fig. 4.1.5.2). There are well defined astrocyte somas found along the periphery of the plaques with processes extending into the coronal halo region. This differs from the human control sections that show normal astrocyte distribution and processes for an aged human sample. The APP/PS1 tissue shows a similar distribution of astrocytes as found in the control mouse tissue samples, with little to no association of astrocytes with Aβ plaques. Astrocytes are classically well known to be involved in inflammatory response to regions of neural-cellular distress and neurodegeneration to aid in distribution of metabolites, provide support and aid in the repair of effected regions. In the AD tissue samples, it is expected that neural tissue will respond as such to the accumulation of beta-amyloid due to the foreign nature of the plaque. Astrocytes in the AD tissue typically show an reduced star like state with a large somo and few processes. This is typical of an astrocyte in a state when responding to cellular injury. In the transgenic model, the samples do not demonstrate this anticipated response, and are viewed as resting astrocytes in a metabolic helper state. It is plausible that the formation of

the transgenic material into beta-amyloid plaques in the APP/PS1 occurs in such a way that the neural tissue doesn't recognize the material as foreign and as such fails to initiate an inflammatory response. It is of considerable interest that the APP/PS1 tissue samples do show a microglial reaction in close proximity with the periphery of the plaques while not presenting an astrocytic response. There remains the possibility that in the human AD tissue the astrocytes are responding not to the beta-amyloid in the region but to cellular distress associated with beta-amyloid. Astrocytes are known to respond to neuronal cellular stress and death in an attempt to aid in neuronal and cellular repair. In the APP tissue the apparent lack of astrocytic response could be due to a lack of cellular distress and death occurring in the vicinity of the plaques.

There is a considerable difference between the amyloidal genesis in the APP/PS1 mouse model and human Alzheimer's, in respect to its relationship *with in vivo* iron stores. Localized focal iron is frequently found in AD tissue samples both in the central core of the human AD neuritic plaques and also in an apparently random fashion in the form of large focal iron deposits in the form of hemosiderin or magnetite (190,233). The Perl's co-stain with thioflavin-S show an exact overlap between the focal iron deposits within the central core of numerous AD plaques (Fig. 4.1.5.6). There is a reduced amount of iron associated with the APP/PS1 transgenic model (Fig. 4.1.5.7). The phase contrast microscopy images allow the halo region to be visualized in the AD tissue samples and the non-fibrillar halo around the transgenic plaques as the wavelength of the light is altered when it passed through this region, while clearly

218

viewing iron only in the AD tissue samples. Only when stained with a modified Perl's stain that breaks down the periphery of the APP/PS1 plaques are traces of iron found (Fig. 4.1.5.8). Similar staining of AD tissue samples with the protein lysis results in a complete staining of iron throughout the tissue. This is presumably due to protein degradation of iron storage proteins (ferritin) and staining of their iron oxide cores. Ferritin antibody staining for tissue sections indicates differential control of iron storage and association with beta-amyloid plaques in transgenic APP/PS1 and AD neural tissue. Microglial cells are known to harbor high quantities of the light ferritin isoforms for long term iron storage, assumedly due to phagocytosis of cells undergoing apoptosis caused by oxidative stress due to iron induced free-radical production (64,213,234). Human AD beta-amyloid plaques exhibit a tight association with L-ferritin as the pattern of staining is indicating that the L-ferritin isoform is found within microglial cells that are surrounding and infiltrating the plaques. The pattern of staining in the AD tissue for L-ferritin is similar to the microglial antibody stain in figure 4.1.5.3. In the APP/PS1 model, L-ferritin staining was found throughout the tissue sample in the granular cell layer and appears to not be associated with microglial cells based on the cellular morphology and pattern of staining compared to the microglial cells in figure 4.1.5.3. The APP/PS1 having no light isoform associated with microglial cells is indicative of a system that is not undergoing excessive iron build up like in the AD tissue where microglial cells are responding to oxidative apoptotic cell death and sequestering high amounts of iron during the phagocytic process. Heavy ferritin staining exhibited positive staining in neurons

within the AD tissue and was not observed in the transgenic mouse tissue. H-ferritin is known to rapidly take up and release iron and is involved in excessive iron detoxification protecting against iron-induced oxidative damage (64,65). The ferritin staining data sets are congruent with an over abundance of iron in the AD tissue and less overall iron in the APP/PS1 neural tissue. Overall, the iron staining data suggest an overall misregulation of iron homeostasis in the AD diseased brain that is not seen in the transgenic mouse tissue.

While it is unknown precisely how Aβ plaque aggregation occurs, it is known that metal ions can play a role in Aβ fibril formation. The conversion of Aβ's secondary protein structure has been shown to occur in the presence of divalent metal ion's (82). Aberrant regulation of iron leading to its focal concentration in brain tissue is believed to be associated with the neurodegenerative process in neurological disorders such as Alzheimer's disease and Parkinson's Disease (55). Abnormal regulation of iron is believed to be associated with the neurodegenerative processes in Alzheimer's disease. Regions of focal iron concentration leading to potential oxidative stress can lead to cell death and apoptosis (87). The relationship of iron to plaque generation is not currently well understood within the literature. It is largely unknown whether the generation of the plaque causes the aggregation of iron to form a core, or if intracellular iron causes the formation of the beta-amyloid protein around it. There is a general agreement that the location of some focal iron regions in brain tissue coincides with some Aβ plaques in certain brain regions. Numerous studies support the hypothesis that oxidative damage surrounding the Aβ

plaques is involved in the human Alzheimer's disease process. Research has

shown that the co-localization of iron with the Aβ plaques is accompanied by

endoplasmic reticulum stress induced apoptosis, DNA oxidation and cellular

damage in cells adjacent to plaques (104,235,236). Conversely, in regions

where Aβ plaques accumulate alone without iron there is no indication of

oxidative stress or apoptosis pathway activation (214). It has been demonstrated

that the toxicity of Aβ is amplified upon the direct interaction of iron ions with the

peptide, while unbound iron itself has no effect upon toxicity (215). This strongly

suggests that iron accumulation in and around plaques is essential for neuronal

damage. Indeed, there has been speculation as to the positive neuro-protective

roll that Aβ might possess in the disease process. The high affinity for human Aβ

to bind iron might be the result of homeostatic pressure to bind and eventually

expel excess iron from the human brain (89). Regardless, overall it is a widely

held belief that the Aβ peptide is involved the neuro-pathogenesis of AD.

Numerous studies support the hypothesis that oxidative damage surrounding the

Aβ plaques is involved in the disease process. This is furthered by the

knowledge that cytotoxic effects can be ameliorated with the usage of free-

radical scavengers and antioxidants (237). The redox-metal dependent

generation of free radicals and highly reactive hydroxyl radicals through a Fenton

type reaction is believed to trigger the neurotoxic effect in cells that are close

proximity to Aβ plaques (238). Neuropathological and biochemical studies have

shown increased activity of free radical defense enzymes, elevated levels of

oxidative damage to mitochondria, DNA fragmentation credited to apoptotic signaling and oxidative stress markers in AD patients (104,238).

The data in this report suggest that there are numerous differences between normal AD disease process and the APP/PS1 transgenic model, which aims at mimicking the genesis of beta-amyloid plaques formation. The morphological differences between the plaques in the transgenic and AD tissue sample are of considerable importance to researchers whom are considering using the model for studies involved in amyloid clearance based on specific beta-amyloid peptide sequence targeting. The difference in plaque composition (Aβ 40 or 42 subtype) and gross plaque morphology in the APP/PS1 model could result in misleading results when translating pharmacological or antibody methodologies to plaque degradation in the AD brain. This also is true due to the increased in size of the transgenic plaques and highly fibrillar hydrophobic core surrounded by thioflavin-S negative coronal region in the transgenic plaques, which warrants caution when considering using this model for these studies. Other methodologies for AD therapeutics involve the augmentation of the immune system inflammatory response to alter the production and/or clearance of the beta-amyloid peptide sequence. This again should be done under the caveat that there is a considerable divergence between the transgenic model and the normal AD inflammatory response as far as with microglial and astrocytic proliferation and plaque association. It is largely unknown as to why human AD neuronal tissue produces beta-amyloid resulting in plaque formation. For the most part, the same does not hold true for the transgenic animal tissue for whom

beta-amyloid and plaque formation is governed by the introduction of two known

human mutations. Herein is the cause of the vast increase in Aβ production

found in the transgenic model. While in the normal AD disease process, the

increase in the amylodogenic beta-amyloid peptide pathway leading to the

disease process is highly complex and represents a multi-faceted discoordination

or miss-regulation of numerous endogenous systems. Of those systems, three

are outlined throughout this work upon which each shows considerable

differences in morphology, inflammatory response, and iron management

between the natural AD process and transgenic model. It should be understood

that these systematic biochemical errors represent a small proportion of the

potential plethora associated with the normal AD disease process.

Chapter 5

General Conclusions

5.1 – Utilizing Magnetic Resonance Imaging for the Visualization of

   Beta-Amyloid Plaques

      Magnetic resonance imaging is an extremely powerful technology which has pushed forward our ability to diagnose and treat injury and disease into what many would call the modern age of medicine. With the advancement of MR technology, magnets with higher strength fields are becoming commonplace in medical institutions around the world. There is a hope that these magnets will usher in an era with the ability to image human tissue at higher resolutions in less time than ever before. Nevertheless, even at these high field strengths we are pushing the' technological envelope' with microscopic magnetic resonance imaging.

      The small size of beta-amyloid plaques and the current clinical resolutions available to the majority of health care providers is a limitation in our ability to image Aβ plaques. With this said, there are a number of researchers who have investigated imaging beta-amyloid plaques with MRI, in both human AD (183,187,219,239) and transgenic APP/PS1 mice (184-186,193,194,239-243). There has been a great deal of success in imaging neural tissue at high resolution with microscopic MRI techniques (155,163,166,187). The majority of these studies involve the usage of home build RF coils that are very specific and conform to the dimensions of tissue being imaged. Coil specificity aids in creating higher resolution images with increased signal to noise ratios with less

224

imaging time. There is a downside to this however; transferring these results to other systems utilizing traditional volume, surface, or even multi-array coils. These apparati cannot produce comparable high resolution images in an adequate time frame for *in vivo* imaging (whole or partial brain). Here we are left with a conundrum; the technology exists to microscopically MR image tissue with sufficient resolution to view individual plaques (186,187) but the inability to currently translate this to clinical systems. Attempts to compare the transverse relaxation value of large regions of interest and then measure plaque burden in these regions have largely proven to be marginally successful in detailed quantification of plaque burden (195,241,244). The resolution used in these studies would be comparable to clinical *in vivo* studies of AD patients, so the results would hypothetically be directly comparable. The main problem with this line of research is that the plaques in the transgenic model are not only distinctly different in morphology from the human AD plaques but also have differences in iron load. These factors are pivotal in the relaxation associated with the transgenic plaques. It is also of note that within the AD brain there is a sizeable amount of focal iron that is not associated with plaques. This iron would invariably account for a large portion of the transverse relaxation of a large region of interest containing number plaques and iron deposits. As such, the measurement of relaxation in this region would not be a direct measure of plaque burden but instead a mixture of both plaque and iron load. With the knowledge that the mouse model does not have considerable amounts of iron present; the quantification of regions in the transgenic mouse would be a more direct

measure of plaque burden. This would be in large part due to the fact that the plaques themselves in the APP/PS1 model have transverse relaxation associated with them due to proton relaxation in the vicinity of the protein mass. The human AD Aβ plaques also have relaxation associated with them but it seems that iron found in and around the plaques is the dominant cause of transverse relaxation.

The data collected in these studies emphasize the progression of MR technology to microscopically MR image tissue samples. Translating these results to current *in vivo* MR scanners in a clinical setting is challenging. The main limitation, at the moment, exists due to the current resolution of clinical scanners. Ideally, with enough imaging time and image averaging, a lower field MR system could produce a comparable high resolution image. However, in a clinical setting there are time constraints on how long a patient may remain in the scanner for both safety and feasibility reasons. While the scans taken in this work took approximately 6 hours to image at 7.0 Tesla, the time to produce such images at a clinical 3.0 T system are not allowable (on the order of multiple days). In the future, as higher field strengths are used for clinical imaging there is the possibility of acquiring images with similar resolution. There remains the question; Why would we want to image beta-amyloid plaques in the human brain *in vivo*? The easy answer is to be able to detect plaques in the brain for earlier diagnosis of AD. This in itself is challenging, as the work here shows that there is a general iron overload in the AD brain as well as beta-amyloid plaques. These both represent sources of potential transverse T_2 relaxation, and as such

are difficult to tease apart. Early in MR imaging it was realized that T_2 weighted

images were sensitive to brain pathologies, and it was hoped that this would lead

to the ability to utilize T_2 relaxation to specifically address disease pathology

(245). This was not fully realized after extensive research for a number of

reasons, most notably because proton transverse relaxation is multi-dimensional

and occurs due to a number of reasons but ultimately is shown on a single

dimension scale as image contrast. Teasing apart the different relaxation curves

that make up the summated transverse relaxation would help to understand the

mechanisms associated with proton compartmentalization. Comparing these

results to different brain pathologies, specifically beta-amyloid plaques, might aid

in understanding and translating these results to a clinical setting. This would

first be accomplished on microscopic scale, and then broadened to the larger

voxel resolutions in a clinical setting with the understanding that partial volume

effects would be present.

5.2 – Using MRI to diagnose early AD and Mild Cognitive Impairment

There have been a number of proposed mechanisms to determine the

clinical onset and progression into Alzheimer's disease utilizing magnetic

resonance imaging. They include utilizing various MR methodologies such as

functional imaging (246-252), diffusion tensor (253-255), quantitative

measurements of regions of interest (252,256,257) and direct imaging of plaques

(183,185,187,190). The hope is that there are measureable biomarkers such as

olfactory deficits, cortical thinning, white matter track alterations or changes in

227

relaxation that can predict changes in cognition that eventually lead to clinical

onset of Alzheimer's. Individually these studies have shown that there are

structural changes in the AD brain that differ from normal aged matched controls.

Going from the realm of research to a comprehensive clinical test has proven

quite difficult as individual markers lack the ability to accurately predict

progression into Alzheimer's. If a cross modality approach to the data is taken

and it is organized in a regression analysis there is prospect in their ability to

accurately predict disease progression. This is difficult, as a battery of MR and

cognitive tests would be required at the same institution or cross institutionally.

Many have placed emphasis on the utility of imaging and quantification of

plaques and associated iron deposition for potential clinical examination. As

accentuated in the previous section, there are a number of considerations in this

approach that are large hurdles to overcome.

5.3 – The APP/PS1 mouse model of Alzheimer's disease

The majority of the studies involving MR imaging of plaques have

assumed that the ability to view them has been due to the localization of iron

within and around these plaques (193,258). Detailed analyses of plaques in the

transgenic APP/PS1 model have revealed that there are distinct differences in

the relationship between iron and their plaques and also in plaque morphology.

This difference has been mentioned in the literature relatively recently

(109,193,201,229,259), but these dissimilarities and the cause of transverse

relaxation have not been drawn fully into the magnetic resonance discipline. The

reason for the clear difference in plaque morphology is at first glance relatively straight forward; the attempt to generate Aβ plaques in a mouse model that naturally does not do so. In reality the circumstances are complex and multifaceted, with a number of factors that seem to have individual roles that coalesce. The natural APP processing in the murine brain does not result in the production of fibrillar amyloid, and as such does not generate plaques. With the introduction of human genetic mutations into the APP/PS1 mouse model we have created plaques, but not in the same way they are produced in the human AD brain. In the APP/PS1 brain there are two systems are play during APP processing, the endogenous APP and γ-secretase (PS1) and then the introduced human FAD mutations in APP and PS1. Unlike the human AD brain, the APP/PS1 model now has the ability to produce both a natural non-fibrillar product and the fibrillar AD Aβ. When initial seeding of fibrillar Aβ occurs in the transgenic model it provides scaffolding that allows the natural product to potentially bind. Indeed, it has been shown that APP/PS1 animal plaques can be composed of both human and mouse amyloid (202,260). There are also different post translational modifications to the beta-amyloid that is produced in the mouse model (209). The environment within the mouse brain is very different from the human brain in a number of aspects. The levels of various metals, especially iron, are a great deal reduced in murine neural tissue compared to the human brain (192,261).

A very important consideration when using the APP/PS1 transgenic model is the ability to transfer acquired datasets to the natural AD process. There has

been great emphasis placed on using various methods to reduce plaque burden, chelate metals coupled to plaques or institute pharmacological methods in an effort to decrease neuronal damage associated with Aβ plaque deposition. While the model does show some similarity to AD pathogenesis, there is an inherent caveat that must be disclosed. The mouse model generates beta-amyloid plaques in a different manner than those produced in the AD brain. The APP/PS1 model generates plaques in response to the drastic overproduction of fibrillar beta-amyloid. The over production of APP in the murine model is evident when looking at both microscopic images and quantification of beta-amyloid peptides with protein quantification. The murine model possesses an endogenous APP variant that does not get processed into amyloidogenic beta-amyloid fragments to product plaques. The increase in amyloidogenic peptides is directly related to the introduction of human familial Alzheimer's genetics. A noteworthy question is why does the murine model over produce the introduced human variants to such a degree? It is possible that the mouse model is unable to break down the amyloidogenic human peptides as well as the endogenous murine forms, leading to accumulation of human forms. This seems unlikely however with recent data suggesting that wild-type mouse apolipoprotein is able to efficiently degrade both soluble and insoluble beta-amyloid and eliminate thioflavine-S positive amyloid deposits (262). It does seem that overproduction or accumulation of the human peptides is not specific for certain neural structures in the mouse brain. In the human AD tissue, plaques form predominately in the middle cortex layers and plaque production starts near the entorhinal cortex and

eventually spreads throughout the brain. In the APP mouse model, plaques for

throughout the brain. They are non-specifically produced not only in cortical

tissue but also in deep brain matter and white matter tracks. It seems that there

is there is a vast overproduction of Aβ in all APP neural cell types that is clearly

not seen in the naturally occurring human AD brain. The direct cause behind

why human AD tissue produces plaques is not known, but there are theories that

support the current available data. Beta-amyloid is a natural product of APP

processing, and is found in normal cognitively intact individuals and also in the

murine brain but not in the fibrillar form. The formation of beta-amyloid plaques

is not limited to the AD brain, as the normal aging process produces plaques in

aged individuals (217,263). The divergence point between a cognitively intact

individual and a person with AD is hard to place a finger on. Many would place

emphasis on the genetic mutations found in familial AD cases. There is a wealth

of data to support this, but the majority of individuals diagnosed with AD do not

have mutations that are currently associated with the disease process. The

foundation of the APP/PS1 model focuses on the genetic mutations of AD, and

generation of plaques is a direct result of this. However, there are clearly other

factors that have not been accounted for in the natural AD brain. A threshold of

cognitive decline has been suggested in that individuals may appear cognitively

intact because they have yet to reach a specific point of atrophy in the brain

where it can no longer compensate for lost tissue. This would suggest that it is

not the generation of plaques, per se, but the loss of neural tissue that is

responsible for cognitive decline. The literature currently agrees with this, as

there have been clear results showing cortical loss associated with cognitive decline in AD (264,265). The reason for the cortical loss is the key element in the disease process. Staging of AD has clearly shown that cognitive decline is associated with an increase in Aβ plaque and NFT burden (4,43,44). This has led the majority of the field to conclude that these hallmarks are responsible, in some way, for the loss of neurons in the AD brain.

5.4 – Plaques and Iron, what is their relationship and which comes first?

The involvement of iron in the pathogenesis of Alzheimer's has been well established. The incorrect regulation of iron management proteins and irregular storage of iron within AD neural tissue results in the accumulation of excess amounts of free iron. It appears that these conditions are not separate from the AD process, as they are found in the majority of AD cases. Increased stored iron is associated with a number of medical conditions, such as type 2 diabetes and vascular disease, which increase the risk for progression into AD (266). Body iron stores increase with age in both men and women with markers for iron stores increasing sharply between the teenage years until iron levels plateau in middle age. Alzheimer's is generally considered a disease of aging with increased risk of developing AD after 60 years of age. The age related increase in iron precedes the disease associated cognitive decline by decades. It seems highly probably that the natural increase in iron precedes clinical AD symptoms. Other diseases such as heart disease and atherosclerosis have been shown to escalate in parallel to the increase in iron storage in the body (266-269). It has

232

been proposed that the age-associated increase in body iron stores could be responsible for the start of the pathophysiological cascade that promotes Alzheimer's disease progression. Genetic and environmental factors associated with abnormal iron homeostasis may go unnoticed for decades, as the body is able to maintain excessive iron storage for a period of time.   However, there comes a moment when the body can no longer maintain this threshold of iron maintenance and the system overloads. Excessive iron has been shown to mediate and increase the production of the APP peptide, which ultimately then is cleaved to form the Aβ peptide (270). It has been hypothesized that this is due to the metal binding properties of the beta-amyloid peptide. It has been suggested that neural tissue produces the peptide to help aid in the sequestering of excessive iron that the body's normal storage mechanisms can no longer keep up pace with (88,89). This might help in the short term, but as the Aβ peptide binds more iron and plaque aggregation occurs the accumulation of iron in plaques increases and produces focal regions of iron deposition. In the midst of this, more iron is continually being shuttled into the brain, which cascades to produce more Aβ peptide which amasses into additional beta-amyloid plaques. As this 'backup' system of sorts fails to sequester errant iron, accumulation of hemosiderin and magnetite occurs in the AD brain (271). The plaques and other regions of highly focal iron now function as reduction and oxidation centers; reactive oxygen species and free radicals are produced, cells undergo excessive amounts of oxidative stress, they tumble into apoptotic signaling and neuronal atrophy occurs.

5.5 – Potential Follow-Up Studies

It is important to understand that the transgenic mouse models of AD created to date do note exhibit iron imbalances in their neural tissue. There is no focal iron found throughout their brains and Aβ plaques that form have only a minimal amount of iron. This is a strict limitation of the animal model, and ultimately might prove to be a cause for the lack of atrophy on the scale seen in AD. This also might explain why plaques form differently within the APP/PS1 brain with a completely different morphology. It would be very interesting to see how increased iron in neural tissue would affect plaque generation and morphology along with markers of oxidative stress and apoptotic signaling. Increasing iron storage in neural tissue is not a normal process in the murine brain. An alternative means at increasing iron systemically throughout the body is required. This can be done with lipophilic iron compounds such as TMH-ferrocene [(3,5,5-trimethylhexanoyl)ferrocene] (272). A similar study of increasing iron stores in the mouse for quantification and measurement via MRI has been undertaken and is found within the appendix of this thesis. Iron concentration levels do increase in the neural tissue with a concomitant increase in neuronal L-ferritin (272-277). The next step would be to feed APP/PS1 mice food with TMH-ferrocene from birth. A detailed evaluation of iron load and plaque genesis compared to litter-mate transgenic mice feed a normal or low iron diet would be essential. Magnetic resonance imaging sequentially throughout this period would help understand how relaxation associated with plaques is changing. It is hypothesized that iron load would increase throughout specific

regions in the neural tissue as viewable with MRI (view appendix) and that

plaque generation would be altered in the mice feed the lipophilic iron compound.

Plaques would contain more focal iron and potentially would form more akin to

the way they do in the Alzheimer's brain. Oxidative stress markers would

increase in neural tissue surrounding the plaques and neuronal death would

occur in close proximity to beta-amyloid plaques. This would help create a more

realistic animal model of AD that incorporates not only the generation of plaques

but also some of the iron imbalances known to be associated with the disease.

Understanding the differences in inflammatory response between the APP

model and human AD would be important in future development and testing of

therapies for AD. The data here show that there are differences between

neuronal stress markers and cellular death in the APP and AD brains around the

plaques. This might be why there are histological differences between astrocytic

and microglial response between the two systems. Detailed measurements of

neuronal stress proteins are reactive oxygen species in the vicinity of the plaques

would help tease apart these differences.

Another line of study would be the further usage of the histological coil in

aiding to understand the MR relaxation associated with Aβ plaques. At the time

of the studies pursued here we were unable to quantify the amount of iron

present at the plaque locations. There are two available methods to measure

this. Using laser dissection of individual plaques followed by atomic-absorption

spectroscopy (AAS) of the samples or another method that directly uses a laser

to vaporize the tissue in a XY plotter like fashion that then measures the gases

235

produced during vaporization to evaluate metal ion concentration. The first method would require individual plaque dissection, which would be very time consuming to undertake, and involves a certain amount of error when measuring such small pieces of dissected tissue with AAS. The second method would vaporize an entire sample, but would give a detailed three dimensional graph with XY being spatial locations and Z being iron (or another metal) concentration. The latter method would seem to best available option but would require the equipment, which would be best done with collaborative efforts considering the considerable resources involved. There is also the possibility that the second method could measure beta-amyloid concentration. It would be hypothesized that quantitative measurements of transverse relaxation would correlate to the concentration of iron or amyloid present. This would generate a noteworthy finding in understanding how transverse relaxation is affected by both protein and metal ion concentration in both human AD and APP/PS1 tissue samples. Potential follow-up studies to further evaluate the mechanism by which the beta-amyloid protein in the plaques elicits transverse relaxation would be beneficial. It was hypothesized that the close interaction (i.e. rotational and irrotational binding) of the protein with the protons causes the rapid relaxation of other protons in close proximity. Further testing of this hypothesis is possible by altering the exchange rate of proton-proton interactions via heating or cooling of the sample followed by subsequent measurement of the transverse relaxation rate for plaque regions of interest. Heating the sample would result in increased proton (water) movement and thus increased proton-proton dipole-dipole

interactions resulting in an increased relaxation rate. The opposite holds true for cooling of the sample in that this would decrease the relaxation rate due to decreased proton-proton interactions. It is unknown if heating or cooling at the possible temperature range available would be able to appreciably alter the transverse relaxation of these regions; however, if heating and/or cooling does elicit a difference in relaxation for these regions of interest this would point towards a dipole-dipole interaction of relaxation.

There has been a large push toward molecular and contrast enhanced imaging of beta-amyloid plaques. With the discovery that positron emission topography (PET) imaging of plaque burden is possible with a thioflavin-T molecule with a radioactive C^{11}, otherwise known as Pittsburgh compound B, many have considered an MR alternative. MRI has the unique benefit of spatial resolution over PET imaging, which could allow individual plaque imaging. Testing potential contrast mechanisms in animal models is time consuming and takes considerable resources. Potential contrast agents can come in the form of chelated metal ions (gadolinium or iron oxide particles) bound to proteins or antibodies that bind to specific peptide sequences or other new novel agents (chemical exchange-dependent saturation transfer (CEST)) that also increase proton relaxation. This technology is not limited to study just within the realm of Alzheimer's research, as a great deal of potential MR molecular probes count be tested for specific antigens found on cancerous tissue, specific cell types, or specific regions in the brain or body. Testing both the efficacy on proton relaxation and binding of the probe is important is understanding the utility of this

technology. The most effective probes would elicit proton relaxation when bound

to their respective antigens and would have a potential proton shielding effect

when not bound such that they would not elicit relaxation. The probe must be

able to bind with the antigen with high enough specificity but also be able to

release form the antigen overtime as to not interfere with other potential *in vivo*

mechanisms and be excreted over time. The probe must also be able to cross

the blood brain barrier successfully without opening the tight junctions (i.e.

mannitol).

There also is the investigation of other diseased tissue samples with the

histological coil. Alterations in proton relaxation have been associated with a

number of neurological diseases and other diseases of the body. Detailed MR

evaluation and subsequent histological staining of these tissues with some of the

methods outlined in this work could help in the understanding of how tissue

contrast in many disease processes is related to tissue histology. With careful

changes to MR sequences to allow for a large amount of echoes it is possible to

extrapolate the multiple relaxation curves from multiple proton (water)

compartments in the average T_2 relaxation curve. This would allow for

comparison of multiple exponential T_2 curves in tissue samples with the

histological coil. Comparing these values to histological stains would be of great

interest. Specifically, viewing the ratio the myelin water fraction (MWF) (278) to

Luxol Fast Blue staining of white matter in Amyotrophic Lateral Sclerosis and

control tissue would be interesting to analyze. Also, it would be of considerable

interest to see if multiple MR T_2 relaxation due to differing water

compartmentalization differs between human AD and APP plaques. This would

further aid in the understanding of the mechanism of MR relaxation associated

with the plaques.

Appendix A

Quantitative Measurement of Iron with Magnetic Resonance Imaging

6.1 – Purpose of Appendix Material

The data that follows was a study designed to evaluate and test the

hypothesis that quantitative iron measurements in a phantom and *in vivo* model

system was possible with magnetic resonance imaging. The data collection was

nearly complete, except for difficulties in quantification of protein levels using slot

blot quantification. This work represents a nearly complete study that has not

been completely written in manuscript format. A short introduction, materials and

methods, figures and new discussion of the results are included. It is

incorporated as an appendix in support of using MR for iron imaging.

6.1.1. – Introduction

The role of iron for normal cellular function and body homeostasis has

been well established. Normal neuronal functioning requires a tightly regulated

iron repository and delivery system in order to maintain optimal amounts of free

iron. Normal iron concentration in the body is approximately 40 – 50 mg Fe/kg

body weight in women and men (140). Improper management of iron can lead to

its progressive accumulation and storage in ferritin and hemosiderin. However,

the body's ability to sequester and store iron in these proteins can be

overwhelmed eventually leading to toxic accumulation and systemic overload in

organ systems. This mismanagement of cellular iron can lead to decreased cellular metabolic activity and provides an environment of vulnerability for oxidative damage (78). Accumulation of iron can lead to the production of free radicals through a Fenton-type reaction where reactive oxygen species are produced (279,280). Increasing amounts of evidence over the last decade has pointed toward the causational role of oxidative stress and the pathogenesis of Alzheimer's disease (281). Oxidative damage has been observed in Alzheimer's tissue relative to controls with the up-regulation of antioxidant enzymes indicative of the cellular response to oxidative stress pointing toward the relevance of free radical reactions in the disease process (210,279). Data has shown that iron is required in the pathway leading to amyloid-beta (Aβ) toxicity, suggesting that iron catalyzed production of hydroxyl radicals occurs and excess free iron aids in Aβ induced cell damage (279). The concept of the relationship between iron and Aβ protein aggregates has been addressed within the literature. Ferric iron has been shown enhance the aggregation of synthetic soluble $Aβ_{42}$ (282-284).

Quantification of tissue iron load has been proposed with magnetic resonance imaging techniques for some time. The non-invasive *in vivo* measurement of hepatic iron stores has occurred with some success (128,141,142). The limitation in the technique revolves around the extremely high iron content of the liver where transverse relaxation rates no longer are able to linearly follow the increasing iron concentration (126,130). Even considering this, MRI has proven to yield reliable estimates of *in vivo* tissue iron content (123,140). The presence of iron in tissue acts as a natural contrast agent. Iron

241

is a ferromagnetic compound that causes the dephasing of protons in its vicinity, effectively increasing the relaxation rate of these protons (123). This effect is seen far away from the particle of iron and the size of the hypo-intensities associated with focal iron is an over-exaggeration of particle size (120). The majority of iron in the brain is hemoglobin bound iron (approximately two-thirds), the amount of iron stored in the brain as non-heme iron in ferritin accounts for approximately one-third of the total iron in the brain. The aim of the current study was to measure the concentration of iron in an iron loaded mouse model and compare this measurement to transverse relaxation rates of the same brain structures.

6.1.2. – Materials and Methods

Iron Loading Model

Thirty-six male C57BL/6 mice were divided into six groups; Controls, 0 week, 2 weeks, 4 weeks, 6 weeks and 8 weeks. Animals were fed ad libitum a diet composed of 0.1% 3,5,5-trimethylhexanoyl-Ferrocene (TMH-Ferrocene) (272) mixed into Teklad Global 18% protein rodent diet (Harlan Teklad, Indianapolis, Indiana, USA) for a period of 0, 2, 4, 6, or 8 weeks for iron loading. Control animals were free fed a normal iron 18% protein rodent diet for the eight week period. Experimental animals from the 2, 4, 6, and 8 weeks groups given the TMH-Ferrocene diet were MR imaged after the last day of feeding. Control animals were imaged on time point zero and at week eight for comparative

purposes. Time point zero-week animals were scanned immediately at the beginning of the study.

MRI Data Acquisition

Animals were imaged on a 3.0 T Medspec S300 MR imaging-spectrometer (Bruker Biospin, Ettlingen, Germany) using a home-built gradient (9.5 cm aperture and 100 G/cm). Animals were anesthetized with 1.5% isoflurane (induction and maintenance) in compressed air. An in house built slotted-tube RF coil (160) was used during scans that incorporates a heated water jacket to maintain the animals temperature at 37°C during scanning protocols. T_2 weighted fast spin echo RARE images were taken with a TR = 2500, TE = 8, 128 x 128 matrix, FOV of 23 x 23 mm, RARE factor of 12, with eight averages for an imaging time of 4 minutes. For T_2 parametric mapping, a multi-slice multi-echo T_2 protocol with a TR = 2078 ms, TE = 10.0 ms, 128 x 128 matrix, FOV of 23 x 23 mm, 12 echoes with six averages for a imaging time of 28 minutes. The mGESEPI (285) T_2* parametric mapping protocol was utilized to minimize tissue boundary artifacts. The parameters for the 3D T_2* protocol were TR = 250 ms, TE = 5.34 ms, 128 x 128 x 16 matrix, FOV of 23 x 23 x 10mm, 12 echoes with four averages for an imaging time of 34 minutes. The dimensions of the individual voxels in the protocols were 179 x 179 µm in the in-plane directions and 625 µm in the through plane. Total anesthesia time for each animal during scanning was under 100 minutes. Upon completion of scans animals were taken out of the magnet and allowed to fully recover on a 37°C heating pad. For the

phantom imaging, a 25cm birdcage head volume coil was used with the internal body gradient system. Temperature of the phantoms was maintained at 37ºC with a pneumatically driven vortex heater to mimic the temperature of an *in vivo* system. When up to set-point temperature was reached and maintained, three imaging protocols were utilized. A T_2 weighted multi-slice multi-echo scan was used to provide T_2 measurements with a 2000ms TR, 15.32ms TE, 256 x 256 matrix, 250mm x 250mm FOV, composed of two slices with one average at a slice thickness of 4mm for an imaging time of nine minutes. For T_2* relaxation measurements, a 3D T_2* mGESEPI protocol with a TR = 322ms, TE = 8.0ms, 256 x 196 x 16 matrix, FOV of 250mm x 250mm x 8.8 mm, over two slices with two averages for an imaging time of 33 minutes. For T_1 relaxation measurements a variable timing rate multi-slice multi-echo scan was used with a 128 x 128 matrix, 250mm x 250mm FOV, 10mm single slice thickness, with variable echo times of 30, 50 100, 200, 500, 1000, 2000, 3000, 4000, 6000 and 10,000 ms with one average for a total imaging time of 57 minutes.

Animal Tissue Preparation

Upon completion of the final set of imaging protocols animals were deeply anesthetized with a sodium nebutal barbiturate intraperitoneal injection (100 mg/kg), and weighed. When no pinch response was seen in the animals, they were transcardially perfused with cold Ringer's solution till the solution ran clear then followed by cold 4% paraformaldehyde for 15 minutes. The whole brain tissue and livers were then excised and weights recorded for each. Tissue

samples were placed in 4% paraformaldehyde overnight at 4ºC to allow full

fixation. After fixation, tissue samples were re-weighed and placed in two rinses

of 0.9% phosphate buffered saline (PBS) for 24 hours each to fully leach out the

fixative. Following rinsing the tissue was weighed again and the brains placed in

a 0.5mm tissue cutting matrix. The whole brain was cut coronally at a thickness

of 500µm with a razor blade and slices were then placed into a twelve well plate

with PBS. Regions of interest (RIOs) encompassing the motor/sensory cortex,

caudate/putamen, lateral globus pallidus/internal capsule, anterior cerebellum

and corpus callosum white matter tracks were selected from these sections

following a mouse brain atlas and the T_2* parameter maps. These regions were

precisely excised under a dissecting microscope being careful to include only the

desired RIOs and then placed in pre-weighted 1.5ml conical tubes to obtain a

final wet tissue weight.

Iron Quantification with Atomic Absorption Spectrophotometry

Samples of specific regions of interest and livers for each mouse were

pre-weighted and placed in 400 µl of 70% fuming nitric acid at 65 °C for 24 hours

until the samples were completely digested. Each sample was then diluted in

duplicate 1:100 in 1% Nitric acid in ultra-pure water and standard graphite

furnace atomic absorption spectroscopy (AAS) with a Perkin Elmer

spectrophotometer was used to measure iron concentrations in the

corresponding excised brain regions. Two measurements of each samples iron

concentration were completed. A standard curve was generated from serial

dilutions of a calibrated iron standard. If the samples concentration was found to be outside the standard curves upper or lower limits the sample was re-diluted to increase or decrease its concentration to within this limit. Standards were rerun throughout each analysis to verify measurement accuracy over the analysis time. The variation for each replicate and standard was taken and if the measurement varied more than 3% for each duplicate over both measurements the sample was re-diluted and measured again.

Protein Quantification

Samples from each RIO and livers for individual week mouse groupings were combined and placed into 400 µl of homogenization buffer consisting of Lysis Buffer A with 1/100 (b/v) Protease Inhibitor Cocktail (PIC) (Sigma # P8340, St. Louis, MI, USA) for deep freeze storage until subsequent processing. Tissue samples were then homogenized with draws through 18g, 21g and 23g needles followed by complete homogenization at 4°C with a Branson S-250A ultrasonic sonifier. Following homogenization samples were centrifuged at 3000g for 15 minutes such that the supernatant containing the protein samples was collected. Pellets were rinsed twice and centrifuged again to collect the remaining protein. Total protein quantification was completed using a Bicinchoninic Acid (BCA) Protein Assay Kit (Pierce, Rockford, IL, USA) with serial Albumin standards and read with a Molecular Devices Emax 96 well precision microplate reader at a wave length of 565nm. Samples were diluted to 1µg total protein/100µl in Lysis Buffer A with PIC. Precise quantification of L-Ferritin, H-Ferritin and Transferrin

proteins was accomplished using a 72 well slot-blot array system (Whatman, Middlesex, UK) transferred onto Protran BA85 0.45µm nitrocellulose film. Protein standards were commercially obtained for Apo-Transferrin (Calbiochem # 616419, Darmstadt, Germany), Recombinant L-Ferritin (Calbiochem # 341491, Darmstadt, Germany) and Recombinant H-Ferritin (Calbiochem # 341490, Darmstadt, Germany). Primary antibodies for L-Ferritin Anti-Rabbit IgG (Santa Cruz Biotechnology Inc. #SC-25616 (H-45) 1/2000, Santa Cruz, CA, USA) and Transferrin Anti-Goat IgG (Santa Cruz Biotechnology Inc. #SC-22599 (M-20) 1/1000, Santa Cruz, CA, USA) were commercially obtained. The primary antibody for H-Ferritin was a monoclonal Anti-Mouse IgG that was generously given to us from Dr. Paulo Avosio and used at a dilution of 1/40,000. Anti-Rabbit IgG Horseradish Peroxidase linked antibody (from donkey) (Amersham Biosciences # NA934V 1/2500, GE Healthcare, Pittsburgh, PA, USA) was used as the secondary antibodies for the L-Ferritin primary. Anti-Goat IgG Horseradish Peroxidase linked antibody (from donkey) (Santa Cruz Biotechnology Inc. #SC-2020 1/2500, Santa Cruz, CA, USA) was used as the secondary antibody for the polyclonal Transferrin. Anti-Mouse IgG Horseradish Peroxidase linked antibody (from sheep) (Amersham Biosciences # NA931V 1/2500, GE Healthcare, Pittsburgh, PA, USA) was used as the secondary antibody for the monoclonal H-Ferritin primary. Western Lightning Chemoluminescence Reagent (PerkinElmer Life Sciences, Boston, MA, USA) was used as a light emitting reaction with horse radish peroxidase, images taken

with a Fujifilm LAS-3000 imaging system and analyzed for density measurement with Fujifilm's MultiGuage software.

Phantom Iron Model

To determine the relationship between iron quantity and R_2, R_2^* and R_1 relaxation measurements a phantom model was designed and implemented. Relaxation measurements for both average gray and average white matter T_1 and T_2 were determined from both empirical data and that found in the literature (177,286). The phantoms were made to mimic human gray and white matter T_1 and T_2 relaxation measurements. Average relaxation values for white matter were determined to be 832ms for T_1 and 79ms for T_2. Similar average relaxation values for gray matter were determined to be 1330ms for T_1 and 109ms for T_2. The T_2 relaxation parameter was lowered by creating the phantom with differing base percentages of boiled agar in distilled water, specifically Type A agar (Sigma # A6549, St. Louis, MI, USA). To lower the T_1 relaxation parameter, gadolinium DTPA (Magnevist, gadopentetate dimeglumine, Berlex, Bayer Schering Pharma AG., Berlin, Germany) was employed in different percentages. The phantoms were poured into 15ml conical tubes and floated in a water bath just above the melting temperature of the agar to allow any bubbles that formed to rise to the surface. After solidification of the agar, they were placed inside a specially built insulted holder and brought up to the equivalent *in vivo* body temperature of 37°C. The temperature of the apparatus inside the MR systems bore was maintained during the scanning protocol with a pneumatically driven

vortex heater. Calculation and regressional analysis based on the differing gadolinium and agar percentages were used to create equivalent T_1 and T_2 values of white and gray matter for the two separate phantom types. To mimic differing brain iron concentrations and approximate this within the phantoms, iron (III) chloride ($FeCl_3$) (Sigma # F7134, St. Louis, MI, USA) was used. A stock solution of $FeCl_3$ was prepared and mixed into the agar to create final iron concentrations ranging from 0 μg/g to 240 μg/g wet weight. The $FeCl_3$ solution was added to the phantoms just above the melting temperature of the agar and allowed to slowly solidify to prevent $FeCl_3$ precipitation and to allow bubbles formed during mixing to come to the surface.

Relaxation Measurements and Statistical Analysis

For the phantom study, MR protocol results were loaded into the Chips2005 software (Children's Hospital Image Processing System, Cincinnati, OH) in IDL6.1 (Research Systems, Inc., Boulder, CO). T_2, T_2^* and T_1 parametric maps and relaxation rates were calculated from the corresponding data with a linear regression method. Regions of interest were selected with the Chips2005 software and statistically compared. For the T_2 maps, the first echo image was removed for the T_2 calculation to reduce the T_1 effect.

6.1.3. – Figures

Figure 6.1.3.1

T_2* measurement of the gray matter phantom doped with $FeCl_3$ to mimic physiological iron concentrations. A combination of 1.475% type A agar and 0.02% gadolinium DTPA created an ideal phantom, which precisely mimicked both T_1 and T_2 of human gray matter, with values of 109.8 ± 0.145ms for T_2 and 1333.5 ± 6.178ms.

T2* - Fe Gray Matter
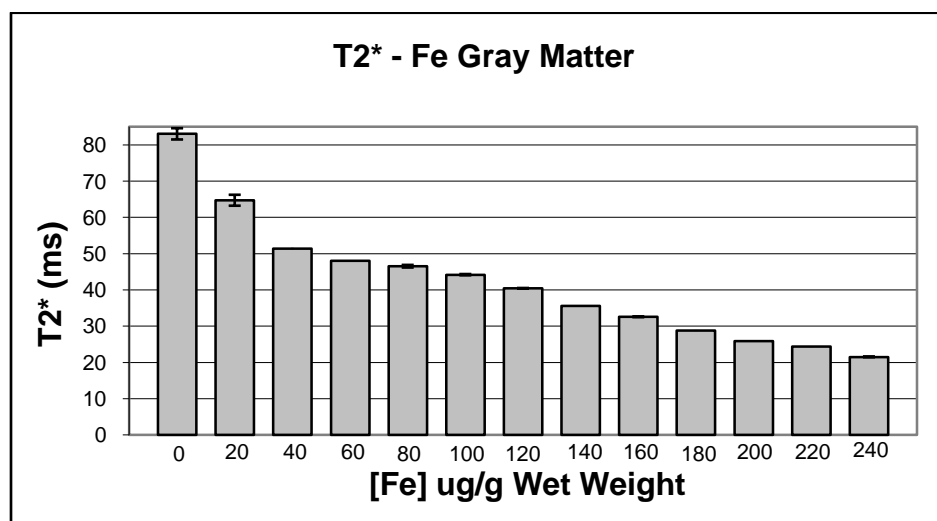
Figure 6.1.3.2

T_2* measurement of the white matter phantom doped with $FeCl_3$ to mimic physiological iron concentrations. It was determined that a phantom consisting of 2.20% type A agar and 0.041% gadolinium DTPA accurately reproduced both T_1 and T_2 relaxation values of human white matter, resulting in values of 79.5 ± 0.0975ms for T_2 and 833.9 ± 5.53ms for T_1.

T2Star - Fe White Matter
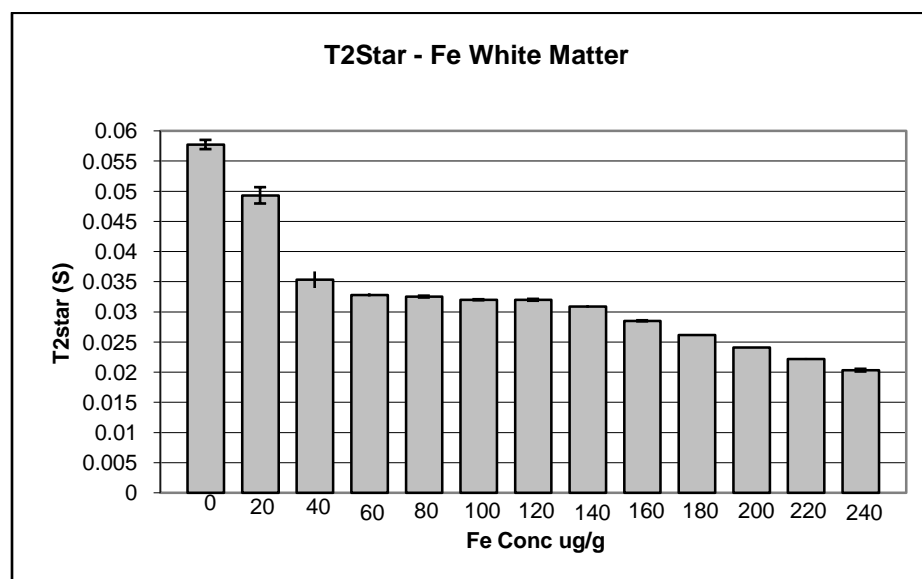
Figure 6.1.3.3

T_2^* parameter map of the iron loaded 37 ⁰C Gray Matter phantom. Higher iron

concentrations result in lower signal intensities and thus are darker on the map.
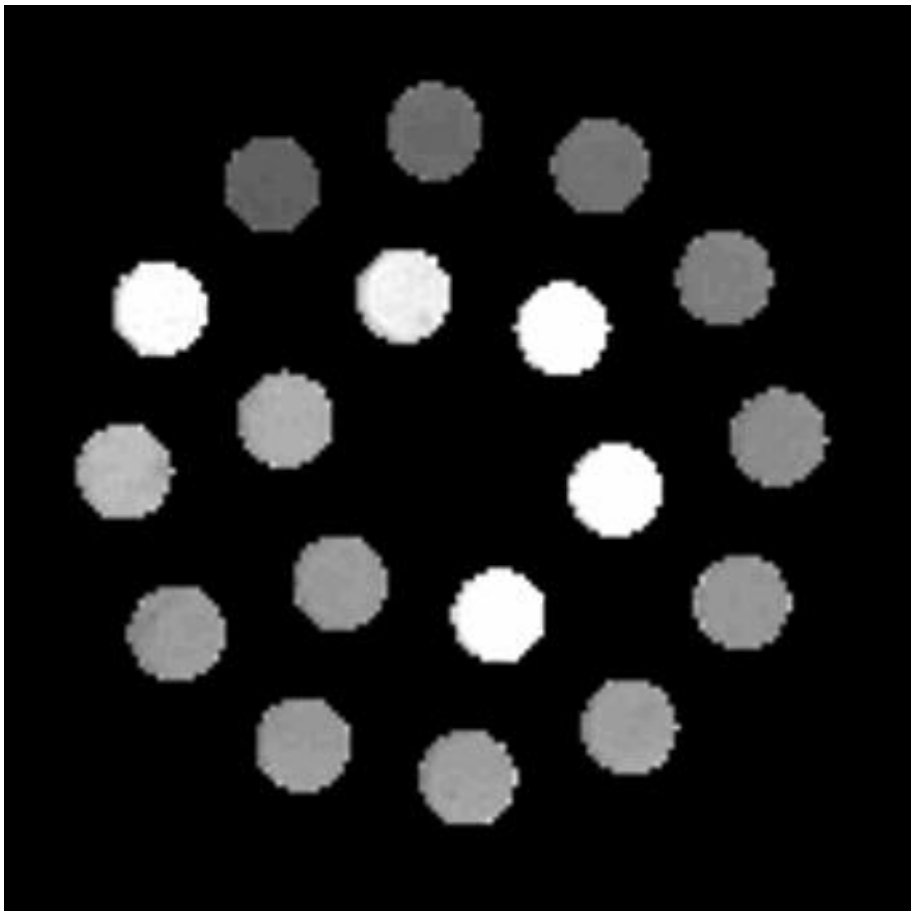
Figure 6.1.3.4

T_2* parameter map of a control mouse (A) and one fed the high iron diet for eight weeks (B). High iron regions show as dark hypo-intensities on the maps. R_2* relaxation rates for the caudate/putamen regions of interest are included. The two parameter maps were created using the same threshold values and are thus comparable for color/contrast.

R_2* = 15.98

R_2* = 17.21

A

B
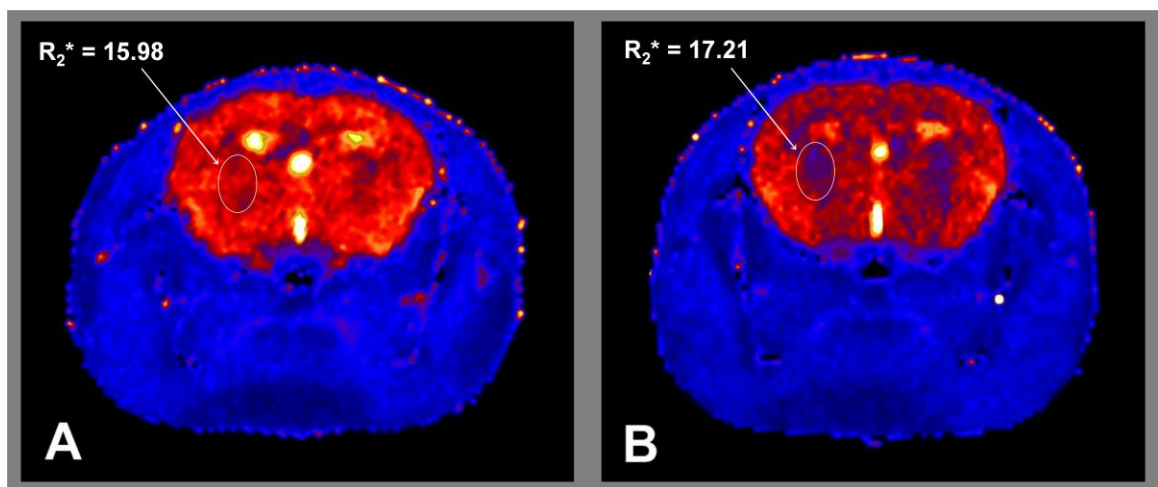
Figure 6.1.3.5

R_2^* relaxation rates for the caudate/putamen. Iron loading with the TMH-Ferrocene over the eight week course resulted in increases in R_2^* relaxation. The data is the average relaxation rate for the groups indicated with standard error bars.

Caudate/Putamen - R2* Measurement
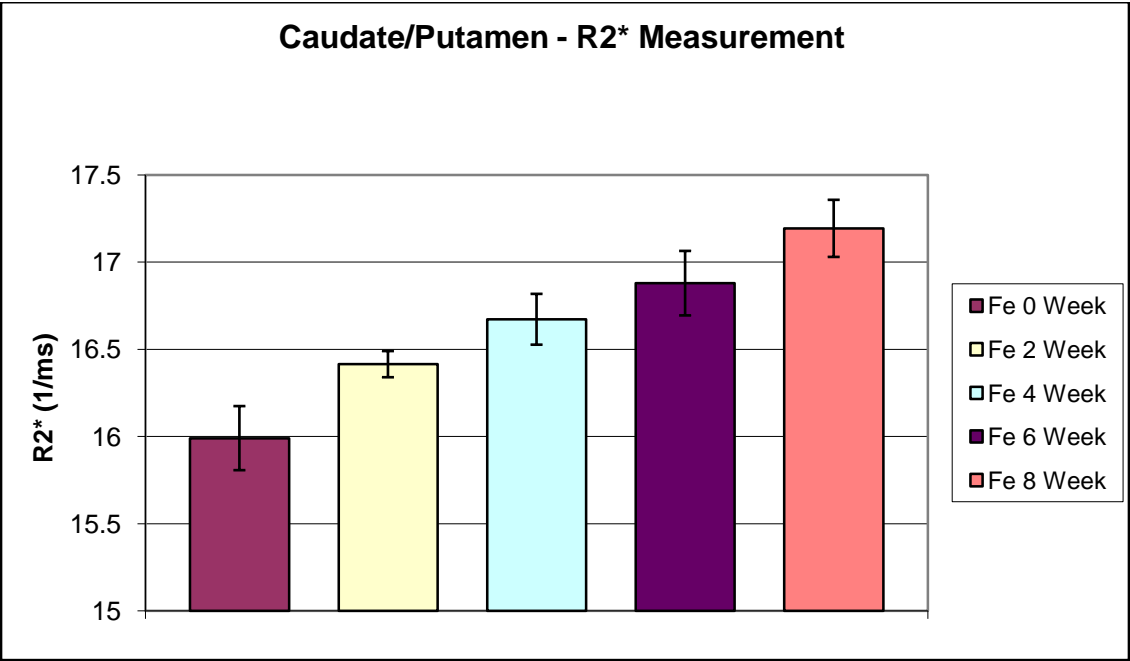
Figure 6.1.3.6

R_2^* relaxation verses iron concentration. The average R_2^* relaxation and iron concentration for the caudate/putamen are included from animals feed the high iron diet for 2 through 8 weeks. The average values have a high correlational coefficient for the dependence of R_2^* transverse relaxation on iron concentration.

R₂* Relaxation vs. Iron Concentration

$y = 4.6259x - 58.501$
$R^2 = 0.9717$

y-axis: **ug Fe / Wet Weight (g)**

x-axis: **R₂* (1/sec)**
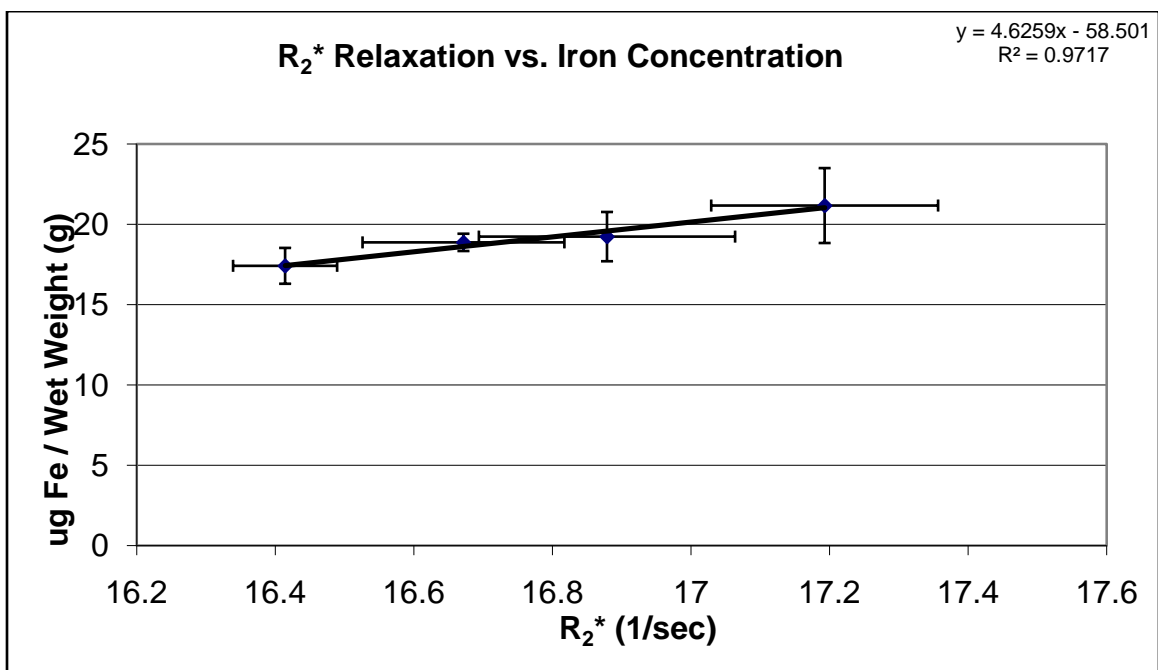
6.1.4. – Brief Discussion and Results

The creation of the phantoms in retrospect was a rather challenging task. The co-variation of both T_1 and T_2 relaxation with agar and gadolinium concentration required extensive testing of different concentrations of both substances. It originally was believed that gadolinium would affect T_1 relaxation while leaving T_2 relaxation relatively unchanged and conversely for agar concentration which was hoped to affect T_2 more profoundly then T_1. While this was generally true, it was found that both changed T_1 and T_2 substantially enough that they were co-variables in the consideration of overall effect on transverse and longitudinal relaxation. After careful experimentation along with trial and error, the concentrations of agar and gadolinium were found that approximated the white matter and gray matter relaxation values very accurately and reproducibly over different experiments. It was then realized that these values were obtained at room temperature, which was not congruent with the desire to create phantoms that approximated near *in vivo* conditions. To account for this, the phantoms were heated in a specially built chamber and retested at 37 °C. It was found, to no surprise, that the data no longer held as approximations of white and gray matter T_1 and T_2 relaxation. The phantoms were recalculated at physiological human temperature with new agar and gadolinium concentrations.

Doping of the white and gray matter phantom with iron proved to be very reproducible over multiple experiments. The data suggests that there is a nearly linear relationship between iron and transverse R_2* relaxation within the

physiological range of about 80 – 200 µg/g wet weight. R_2 and R_1 relaxation rates were found to not respond in a linear fashion to iron doping of the phantoms, suggesting that T_2* relaxation was the best option to measure and quantify iron with MR imaging technology (Figure 6.1.3.1 – 6.1.3.3). After careful consideration of the data, it was believed that there is an inherent drawback to the phantom data. Iron in the form of ferric chloride was used to dope the phantoms. This would represent iron in a free form within the brain while the majority of iron is found within the core of the ferritin complex. Transverse relaxation responds differently to the ferritin complex with its crystalline ferrihydrite core. Attempts were made to create a phantom that used variable amounts of iron loaded horse sleep ferritin along with specific concentrations of gadolinium and agar. The hope was to create a phantom that more accurately represented the iron milieu of the brain. The trek along this path was started but ultimately not concluded due to the considerable difficulty there was in including four variables (agar, gadolinium, ferritin and $FeCl_3$) in the calculation of each individual phantom. The existing phantom showed that T_2* relaxation was more sensitive than either T_1 or T_2 in measuring iron concentration with MRI.

Loading of the mice with the lipophilic iron compound TMH-Ferrocene proved to be moderately successful. The R_2* relaxation measurements for regions of interest largely proven unsuccessful and erratic; mostly due to difficulties in imaging cortical regions with the imaging protocol due to errant susceptibility artifacts caused by the air/tissue boundary in the ears. This was not the case for deep brain structures such as the caudate/putamen which were

generally free of artifacts and produced clear results of a linear increase in R_2* with iron loading time. Figure 6.1.3.4 shows T_2* parameter maps of two mice, one feed a normal iron diet and the other loaded with iron. The relaxation values for the caudate and putamen are seen in figure 6.1.3.5 which shows a nearly linear increase in R_2* relaxation in this region with differing iron loading times. Iron concentration measured with AAS proved to be difficult but the results were promising as far as reproducibility. There was some variability in the iron concentration data due mostly to the minute amounts of tissue present. Weighing and measuring iron concentrations in such small amounts of tissue can introduce some variability into the dataset, based on accuracy of the detection methods (spectrophotometer and scale). Even with these considerations; there is a high correlational coefficient between R_2* relaxation dependence upon iron concentration (Figure 6.1.3.6) for the caudate and putamen region of interest.

Overall the data here are evidence of the potential for quantitative magnetic resonance imaging to measure iron concentration is tissue. There is a limit to the range of the iron concentration that could be measured, as the relaxation largely plateaus or becomes statistically insignificant when a threshold of iron is imaged. These data was collected at a field strength of 3.0 T, which is currently found in many clinical scanners worldwide. It was hoped that a calibration curve would be produced to accurately quantify iron concentration based on R_2* relaxation rate. The data show there this has promise but clearly further study would have to be undertaken in a human system. It is inherently

difficult to create an accurate calibration curve with a phantom system or a

mouse model to be used within human clinical imaging.

Histological Staining Techniques

7.2 – Histological Staining Techniques

The mechanism of action of the various histological staining techniques used throughout this work are described in detail, along with staining procedures for each.

7.2.1 – Thioflavin-S

Thioflavin can refer to either of two benzothiazole salt dyes used for fluorescent histology staining. The two derivatives are known as Thioflavin T (Figure 7.2.1.1) and Thioflavin S (Figure 7.2.1.2). Thioflavin T is obtained by the methylation of dehydrothiotoluidine with methanol in the presence of hydrochloric acid. Thioflavin T is made from the methylation and sulponation of dehydrothiotoluidine with methanol and sulfonic acid (203). Thioflavin S synthesis results in a mixture of planar asymmetric dyes with charged groups at the end of the molecule. They are believed to interact with the crossed β-sheet structure that is common to amyloid plaques. The component β-strands that make of the β-sheets have alternating side chains that when stacked upon one another form channels that run along sheet perpendicular to the strands (Figure 7.2.1.3). Binding studies suggest that the thioflavins bind to the amyloid fibers in these channels. The molecular axis of the thioflavin lies parallel to the amyloid fiber surrounded by charged side chains (287). The elongated planar molecular

structure and negative charge at the ends of thioflavin S allow it to form multiple bonds with numerous side chains along the channel giving it a particularly high affinity for amyloid fibers that have a β-sheet conformation (42,203,288,289). The dyes will both bind to fibrillar strands of beta-amyloid that are composed of protein strands that are 28, 40 and 42 amino-acids long (Figure 7.2.1.4). The charged side chain region of the amyloid peptide resides in the first 28 amino acids. In addition, a change in pH of the aggregation solution outside physiological boundaries and thus conformational changes in protein structure and amino-acid charges cause a reduction in thioflavin binding. This suggests that both bind due to the multiple charges found on the side chains of the amino-acids and not due to hydrophobic amino-acid interaction (288). Thioflavin S fluorescence is stimulated by excitation at 385 nm and emits at 482 nm, allowing the usage of standard FITC filter cubes for microscopy. The emission spectra for thioflavin S is unchanged from that of the dye in a free solution. Thioflavin T in contrast undergoes an excitation spectra change when in the presence of aggregated Aβ with a peak shift towards 450 nm. This suggests that thioflavin T undergoes a slight conformational change when bound to the parallel axis channels. Thioflavin T thus has less background fluorescence than thioflavin S due to this shift in emission from the native dye and is used for the quantification of fibrillar amyloid in solutions due to this. The additional binding characteristics of thioflavin S make it ideal for usage in histological staining and imaging of beta-amyloid plaques due to its resistance to wash out of the channels during staining, but it cannot be used for quantification of fibrillar amyloid formation in solution.

Of considerable interest to this research project is the fact that thioflavin S and T will not bind to amyloid amino acid monomers while they will bind to longer oligomeric species. This is understandable considering that the dyes bind to the channel regions of the long fibrillar Aβ strands. This holds true for diffuse verses fibrillar Aβ species also. Thioflavin will favorably bind to fibrillar Aβ plaques but binds poorly to diffuse plaque formations.

Figure 7.2.1.1

The molecular structure of thioflavin-T; a benzothiazole salt obtained by the methylation of dehydrothiotoluidine with methanol in the presence of hydrochloric acid.
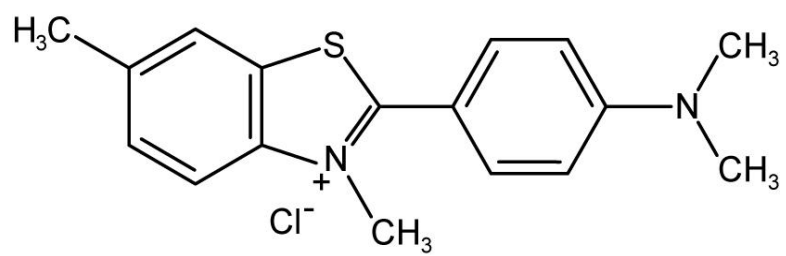
Figure 7.2.1.2

The molecular structure of thioflavine S; a benzothiazole salt obtained by the methylation of dehydrothiotoluidine with methanol in the presence of sulfonic acid. The structural formula for thioflavin S can be altered from a tri-ring structure, like that of thioflavine T, to contain five or seven rings.
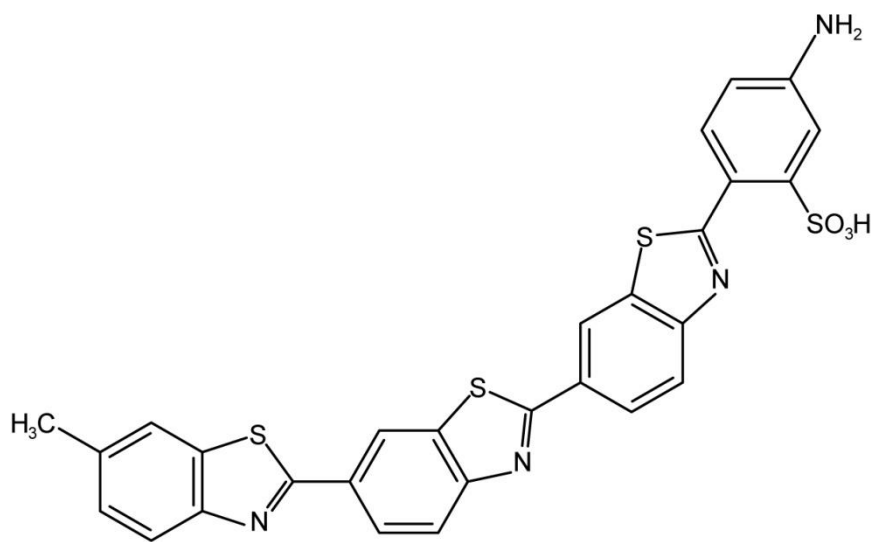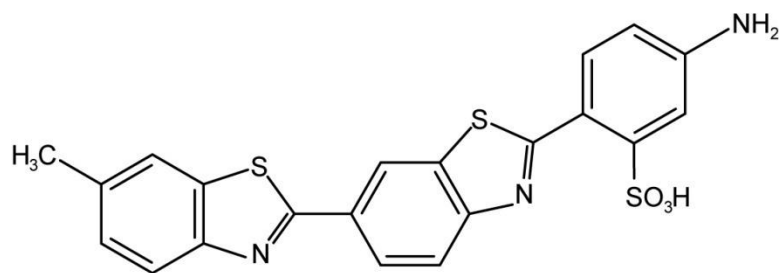
Figure 7.2.1.3

Thioflavin-T and diagram of a β-sheet. (A) Structure of thioflavin-T. The molecule is 4.3 ± 0.1 Å thick. (B) A schematic representation of a β-sheet (290). Indicated are the backbone atoms (N, C, and Ca) and the side chain (R) for one residue. No hydrogen bonds are indicated and this scheme is valid for both parallel and anti-parallel sheets. If part of a fibril, the long axis of the fibrils would be perpendicular to the surface of this page. One of the binding channels is indicated with a double headed arrow. It is thought thioflavin-T binds with its long axis parallel to the long axis of this arrow. In a fibril it is likely only one of the faces of the sheet would be accessible from the solvent. (C) Schematic representation of a protofilament with, arbitrarily, three β-sheets. Individual β-strands are shown by 'zig-zag' lines in black, dark and light grey. Sidechains accessible from the solvent are shown as black circles and point out of the plane of the paper. Note that sidechains on the third, light grey, β-sheet are also accessible from the solvent and point below the plane of the paper (not shown for clarity). Dye molecules are represented by double headed arrows. When several protofilaments form a fibril, some of these surfaces will be obscured, resulting in impeded dye binding in those areas. (Figure and figure text from Krebs, 2005 (287))

A

6.1±0.1 Å

15.2±0.1 Å

B

R

C
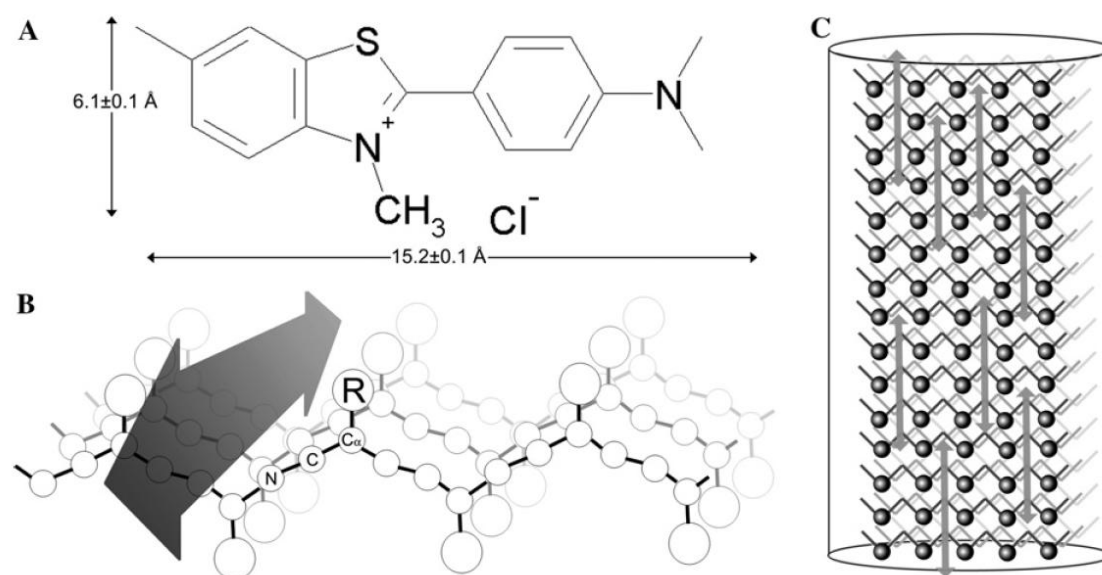
Figure 7.2.1.4

Amino Acid sequence of Human Beta-Amyloid 1-40 and 1-42 with expected

charges on AA's at pH 6.

$$\overset{-}{}\overset{-}{}\overset{+}{}\overset{+}{}\overset{-}{}\overset{}{}\overset{-}{}\overset{+}{}\overset{+}{}\overset{+}{}\overset{--}{}\overset{+}{}$$

DAEFRHDSGYEVHHQKLVFFAEDVGSNKGAIIGLMVGGVVIA

├──────────────── β(1-40) ────────────────┤
├──────────────── β(1-42) ──────────────────┤

7.2.1.1 – Thioflavin-S staining procedure

Staining procedure is adapted from traditional thioflavin S staining procedures and is as follows:

1. The tissue sections are brought to up to dH_2O

2. The sections were stained with 1% Thioflavin-S aqueous solution for 5 minutes.

3. Differentiated in 70% ethanol for 5 minutes with slight agitation throughout.

4. Two final five minute dH_2O rinses.

5. For aqueous mounting: Mount with FluorSave Aqueous mounting medium and coverslip.

   For dehydrated mounting: Dehydrated mounting of Thioflavin S stained tissue sections is not possible. This is because the ethanol and xylene completely leech the Thioflavin S from the section.

The 1% Thioflavin S solution is mixed with dH_2O and allowed to mix completely with a vortex. A slight residual amount of insoluble material is left which can be filtered through a syringe attachment.

7.2.2 – Perl's Stain for Iron

Perl's stain is a highly sensitive and widely used classic metallic-staining method to demonstrate ferric iron (Fe^{+3}) found in tissue samples. Dilute mineral acid hydrolysis with dilute hydrochloric acid releases ferric ions from protein bound tissue deposits. These ions then react with (potassium) ferrocyanide ions

(potassium hexacyanoferrate) to produce a dark blue colored and highly water-insoluble complex known as Prussian blue or chemically as ferric ferrocyanide (ferric hexacyanoferrate) (291).

It has generally been considered that the Prussian blue reaction only reacts with ferric (Fe^{+3}) iron, but there is some speculation that it also reacts with ferrous (Fe^{+2}) iron as well but to a lesser degree (200,292). The Prussian blue reaction of potassium ferrocyanide with ferric iron (Fe^{+3}) to create ferric ferrocyanide (Prussian blue)(ferric hexacyanoferrate) is shown in equation 1 below. Utilizing a 3,3' - diaminobenzidine (DAB) (3,3',4,4'-Tetraamino-diphenyl) (Figure 7.2.2.1) enhanced method of the Perl's stain helps to visualize trace amounts of iron in tissue samples (293). DAB acts as a chromogen dye as ferric ferrocyanide catalyzes the oxidation of benzidine to a polymer by hydrogen peroxide, which gives the brown colored precipitate. The insoluble precipitate may range in color from a light golden brown to dark brown depending upon the amount of catalyst present. The brown precipitate is collectively known as benzidine brown and is composed of many potential stereo-isomer configurations of an azopolymer like that in figure 7.2.2.2 (294). Care must be taken not to allow tissue samples to reside in non-buffered formalin solutions as an acidic environment will leech iron out of tissue into the liquid. Using ~7.3 pH buffered para-formaldehyde or reducing the fixation time is recommended. The acidic nature of the Perl's stain itself also can leech iron out of the tissue samples if the concentration of the hydrochloric acid is too great or the time in solution in too

long. DAB is a suspected carcinogenic agent as its basic benzidine core is

linked to bladder cancer and pancreatic cancer.

The Prussian blue reaction of potassium ferrocyanide with ferric iron (Fe^{+3})

to create ferric ferrocyanide (Prussian blue) in an acidic environment is shown

below:

$$4 \ FeCl_3 + 3 \ K_4Fe(CN)_6 \ \rightarrow \ Fe_4[Fe(CN)_6]_3 + 12 \ KCl$$
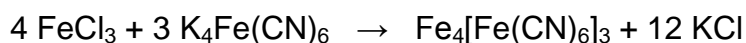
The oxidation of DAB with H_2O_2 in the presence of ferric ferrocyanide is

shown below:

(1) $2 \ Fe(CN)_6^{-4} + H_2O_2 \ \rightarrow \ 2 \ Fe(CN)_6^{-3} + 2 \ OH^{-1}$

(2) $Fe(CN)_6^{-3} + OH^{-1} + DAB \ \rightarrow \ Fe(CN)_6^{-4} + $ Oxidized DAB (benzidine

brown)
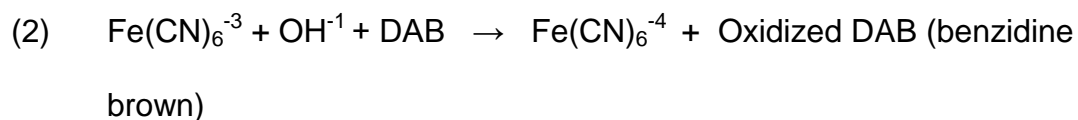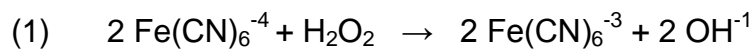
Figure 7.2.2.1

Molecular structure of 3,3'-diaminobenzidine (DAB) (3,3',4,4'-Tetraamino-

diphenyl)
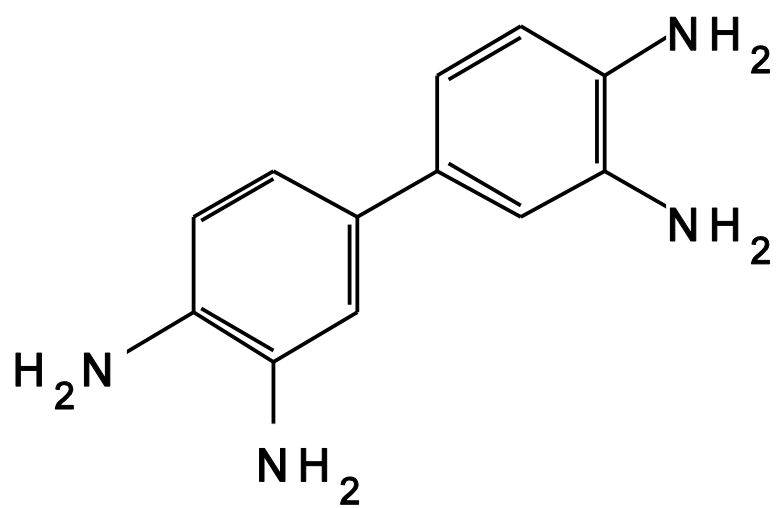
Figure 7.2.2.2

Representative stick bond molecular structure of potential bonding seen in the polymerization of DAB into the water insoluble precipitate benzidine brown. There are any number of possible polymers formed as each amine group can form a double bond to a neighboring amino group (X).

283
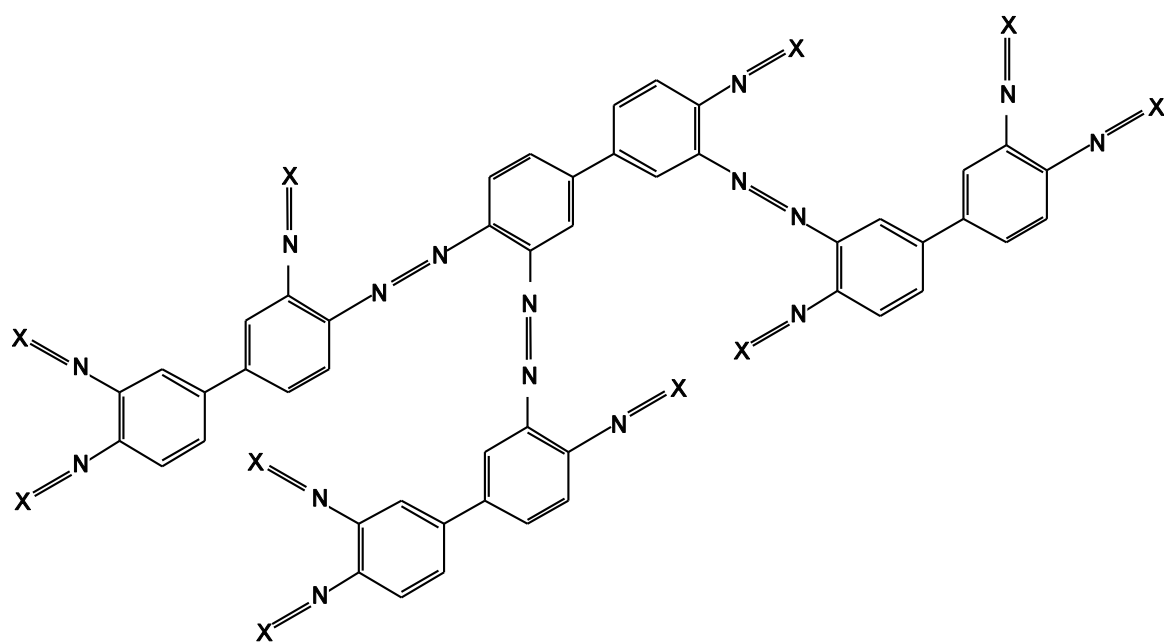
7.2.2.1 – Traditional Perl's Stain Procedure

The basic Perl's stain procedure for sliced tissue (10 – 60 µm) is as follows:

1. Fix tissue in 4% Paraformadehyde for 10 minutes to complete fixation.

2. Tissue must be hydrated in dH_2O to leech out residual formalin in the samples for at least 5 minutes.

3. Place the samples in solution of 2% Hydrochloric Acid and 2% Potassium Ferrocyanide for 30 minutes.

4. Rinse in dH_2O for 5 minutes.

5. Immerse in diaminobenzidine / H_2O_2 solution for 2 – 4 minutes.

6. Rinse twice in dH_2O for 5 minutes each.

7. For aqueous mounting: Mount with FluorSave Aqueous mounting medium and coverslip.

   For dehydrated mounting: Dehydrate in ethanol gradient, 95%, 100% x2 for 5 minutes each, followed by 100% xylene for 5 minutes twice. Mount with Cytoseal 60 mounting medium and coverslip.

Necessary chemicals and preparation for stain:

2% Hydrochloric Acid and 2% Potassium Ferrocyanide:

Consists of 100ml of 4% Hydrochloric Acid and 100 ml of 4% Potassium Ferrocyanide made separately until mixed together just prior to staining. It is recommended to us H_2O that is relatively free of iron contamination and using

well washed glassware, possibly washed with nitric acid to eliminate all trace iron.

3,3'-diaminobenzidine (DAB)

Twenty ml final volume consists of 13.33 mg DAB (Sigma-Aldrich, D5637) + 20 ml PBS, when ready to use mix in 16 µl of 30% H_2O_2. Care must be taken when staining and disposing of product as it is carcinogenic. Dispose of product with sodium hypochlorite (bleach)

7.2.2.2 – Modified Perl's Stain with Proteinase K

Modified Perl's Stain Procedure

The stain was adapted and modified from LeVine (188,189) and employs the usage of proteinase K and detergents to break down the periphery of the plaques forming openings in the highly hydrophobic amyloid plaques. This allows the aqueous Perl's stain to infiltrate into the amyloid mass and is sensitive enough to detect trace amounts of iron in the Aβ plaques.

The staining method consists of the following procedure.

1. Tissue sections were hydrated in PBS for 15 minutes
2. Immersion in sodium borohydride (10 mg/ml PBS, # 213462, Sigma, St. Louis, MO) for 30 minutes.
3. rinsed in PBS twice for five minutes

4. then immersed in proteinase K (30 µg/ml, # P6556, Sigma, St. Louis, MO) and 0.01% Triton X-100 in PBS for 20 minutes.

5. sections were then placed in a solution of 1% hydrochloric acid, 1% potassium ferrocyanide and 1% Triton X-100 in distilled water for 30 minutes.

6. Amplification of the iron staining was accomplished with 0.5 mg/ml 3,3'-diaminobenzidine tetrahydrochloride (DAB) and 2µl/ml of 30% hydrogen peroxide in pH 7.6 0.05 M Tris HCl for 15 minutes.

7. Rinse twice for 5 minutes in dH_2O.

8. For aqueous mounting: Mount with FluorSave Aqueous mounting medium and coverslip.

For dehydrated mounting: Dehydrate in ethanol gradient, 95%, 100% x2 for 5 minutes each, followed by 100% xylene for 5 minutes twice. Mount with Cytoseal 60 mounting medium and coverslip.

7.2.3 – Thioflavin S and Perl's co-staining.

Traditionally, individual stains for ferric iron and beta-amyloid plaques would be carried out on sequential slices of tissue samples and compared to one another. It was found necessary to develop a co-staining technique that allowed both Perl's staining and thioflavin S staining on the same tissue piece. This was required because it permitted the imaging of a piece of tissue with the MR system and subsequent co-staining, which has proved to be essential for this study. The procedure follows sequentially through the Perl's stain then proceeds

to the thioflavin-S stain, both procedures are outlined above. To test for any confounding variables that occurred during the co-staining method, tissue samples were stained with the Perl's and thioflaivin-S methods alone and compared to the co-stained tissue. The procedures used during the thioflavin-S staining do not alter the Perl's results, as the Prussian blue reactant and DAB precipitate are not soluble in the aqueous or ethanol based solutions used in the thioflavin-S stain.

7.2.4 – Antibody Staining

The basic principle behind immunohistochemistry is the usage of specific antibodies to localize antigens in tissue through antigen-antibody interactions. Its usage is advantageous because it involves very specific primary antibody-antigen binding, and thus allows the staining of specific antigens that are restricted to one type of protein or cell for instance. With the usage of this technique with fluorescent secondary antibodies multiple stains for different antigens is possible. Various immunohistochemistry techniques have become a widely used with the medical research community and have become vital in numerous scientific discoveries.

The selection of primary and secondary antibodies is critical to successful staining of tissue samples. Primary antibodies must be chosen for a target antigen and able to bind with selective specificity. Different antibodies are raised in different host systems, and selection of the host system is important for secondary antibody specificity for the primary antigen. For multiple staining

techniques, primary antibodies should be chosen from two (or more, depending on the total number of co-stains) host systems such that the secondary antibodies will be specific for the host system used. Fluorescent secondary antibodies should not only be chosen for a specific house match to the primary antibody, but also must be chosen to fluoresce under a different wavelength (color) such that they can each individually be viewed under the microscope at their respective wavelengths. Other important considerations are the blocking of tissue samples and antigen retrieval. To allow the specific binding of the primary and secondary antibodies to their targets, the tissue must be washed in a mixture of protein wash. This allows the selective binding of the primary and secondary antibody due do to the extremely high binding affinity of these antibodies to their antigen targets, they essentially outcompete other proteins for these target sites. The majority of tissue samples stained with these methods are fixed prior to staining which creates cross-links between and within proteins. In order to have the antibodies bind specific proteins that have been cross-linked, proteins must have these cross-links broken to open up their binding sites. This can be done in a variety of ways, with the two most popular methods being heat induced epitope retrieval and proteolytic induced epitope retrieval. Heat induced retrieval literally heats the tissue sample up to break the cross-links, which the proteolytic approach uses enzyme digestion.

7.2.4.1 – Antibody Staining Techniques

The immunohistochemistry staining technique used in these studies is as follows:

1. Warm slides with tissue sample on them at 50 °C to help bind fatty tissue to the slides, place slides in slide holder.

2. Place slides in 95 °C citrate buffer for 15 minutes (heat induced epitope retrieval).

3. Rinse slides three times in PBS for five minutes each.

4. Use a hydrophobic barrier pen (PAP pen) to create individual wells around each tissue sample.

5. Incubate tissue with 1% bovine serum albumen (BSA) (A9430, Sigma Aldrich, St. Louis, Mo). in PBS-Tween (PBST) for 30 minutes to block unspecific binding of antibodies.

6. Decant the blocking mixture, and incubate tissue with the mixture of properly diluted primary and secondary antibodies in 1% BSA in PBST overnight at room temperature.

7. Decant mixture, and rinse with PBS three times for five minutes each.

8. Incubate tissue with the mixture of fluorescent antibodies in 1% BSA for at least one hour at room temperature. This must be done in the dark.

9. Decant mixture and rinse three times with PBS for five minutes each.

10. Mount tissue with an anti-fade fluorescent mounting media and coverslip.

The solutions used in these stains are as follows:

Phosphate Buffered Saline with Tween:
Mixture of PBS with 0.1% Tween 20x (P1379 Sigma Aldrich, St. Louis, Mo).

Citrate buffer 10mM:

1.92g / l of Sodium citrate tribasic dehydrate (C7254 Sigma Aldrich, St. Louis, Mo) in dH$_2$O. Adjust pH to 6.0.

7.2.5 – Fluoro-Jade C

Fluoro-Jade C (FJC) is a poly-anionic fluorescein derivative whose exact molecular formula and chemical structure currently remains to be elucidated. Being a derivation of the basic fluorescein molecule, Fluoro-Jade C must have at least some similarity to the known structures of fluorescein (Figure 7.2.5.1) and Fluorescein isothiocyanate (FITC) (Figure 7.2.5.2). Recently, the compound has been reported as useful for detecting neuronal specific degeneration in brain slices (295). Based on the fact that Fluoro-Jade C is a known anionic compound, it is speculated that the biochemical molecules that the compound binds to would include molecules with multiple positive charges on them. There is some evidence that molecules with a strong electrostatic attraction to Fluoro-Jade –C include spermidine, putrescine, and cadaverine (296,297). Putrescine and cadaverine are both organic chemical compounds consisting of four (putrescine) or five (cadaverine) carbon atom chains with amine groups at the first and last carbons. Both molecules are produced as a result of the breakdown of amino acids in living cells. Spermidine is a similar polybasic amine with an amine group situated between three and four carbon chains with amine at the terminal ends. Although it has not been resolved what exactly FJC binds to or its mode of

biochemical action, it is known that it binds to (believed to be intracellular) and

thus detects dead neurons regardless of the cause of death.

Figure 7.2.5.1

Molecular structure of fluorescein, a fluorophore commonly used in microscopy. Fluorescein dissolved in water has an absorption maximum at 494 nm and emission maximum of 521 nm. Fluoro-Jade C has an emission peak at 450nm and excitation at 530 nm.
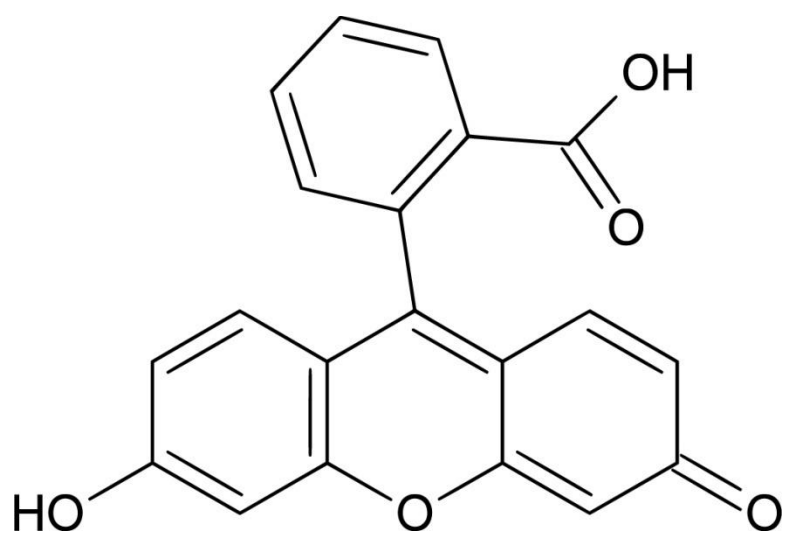
Figure 7.2.5.2

Molecular structure of fluorescein isothiocyanate (FITC). The molecular structure

of FITC used the original fluorescein molecule as a backbone with a different

isothiocyanate functional group (-N=C=S), replacing a hydrogen atom.

295
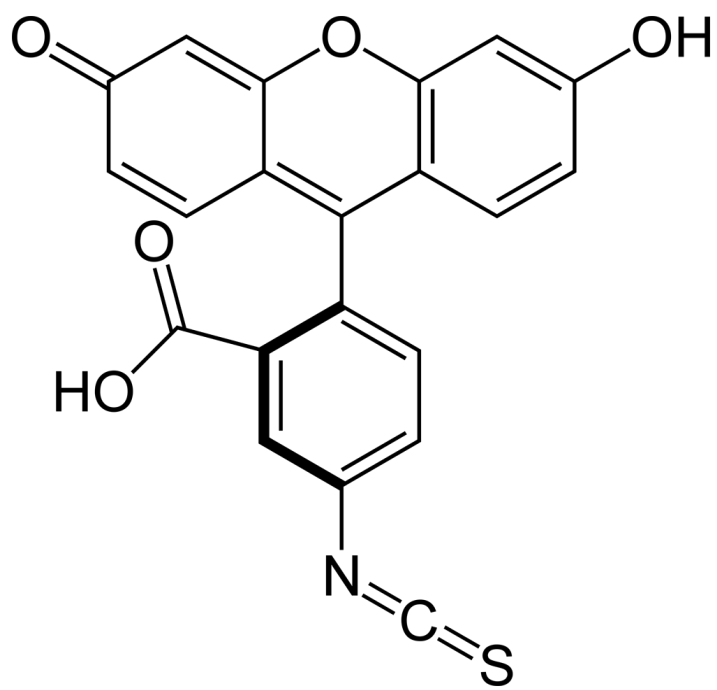
7.2.5.1 Fluoro-Jade C Staining Procedure

Basic Tissue Preparation:

Tissue samples were fixed with 4% paraformaldehyde and cryogenically protected with a gradient of sucrose solutions up to 30% sucrose in distilled water. Tissue samples were frozen at -18 °C and cut at a thickness of 16 µm with a cryostat. Cut samples were thawed on slides double coated with gelatin and poly-lysine and stored at -80 °C until usage. The following procedure was adapted from the manufacture's (Chemicon International) instructions:

1. If co-staining with an antibody stain (fluorescent or otherwise), follow normal antibody procedure until after the secondary antibody ready to be discarded from the slides.

2. Rinse the slides twice for five minutes each in PBS.

3. Slides were dried for 30 minutes at 50°C.

4. Rinse the slides for two minutes in distilled water.

5. Immerse the slides in 0.06% Potassium Permanganate for ten minutes.

6. Rinse the slides for two minutes in distilled water.

7. Immerse the slides in the working 0.0001% Fluoro-Jade C solution for ten minutes.

8. Rinse the slides three times for one minutes each.

9. Air dehydrate the slides for 30 minutes at 50°C.

10. Immerse the slides in xylene twice for five minutes each.

11. Mount with cytoseal, or another xylene based mounting media, and coverslip.

Necessary chemicals and preparation for stain:

Fluoro-Jade C stock solution consists of 0.01% in distilled water. The working Fluoro-Jade C solution is made by the addition of 1ml of stock solution in 99 ml of 0.1% acetic acid vehicle.

Potassium Permanganate solution is made is distilled water to a final concentration of 0.06%.

7.2.6 – Transmission Electron Microscopy Procedure

A. Fixation

Fixative used for EM is 2% paraformaldehyde and 2% gluteraldehyde in 1x PBS

1. Harvest the tissue as quickly as possible and place it in cold fixative. Ideal size of tissue pieces is 1mm cubed.

2. Fix the tissue for 2 hours in cold fixative on ice.

3. Rinse with cold PBS on ice three times for 10 minutes each.

4. Fix the tissue in 1% PBS buffered osmium tetroxide overnight in the refrigerator.

5. Rinse with cold PBS on ice three times for 10 minutes each.

B. Dehydration

1. 50% ethanol for 15 minutes.

2. 70% ethanol for 30 minutes.

3. 90% ethanol for 15 minutes.

4. 95% ethanol for 15 minutes.

5. 95% ethanol for 15 minutes.

6. 100% ethanol for 30 minutes.

7. 100% ethanol for 30 minutes.

8. 100% ethanol for 30 minutes.

9. 100% propylene oxide for 30 minutes.

10. 100% propylene oxide for 30 minutes.

C. Embedding

Embedding resin is composed of 10ml Embed 812, 8ml Dodecenyl Succinic

Anhydride (DDSA), 4ml Methyl-5-Norbornene-2,3-Dicarboxylic Anhydride (NMA)

and 0.35ml 2,4,6-Tri(dimethylaminomethyl) phenol (DMP-30). Any volume made

with these volumetric ratios is sufficient. All chemicals can be purchased as a kit

from Electron Microscopy Sciences (#14120 - EMbed-812 Kit, EMS, Hatfield,

PA).

1. Propylene oxide : resin (2:1, volume/volume) for 1 hour.

2. Propylene oxide : resin (1:1, volume/volume) for 1 hour.

3. Propylene oxide : resin (1:2, volume/volume) for 1 hour.

4. 100% resin for two hours.

5. 100% resin for two hours.

6. 100% resin overnight.

7. Place specimens in molds, pour fresh vacuumed resin over them and place them in a vacuum chamber for 2 hours.

8. Place molds in 60°C oven overnight to cure resin.

D. TEM Tissue Preparation

1. Cut tissue from hardened resin with a jeweler's saw and mount onto chuck.

2. Cut tissue at 90nm with a diamond knife on an ultra-microtome.

3. Float slices on dH_2O and place them on 200 mesh copper grids.

4. Stain with 2% aqueous uranyl acetate for 10 minutes.

5. Stain with Reynolds lead citrate for 5 minutes.

6. Rinse with dH_2O and dry sections prior to TEM imaging.

BIBLIOGRAPHY

1.   Terry RD, Masliah E, Salmon DP, Butters N, DeTeresa R, Hill R, Hansen LA, Katzman R. Physical basis of cognitive alterations in Alzheimer's disease: synapse loss is the major correlate of cognitive impairment. Ann Neurol 1991;30(4):572-580.

2.   Evans DA, Funkenstein HH, Albert MS, Scherr PA, Cook NR, Chown MJ, Hebert LE, Hennekens CH, Taylor JO. Prevalence of Alzheimer's disease in a community population of older persons. Higher than previously reported. JAMA 1989;262(18):2551-2556.

3.   Alzheimer A, Stelzmann RA, Schnitzlein HN, Murtagh FR. An English translation of Alzheimer's 1907 paper, "Uber eine eigenartige Erkankung der Hirnrinde". Clin Anat 1995;8(6):429-431.

4.   Braak H, Braak E. Frequency of stages of Alzheimer-related lesions in different age categories. Neurobiol Aging 1997;18(4):351-357.

5.   Thinakaran G. The role of presenilins in Alzheimer's disease. J Clin Invest 1999;104(10):1321-1327.

6.   Marzolo MP, Bu G. Lipoprotein receptors and cholesterol in APP trafficking and proteolytic processing, implications for Alzheimer's disease. Semin Cell Dev Biol 2008.

7.   Priller C, Bauer T, Mitteregger G, Krebs B, Kretzschmar HA, Herms J. Synapse formation and function is modulated by the amyloid precursor protein. J Neurosci 2006;26(27):7212-7221.

8.   Phinney AL, Calhoun ME, Wolfer DP, Lipp HP, Zheng H, Jucker M. No hippocampal neuron or synaptic bouton loss in learning-impaired aged beta-amyloid precursor protein-null mice. Neuroscience 1999;90(4):1207-1216.

9.   Zheng H, Koo EH. The amyloid precursor protein: beyond amyloid. Mol Neurodegener 2006;1:5.

10.   Czech C, Tremp G, Pradier L. Presenilins and Alzheimer's disease: biological functions and pathogenic mechanisms. Prog Neurobiol 2000;60(4):363-384.

11.   Yoshikai S, Sasaki H, Doh-ura K, Furuya H, Sakaki Y. Genomic organization of the human amyloid beta-protein precursor gene. Gene 1990;87(2):257-263.

12.   Haass C, Lemere CA, Capell A, Citron M, Seubert P, Schenk D, Lannfelt L, Selkoe DJ. The Swedish mutation causes early-onset Alzheimer's disease by beta-secretase cleavage within the secretory pathway. Nat Med 1995;1(12):1291-1296.

13.   Octave JN, Essalmani R, Tasiaux B, Menager J, Czech C, Mercken L. The role of presenilin-1 in the gamma-secretase cleavage of the amyloid

precursor protein of Alzheimer's disease. J Biol Chem 2000;275(3):1525-1528.

14. Ponting CP, Hutton M, Nyborg A, Baker M, Jansen K, Golde TE. Identification of a novel family of presenilin homologues. Hum Mol Genet 2002;11(9):1037-1044.

15. Smialowska A, Baumeister R. Presenilin function in Caenorhabditis elegans. Neurodegener Dis 2006;3(4-5):227-232.

16. Bentahir M, Nyabi O, Verhamme J, Tolia A, Horre K, Wiltfang J, Esselmann H, De Strooper B. Presenilin clinical mutations can affect gamma-secretase activity by different mechanisms. J Neurochem 2006;96(3):732-742.

17. Citron M, Westaway D, Xia W, Carlson G, Diehl T, Levesque G, Johnson-Wood K, Lee M, Seubert P, Davis A, Kholodenko D, Motter R, Sherrington R, Perry B, Yao H, Strome R, Lieberburg I, Rommens J, Kim S, Schenk D, Fraser P, St George Hyslop P, Selkoe DJ. Mutant presenilins of Alzheimer's disease increase production of 42-residue amyloid beta-protein in both transfected cells and transgenic mice. Nat Med 1997;3(1):67-72.

18. Esler WP, Kimberly WT, Ostaszewski BL, Ye W, Diehl TS, Selkoe DJ, Wolfe MS. Activity-dependent isolation of the presenilin- gamma -secretase complex reveals nicastrin and a gamma substrate. Proc Natl Acad Sci U S A 2002;99(5):2720-2725.

19. Raber J, Huang Y, Ashford JW. ApoE genotype accounts for the vast majority of AD risk and AD pathology. Neurobiol Aging 2004;25(5):641-650.

20. Holtzman DM, Bales KR, Tenkova T, Fagan AM, Parsadanian M, Sartorius LJ, Mackey B, Olney J, McKeel D, Wozniak D, Paul SM. Apolipoprotein E isoform-dependent amyloid deposition and neuritic degeneration in a mouse model of Alzheimer's disease. Proc Natl Acad Sci U S A 2000;97(6):2892-2897.

21. Carter DB. The interaction of amyloid-beta with ApoE. Subcell Biochem 2005;38:255-272.

22. Jiang Q, Lee CY, Mandrekar S, Wilkinson B, Cramer P, Zelcer N, Mann K, Lamb B, Willson TM, Collins JL, Richardson JC, Smith JD, Comery TA, Riddell D, Holtzman DM, Tontonoz P, Landreth GE. ApoE promotes the proteolytic degradation of Abeta. Neuron 2008;58(5):681-693.

23. Hirsch-Reinshagen V, Burgess BL, Wellington CL. Why lipids are important for Alzheimer disease? Mol Cell Biochem 2008.

24. Deane R, Sagare A, Hamm K, Parisi M, Lane S, Finn MB, Holtzman DM, Zlokovic BV. apoE isoform-specific disruption of amyloid beta peptide clearance from mouse brain. J Clin Invest 2008;118(12):4002-4013.

25. Thal DR, Capetillo-Zarate E, Schultz C, Rub U, Saido TC, Yamaguchi H, Haass C, Griffin WS, Del Tredici K, Braak H, Ghebremedhin E. Apolipoprotein E co-localizes with newly formed amyloid beta-protein (Abeta) deposits lacking immunoreactivity against N-terminal epitopes of

Abeta in a genotype-dependent manner. Acta Neuropathol 2005;110(5):459-471.

26. Tamamizu-Kato S, Cohen JK, Drake CB, Kosaraju MG, Drury J, Narayanaswami V. Interaction with amyloid beta peptide compromises the lipid binding function of apolipoprotein E. Biochemistry 2008;47(18):5225-5234.

27. Lashuel HA, Lansbury PT, Jr. Are amyloid diseases caused by protein aggregates that mimic bacterial pore-forming toxins? Q Rev Biophys 2006;39(2):167-201.

28. Stefani M, Dobson CM. Protein aggregation and aggregate toxicity: new insights into protein folding, misfolding diseases and biological evolution. J Mol Med 2003;81(11):678-699.

29. Dobson CM. Protein misfolding, evolution and disease. Trends Biochem Sci 1999;24(9):329-332.

30. De Strooper B, Annaert W. Proteolytic processing and cell biological functions of the amyloid precursor protein. J Cell Sci 2000;113 (Pt 11):1857-1870.

31. Turner PR, O'Connor K, Tate WP, Abraham WC. Roles of amyloid precursor protein and its fragments in regulating neural activity, plasticity and memory. Prog Neurobiol 2003;70(1):1-32.

32. Hilbich C, Kisters-Woike B, Reed J, Masters CL, Beyreuther K. Substitutions of hydrophobic amino acids reduce the amyloidogenicity of Alzheimer's disease beta A4 peptides. J Mol Biol 1992;228(2):460-473.

33. Gorevic PD, Castano EM, Sarma R, Frangione B. Ten to fourteen residue peptides of Alzheimer's disease protein are sufficient for amyloid fibril formation and its characteristic x-ray diffraction pattern. Biochem Biophys Res Commun 1987;147(2):854-862.

34. Kim W, Hecht MH. Generic hydrophobic residues are sufficient to promote aggregation of the Alzheimer's Abeta42 peptide. Proc Natl Acad Sci U S A 2006;103(43):15824-15829.

35. Fraser PE, McLachlan DR, Surewicz WK, Mizzen CA, Snow AD, Nguyen JT, Kirschner DA. Conformation and fibrillogenesis of Alzheimer A beta peptides with selected substitution of charged residues. J Mol Biol 1994;244(1):64-73.

36. Serpell LC, Sunde M, Blake CC. The molecular basis of amyloidosis. Cell Mol Life Sci 1997;53(11-12):871-887.

37. Stromer T, Serpell LC. Structure and morphology of the Alzheimer's amyloid fibril. Microsc Res Tech 2005;67(3-4):210-217.

38. Nelson R, Sawaya MR, Balbirnie M, Madsen AO, Riekel C, Grothe R, Eisenberg D. Structure of the cross-beta spine of amyloid-like fibrils. Nature 2005;435(7043):773-778.

39. Dickson TC, Vickers JC. The morphological phenotype of beta-amyloid plaques and associated neuritic changes in Alzheimer's disease. Neuroscience 2001;105(1):99-107.

40. Dickson DW. The pathogenesis of senile plaques. J Neuropathol Exp Neurol 1997;56(4):321-339.

41. Wisniewski HM, Bancher C, Barcikowska M, Wen GY, Currie J. Spectrum of morphological appearance of amyloid deposits in Alzheimer's disease. Acta Neuropathol 1989;78(4):337-347.
42. LeVine H, 3rd. Thioflavine T interaction with amyloid β-sheet structures. Amyloid 1995;2(1):1-6.
43. Braak H, Braak E. Neuropathological stageing of Alzheimer-related changes. Acta Neuropathol (Berl) 1991;82(4):239-259.
44. Braak H, Alafuzoff I, Arzberger T, Kretzschmar H, Del Tredici K. Staging of Alzheimer disease-associated neurofibrillary pathology using paraffin sections and immunocytochemistry. Acta Neuropathol (Berl) 2006.
45. Vickers JC, Dickson TC, Adlard PA, Saunders HL, King CE, McCormack G. The cause of neuronal degeneration in Alzheimer's disease. Prog Neurobiol 2000;60(2):139-165.
46. Kienlen-Campard P, Miolet S, Tasiaux B, Octave JN. Intracellular amyloid-beta 1-42, but not extracellular soluble amyloid-beta peptides, induces neuronal apoptosis. J Biol Chem 2002;277(18):15666-15670.
47. Pike CJ, Burdick D, Walencewicz AJ, Glabe CG, Cotman CW. Neurodegeneration induced by beta-amyloid peptides in vitro: the role of peptide assembly state. J Neurosci 1993;13(4):1676-1687.
48. Calhoun ME, Wiederhold KH, Abramowski D, Phinney AL, Probst A, Sturchler-Pierrat C, Staufenbiel M, Sommer B, Jucker M. Neuron loss in APP transgenic mice. Nature 1998;395(6704):755-756.
49. Li M, Chen L, Lee DH, Yu LC, Zhang Y. The role of intracellular amyloid beta in Alzheimer's disease. Prog Neurobiol 2007;83(3):131-139.
50. Su JH, Anderson AJ, Cummings BJ, Cotman CW. Immunohistochemical evidence for apoptosis in Alzheimer's disease. Neuroreport 1994;5(18):2529-2533.
51. Oddo S, Caccamo A, Smith IF, Green KN, LaFerla FM. A dynamic relationship between intracellular and extracellular pools of Abeta. Am J Pathol 2006;168(1):184-194.
52. Lazarov O, Lee M, Peterson DA, Sisodia SS. Evidence that synaptically released beta-amyloid accumulates as extracellular deposits in the hippocampus of transgenic mice. J Neurosci 2002;22(22):9785-9793.
53. El-Amouri SS, Zhu H, Yu J, Gage FH, Verma IM, Kindy MS. Neprilysin protects neurons against Abeta peptide toxicity. Brain Res 2007;1152:191-200.
54. D'Andrea MR, Nagele RG, Gumula NA, Reiser PA, Polkovitch DA, Hertzog BM, Andrade-Gordon P. Lipofuscin and Abeta42 exhibit distinct distribution patterns in normal and Alzheimer's disease brains. Neurosci Lett 2002;323(1):45-49.
55. Gerlach M, Ben-Shachar D, Riederer P, Youdim MB. Altered brain metabolism of iron as a cause of neurodegenerative diseases? J Neurochem 1994;63(3):793-807.
56. Loeffler DA, Connor JR, Juneau PL, Snyder BS, Kanaley L, DeMaggio AJ, Nguyen H, Brickman CM, LeWitt PA. Transferrin and iron in normal,

Alzheimer's disease, and Parkinson's disease brain regions. J Neurochem 1995;65(2):710-724.

57. Thompson KJ, Shoham S, Connor JR. Iron and neurodegenerative disorders. Brain Res Bull 2001;55(2):155-164.

58. Connor JR, Menzies SL. Relationship of iron to oligodendrocytes and myelination. Glia 1996;17(2):83-93.

59. Ezquer F, Nunez MT, Rojas A, Asenjo J, Israel Y. Hereditary hemochromatosis: an opportunity for gene therapy. Biol Res 2006;39(1):113-124.

60. Fleming RE, Bacon BR. Orchestration of iron homeostasis. N Engl J Med 2005;352(17):1741-1744.

61. Andrews NC. Disorders of iron metabolism. N Engl J Med 1999;341(26):1986-1995.

62. Bauminger ER, Treffry A, Hudson AJ, Hechel D, Hodson NW, Andrews SC, Levi S, Nowik I, Arosio P, Guest JR, et al. Iron incorporation into ferritins: evidence for the transfer of monomeric Fe(III) between ferritin molecules and for the formation of an unusual mineral in the ferritin of Escherichia coli. Biochem J 1994;302 (Pt 3):813-820.

63. Vymazal J, Brooks RA, Zak O, McRill C, Shen C, Di Chiro G. T1 and T2 of ferritin at different field strengths: effect on MRI. Magn Reson Med 1992;27(2):368-374.

64. Connor JR, Boeshore KL, Benkovic SA, Menzies SL. Isoforms of ferritin have a specific cellular distribution in the brain. J Neurosci Res 1994;37(4):461-465.

65. Telfer JF, Brock JH. Expression of ferritin, transferrin receptor, and non-specific resistance associated macrophage proteins 1 and 2 (Nramp1 and Nramp2) in the human rheumatoid synovium. Ann Rheum Dis 2002;61(8):741-744.

66. Connor JR, Menzies SL, St Martin SM, Mufson EJ. Cellular distribution of transferrin, ferritin, and iron in normal and aged human brains. J Neurosci Res 1990;27(4):595-611.

67. Hallgren B, Sourander P. The effect of age on the non-haemin iron in the human brain. J Neurochem 1958;3(1):41-51.

68. Morris CM, Candy JM, Oakley AE, Bloxham CA, Edwardson JA. Histochemical distribution of non-haem iron in the human brain. Acta Anat (Basel) 1992;144(3):235-257.

69. Wu LJ, Leenders AG, Cooperman S, Meyron-Holtz E, Smith S, Land W, Tsai RY, Berger UV, Sheng ZH, Rouault TA. Expression of the iron transporter ferroportin in synaptic vesicles and the blood-brain barrier. Brain Res 2004;1001(1-2):108-117.

70. Bartzokis G, Cummings JL, Markham CH, Marmarelis PZ, Treciokas LJ, Tishler TA, Marder SR, Mintz J. MRI evaluation of brain iron in earlier- and later-onset Parkinson's disease and normal subjects. Magn Reson Imaging 1999;17(2):213-222.

71. Griffiths PD, Dobson BR, Jones GR, Clarke DT. Iron in the basal ganglia in Parkinson's disease. An in vitro study using extended X-ray absorption

fine structure and cryo-electron microscopy. Brain 1999;122 (Pt 4):667-673.

72.   Graham JM, Paley MN, Grunewald RA, Hoggard N, Griffiths PD. Brain iron deposition in Parkinson's disease imaged using the PRIME magnetic resonance sequence. Brain 2000;123 Pt 12:2423-2431.

73.   Yasui M, Ota K, Garruto RM. Concentrations of zinc and iron in the brains of Guamanian patients with amyotrophic lateral sclerosis and parkinsonism-dementia. Neurotoxicology 1993;14(4):445-450.

74.   Connor JR, Boyer PJ, Menzies SL, Dellinger B, Allen RP, Ondo WG, Earley CJ. Neuropathological examination suggests impaired brain iron acquisition in restless legs syndrome. Neurology 2003;61(3):304-309.

75.   Connor JR, Menzies SL, St Martin SM, Mufson EJ. A histochemical study of iron, transferrin, and ferritin in Alzheimer's diseased brains. J Neurosci Res 1992;31(1):75-83.

76.   Ehmann WD, Markesbery WR, Alauddin M, Hossain TI, Brubaker EH. Brain trace elements in Alzheimer's disease. Neurotoxicology 1986;7(1):195-206.

77.   Connor JR, Snyder BS, Beard JL, Fine RE, Mufson EJ. Regional distribution of iron and iron-regulatory proteins in the brain in aging and Alzheimer's disease. J Neurosci Res 1992;31(2):327-335.

78.   Connor JR, Menzies SL. Cellular management of iron in the brain. J Neurol Sci 1995;134 Suppl:33-44.

79.   Smith DG, Cappai R, Barnham KJ. The redox chemistry of the Alzheimer's disease amyloid beta peptide. Biochim Biophys Acta 2007.

80.   Minicozzi V, Stellato F, Comai M, Serra MD, Potrich C, Meyer-Klaucke W, Morante S. Identifying the minimal copper- and zinc-binding site sequence in amyloid-beta peptides. J Biol Chem 2008;283(16):10784-10792.

81.   Atwood CS, Scarpa RC, Huang X, Moir RD, Jones WD, Fairlie DP, Tanzi RE, Bush AI. Characterization of copper interactions with alzheimer amyloid beta peptides: identification of an attomolar-affinity copper binding site on amyloid beta1-42. J Neurochem 2000;75(3):1219-1233.

82.   Miura T, Mitani S, Takanashi C, Mochizuki N. Copper selectively triggers beta-sheet assembly of an N-terminally truncated amyloid beta-peptide beginning with Glu3. J Inorg Biochem 2004;98(1):10-14.

83.   Benveniste EN, Nguyen VT, O'Keefe GM. Immunological aspects of microglia: relevance to Alzheimer's disease. Neurochem Int 2001;39(5-6):381-391.

84.   Hayes A, Thaker U, Iwatsubo T, Pickering-Brown SM, Mann DM. Pathological relationships between microglial cell activity and tau and amyloid beta protein in patients with Alzheimer's disease. Neurosci Lett 2002;331(3):171-174.

85.   Wegiel J, Wang KC, Tarnawski M, Lach B. Microglia cells are the driving force in fibrillar plaque formation, whereas astrocytes are a leading factor in plague degradation. Acta Neuropathol 2000;100(4):356-364.

86.   Huang X, Atwood CS, Moir RD, Hartshorn MA, Tanzi RE, Bush AI. Trace metal contamination initiates the apparent auto-aggregation, amyloidosis,

and oligomerization of Alzheimer's Abeta peptides. J Biol Inorg Chem 2004;9(8):954-960.

87. Khan A, Dobson JP, Exley C. Redox cycling of iron by Abeta42. Free Radic Biol Med 2006;40(4):557-569.

88. Bishop GM, Robinson SR. Human Abeta1-42 reduces iron-induced toxicity in rat cerebral cortex. J Neurosci Res 2003;73(3):316-323.

89. Bishop GM, Robinson SR. The amyloid paradox: amyloid-beta-metal complexes can be neurotoxic and neuroprotective. Brain Pathol 2004;14(4):448-452.

90. Cuajungco MP, Faget KY, Huang X, Tanzi RE, Bush AI. Metal chelation as a potential therapy for Alzheimer's disease. Ann N Y Acad Sci 2000;920:292-304.

91. Cherny RA, Atwood CS, Xilinas ME, Gray DN, Jones WD, McLean CA, Barnham KJ, Volitakis I, Fraser FW, Kim Y, Huang X, Goldstein LE, Moir RD, Lim JT, Beyreuther K, Zheng H, Tanzi RE, Masters CL, Bush AI. Treatment with a copper-zinc chelator markedly and rapidly inhibits beta-amyloid accumulation in Alzheimer's disease transgenic mice. Neuron 2001;30(3):665-676.

92. Price KA, Crouch PJ, White AR. Therapeutic treatment of Alzheimer's disease using metal complexing agents. Recent Pat CNS Drug Discov 2007;2(3):180-187.

93. Bush AI, Tanzi RE. Therapeutics for Alzheimer's disease based on the metal hypothesis. Neurotherapeutics 2008;5(3):421-432.

94. Crouch PJ, Tew DJ, Du T, Nguyen DN, Caragounis A, Filiz G, Blake RE, Trounce IA, Soon CP, Laughton K, Perez KA, Li QX, Cherny RA, Masters CL, Barnham KJ, White AR. Restored degradation of the Alzheimer's amyloid-beta peptide by targeting amyloid formation. J Neurochem 2009.

95. Smith MA, Sayre LM, Perry G. Is Alzheimer's a disease of oxidative stress? Alzheimer's Disease Review 1996;1:63-67.

96. Sies H. Oxidative stress: oxidants and antioxidants. Exp Physiol 1997;82(2):291-295.

97. Huang X, Atwood CS, Hartshorn MA, Multhaup G, Goldstein LE, Scarpa RC, Cuajungco MP, Gray DN, Lim J, Moir RD, Tanzi RE, Bush AI. The A beta peptide of Alzheimer's disease directly produces hydrogen peroxide through metal ion reduction. Biochemistry 1999;38(24):7609-7616.

98. Pamplona R, Dalfo E, Ayala V, Bellmunt MJ, Prat J, Ferrer I, Portero-Otin M. Proteins in human brain cortex are modified by oxidation, glycoxidation, and lipoxidation. Effects of Alzheimer disease and identification of lipoxidation targets. J Biol Chem 2005;280(22):21522-21530.

99. Hensley K, Hall N, Subramaniam R, Cole P, Harris M, Aksenov M, Aksenova M, Gabbita SP, Wu JF, Carney JM, et al. Brain regional correspondence between Alzheimer's disease histopathology and biomarkers of protein oxidation. J Neurochem 1995;65(5):2146-2156.

100. Butterfield DA, Yatin SM, Link CD. In vitro and in vivo protein oxidation induced by Alzheimer's disease amyloid beta-peptide (1-42). Ann N Y Acad Sci 1999;893:265-268.

101. Aksenov MY, Aksenova MV, Butterfield DA, Geddes JW, Markesbery WR. Protein oxidation in the brain in Alzheimer's disease. Neuroscience 2001;103(2):373-383.

102. Aksenova MV, Aksenov MY, Payne RM, Trojanowski JQ, Schmidt ML, Carney JM, Butterfield DA, Markesbery WR. Oxidation of cytosolic proteins and expression of creatine kinase BB in frontal lobe in different neurodegenerative disorders. Dement Geriatr Cogn Disord 1999;10(2):158-165.

103. Lyras L, Cairns NJ, Jenner A, Jenner P, Halliwell B. An assessment of oxidative damage to proteins, lipids, and DNA in brain from patients with Alzheimer's disease. J Neurochem 1997;68(5):2061-2069.

104. Lovell MA, Markesbery WR. Oxidative damage in mild cognitive impairment and early Alzheimer's disease. J Neurosci Res 2007.

105. Lovell MA, Xie C, Markesbery WR. Decreased glutathione transferase activity in brain and ventricular fluid in Alzheimer's disease. Neurology 1998;51(6):1562-1566.

106. Marcus DL, Strafaci JA, Freedman ML. Differential neuronal expression of manganese superoxide dismutase in Alzheimer's disease. Med Sci Monit 2006;12(1):BR8-14.

107. Nakamura S, Murayama N, Noshita T, Annoura H, Ohno T. Progressive brain dysfunction following intracerebroventricular infusion of beta(1-42)-amyloid peptide. Brain Res 2001;912(2):128-136.

108. Borchelt DR, Davis J, Fischer M, Lee MK, Slunt HH, Ratovitsky T, Regard J, Copeland NG, Jenkins NA, Sisodia SS, Price DL. A vector for expressing foreign genes in the brains and hearts of transgenic mice. Genet Anal 1996;13(6):159-163.

109. Duyckaerts C, Potier MC, Delatour B. Alzheimer disease models and human neuropathology: similarities and differences. Acta Neuropathol 2008;115(1):5-38.

110. LaFerla FM, Tinkle BT, Bieberich CJ, Haudenschild CC, Jay G. The Alzheimer's A beta peptide induces neurodegeneration and apoptotic cell death in transgenic mice. Nat Genet 1995;9(1):21-30.

111. Richardson JA, Burns DK. Mouse models of Alzheimer's disease: a quest for plaques and tangles. Ilar J 2002;43(2):89-99.

112. Borchelt DR, Ratovitski T, van Lare J, Lee MK, Gonzales V, Jenkins NA, Copeland NG, Price DL, Sisodia SS. Accelerated amyloid deposition in the brains of transgenic mice coexpressing mutant presenilin 1 and amyloid precursor proteins. Neuron 1997;19(4):939-945.

113. Jankowsky JL, Slunt HH, Ratovitski T, Jenkins NA, Copeland NG, Borchelt DR. Co-expression of multiple transgenes in mouse CNS: a comparison of strategies. Biomol Eng 2001;17(6):157-165.

114. Borchelt DR, Lee MK, Gonzales V, Slunt HH, Ratovitski T, Jenkins NA, Copeland NG, Price DL, Sisodia SS. Accumulation of proteolytic fragments of mutant presenilin 1 and accelerated amyloid deposition are co-regulated in transgenic mice. Neurobiol Aging 2002;23(2):171-177.

115. Rabi II. A new method of measuring nuclear magnetic moments. Phys Rev 1938;53:318.
116. Bloch F. Nuclear induction. Phys Rev 1946;70:460.
117. Purcell EM, Torrey HC, Pound RV. Resonance absorption by nuclear magnetic moments in a solid. Phys Rev 1946;69:37.
118. Sands MJ, Levitin A. Basics of magnetic resonance imaging. Semin Vasc Surg 2004;17(2):66-82.
119. Haacke EM. Magnetic resonance imaging : physical principles and sequence design. New York: Wiley; 1999. xxvii, 914 p. p.
120. Stark DD, Bradley WG. Magnetic resonance imaging. St. Louis: Mosby; 1999.
121. Abragam A. The principles of nuclear magnetism. Oxford,: Clarendon Press; 1961. 599 p. p.
122. Green DK, Powles JG. Nuclear spin-lattice relaxation, including the spin-rotation interaction, in liquid benzene and several benzene derivatives up to the critical temperature. Proc Phys Soc 1965;85:87 - 102.
123. Haacke EM, Cheng NY, House MJ, Liu Q, Neelavalli J, Ogg RJ, Khan A, Ayaz M, Kirsch W, Obenaus A. Imaging iron stores in the brain using magnetic resonance imaging. Magn Reson Imaging 2005;23(1):1-25.
124. Thomas LO, Boyko OB, Anthony DC, Burger PC. MR detection of brain iron. AJNR Am J Neuroradiol 1993;14(5):1043-1048.
125. Vymazal J, Brooks RA, Bulte JW, Gordon D, Aisen P. Iron uptake by ferritin: NMR relaxometry studies at low iron loads. J Inorg Biochem 1998;71(3-4):153-157.
126. Alexopoulou E, Stripeli F, Baras P, Seimenis I, Kattamis A, Ladis V, Efstathopoulos E, Brountzos EN, Kelekis AD, Kelekis NL. R2 relaxometry with MRI for the quantification of tissue iron overload in beta-thalassemic patients. J Magn Reson Imaging 2006;23(2):163-170.
127. Carneiro AA, Fernandes JP, de Araujo DB, Elias J, Jr., Martinelli AL, Covas DT, Zago MA, Angulo IL, St Pierre TG, Baffa O. Liver iron concentration evaluated by two magnetic methods: magnetic resonance imaging and magnetic susceptometry. Magn Reson Med 2005;54(1):122-128.
128. Gandon Y, Olivie D, Guyader D, Aube C, Oberti F, Sebille V, Deugnier Y. Non-invasive assessment of hepatic iron stores by MRI. Lancet 2004;363(9406):357-362.
129. Schenck JF. Magnetic resonance imaging of brain iron. J Neurol Sci 2003;207(1-2):99-102.
130. Gossuin Y, Roch A, Muller RN, Gillis P, Lo Bue F. Anomalous nuclear magnetic relaxation of aqueous solutions of ferritin: an unprecedented first-order mechanism. Magn Reson Med 2002;48(6):959-964.
131. Gossuin Y, Muller RN, Gillis P. Relaxation induced by ferritin: a better understanding for an improved MRI iron quantification. NMR Biomed 2004;17(7):427-432.

132. Gossuin Y, Roch A, Muller RN, Gillis P. Relaxation induced by ferritin and ferritin-like magnetic particles: the role of proton exchange. Magn Reson Med 2000;43(2):237-243.

133. Bulte JW, Vymazal J, Brooks RA, Pierpaoli C, Frank JA. Frequency dependence of MR relaxation times. II. Iron oxides. J Magn Reson Imaging 1993;3(4):641-648.

134. Gillis P, Koenig SH. Transverse relaxation of solvent protons induced by magnetized spheres: application to ferritin, erythrocytes, and magnetite. Magn Reson Med 1987;5(4):323-345.

135. Gillis P, Moiny F, Brooks RA. On T(2)-shortening by strongly magnetized spheres: a partial refocusing model. Magn Reson Med 2002;47(2):257-263.

136. Vymazal J, Brooks RA, Baumgarner C, Tran V, Katz D, Bulte JW, Bauminger R, Di Chiro G. The relation between brain iron and NMR relaxation times: an in vitro study. Magn Reson Med 1996;35(1):56-61.

137. Bizzi A, Brooks RA, Brunetti A, Hill JM, Alger JR, Miletich RS, Francavilla TL, Di Chiro G. Role of iron and ferritin in MR imaging of the brain: a study in primates at different field strengths. Radiology 1990;177(1):59-65.

138. Yablonskiy DA, Haacke EM. Theory of NMR signal behavior in magnetically inhomogeneous tissues: the static dephasing regime. Magn Reson Med 1994;32(6):749-763.

139. Michel FM, Ehm L, Antao SM, Lee PL, Chupas PJ, Liu G, Strongin DR, Schoonen MA, Phillips BL, Parise JB. The structure of ferrihydrite, a nanocrystalline material. Science 2007;316(5832):1726-1729.

140. Brittenham GM, Badman DG. Noninvasive measurement of iron: report of an NIDDK workshop. Blood 2003;101(1):15-19.

141. Li TQ, Aisen AM, Hindmarsh T. Assessment of hepatic iron content using magnetic resonance imaging. Acta Radiol 2004;45(2):119-129.

142. Ghugre NR, Coates TD, Nelson MD, Wood JC. Mechanisms of tissue-iron relaxivity: nuclear magnetic resonance studies of human liver biopsy specimens. Magn Reson Med 2005;54(5):1185-1193.

143. Clark PR, Chua-Anusorn W, St Pierre TG. Proton transverse relaxation rate (R2) images of liver tissue; mapping local tissue iron concentrations with MRI [corrected]. Magn Reson Med 2003;49(3):572-575.

144. Wood JC, Otto-Duessel M, Aguilar M, Nick H, Nelson MD, Coates TD, Pollack H, Moats R. Cardiac iron determines cardiac T2*, T2, and T1 in the gerbil model of iron cardiomyopathy. Circulation 2005;112(4):535-543.

145. Ordidge RJ, Gorell JM, Deniau JC, Knight RA, Helpern JA. Assessment of relative brain iron concentrations using T2-weighted and T2*-weighted MRI at 3 Tesla. Magn Reson Med 1994;32(3):335-341.

146. Parsey RV, Krishnan KR. Quantitative analysis of T2 signal intensities in Alzheimer's disease. Psychiatry Res 1998;82(3):181-185.

147. Pfefferbaum A, Sullivan EV, Adalsteinsson E, Garrick T, Harper C. Postmortem MR imaging of formalin-fixed human brain. Neuroimage 2004;21(4):1585-1595.

148. Schenck JF, Zimmerman EA, Li Z, Adak S, Saha A, Tandon R, Fish KM, Belden C, Gillen RW, Barba A, Henderson DL, Neil W, O'Keefe T. High-field magnetic resonance imaging of brain iron in Alzheimer disease. Top Magn Reson Imaging 2006;17(1):41-50.

149. Sener RN. Echo-planar and gradient-echo diffusion MRI of normal brain iron in the globus pallidus. Clin Imaging 2002;26(6):371-374.

150. Banson ML, Cofer GP, Black R, Johnson GA. A probe for specimen magnetic resonance microscopy. Invest Radiol 1992;27(2):157-164.

151. Glowinski A, Adam G, Bucker A, van Vaals J, Gunther RW. A perspective on needle artifacts in MRI: an electromagnetic model for experimentally separating susceptibility effects. IEEE Trans Med Imaging 2000;19(12):1248-1252.

152. Yamada K, Gonzalez RG, L OS, Komili S, Weisskoff RM, Rosen BR, Koroshetz WJ, Nishimura T, Sorensen AG. Iron-induced susceptibility effect at the globus pallidus causes underestimation of flow and volume on dynamic susceptibility contrast-enhanced MR perfusion images. AJNR Am J Neuroradiol 2002;23(6):1022-1029.

153. Bartzokis G, Beckson M, Hance DB, Marx P, Foster JA, Marder SR. MR evaluation of age-related increase of brain iron in young adult and older normal males. Magn Reson Imaging 1997;15(1):29-35.

154. Webb AG. Radiofrequency microcoils in magnetic resonance. Progress in nuclear magnetic resonance spectroscopy 1997;31(1):1-41.

155. Chang C, Jang T. Magnetic resonance microscopy of hamster olfactory bulb: a histological correlation. Anat Rec 1995;242(1):132-135.

156. Rohlfing T, Schaupp F, Haddad D, Brandt R, Haase A, Menzel R, Maurer CR, Jr. Unwarping confocal microscopy images of bee brains by nonrigid registration to a magnetic resonance microscopy image. J Biomed Opt 2005;10(2):024018.

157. Breen MS, Lazebnik RS, Wilson DL. Three-dimensional registration of magnetic resonance image data to histological sections with model-based evaluation. Ann Biomed Eng 2005;33(8):1100-1112.

158. Black RD, Early TA, Roemer PB, Mueller OM, Mogro-Campero A, Turner LG, Johnson GA. A high-temperature superconducting receiver for nuclear magnetic resonance microscopy. Science 1993;259(5096):793-795.

159. McFarland EW, Mortara A. Three-dimensional NMR microscopy: improving SNR with temperature and microcoils. Magn Reson Imaging 1992;10(2):279-288.

160. Bobroff S, McCarthy MJ. Variations on the slotted-tube resonator: rectangular and elliptical coils. Magn Reson Imaging 1999;17(5):783-789.

161. Stollberger R, Wach P. Imaging of the active B1 field in vivo. Magn Reson Med 1996;35(2):246-251.

162. Zhang X, Zhu XH, Chen W. Higher-order harmonic transmission-line RF coil design for MR applications. Magn Reson Med 2005;53(5):1234-1239.

163. Blackband SJ, Bui JD, Buckley DL, Zelles T, Plant HD, Inglis BA, Phillips MI. MR microscopy of perfused brain slices. Magn Reson Med 1997;38(6):1012-1015.

164. Shepherd TM, Scheffler B, King MA, Stanisz GJ, Steindler DA, Blackband SJ. MR microscopy of rat hippocampal slice cultures: a novel model for studying cellular processes and chronic perturbations to tissue microstructure. Neuroimage 2006;30(3):780-786.

165. Hall LD, Luck S, Rajanayagam V. Construction of a high-resolution NMR probe for imaging with submillimeter spatial resolution. Journal of Magnetic Resonance 1986;66:349-351.

166. Glover PM, Bowtell RW, Brown GD, Mansfield P. A microscope slide probe for high resolution imaging at 11.7 Tesla. Magn Reson Med 1994;31(4):423-428.

167. Bowtell RW, Brown GD, Glover PM, McJury M, Mansfield P. Resolution of Cellular Structures by NMR Microscopy at 11.7 T. Philos Trans R Soc Lond Biol 1990;333:457-467.

168. Kneeland JB, Jesmanowicz A, Froncisz W, Grist TM, Hyde JS. High-resolution MR imaging using loop-gap resonators. Work in progress. Radiology 1986;158(1):247-250.

169. Grist TM, Hyde JS. Resonators for in Vivo 31P NMR at 1.5 T. J Magn Reson 1985;61:571-578.

170. Froncisz W, Hyde JS. The loop-gap resonator: A new microwave lumped circuit ESR sample structure. J Magn Reson 1982;47:515-521.

171. Hornak JP, Ceckler TL, Bryant RG. Phosphorus-31 NMR spectroscopy using a loop-gap resonator. J Magn Reson 1986;68:319-322.

172. Li S, Yang QX, Smith MB. RF coil optimization: evaluation of B1 field homogeneity using field histograms and finite element calculations. Magn Reson Imaging 1994;12(7):1079-1087.

173. Peck TL, Magin RL, Lauterbur PC. Design and analysis of microcoils for NMR microscopy. J Magn Reson B 1995;108(2):114-124.

174. Nakata-Kudo Y, Mizuno T, Yamada K, Shiga K, Yoshikawa K, Mori S, Nishimura T, Nakajima K, Nakagawa M. Microbleeds in Alzheimer disease are more related to cerebral amyloid angiopathy than cerebrovascular disease. Dement Geriatr Cogn Disord 2006;22(1):8-14.

175. Quintana C, Bellefqih S, Laval JY, Guerquin-Kern JL, Wu TD, Avila J, Ferrer I, Arranz R, Patino C. Study of the localization of iron, ferritin, and hemosiderin in Alzheimer's disease hippocampus by analytical microscopy at the subcellular level. J Struct Biol 2006;153(1):42-54.

176. Butts K, Pauly JM, Daniel BL, Kee S, Norbash AM. Management of biopsy needle artifacts: techniques for RF-refocused MRI. J Magn Reson Imaging 1999;9(4):586-595.

177. Wansapura JP, Holland SK, Dunn RS, Ball WS, Jr. NMR relaxation times in the human brain at 3.0 tesla. J Magn Reson Imaging 1999;9(4):531-538.

178. Blamire AM, Rowe JG, Styles P, McDonald B. Optimising imaging parameters for post mortem MR imaging of the human brain. Acta Radiol 1999;40(6):593-597.

179. Yong-Hing CJ, Obenaus A, Stryker R, Tong K, Sarty GE. Magnetic resonance imaging and mathematical modeling of progressive formalin fixation of the human brain. Magn Reson Med 2005;54(2):324-332.

180. Helander KG. Kinetic studies of formaldehyde binding in tissue. Biotech Histochem 1994;69(3):177-179.

181. Sun SW, Neil JJ, Liang HF, He YY, Schmidt RE, Hsu CY, Song SK. Formalin fixation alters water diffusion coefficient magnitude but not anisotropy in infarcted brain. Magn Reson Med 2005;53(6):1447-1451.

182. Sun SW, Neil JJ, Song SK. Relative indices of water diffusion anisotropy are equivalent in live and formalin-fixed mouse brains. Magn Reson Med 2003;50(4):743-748.

183. Benveniste H, Einstein G, Kim KR, Hulette C, Johnson GA. Detection of neuritic plaques in Alzheimer's disease by magnetic resonance microscopy. Proc Natl Acad Sci U S A 1999;96(24):14079-14084.

184. Jack CR, Jr., Garwood M, Wengenack TM, Borowski B, Curran GL, Lin J, Adriany G, Grohn OH, Grimm R, Poduslo JF. In vivo visualization of Alzheimer's amyloid plaques by magnetic resonance imaging in transgenic mice without a contrast agent. Magn Reson Med 2004;52(6):1263-1271.

185. Jack CR, Jr., Marjanska M, Wengenack TM, Reyes DA, Curran GL, Lin J, Preboske GM, Poduslo JF, Garwood M. Magnetic resonance imaging of Alzheimer's pathology in the brains of living transgenic mice: a new tool in Alzheimer's disease research. Neuroscientist 2007;13(1):38-48.

186. Jack CR, Jr., Wengenack TM, Reyes DA, Garwood M, Curran GL, Borowski BJ, Lin J, Preboske GM, Holasek SS, Adriany G, Poduslo JF. In vivo magnetic resonance microimaging of individual amyloid plaques in Alzheimer's transgenic mice. J Neurosci 2005;25(43):10041-10048.

187. Meadowcroft MD, Zhang S, Liu W, Park BS, Connor JR, Collins CM, Smith MB, Yang QX. Direct magnetic resonance imaging of histological tissue samples at 3.0T. Magn Reson Med 2007;57(5):835-841.

188. LeVine SM. Iron deposits in multiple sclerosis and Alzheimer's disease brains. Brain Res 1997;760(1-2):298-303.

189. LeVine SM. Oligodendrocytes and myelin sheaths in normal, quaking and shiverer brains are enriched in iron. J Neurosci Res 1991;29(3):413-419.

190. Collingwood JF, Chong RK, Kasama T, Cervera-Gontard L, Dunin-Borkowski RE, Perry G, Posfai M, Siedlak SL, Simpson ET, Smith MA, Dobson J. Three-dimensional tomographic imaging and characterization of iron compounds within Alzheimer's plaque core material. J Alzheimers Dis 2008;14(2):235-245.

191. Gerber MR, Connor JR. Do oligodendrocytes mediate iron regulation in the human brain? Ann Neurol 1989;26(1):95-98.

192. Hill JM, Switzer RC, 3rd. The regional distribution and cellular localization of iron in the rat brain. Neuroscience 1984;11(3):595-603.

193. Dhenain M, El Tannir El Tayara N, Wu TD, Guegan M, Volk A, Quintana C, Delatour B. Characterization of in vivo MRI detectable thalamic amyloid plaques from APP/PS1 mice. Neurobiol Aging 2007.

194. Vanhoutte G, Dewachter I, Borghgraef P, Van Leuven F, Van der Linden A. Noninvasive in vivo MRI detection of neuritic plaques associated with iron in APP[V717I] transgenic mice, a model for Alzheimer's disease. Magn Reson Med 2005;53(3):607-613.

195. Falangola MF, Ardekani BA, Lee SP, Babb JS, Bogart A, Dyakin VV, Nixon R, Duff K, Helpern JA. Application of a non-linear image registration algorithm to quantitative analysis of T2 relaxation time in transgenic mouse models of AD pathology. J Neurosci Methods 2005;144(1):91-97.

196. Galvez N, Fernandez B, Sanchez P, Cuesta R, Ceolin M, Clemente-Leon M, Trasobares S, Lopez-Haro M, Calvino JJ, Stephan O, Dominguez-Vera JM. Comparative structural and chemical studies of ferritin cores with gradual removal of their iron contents. J Am Chem Soc 2008;130(25):8062-8068.

197. Drayer B, Burger P, Darwin R, Riederer S, Herfkens R, Johnson GA. MRI of brain iron. AJR Am J Roentgenol 1986;147(1):103-110.

198. Gossuin Y, Hautot D, Muller RN, Pankhurst Q, Dobson J, Morris C, Gillis P, Collingwood J. Looking for biogenic magnetite in brain ferritin using NMR relaxometry. NMR Biomed 2005;18(7):469-472.

199. Vymazal J, Zak O, Bulte JW, Aisen P, Brooks RA. T1 and T2 of ferritin solutions: effect of loading factor. Magn Reson Med 1996;36(1):61-65.

200. Meguro R, Asano Y, Iwatsuki H, Shoumura K. Perfusion-Perls and -Turnbull methods supplemented by DAB intensification for nonheme iron histochemistry: demonstration of the superior sensitivity of the methods in the liver, spleen, and stomach of the rat. Histochem Cell Biol 2003;120(1):73-82.

201. Bussiere T, Bard F, Barbour R, Grajeda H, Guido T, Khan K, Schenk D, Games D, Seubert P, Buttini M. Morphological characterization of Thioflavin-S-positive amyloid plaques in transgenic Alzheimer mice and effect of passive Abeta immunotherapy on their clearance. Am J Pathol 2004;165(3):987-995.

202. van Groen T, Kiliaan AJ, Kadish I. Deposition of mouse amyloid beta in human APP/PS1 double and single AD model transgenic mice. Neurobiol Dis 2006;23(3):653-662.

203. Stopa B, Piekarska B, Konieczny L, Rybarska J, Spolnik P, Zemanek G, Roterman I, Krol M. The structure and protein binding of amyloid-specific dye reagents. Acta Biochim Pol 2003;50(4):1213-1227.

204. Matsuoka Y, Picciano M, Malester B, LaFrancois J, Zehr C, Daeschner JM, Olschowka JA, Fonseca MI, O'Banion MK, Tenner AJ, Lemere CA, Duff K. Inflammatory responses to amyloidosis in a transgenic mouse model of Alzheimer's disease. Am J Pathol 2001;158(4):1345-1354.

205. Luhrs T, Ritter C, Adrian M, Riek-Loher D, Bohrmann B, Dobeli H, Schubert D, Riek R. 3D structure of Alzheimer's amyloid-beta(1-42) fibrils. Proc Natl Acad Sci U S A 2005;102(48):17342-17347.

206. Yan Y, Liu J, McCallum SA, Yang D, Wang C. Methyl dynamics of the amyloid-beta peptides Abeta40 and Abeta42. Biochem Biophys Res Commun 2007;362(2):410-414.

207. Fullerton GD, Potter JL, Dornbluth NC. NMR relaxation of protons in tissues and other macromolecular water solutions. Magn Reson Imaging 1982;1(4):209-226.

208. Fullerton GD, Finnie MF, Hunter KE, Ord VA, Cameron IL. The influence of macromolecular polymerization of spin-lattice relaxation of aqueous solutions. Magn Reson Imaging 1987;5(5):353-370.

209. Guntert A, Dobeli H, Bohrmann B. High sensitivity analysis of amyloid-beta peptide composition in amyloid deposits from human and PS2APP mouse brain. Neuroscience 2006;143(2):461-475.

210. Perry G, Cash AD, Smith MA. Alzheimer Disease and Oxidative Stress. J Biomed Biotechnol 2002;2(3):120-123.

211. Smith MA. Oxidative stress and iron imbalance in Alzheimer disease: how rust became the fuss! J Alzheimers Dis 2006;9(3 Suppl):305-308.

212. Wegiel J, Wang KC, Imaki H, Rubenstein R, Wronska A, Osuchowski M, Lipinski WJ, Walker LC, LeVine H. The role of microglial cells and astrocytes in fibrillar plaque evolution in transgenic APP(SW) mice. Neurobiol Aging 2001;22(1):49-61.

213. Mehlhase J, Gieche J, Widmer R, Grune T. Ferritin levels in microglia depend upon activation: modulation by reactive oxygen species. Biochim Biophys Acta 2006;1763(8):854-859.

214. Ghribi O, Golovko MY, Larsen B, Schrag M, Murphy EJ. Deposition of iron and beta-amyloid plaques is associated with cortical cellular damage in rabbits fed with long-term cholesterol-enriched diets. J Neurochem 2006;99(2):438-449.

215. Rottkamp CA, Raina AK, Zhu X, Gaier E, Bush AI, Atwood CS, Chevion M, Perry G, Smith MA. Redox-active iron mediates amyloid-beta toxicity. Free Radic Biol Med 2001;30(4):447-450.

216. Wengenack TM, Whelan S, Curran GL, Duff KE, Poduslo JF. Quantitative histological analysis of amyloid deposition in Alzheimer's double transgenic mouse brain. Neuroscience 2000;101(4):939-944.

217. Satou T, Cummings BJ, Head E, Nielson KA, Hahn FF, Milgram NW, Velazquez P, Cribbs DH, Tenner AJ, Cotman CW. The progression of beta-amyloid deposition in the frontal cortex of the aged canine. Brain Res 1997;774(1-2):35-43.

218. Connor JR, Snyder BS, Arosio P, Loeffler DA, LeWitt P. A quantitative analysis of isoferritins in select regions of aged, parkinsonian, and Alzheimer's diseased brains. J Neurochem 1995;65(2):717-724.

219. Nakada T, Matsuzawa H, Igarashi H, Fujii Y, Kwee IL. In vivo visualization of senile-plaque-like pathology in Alzheimer's disease patients by MR microscopy on a 7T system. J Neuroimaging 2008;18(2):125-129.

220. Hardy J, Selkoe DJ. The amyloid hypothesis of Alzheimer's disease: progress and problems on the road to therapeutics. Science 2002;297(5580):353-356.

221. Siman R, Reaume AG, Savage MJ, Trusko S, Lin YG, Scott RW, Flood DG. Presenilin-1 P264L knock-in mutation: differential effects on abeta

production, amyloid deposition, and neuronal vulnerability. J Neurosci 2000;20(23):8717-8726.

222. Casas C, Sergeant N, Itier JM, Blanchard V, Wirths O, van der Kolk N, Vingtdeux V, van de Steeg E, Ret G, Canton T, Drobecq H, Clark A, Bonici B, Delacourte A, Benavides J, Schmitz C, Tremp G, Bayer TA, Benoit P, Pradier L. Massive CA1/2 neuronal loss with intraneuronal and N-terminal truncated Abeta42 accumulation in a novel Alzheimer transgenic model. Am J Pathol 2004;165(4):1289-1300.

223. Richards JG, Higgins GA, Ouagazzal AM, Ozmen L, Kew JN, Bohrmann B, Malherbe P, Brockhaus M, Loetscher H, Czech C, Huber G, Bluethmann H, Jacobsen H, Kemp JA. PS2APP transgenic mice, coexpressing hPS2mut and hAPPswe, show age-related cognitive deficits associated with discrete brain amyloid deposition and inflammation. J Neurosci 2003;23(26):8989-9003.

224. Dewachter I, Reverse D, Caluwaerts N, Ris L, Kuiperi C, Van den Haute C, Spittaels K, Umans L, Serneels L, Thiry E, Moechars D, Mercken M, Godaux E, Van Leuven F. Neuronal deficiency of presenilin 1 inhibits amyloid plaque formation and corrects hippocampal long-term potentiation but not a cognitive defect of amyloid precursor protein [V717I] transgenic mice. J Neurosci 2002;22(9):3445-3453.

225. Allsop D, Landon M, Kidd M. The isolation and amino acid composition of senile plaque core protein. Brain Res 1983;259(2):348-352.

226. Naslund J, Haroutunian V, Mohs R, Davis KL, Davies P, Greengard P, Buxbaum JD. Correlation between elevated levels of amyloid beta-peptide in the brain and cognitive decline. Jama 2000;283(12):1571-1577.

227. Knowles RB, Gomez-Isla T, Hyman BT. Abeta associated neuropil changes: correlation with neuronal loss and dementia. J Neuropathol Exp Neurol 1998;57(12):1122-1130.

228. Schwab C, Hosokawa M, McGeer PL. Transgenic mice overexpressing amyloid beta protein are an incomplete model of Alzheimer disease. Exp Neurol 2004;188(1):52-64.

229. Kuo YM, Kokjohn TA, Beach TG, Sue LI, Brune D, Lopez JC, Kalback WM, Abramowski D, Sturchler-Pierrat C, Staufenbiel M, Roher AE. Comparative analysis of amyloid-beta chemical structure and amyloid plaque morphology of transgenic mouse and Alzheimer's disease brains. J Biol Chem 2001;276(16):12991-12998.

230. Yang AJ, Chandswangbhuvana D, Shu T, Henschen A, Glabe CG. Intracellular accumulation of insoluble, newly synthesized abetan-42 in amyloid precursor protein-transfected cells that have been treated with Abeta1-42. J Biol Chem 1999;274(29):20650-20656.

231. von Bernhardi R, Ramirez G. Microglia-astrocyte interaction in Alzheimer's disease: friends or foes for the nervous system? Biol Res 2001;34(2):123-128.

232. Wegiel J, Imaki H, Wang KC, Wronska A, Osuchowski M, Rubenstein R. Origin and turnover of microglial cells in fibrillar plaques of APPsw transgenic mice. Acta Neuropathol 2003;105(4):393-402.

233. Collingwood J, Dobson J. Mapping and characterization of iron compounds in Alzheimer's tissue. J Alzheimers Dis 2006;10(2-3):215-222.

234. Han J, Day JR, Connor JR, Beard JL. H and L ferritin subunit mRNA expression differs in brains of control and iron-deficient rats. J Nutr 2002;132(9):2769-2774.

235. Atwood CS, Huang X, Moir RD, Tanzi RE, Bush AI. Role of free radicals and metal ions in the pathogenesis of Alzheimer's disease. Met Ions Biol Syst 1999;36:309-364.

236. Perry G, Nunomura A, Hirai K, Zhu X, Perez M, Avila J, Castellani RJ, Atwood CS, Aliev G, Sayre LM, Takeda A, Smith MA. Is oxidative damage the fundamental pathogenic mechanism of Alzheimer's and other neurodegenerative diseases? Free Radic Biol Med 2002;33(11):1475-1479.

237. Srinivasan V, Pandi-Perumal SR, Cardinali DP, Poeggeler B, Hardeland R. Melatonin in Alzheimer's disease and other neurodegenerative disorders. Behav Brain Funct 2006;2:15.

238. Sayre LM, Zagorski MG, Surewicz WK, Krafft GA, Perry G. Mechanisms of neurotoxicity associated with amyloid beta deposition and the role of free radicals in the pathogenesis of Alzheimer's disease: a critical appraisal. Chem Res Toxicol 1997;10(5):518-526.

239. Poduslo JF, Wengenack TM, Curran GL, Wisniewski T, Sigurdsson EM, Macura SI, Borowski BJ, Jack CR, Jr. Molecular targeting of Alzheimer's amyloid plaques for contrast-enhanced magnetic resonance imaging. Neurobiol Dis 2002;11(2):315-329.

240. Dhenain M, Delatour B, Walczak C, Volk A. Passive staining: a novel ex vivo MRI protocol to detect amyloid deposits in mouse models of Alzheimer's disease. Magn Reson Med 2006;55(3):687-693.

241. Falangola MF, Dyakin VV, Lee SP, Bogart A, Babb JS, Duff K, Nixon R, Helpern JA. Quantitative MRI reveals aging-associated T(2) changes in mouse models of Alzheimer's disease. NMR Biomed 2007;20(3):343-351.

242. Wadghiri YZ, Sigurdsson EM, Sadowski M, Elliott JI, Li Y, Scholtzova H, Tang CY, Aguinaldo G, Pappolla M, Duff K, Wisniewski T, Turnbull DH. Detection of Alzheimer's amyloid in transgenic mice using magnetic resonance microimaging. Magn Reson Med 2003;50(2):293-302.

243. Zhang J, Yarowsky P, Gordon MN, Di Carlo G, Munireddy S, van Zijl PC, Mori S. Detection of amyloid plaques in mouse models of Alzheimer's disease by magnetic resonance imaging. Magn Reson Med 2004;51(3):452-457.

244. El Tannir El Tayara N, Delatour B, Le Cudennec C, Guegan M, Volk A, Dhenain M. Age-related evolution of amyloid burden, iron load, and MR relaxation times in a transgenic mouse model of Alzheimer's disease. Neurobiol Dis 2006;22(1):199-208.

245. MacKay A, Laule C, Vavasour I, Bjarnason T, Kolind S, Madler B. Insights into brain microstructure from the T2 distribution. Magn Reson Imaging 2006;24(4):515-525.

246. Leyhe T, Erb M, Milian M, Eschweiler GW, Ethofer T, Grodd W, Saur R. Changes in Cortical Activation during Retrieval of Clock Time Representations in Patients with Mild Cognitive Impairment and Early Alzheimer's Disease. Dement Geriatr Cogn Disord 2009;27(2):117-132.

247. Murphy C, Cerf-Ducastel B, Calhoun-Haney R, Gilbert PE, Ferdon S. ERP, fMRI and functional connectivity studies of brain response to odor in normal aging and Alzheimer's disease. Chem Senses 2005;30 Suppl 1:i170-171.

248. Murphy C, Gilmore MM, Seery CS, Salmon DP, Lasker BR. Olfactory thresholds are associated with degree of dementia in Alzheimer's disease. Neurobiol Aging 1990;11(4):465-469.

249. Murphy C, Jernigan TL, Fennema-Notestine C. Left hippocampal volume loss in Alzheimer's disease is reflected in performance on odor identification: a structural MRI study. J Int Neuropsychol Soc 2003;9(3):459-471.

250. Albers MW, Tabert MH, Devanand DP. Olfactory dysfunction as a predictor of neurodegenerative disease. Curr Neurol Neurosci Rep 2006;6(5):379-386.

251. Devanand DP, Tabert MH, Cuasay K, Manly JJ, Schupf N, Brickman AM, Andrews H, Brown TR, Decarli C, Mayeux R. Olfactory identification deficits and MCI in a multi-ethnic elderly community sample. Neurobiol Aging 2008.

252. McEvoy LK, Fennema-Notestine C, Roddey JC, Hagler Jr DJ, Jr., Holland D, Karow DS, Pung CJ, Brewer JB, Dale AM. Alzheimer Disease: Quantitative Structural Neuroimaging for Detection and Prediction of Clinical and Structural Changes in Mild Cognitive Impairment. Radiology 2009.

253. Bai F, Zhang Z, Watson DR, Yu H, Shi Y, Yuan Y, Qian Y, Jia J. Abnormal integrity of association fiber tracts in amnestic mild cognitive impairment. J Neurol Sci 2009;278(1-2):102-106.

254. Medina DA, Gaviria M. Diffusion tensor imaging investigations in Alzheimer's disease: the resurgence of white matter compromise in the cortical dysfunction of the aging brain. Neuropsychiatr Dis Treat 2008;4(4):737-742.

255. Nakata Y, Sato N, Abe O, Shikakura S, Arima K, Furuta N, Uno M, Hirai S, Masutani Y, Ohtomo K, Aoki S. Diffusion abnormality in posterior cingulate fiber tracts in Alzheimer's disease: tract-specific analysis. Radiat Med 2008;26(8):466-473.

256. Feczko E, Augustinack JC, Fischl B, Dickerson BC. An MRI-based method for measuring volume, thickness and surface area of entorhinal, perirhinal, and posterior parahippocampal cortex. Neurobiol Aging 2009;30(3):420-431.

257. Gouw AA, Seewann A, Vrenken H, van der Flier WM, Rozemuller JM, Barkhof F, Scheltens P, Geurts JJ. Heterogeneity of white matter hyperintensities in Alzheimer's disease: post-mortem quantitative MRI and neuropathology. Brain 2008;131(Pt 12):3286-3298.

258. Falangola MF, Lee SP, Nixon RA, Duff K, Helpern JA. Histological co-localization of iron in Abeta plaques of PS/APP transgenic mice. Neurochem Res 2005;30(2):201-205.

259. Garcia-Alloza M, Robbins EM, Zhang-Nunes SX, Purcell SM, Betensky RA, Raju S, Prada C, Greenberg SM, Bacskai BJ, Frosch MP. Characterization of amyloid deposition in the APPswe/PS1dE9 mouse model of Alzheimer disease. Neurobiol Dis 2006;24(3):516-524.

260. Jankowsky JL, Younkin LH, Gonzales V, Fadale DJ, Slunt HH, Lester HA, Younkin SG, Borchelt DR. Rodent A beta modulates the solubility and distribution of amyloid deposits in transgenic mice. J Biol Chem 2007;282(31):22707-22720.

261. Thompson K, Menzies S, Muckenthaler M, Torti FM, Wood T, Torti SV, Hentze MW, Beard J, Connor J. Mouse brains deficient in H-ferritin have normal iron concentration but a protein profile of iron deficiency and increased evidence of oxidative stress. J Neurosci Res 2003;71(1):46-63.

262. Zhao L, Lin S, Bales KR, Gelfanova V, Koger D, Delong C, Hale J, Liu F, Hunter JM, Paul SM. Macrophage-mediated degradation of beta-amyloid via an apolipoprotein E isoform-dependent mechanism. J Neurosci 2009;29(11):3603-3612.

263. Shoji M, Golde TE, Ghiso J, Cheung TT, Estus S, Shaffer LM, Cai XD, McKay DM, Tintner R, Frangione B, et al. Production of the Alzheimer amyloid beta protein by normal proteolytic processing. Science 1992;258(5079):126-129.

264. Thompson PM, Hayashi KM, de Zubicaray G, Janke AL, Rose SE, Semple J, Herman D, Hong MS, Dittmer SS, Doddrell DM, Toga AW. Dynamics of gray matter loss in Alzheimer's disease. J Neurosci 2003;23(3):994-1005.

265. Thompson PM, Mega MS, Woods RP, Zoumalan CI, Lindshield CJ, Blanton RE, Moussai J, Holmes CJ, Cummings JL, Toga AW. Cortical change in Alzheimer's disease detected with a disease-specific population-based brain atlas. Cereb Cortex 2001;11(1):1-16.

266. Dwyer BE, Zacharski LR, Balestra DJ, Perry G, Smith MA, Zhu X. Getting the iron out: Phlebotomy for Alzheimer's disease? Med Hypotheses 2009.

267. Haidari M, Javadi E, Sanati A, Hajilooi M, Ghanbili J. Association of increased ferritin with premature coronary stenosis in men. Clin Chem 2001;47(9):1666-1672.

268. Zacharski LR, Chow B, Lavori PW, Howes PS, Bell MR, DiTommaso MA, Carnegie NM, Bech F, Amidi M, Muluk S. The iron (Fe) and atherosclerosis study (FeAST): a pilot study of reduction of body iron stores in atherosclerotic peripheral vascular disease. Am Heart J 2000;139(2 Pt 1):337-345.

269. Zacharski LR, Ornstein DL, Woloshin S, Schwartz LM. Association of age, sex, and race with body iron stores in adults: analysis of NHANES III data. Am Heart J 2000;140(1):98-104.

270. Rogers JT, Randall JD, Cahill CM, Eder PS, Huang X, Gunshin H, Leiter L, McPhee J, Sarang SS, Utsuki T, Greig NH, Lahiri DK, Tanzi RE, Bush

AI, Giordano T, Gullans SR. An iron-responsive element type II in the 5'-untranslated region of the Alzheimer's amyloid precursor protein transcript. J Biol Chem 2002;277(47):45518-45528.

271. Castellani RJ, Moreira PI, Liu G, Dobson J, Perry G, Smith MA, Zhu X. Iron: the Redox-active center of oxidative stress in Alzheimer disease. Neurochem Res 2007;32(10):1640-1645.

272. Malecki EA, Cable EE, Isom HC, Connor JR. The lipophilic iron compound TMH-ferrocene [(3,5,5-trimethylhexanoyl)ferrocene] increases iron concentrations, neuronal L-ferritin, and heme oxygenase in brains of BALB/c mice. Biol Trace Elem Res 2002;86(1):73-84.

273. Cable EE, Connor JR, Isom HC. Accumulation of iron by primary rat hepatocytes in long-term culture: changes in nuclear shape mediated by non-transferrin-bound forms of iron. Am J Pathol 1998;152(3):781-792.

274. Nielsen P, Heinelt S, Dullmann J. Chronic feeding of carbonyl-iron and TMH-ferrocene in rats. Comparison of two iron-overload models with different iron absorption. Comp Biochem Physiol C 1993;106(2):429-436.

275. Cable EE, Isom HC. Metabolism of 3,5,5-trimethylhexanoyl-ferrocene by rat liver: release of iron from 3,5,5-trimethylhexanoyl-ferrocene by a microsomal, phenobarbital-inducible cytochrome P-450. Drug Metab Dispos 1999;27(2):255-260.

276. Nielsen P, Heinrich HC. Metabolism of iron from (3,5,5-trimethylhexanoyl)ferrocene in rats. A dietary model for severe iron overload. Biochem Pharmacol 1993;45(2):385-391.

277. Braumann A, Wulfhekel U, Nielsen P, Balkenhol B, Dullmann J. Pattern of iron storage in the rat heart following iron overloading with trimethylhexanoyl-ferrocene. Acta Anat (Basel) 1994;150(1):45-54.

278. Minty EP, Bjarnason TA, Laule C, MacKay AL. Myelin water measurement in the spinal cord. Magn Reson Med 2009;61(4):883-892.

279. Schubert D, Chevion M. The role of iron in beta amyloid toxicity. Biochem Biophys Res Commun 1995;216(2):702-707.

280. Marlatt M, Lee HG, Perry G, Smith MA, Zhu X. Sources and mechanisms of cytoplasmic oxidative damage in Alzheimer's disease. Acta Neurobiol Exp (Wars) 2004;64(1):81-87.

281. Smith MA, Harris PL, Sayre LM, Perry G. Iron accumulation in Alzheimer disease is a source of redox-generated free radicals. Proc Natl Acad Sci U S A 1997;94(18):9866-9868.

282. Exley C. Aluminium and iron, but neither copper nor zinc, are key to the precipitation of beta-sheets of Abeta_{42} in senile plaque cores in Alzheimer's disease. J Alzheimers Dis 2006;10(2-3):173-177.

283. House E, Collingwood J, Khan A, Korchazkina O, Berthon G, Exley C. Aluminium, iron, zinc and copper influence the in vitro formation of amyloid fibrils of Abeta42 in a manner which may have consequences for metal chelation therapy in Alzheimer's disease. J Alzheimers Dis 2004;6(3):291-301.

284. Mantyh PW, Ghilardi JR, Rogers S, DeMaster E, Allen CJ, Stimson ER, Maggio JE. Aluminum, iron, and zinc ions promote aggregation of

physiological concentrations of beta-amyloid peptide. J Neurochem 1993;61(3):1171-1174.

285. Yang QX, Williams GD, Demeure RJ, Mosher TJ, Smith MB. Removal of local field gradient artifacts in T2*-weighted images at high fields by gradient-echo slice excitation profile imaging. Magn Reson Med 1998;39(3):402-409.

286. Stanisz GJ, Odrobina EE, Pun J, Escaravage M, Graham SJ, Bronskill MJ, Henkelman RM. T1, T2 relaxation and magnetization transfer in tissue at 3T. Magn Reson Med 2005;54(3):507-512.

287. Krebs MR, Bromley EH, Donald AM. The binding of thioflavin-T to amyloid fibrils: localisation and implications. J Struct Biol 2005;149(1):30-37.

288. LeVine H, 3rd. Thioflavine T interaction with synthetic Alzheimer's disease beta-amyloid peptides: detection of amyloid aggregation in solution. Protein Sci 1993;2(3):404-410.

289. Khurana R, Coleman C, Ionescu-Zanetti C, Carter SA, Krishna V, Grover RK, Roy R, Singh S. Mechanism of thioflavin T binding to amyloid fibrils. J Struct Biol 2005;151(3):229-238.

290. Brändén C-I, Tooze J. Introduction to protein structure. New York: Garland Pub.; 1991. xv, 302 p. p.

291. Perl DP, Good PF. Comparative techniques for determining cellular iron distribution in brain tissues. Ann Neurol 1992;32 Suppl:S76-81.

292. Meguro R, Asano Y, Odagiri S, Li C, Iwatsuki H, Shoumura K. The presence of ferric and ferrous iron in the nonheme iron store of resident macrophages in different tissues and organs: histochemical demonstrations by the perfusion-Perls and -Turnbull methods in the rat. Arch Histol Cytol 2005;68(3):171-183.

293. Nguyen-Legros J, Bizot J, Bolesse M, Pulicani JP. ["Diaminobenzidine black" as a new histochemical demonstration of exogenous iron (author's transl)]. Histochemistry 1980;66(3):239-244.

294. Josephy PD, Eling TE, Mason RP. Co-oxidation of benzidine by prostaglandin synthase and comparison with the action of horseradish peroxidase. J Biol Chem 1983;258(9):5561-5569.

295. Schmued LC, Albertson C, Slikker W, Jr. Fluoro-Jade: a novel fluorochrome for the sensitive and reliable histochemical localization of neuronal degeneration. Brain Res 1997;751(1):37-46.

296. Schmued LC, Hopkins KJ. Fluoro-Jade: novel fluorochromes for detecting toxicant-induced neuronal degeneration. Toxicol Pathol 2000;28(1):91-99.

297. Schmued LC, Hopkins KJ. Fluoro-Jade B: a high affinity fluorescent marker for the localization of neuronal degeneration. Brain Res 2000;874(2):123-130.

Curriculum Vitae
Mark D. Meadowcroft

Academic Background

1995 – 1999   Bachelor of Science, Biology and Psychology
                     Allegheny College, Meadville, Pa

2001 – Present   Ph.D. Candidate, Graduate Program in Neuroscience
                     Department of Neural and Behavioral Sciences
                     Pennsylvania State University – College of Medicine, Hershey, Pa

Research Experience

2001 – Present   Pre-doctoral Fellow/ Ph. D. Research,
                     Department of Radiology, Pennsylvania State University, Hershey
                     Medical Center, Hershey, Pa.

1998 – 1999   Undergraduate Comprehensive Project:
                     Departments of Biology and Psychology,
                     Allegheny College, Meadville, Pa.

Publications

Meadowcroft, M.D., Zhang, S., Liu, W., Park, B.S., Connor, J. R.,Collins, C. M., Smith, M. B., and Yang, Q. X., "Direct Magnetic Resonance Imaging of Histological Tissue Samples at 3.0 T" Magnetic Resonance in Medicine. 2007 May; 57(5): 835-41.

Meadowcroft, M.D., Connor, J. R., Smith, M. B., and Yang, Q. X., "MRI and histological analysis of beta-amyloid plaques in both human Alzheimer's disease and APP/PS1 transgenic mice" Journal of Magnetic Resonance Imaging. 2009; 29(5): 997-1007

Bigler, D.C., **Meadowcroft, M. D.**, Sun, X., Vesek J., Dresner, A., Smith, M. B., and Yang, Q. X., "MR Parameter Map Suite: ITK Classes for Calculating Magnetic Resonance T2 and T1 Parameter Maps" The Insight Journal – 2008 January - June

Qing X. Yang, Jianli Wang, Michael B. Smith, **Mark Meadowcroft**, Paul Eslinger, Xiaoyu Sun, Peter C.M. van Zijl, and Xavier Golay. "Reduction of magnetic field inhomogeneity artifacts in echo planar imaging with SENSE and GESEPI at high field" Magnetic Resonance in Medicine. 2004 Dec;52(6): 1418-23.

Meadowcroft, M. D., Connor, J. R., Smith, M. B., and Yang Q. X., "Histological and Cellular Differences Between Beta-Amyloid Plaques in APP/PS1 Transgenic Mice and Human Alzheimer's Disease" *In submission*.

Park, B. S., **Meadowcroft, M. D.**, Collins, C. M., Bigler, D. C., Sun, X., Smith, M.B., Yang, Q.X., "RF coil design for MRI of Histological Tissue samples at 7.0 T" *In preparation.*

Yang, Q.X., Eslinger, P.J., Zimmerman, E. K., Grunfeld, R., Vesek, J., **Meadowcroft, M.D.**, Smith, M.B., Wang, J., Connor, J.R. "fMRI Investigation of Central Olfactory Deficit in Early Alzheimer's Disease" *In preparation.*

Robinson, M., Wang, J., Eslinger, P.J., **Meadowcroft, M. D.**, Xavier, G., Yang, Q.X. "The Bold Signal Response Differences Between Encoding and Recognition Memory of Face-Name Associations" *In preparation.*